Comptes Rendus
de l'Académie des sciences

Géoscience
Sciences de la Planète

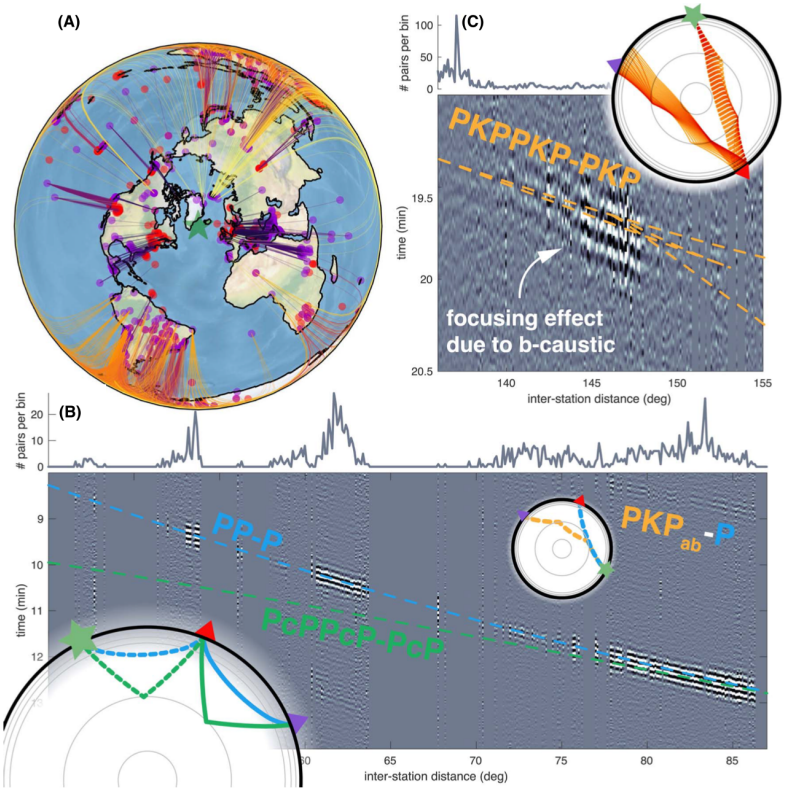

Volume 356, Special Issue S4, 2024

Special issue / *Numéro spécial*

New Developments in Passive Seismic Imaging and Monitoring / *Nouveaux développements dans le domaine de l'imagerie et de la surveillance sismique passive*

Guest editors / *Rédacteurs en chef invités*

Michel Campillo, Andrew Curtis, Anne Obermann, Nikolai Shapiro

ACADÉMIE DES SCIENCES
INSTITUT DE FRANCE

Académie des sciences — Paris

ISSN: 1778-7025 (electronic)

CENTRE MERSENNE

Comptes Rendus

Géoscience

Objective of the journal

Comptes Rendus Géoscience — Sciences de la Planète is an international peer-reviewed electronic journal, covering all areas of earth sciences and sustainable development.

It publishes original research articles, review articles, historical perspectives, pedagogical texts or conference proceedings, without length limit, in English or in French and in a format as flexible as necessary (figures, associated data, etc.).

Comptes Rendus Géoscience — Sciences de la Planète is published since 2020 with the centre Mersenne pour l'édition scientifique ouverte (Mersenne Center for open scientific publishing), according to a virtuous Diamond Open Access policy, free for authors (no author processing charges nor publishing fees) as well as for readers (immediate and permanent open access).

About the journal

Comptes Rendus Géoscience — Sciences de la Planète is published exclusively in electronic format. All information on the journal, as well as the full text of all articles, is available on its website at: https://comptes-rendus.academie-sciences.fr/geoscience/.

Author enquiries

For any inquiries about submitting a manuscript, please refer to the journal's website: https://comptes-rendus.academie-sciences.fr/geoscience/.

Contact

Académie des sciences
23 quai de Conti
75006 Paris (France)
cr-geoscience@academie-sciences.fr

Comptes Rendus
Géoscience — Sciences de la Planète
2024, 356, nº S4

Contents / *Sommaire*

ACADÉMIE DES SCIENCES
INSTITUT DE FRANCE

Comptes Rendus. Géoscience — Sciences de la Planète
2024, Vol. 356, Special issue S4, p. 1-3
https://doi.org/10.5802/crgeos.281

Foreword

New Developments in Passive Seismic Imaging and Monitoring

Foreword to New developments in passive seismic imaging and monitoring

Nikolai M. Shapiro [a], **Michel Campillo** [a], **Anne Obermann** [b] **and Andrew Curtis** [c]

[a] Institut des Sciences de la Terre, University Grenoble Alpes, CNRS, University Savoie Mont Blanc, IRD, University Gustave Eiffel, Grenoble, France

[b] Swiss Seismological Service, ETH Zurich, Switzerland

[c] School of GeoSciences, University of Edinburgh, Edinburgh EH9 3FE, UK

E-mails: nikolai.shapiro@univ-grenoble-alpes.fr (N. M. Shapiro), michel.campillo@univ-grenoble-alpes.fr (M. Campillo), anne.obermann@sed.ethz.ch (A. Obermann), andrew.curtis@ed.ac.uk (A. Curtis)

Funding. ERC Advanced Grants F-Image, SEISMAZE, FaultScan.

During the last two decades, imaging and monitoring methods based on cross-correlations of ambient seismic noise have been extensively developed and have become widely used at different scales and in different natural and human-controlled environments. Application of these methods has been facilitated by improved availability of data from large and dense seismic networks and by several open software packages. At the same time, noise-based imaging and monitoring is far from becoming just a set of "standard" and "routine" methods. As discussed in this special issue, the origin and nature of the seismic noise wavefields, their correlation properties as well as their sensitivity to the medium structure and changes, remain areas of active study. Improving their understanding is necessary in order to refine the existing methods and to develop new approaches for imaging and monitoring. Therefore, noise-based passive seismology remains a dynamic field of research with some first-order problems yet to be solved. In this context, 13 years after the first thematic issue of Comptes Rendus Géoscience on passive seismic noise-based imaging and monitoring [e.g., Campillo et al., 2011] we introduce a new special issue devoted to this topic.

Most passive noise-based seismic imaging and monitoring methods are based on the so-called "noise cross-correlation theorem" [e.g., Lobkis and Weaver, 2001, Wapenaar, 2004, Roux et al., 2005, Campillo, 2006, Gouédard et al., 2008] which states that the time derivative of cross-correlation of an ideal fully diffuse wavefield converge to the Green's function of the medium in which the waves are propagating. The fully diffuse wavefield can be defined either as being composed of all possible medium vibration modes with equally partitioned energy, or locally as composed of isotropic combination of plane waves, or as generated by homogenously distributed random sources. Neither of these definitions applies to the real Earth's seismic noise whose main sources are inhomogeneously distributed over the surface. This makes direct application of the "full" cross-correlation theorem to real seismological data questionable, and requires that we further improve our understanding of seismic noise cross-correlations to develop accurate methods.

So far, the surface wave part of Green's functions has been most reliably reconstructed from the correlations of the ambient seismic noise. Since initial demonstration of this possibility [e.g., Shapiro

and Campillo, 2004, Shapiro et al., 2005, Sabra et al., 2005a,b] a family of methods known as Ambient Noise Surface Wave Tomography (ANSWT) has been developed and successfully applied in many studies [e.g., Ritzwoller et al., 2011, Shapiro, 2018]. A systematic application of this approach to image the European Alps is presented by Paul et al. [2024]. The authors show how methodological advances of this approach evolving from simple isotropic group velocity tomography to wave-equation based inversions, and those based on trans-dimensional Bayesian formalism and including anisotropy, significantly improved knowledge of the structure of the crust and shallow mantle beneath the Alps-Apennines system.

Giammarinaro et al. [2024] use two-dimensional simulations of wave propagation to investigate the lateral resolution power of an alternative approach to ANSWT: seismic Rayleigh wave focal spot imaging. They demonstrate that the station configuration can be tuned to improve image quality and properties, and that high-quality data from dense networks can result in super-resolution.

Lavoué et al. [2024] investigate the applicability of the ANSWT at small scales, i.e., those of a single sedimentary basin, to resolve the near-surface structure for estimation of site amplifications required for seismic hazard models. They show that, while ANSWT results reproduce well the main geological structures of the basin, they have limited capability to accurately predict the numerical amplification near the basin edges and other locations with significant 3D wave propagation effects. This allows the authors to suggest perspectives for future improvement of ANSWT, that shows promise for site effect assessment in low- to moderate-seismicity contexts.

Boué and Tomasetto [2024] investigate how the teleseismic body waves are generated by oceanic forcing on the Earth's surface, resulting in a spatially inhomogeneous distribution of microseismic sources. The authors show that, despite the inherent complexity of these noise sources, cross-correlation based methods applied to properly selected pairs of stations result in the isolation of coherent waves for imaging applications and propose a workflow based on ocean sea state models to extract robust interferences.

Influence of the heterogeneous distribution of noise sources on the accuracy of noise-based seismic monitoring is studied by Stehly et al. [2024] who perform a single station analysis at all available European broadband stations. They show that at short periods (<3 s), the noise field in Europe is dominated by surface waves coming from two sources: (1) the north Atlantic Ocean dominating during winters, and (2) the Adriatic and Aegean Seas increasing in summer. The interplay of these two source regions leads to time and space dependent convergence of the coda part of cross-correlations, and thus in across-Europe variations of the accuracy and temporal resolution of detected seismic velocity changes.

Other important aspects of the noise-based seismic monitoring are addressed by Canel et al. [2024] who investigate the physical mechanisms that could explain the seismic velocity changes measured from the noise cross-correlations in the vicinity of active fault zones. The authors perform a set of numerical experiments to test a simple model of a cohesive granular medium and to study the relationship between the damage and velocity of elastic waves. They show that the microscopic deformation of cohesive discrete media quickly becomes very heterogeneous with a small amount of damage inducing a strong decrease in the elastic velocity. As a consequence, they suggest that monitoring the wave velocities in such media could measure subtle transient deformation processes, such as earthquake initiation phases.

Acknowledgments

The content of the present thematic Issue was discussed during the 6th edition of the school on Passive Imaging and Monitoring in Wave Physics: From Seismology to Ultrasound, that was held on April 18–22, 2022 at the Institut d'Études Scientifiques de Cargèse in Corsica, France. We thank the contributors of the special issue and the participants to the workshop as well as all people who contributed to its logistics. The workshop and the organization of this issue were made possible by the support of CNRS (France), and Université Grenoble Alpes (Grenoble, France). The authors acknowledge support from the ERC Advanced Grants F-Image, SEISMAZE, and FaultScan.

References

Boué, P. and Tomasetto, L. (2024). Opportune detections of global P-wave propagation from microseisms interferometry. *C. R. Géosci.*, 356(S4), 85–100.

Campillo, M. (2006). Phase and correlation in 'random' seismic fields and the reconstruction of the green function. *Pure Appl. Geophys.*, 163, 475–502.

Campillo, M., Sato, H., Shapiro, N. M., and van der Hilst, R. D. (2011). New developments on imaging and monitoring with seismic noise. *C. R. Géosci.*, 343(8–9), 487–495.

Canel, V., Campillo, M., Jia, X., and Ionescu., I. R. (2024). Damage in cohesive granular materials: simulations and geophysical implications. *C. R. Géosci.*, 356(S4), 125–145.

Giammarinaro, B., Tsarsitalidou, C., and Hillers, G. (2024). Investigating the lateral resolution of the Rayleigh wave focal spot imaging technique using two-dimensional acoustic simulations. *C. R. Géosci.*, 356(S4), 41–57.

Gouédard, P., Stehly, L., Brenguier, F., et al. (2008). Cross-correlation of random fields: mathematical approach and applications. *Geophys. Prospect.*, 56, 375–393.

Lavoué, F., Froment, B., Gélis, C., et al. (2024). Potential and limitations of noise-based surface-wave tomography for numerical site effect estimation: a case study in the French Rhône valley. *C. R. Géosci.*, 356(S4), 59–84.

Lobkis, O. I. and Weaver, R. L. (2001). On the emergence of the Green's function in the correlations of a diffuse field. *J. Acoust. Soc. Am.*, 110(6), 3011–3017.

Paul, A., Pedersen, H. A., Bodin, T., Kästle, E., Soergel, D., Alder, C., Lu, Y., and Nouibat, A. (2024). Methodological advances in seismic noise imaging of the Alpine area. *C. R. Géosci.*, 356(S4), 5–39.

Ritzwoller, M. H., Lin, F.-C., and Shen, W. (2011). Ambient noise tomography with a large seismic array. *C. R. Géosci.*, 343(8), 558–570.

Roux, P., Sabra, K. G., Kuperman, W. A., and Roux, A. (2005). Ambient noise cross correlation in free space: Theoretical approach. *J. Acoust. Soc. Am.*, 117(1), 79–84.

Sabra, K. G., Gerstoft, P., Roux, P., Kuperman, W. A., and Fehler, M. C. (2005a). Extracting time-domain Green's function estimates from ambient seismic noise. *Geophys. Res. Lett.*, 32, article no. L03310.

Sabra, K. G., Gerstoft, P., Roux, P., Kuperman, W. A., and Fehler, M. C. (2005b). Surface wave tomography from microseisms in Southern California. *Geophys. Res. Lett.*, 32, article no. L14311.

Shapiro, N. M. (2018). Applications with surface waves extracted from ambient seismic noise. In Nakata, N., Gualtieri, L., and Fichtner, A., editors, *Seismic Ambient Noise*. Cambridge University Press, Cambridge.

Shapiro, N. M. and Campillo, M. (2004). Emergence of broadband Rayleigh waves from correlations of the ambient seismic noise. *Geophys. Res. Lett.*, 31, article no. L07614.

Shapiro, N. M., Campillo, M., Stehly, L., and Ritzwoller, M. H. (2005). High resolution surface wave tomography from ambient seismic noise. *Science*, 307, 1615–1618.

Stehly, L., Delouche, E., Tomasetto, L., and Ranjan, P. (2024). Dynamic of seismic noise sources in the Mediterranean Sea: implication for monitoring using noise correlations. *C. R. Géosci.*, 356(S4), 101–124.

Wapenaar, K. (2004). Retrieving the elastodynamic Green's function of an arbitrary inhomogeneous medium by cross correlation. *Phys. Rev. Lett.*, 93(25), article no. 254301.

ACADÉMIE DES SCIENCES
INSTITUT DE FRANCE

Comptes Rendus. Géoscience — Sciences de la Planète
2024, Vol. 356, Special issue S4, p. 5-39
https://doi.org/10.5802/crgeos.261

Research article

New Developments in Passive Seismic Imaging and Monitoring

Methodological advances in seismic noise imaging of the Alpine area

Anne Paul[*,a], **Helle A. Pedersen**[a], **Thomas Bodin**[b], **Emanuel Kästle**[c], **Dorian Soergel**[a], **Chloé Alder**[b], **Yang Lu**[a] **and Ahmed Nouibat**[a]

[a] Univ. Grenoble Alpes, Univ. Savoie Mont Blanc, CNRS, IRD, UGE, ISTerre, Grenoble, France

[b] Univ. Lyon, Univ. Lyon 1, ENSL, UJM-Saint-Etienne, CNRS, LGL-TPE, F-69622, Villeurbanne, France

[c] Institute of Geological Sciences, Freie Universität Berlin, Berlin, Germany

Current addresses: Berkeley Seismological Laboratory, University of California, Berkeley, CA 94720, USA (D. Soergel), Department of Meteorology and Geophysics, University of Vienna, Vienna, Austria (Y. Lu), ITES-EOST, CNRS/Université de Strasbourg, 67000 Strasbourg, France (A. Nouibat)

E-mails: anne.paul@univ-grenoble-alpes.fr (A. Paul), helle.pedersen@univ-grenoble-alpes.fr (H. A. Pedersen), thomas.bodin@ens-lyon.fr (T. Bodin), emanuel.kaestle@fu-berlin.de (E. Kästle), soergeldorian@gmail.com (D. Soergel), chloe.alder@gmx.fr (C. Alder), yang.lu@univie.ac.at (Y. Lu), ahmed.nouibat@univ-grenoble-alpes.fr (A. Nouibat)

Abstract. Methodological advances in seismic tomography are often driven by the quality of data sets. The dense and homogeneous spatial coverage of the AlpArray seismic network, including hundreds of permanent and temporary broadband stations, has motivated a series of methodological developments of ambient-noise-based tomography of the lithosphere across the entire Alps-Apennines regions, which have been published and are reviewed here. To take full advantage of the ocean-bottom seismometers (OBS) in the Ligurian-Provence basin, reconstructed Rayleigh wave signals between OBS have been improved by second-order correlations with onland stations. A Bayesian or fully trans-dimensional formalism has been introduced in both steps of isotropic ambient noise tomography. The three-dimensional S-wave velocity models have been further improved by wave-equation based inversions accounting for the physics of seismic wave propagation, including elastic–acoustic coupling at the sea bottom. A beamforming approach has been developed to avoid systematic errors in the measurement of azimuthal anisotropy from seismic noise. Probabilistic inversions for depth variations of azimuthal and radial anisotropy have provided robust estimates of anisotropic parameters in the crust and upper mantle that differ significantly from earlier surface-wave tomography studies. These methodological improvements have taken the full benefit of the quality of available seismic data to significantly improve knowledge of the seismic structure of the crust and shallow mantle beneath the Alps-Apennines system. Our findings include detailed mapping of strong and abrupt Moho depth changes under the Western Alps, contrasting orientations of fast velocity directions between the upper and lower Alpine crust, and the absence of significant radial anisotropy everywhere in the European

[*] Corresponding author

crust and shallow upper mantle, except in the Apenninic lower crust. These methods can be applied to similar dense arrays with equivalent potential benefits.

Keywords. Seismic tomography, Ambient noise, Bayesian inversion, Seismic anisotropy, Lithospheric structure, European Alps.

Funding. Agence Nationale de la Recherche, France (contract ANR-15-CE31-0015), Labex OSUG@2020 (Investissement d'Avenir, ANR-10-LABX-56), European Research Council under the European Union Horizon 2020 research and innovation program (grant agreement no. 716542 – TRANSCALE), project LisAlps (contract ANR-20-CE49-0007), German Science Foundation DFG (SPP-2017, Project Ha 2403/21-1).

Manuscript received 25 October 2023, revised 19 April 2024, accepted 26 April 2024.

1. Introduction

The Alpine mountain range is part of the continental collision ranges created by the convergence of the Eurasian and African plates in the Mediterranean region. It results from the subduction of the Alpine Tethys under the Adriatic microplate since the Late Cretaceous, and the subsequent continental collision between the European and Adriatic paleomargins in the Cenozoic [e.g., Handy et al., 2010]. The Alpine belt is an outstanding example of subduction and continental collision studies, which has been investigated by geologists for more than 150 years. Several major concepts of modern geology have been developed in the Alps, such as nappes, when the prominence of horizontal over vertical displacements was proposed by Emile Argand [Argand, 1922]. More recently, the identification of coesite, which is a high-pressure polymorph of quartz, in gneisses of the Dora Maira massif (south-western Alps, Italy) led Chopin [1984] to propose that continental crust may be subducted to depths of 90 km or more. The amount of geological knowledge about the Alps is unparalleled in any other mountain range, and they provide a unique natural laboratory to advance our understanding of orogenesis and its relationship to present and past mantle dynamics. The Alpine mountain belt is also a populated area where millions of Europeans are affected by its topography, geology and associated natural hazards such as earthquakes or landslides. Yet, accurate information on the lithospheric structure of that emblematic and populated mountain range was hampered by insufficient and spatially heterogeneous geophysical data until the last few years. Filling that gap was the primary motivation for the AlpArray initiative, which gathered a large number of European research institutions to deploy a dense and homogeneous temporary broadband seismological network over the Alps and its forelands to complement the permanent networks [Hetényi et al., 2018a].

In addition to gaining knowledge of Alpine lithospheric structure, the high spatial coverage of AlpArray temporary stations and permanent networks has given us the opportunity to develop new methods of seismic tomography at this large regional scale based on ambient noise. A review of these methodological developments is gathered in this paper because they could be applied with great benefit to other similary dense networks.

1.1. *Seismic imaging in the Alps*

Seismic imaging is an essential complement to geological studies to build lithospheric-scale interpretive models and improve the understanding of the dynamics of the mountain belt in space and time. The geometry and depth of the crust-mantle boundary, only accessible with geophysics and in particular active-source seismology and earthquake seismology, are key information for geological and geodynamic modeling. Each of these methods has limitations and provides partial information, which is why noise-based tomography methods are a valuable complement. In the Alps, deep seismic sounding (DSS) experiments including ECORS-CROP in the Western Alps [e.g., Nicolas et al., 1990], NFP-20 in the Central Alps [e.g., Frei et al., 1990], and TRANSALP in the Eastern Alps [e.g., Lüschen et al., 2006] provided crucial data for interpretive crustal-scale sections along a number of crooked lines mostly transverse to the belt. The results from these localised studies cannot be extrapolated to other locations along the belt due to its arcuate, non-cylindrical geometry. DSS profiles provide high-frequency reflectivity images of the crust, hence sharp and subhorizontal velocity contrasts with no or poor information on absolute velocities. Thus, they can-

not be interpreted in terms of petrology. Moreover, the European Moho, defined as the base of the highly reflective lower crust, was not detected below the intensely deformed and highly heterogeneous crust of the internal zones in the ECORS-CROP and NFP-20 W5 and E1 profiles across the Western and Central Alps [e.g., Nicolas et al., 1990, Marchant and Stampfli, 1997]. The deep European Moho has only been detected by the ECORS-CROP wide-angle seismic reflection experiment under part of the internal zones to a maximum depth of 55 km [ECORS-CROP Deep Seismic Sounding Group, 1989].

A similar type of information on velocity contrasts beneath seismic stations is provided at lower frequencies by receiver function (RF) analysis in particular for Moho depth estimates [e.g., Kummerow et al., 2004, Lombardi et al., 2008, Zhao et al., 2015, Hetényi et al., 2018b, Paul et al., 2022, Michailos et al., 2023]. In some specific cases, such as in the presence of a very heterogeneous, scattering crust, receiver function analysis can be more effective at detecting the crust-mantle boundary than reflection seismics because it uses low-frequency, high-energy waves from teleseismic earthquakes that travel across the heterogeneous crust only once. Moreover, receiver functions computed for station arrays provide estimates of Moho depth with 2-D coverage. Indeed, Spada et al. [2013] generated a Moho depth map of Italy, including the Alpine region, which combines DSS data with receiver functions. Spada et al. [2013]'s model displays three Moho surfaces, European, Adriatic-Ionian and Ligurian–Corsican–Sardinian–Tyrrhenian. As this model allows only one Moho at a given location, the Moho surfaces never overlap, even though the European lithosphere is known to underthrust Adria.

The polarity of converted waves in receiver functions provides useful information on the sign of velocity change with depth. For example, Zhao et al. [2015] observed negative-polarity P-to-S converted waves in RF of the CIFALPS profile close to the so-called Ivrea body positive Bouguer anomaly (blue line in Figure 1). This gravity anomaly high is known since the first geophysical experiments in the Alps that also reported high-velocity refracted waves (V_p = 7.4 km/s) at 10 km depth in the same area of the Italian Piemonte region [Closs and Labrouste, 1963]. The source of this gravity and seismic velocity anomaly is called the Ivrea body and it is interpreted as a slice of Adriatic upper mantle at unusually shallow depth [e.g., Nicolas et al., 1990]. The negative-polarity converted phases in the RF of the CIFALPS profile were the first evidence for the inverted Moho beneath the Ivrea body, as the contact between the high-velocity Adriatic mantle wedge on top and the lower velocity European crust or subduction interface below [Zhao et al., 2015]. These negative-polarity converted waves from 20–60 km depth and the positive-polarity conversions at 75–80 km depth were the first seismic evidence for continental subduction of the European lithosphere beneath Adria, according to Zhao et al. [2015]. Like deep seismic sounding, however, receiver functions yield no clues on absolute velocities.

Local earthquake tomography (LET), which relies on the inversion of body-wave arrival times (mostly direct P and S waves) from local earthquakes for absolute velocities (V_p and V_s or V_p/V_s) is an efficient tool to get 3-D images and complement 2-D DSS or receiver function reflectivity images. The size of the imaged crustal volume and the resolution of the tomography depend on the distribution of seismic stations at the surface and earthquake hypocenters at depth. In the Alps, the seismicity level is low to moderate, with rare events of magnitude >5. Many years of recording are therefore required to reach sufficient ray coverage in local earthquake tomography studies of the whole Alpine region like in Diehl et al. [2009]: 12 years (1996–2007) for 1500 events of $M_l > 2.5$. Another issue is that most earthquake sources in the Alps are shallow (focal depths < 15 km), except in the westernmost part of the Po basin where hypocenters on the Rivoli-Marene fault reach 70–80 km depth [Eva et al., 2015]. Due to low magnitudes, these deep events are only detected by stations close to epicenters. They, however, proved useful to image the deep parts of the subduction wedge of the western Alps by LET including the high-velocity Ivrea body [Solarino et al., 1997, Paul et al., 2001, Solarino et al., 2018, Virieux et al., 2024]. Imaging the crust to Moho depth with LET in most of the Alps requires records of Pn waves, thus sufficient-magnitude earthquakes and station arrays of large spatial extent. Until recent years, this last condition was only reached by compiling records of a large number of regional and national networks with heterogeneous data sharing policies and traveltime picking strategies, at the cost

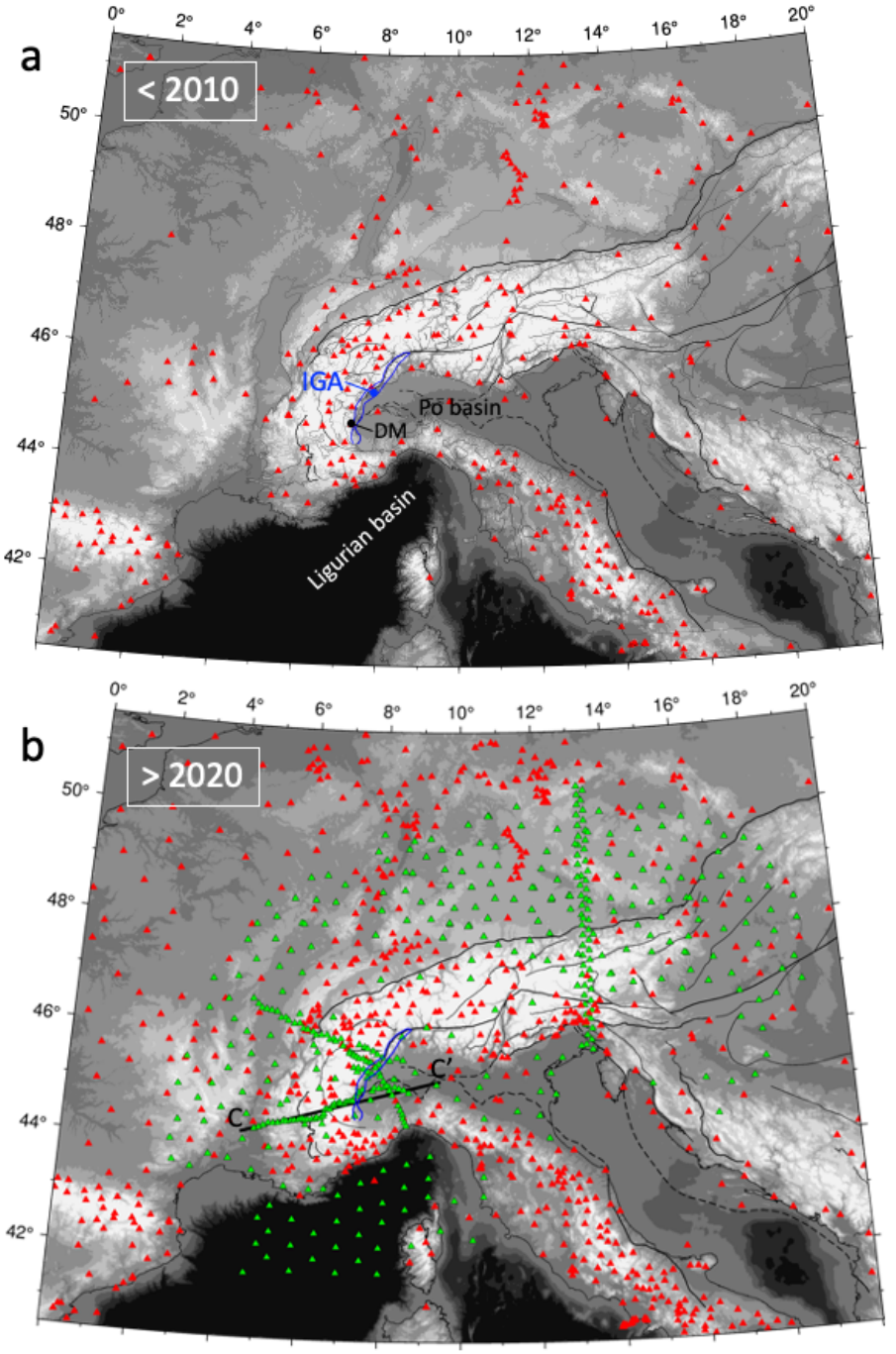

Figure 1. Maps of broadband seismic stations in the Alps and surrounding regions including all stations used in the studies discussed in Sections 2–3; (a) before 2010: red triangles are public permanent stations in 2009; (b) after 2020: red triangles are permanent stations in 2019; green triangles are temporary stations used in the studies described in this paper (EASI, AlpArray, CIFALPS and CIFALPS-2). The blue line in (a) and (b) is the 0 mgal contour of the Ivrea Bouguer anomaly. Black lines: main geological units and faults from the tectonic map compiled by M. R. Handy. The thick black line CC′ is the CIFALPS profile used in Figure 3. DM: Dora Maira massif; IGA: Ivrea gravity anomaly.

of heavy homogenization work [13 networks used in Diehl et al., 2009, Bagagli et al., 2022, and Virieux et al., 2024].

In addition to low-to-moderate seismicity and heterogeneous coverage of permanent seismic networks, the strong crustal heterogeneity and its very 3-D character are other challenges in seismic tomography of the Alpine lithosphere. Crustal heterogeneity is not surprising for a collisional belt with a long tectonic history. However, the arcuate shape of the western Alps, the presence of large and deep basins including the Po basin and its unconsolidated sediment layers and high level of anthropogenic noise close to the heart of the belt make seismic imaging of the Alpine lithosphere particularly challenging.

Since Aki et al. [1977], the most basic and often used method to image seismic heterogeneities in the upper mantle is teleseismic tomography. It is based on the inversion of observed relative arrival times of P (or S) waves generated by earthquakes at teleseismic distances (>20°) for relative variations of P (or S) wave velocity (V_p, or V_s) in the upper mantle beneath a seismic array. Teleseismic tomography has been widely used to image fast-velocity slabs interpreted as subducted continental and/or oceanic lithosphere in the Alpine upper mantle [e.g., Lippitsch et al., 2003, Piromallo and Morelli, 2003, Zhao et al., 2016a, Paffrath et al., 2021]. Contrasting results of these mantle tomography studies have led to controversies about the geometry of the slabs at depth, including whether the European slab is attached or detached in the western Alps [e.g., Zhao et al., 2016a], or whether Europe is the upper or lower plate in the eastern Alps [e.g., Lippitsch et al., 2003]. These questions are still of the utmost importance to understand the past and present dynamics of the mountain belt. A major issue for teleseismic tomography is the difficulty in separating the contribution of the crust from that of the mantle in arrival times for near-vertical ray paths [e.g., Waldhauser et al., 2002]. This is of particular importance in mountain ranges such as the Alps due to strong changes in crustal thickness.

The mantle structure can also be imaged with teleseismic surface-wave tomography [e.g., El-Sharkawy et al., 2020]. Frequency-dependent traveltime data of surface waves are inverted for S-wave velocity as for ambient-noise tomography, but using periods >30 s. To overcome the poor sensitivity of such long period surface waves to crustal structure, Kästle et al. [2018] have jointly inverted dispersion data from ambient noise correlations in the short-period band (8–30 s) with data from teleseismic surface-wave records at longer periods. The horizontal resolution of the resulting shear-wave velocity models however remains rather low in the upper mantle, limiting the value of this type of model in the debates on slab geometry beneath the Alpine range.

1.2. *Ambient noise imaging in the Alps before AlpArray*

Ambient noise tomography (ANT) is particularly well suited to imaging the Alpine crust as a complement to the methods outlined in the previous section because (a) it does not require local earthquakes [Shapiro et al., 2005], and (b) the period range of seismic noise is adequate for crustal imaging, in contrast to teleseismic surface wave tomography which is dominated by longer wavelengths. A sufficient coverage of the study region by seismic arrays is the only requirement for a fairly resolved 3-D velocity model since each station becomes a wave source for all other stations in the noise cross-correlation process [Campillo and Paul, 2003, Shapiro and Campillo, 2004].

Since the first application of ambient noise tomography to the Alps by Stehly et al. [2009], station coverage has improved significantly in density but also in spatial homogeneity. This improvement is due to numerous new permanent broadband stations (in Austria, Germany, France, etc.) and to temporary networks, most importantly the AlpArray seismic network [AASN; AlpArray Seismic Network, 2015]. Indeed the AASN, which included more than 600 stations, was designed to fill in gaps between permanent stations and to homogenize spatial coverage in a way that no location in the Alps was more than 30 km away from a seismic station onland [Hetényi et al., 2018a]. The AASN also had a marine component with 29 ocean-bottom seismometers (OBS) deployed for 8 months in the Ligurian basin. It was complemented by denser quasi-linear or 2-D temporary arrays on targets of specific interest. The most important ones were EASI across the Eastern Alps [AlpArray Seismic Network, 2014], CIFALPS and CIFALPS-2 across the Western Alps [Zhao et al., 2016b, 2018], and Swath-D in the Central and Eastern Alps [Heit et al., 2017]. Figure 1 shows the seismological stations prior to

2010, and the stations which were used in the studies summarised in this review. For seismic tomography in general, and ambient noise tomography in particular, there is clearly a time before and a time after AlpArray.

Before AlpArray, the limited coverage of large parts of the Alpine area only allowed for ambient noise tomography studies of the central Alps, relying mainly on the dense Italian and Swiss permanent networks [Stehly et al., 2009, Verbeke et al., 2012, Molinari et al., 2015]. The pioneering application of ANT to the Alps by Stehly et al. [2009] used records of 150 broadband stations in Switzerland and neighbouring countries. They applied a classical two-step procedure, with an inversion of dispersion measurements for group velocity maps of Rayleigh waves in the 5–80 s period band, followed by a non-linear Monte Carlo inversion of the dispersion curve in each cell for a 1-D shear-wave velocity model. The set of 1-D models were then merged into a so-called 3-D V_s model that should more properly be called pseudo 3-D. This study provided a data constrained Moho depth map of the Western Alps, because crustal thickness was a free parameter in the inversion. This Moho map shared many similarities with the reference map computed by Waldhauser et al. [1998] from depth-migrated controlled-source seismic data, including strong and abrupt Moho depth changes from 25–30 km beneath the European forelands and the Po plain, to 55 km beneath the internal Alpine arc from southern Switzerland to the Dora Maira massif (Piemonte, Italy). This first successful application of ANT in the Alps was considered a proof of concept. The tomography by Stehly et al. [2009] was followed by those of Verbeke et al. [2012] and Molinari et al. [2015], who expanded the station array to the Italian and Slovenian permanent broadband networks and the tomography to the Apennines, and used both group and phase velocity dispersion data.

In the last large-scale ANT before AlpArray, Kästle et al. [2018] used records of 313 permanent stations covering the broad Alpine region and the Apennines. To overcome the sparse station coverage in the external, western and northern Alps, they complemented ambient noise phase dispersion measurements with two-station measurements from regional and teleseismic earthquake records. The ambient noise and earthquake-based dispersion datasets agreed well enough in the overlapping period band 8–60 s to be jointly inverted for Rayleigh and Love wave phase velocity maps in the broad period range 4–250 s [Kästle et al., 2016]. In a second stage, Kästle et al. [2018] jointly inverted Rayleigh and Love-wave phase dispersion data in each cell for 1-D V_p and V_s models of the crust and upper mantle. According to the authors, the 3-D V_s model of the upper mantle derived from joint inversion has much higher resolution than when each individual dataset, ambient noise and earthquake-based, is inverted alone. By averaging the crustal thickness of the 500 best-fitting V_s models, Kästle et al. [2018] computed a Moho depth map that compares remarkably well with receiver function and DSS Moho depth estimates along numerous profiles across the Alps and Apennines [Kummerow et al., 2004, Spada et al., 2013, Zhao et al., 2015].

The installation of the AlpArray temporary seismic network started in Austria in the summer of 2015 and ~200 of the planned 267 temporary stations were operating by mid-2016 [Hetényi et al., 2018a]. By adding the first months of AASN recordings (until June 2016) to a four-year noise dataset from European-wide permanent broadband networks, Lu et al. [2018] achieved the first ANT of the broad Alpine region with fairly homogeneous coverage and an average station spacing of ~50 km. This study was the first in a series of noise-based isotropic and anisotropic tomography studies on the Alpine lithosphere that have built on the spatial homogeneity and density of the AlpArray dataset (from both permanent and temporary stations) to develop and apply new data analysis and imaging methods.

Indeed, the high spatial density of AASN and associated permanent and temporary networks has driven methodological advances in ambient noise tomography, just as the USArray Transportable Array has driven the advent of Eikonal tomography [Lin et al., 2009]. The present paper focuses on key methodological advances on isotropic (Section 2) and anisotropic (Section 3) imaging. We also show how the application of these new methods to Alpine data opens new perspectives (Section 4) for the geological and geodynamic modeling of the Alpine belt.

2. Isotropic ambient noise tomography

The homogeneous coverage provided by the AASN motivated a number of ambient noise isotropic tomography studies on regional targets in and around

the Alps [e.g., Guerin et al., 2020, Molinari et al., 2020, Sadeghi-Bagherabadi et al., 2021, Schippkus et al., 2018, Szanyi et al., 2021]. In this section we focus on noise-based isotropic tomography studies of the broad Alpine region and surroundings using all or most available stations in Western Europe at the time of study. We describe three key improvements to isotropic imaging with cross correlations in this highly heterogeneous area.

2.1. *Second-order cross-correlation techniques*

The Ligurian basin, which separates the Corsica–Sardinia block from the southern coast of France and north-western Italy (Figure 1) is a back-arc basin generated by the rollback of the Adriatic slab in Oligo-Miocene time [e.g., Rollet et al., 2002]. Situated at the transition between the Alps and Apennines mountain ranges, it was considered an important target for the AlpArray temporary seismic experiment, which therefore included 24 broadband ocean-bottom seismometers (OBS, Figure 1).

Ambient noise tomography of an offshore area is possible without OBSs provided that it is surrounded by land stations. For example, Magrini et al. [2022] have computed an S-wave velocity model of the west-central Mediterranean, including the Ligurian basin, from surface-wave tomography using records of on-land stations in Europe and North Africa. Lateral resolution in the Ligurian basin and its margins remains limited, due to lack of OBS data, illustrating that the integration of land and sea-based observations is a key target for noise-based imaging in coastal and offshore areas. Such land-sea data integration was the target of a specific effort for methodological development by Nouibat et al. [2022b]. This work aimed at solving the issues of ANT from OBS data, as OBSs are generally deployed for less than a year, and signal quality is lower than that of land stations. In this section, we summarize how Nouibat et al. [2022b] enhanced the signal-to-noise ratio of noise correlations between sea-bottom stations by computing second-order correlations with on-land stations as virtual sources.

At periods longer than 20 s, OBS recordings are affected by tilt and compliance noise induced by the soft seabed on which the instruments rest. Crawford et al. [1998] and Crawford and Webb [2000] have derived a specific pre-processing scheme based on the recordings of the pressure component of OBS records and comparison between horizontal and vertical velocity components. Nouibat et al. [2022a] and Nouibat et al. [2022b] applied this pre-processing to the AlpArray OBS recordings, along with corrections for instrument noise (glitches) at a few stations.

These noise reduction procedures were insufficient to ensure the emergence of clean Rayleigh waves in noise correlations for OBS station pairs, due to seafloor currents, boat traffic, marine animals and seismic waves in the water column. Since the recordings of onshore stations are free of such noise, Nouibat et al. [2022a,b] have synthesized Rayleigh waves between OBS stations by using onshore stations as virtual sources. This procedure is named C2, or iterative noise correlation because it recovers the Rayleigh-wave signal between two OBSs by correlating Rayleigh-wave signals emerging from correlations between these OBSs and onland stations. The C2 method relies on the stationary phase theorem. Onland stations used as virtual sources must be located close to the azimuth of the OBS pair to optimize constructive interference of the wavefields radiated by the source and recorded by the two OBS. In Nouibat et al. [2022a,b], virtual sources were selected in azimuths close (±20°) to the azimuth of the OBS pair. Since virtual sources are mostly distributed to the North and East of the OBS array, Nouibat et al. [2022b] enhanced the coverage by separate use of the causal and anticausal parts of the first-order correlations (C1: between OBSs and land stations) to compute the OBS–OBS second-order correlations (C2). Extensive tests show that Rayleigh wave signal quality may be higher in OBS–OBS correlations (C1) than in C2 correlations in the 5–10 s period range with lower water column noise. For each OBS–OBS pair, Nouibat et al. [2022b] selected the correlation of highest quality after checking the coherence of C1 and C2 correlations. Figure 2 documents how this procedure improves inter-OBS signal quality, and thus ray coverage inside the Ligurian basin, enabling high-resolution ambient noise tomography of the crust in the basin.

2.2. *Bayesian and transdimensional inference*

A primary objective of (isotropic) seismic tomography of the Alpine lithosphere is a depth map of the crust-mantle boundary at a resolution of a few tens

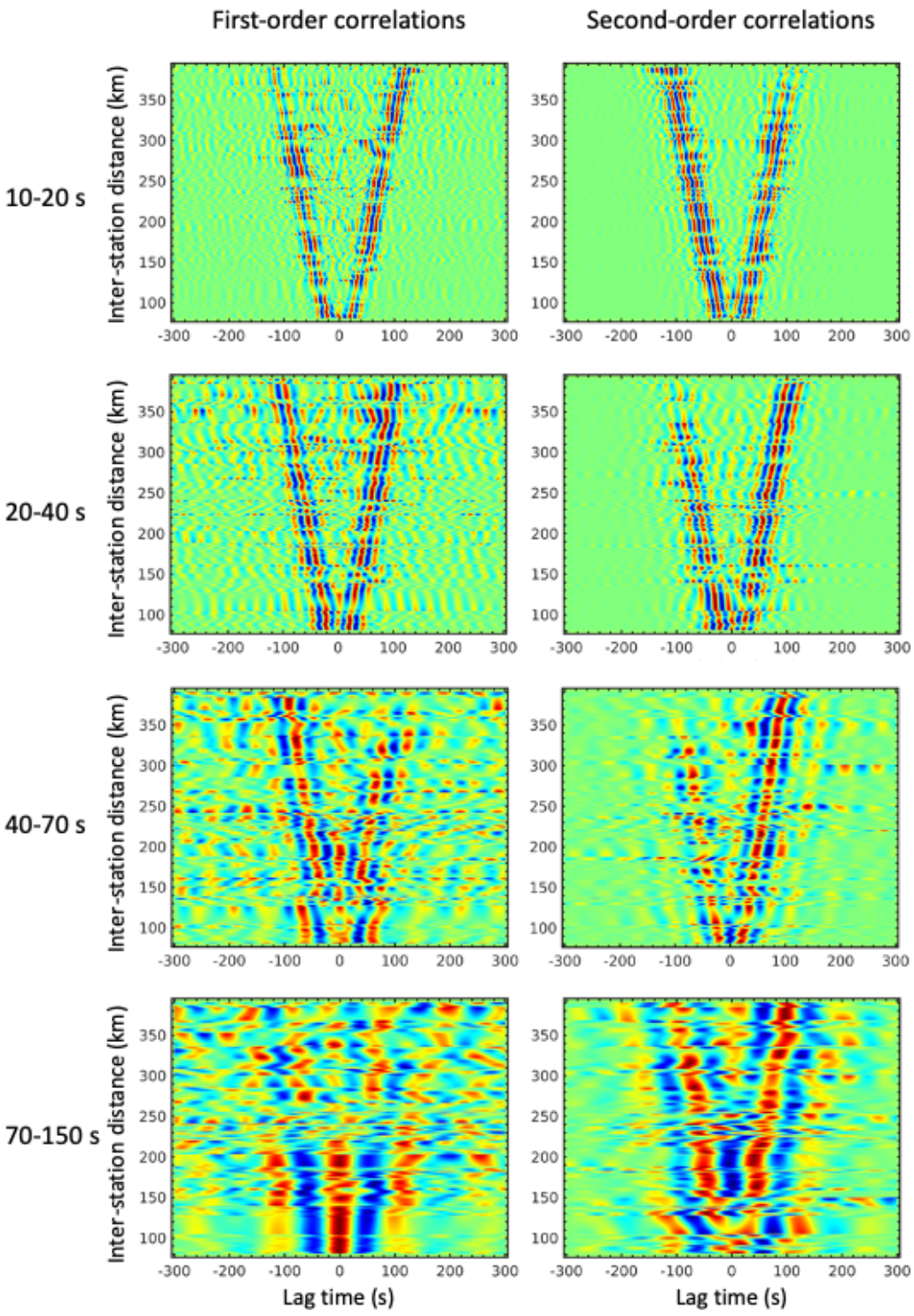

Figure 2. Inter-OBS noise correlation waveforms (Z comp.) generated in four frequency bands by: (left) first-order, standard correlation of pre-processed noise records; (right) second-order correlation using land stations as virtual sources. Modified from Nouibat et al. [2022b].

of km. More precisely, a geological [Calcagno et al., 2008] and potentially geodynamic modeling of the mountain belt requires depth maps of the superposed European, Adriatic and Ligurian Moho surfaces affected by the subduction of the Alpine Tethys, the following collision of the European and Adriatic margins, and the opening of the Ligurian backarc basin. Seismic studies prior to the AlpArray project mapped the European Moho to a maximum depth of 55 km below the belt axis [e.g., Spada et al., 2013, Stehly et al., 2009, Kästle et al., 2018]. Receiver functions of the CIFALPS transect in the south-western Alps provided the first seismic evidence for continental subduction, including converted waves on the deep European Moho at 75–80 km beneath the westernmost Po plain, and negative-polarity conversions on an "inverted" Moho between the Adriatic mantle wedge on top and the European crust below, as shown in Figure 3b [Zhao et al., 2015, Paul et al., 2022].

To take full advantage of the increased station density and to avoid dependence on arbitrary choices such as an initial model, several improvements were made to the inversions for V_s with depth.

2.2.1. *1-D depth inversion for V_s with a full exploration of the model space*

A first improvement of the 1-D inversion for V_s was performed by Lu et al. [2018], who used a subset of AlpArray data, as station installation was still ongoing. Their inversion for group velocity maps involved a linearized inversion method based on ray theory [Boschi and Dziewonski, 1999], and an adaptive parameterization scheme that reduced cell size in areas with high path density.

In the 1-D inversion stage for V_s, they built upon the inversion method of Macquet et al. [2014], where a full exploration of the model space was combined with a linear inversion for V_s. In this way, Lu et al. [2018]'s inversion for V_s included two steps. The first one used a grid search approach to uniformly sample and calculate group velocity dispersion curves for a low-dimensional model space based on a three-layer crust above a mantle half-space. This full model exploration was feasible because the dispersion curves can be computed with normal mode summation, and is computationally tractable. It was thus possible to determine an ensemble of models for which the dispersion curve matched the observed one. This first inversion step provided for each geographical grid cell a probabilistic V_s model and the probability to have a layer boundary at a given depth. However, to reduce the size of the model space to explore, the parameterization did not allow for low velocity zones. The second step was a linear inversion for V_s, where the problem was linearized around the mean of the probability distribution obtained at the previous step.

The dense station coverage and the two-step 1-D inversion scheme for V_s combining probabilistic sampling and linear inversion resulted in a (pseudo) 3-D V_s model with significantly higher spatial resolution than, for example, the model by Kästle et al. [2018]. Comparison with controlled-source reflection profiles [ECORS-CROP: Sénéchal and Thouvenot, 1991; TRANSALP: Kummerow et al., 2004] and receiver function stacked sections across the Alpine belt [TRANSALP: Kummerow et al., 2004; CIFALPS: Zhao et al., 2015, Paul et al., 2022] displayed striking coincidence in Moho depth despite the poor sensitivity of surface-wave dispersion to layer boundaries (see Figures 3b,c for the CIFALPS transect). Lu et al. [2018] computed three depth maps of Moho proxies in the Alpine region using the probability of interface occurrence, the depth gradient of V_s and the isovelocity surface V_s = 4.2 km/s. These maps revealed new features such as an 8-km abrupt Moho step beneath the external crystalline massifs of the Western Alps, from Pelvoux to Mont-Blanc, which had not been detected by the ECORS-CROP DSS profile presumably due to poor signal penetration.

The 3-D V_s model by Lu et al. [2018] however failed to clearly image the continental subduction of Europe beneath Adria in the western Alps, which had been identified by receiver functions (Figures 3b,c). Since the inversion of Lu et al. [2018] was based on a simplified parameterization (only three crustal layers), and on a final optimization framework, the solution was a unique model that explains observations, but without associated uncertainties and trade-offs. In this way, this unique solution did not depict the full state of information contained in the data.

2.2.2. *1-D depth inversion for V_s with transdimensional inference*

The next step in methodological improvement was therefore to carry out inversions within a full

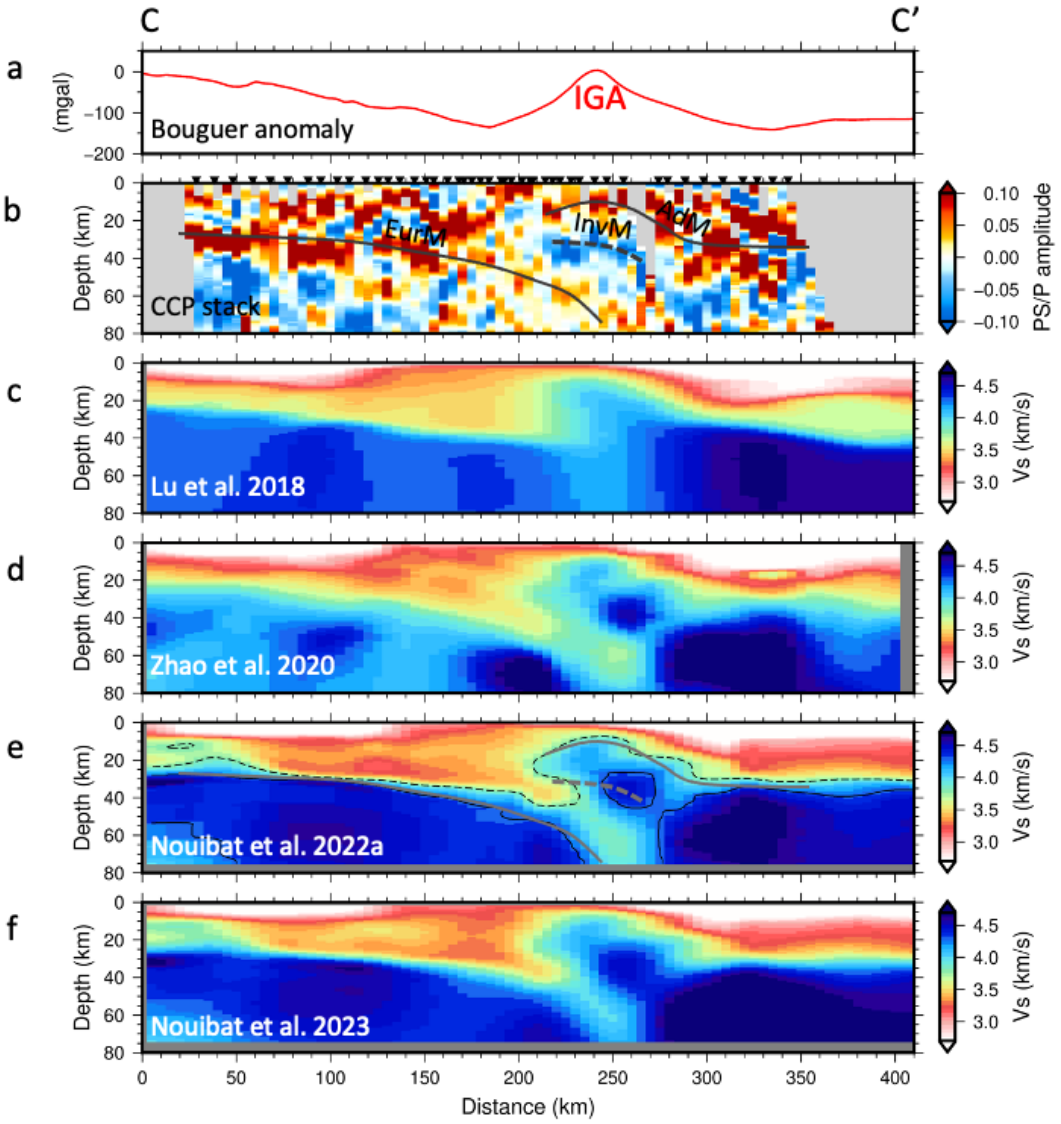

Figure 3. Cross-sections along the CIFALPS profile in the southwestern Alps (CC′, location shown in Figure 1b). (a) Bouguer anomaly from Zahorec et al. [2021]; IGA: Ivrea gravity anomaly. (b) Common-conversion point (CCP) stack of receiver functions at stations of the CIFALPS experiment; locations of stations projected onto the CIFALPS profile are shown as black inverted triangles at the surface; the solid thick black lines are the European Moho (EurM) and the Adriatic Moho (AdM) that appear as converted waves of positive amplitude (in orange-red); the dotted thick black line shows an inverted Moho (InvM, higher velocity on top than on the bottom), which is marked by converted waves of negative amplitude (in blue); modified from Paul et al. [2022]. (c) Shear-wave velocity model from the ambient noise tomography of Lu et al. [2018]. (d) Shear-wave velocity model from the ANT with transdimensional inversion to V_s by Zhao et al. [2020]. (e) Shear-wave velocity model from the ambient noise tomography of Nouibat et al. [2022a]; dashed black line: V_s = 3.8 km/s velocity contour; continuous black line: V_s = 4.3 km/s velocity contour (Moho proxy); the thick grey lines are the Moho boundaries shown as black lines in (b). (f) Shear-wave velocity model from the ambient noise wave-equation tomography of Nouibat et al. [2023].

Bayesian framework and a fully adaptive parameterization, without any linearization, and where the solution is a full probability distribution, therefore providing uncertainty estimates. In this context, Zhao et al. [2020] performed a Bayesian transdimensional inversion of the group-velocity Rayleigh-wave dispersion data of Lu et al. [2018] with a focus on the western Alps (4.5°E–9°E; 44°N–46.7°N). Unlike the inversion by Lu et al. [2018], which assumed a four-layer model, the transdimensional inversion treats the number of layers as an unknown parameter [Bodin et al., 2012, Yuan and Bodin, 2018]. At each gridpoint, Zhao et al. [2020] inverted dispersion data for V_s perturbations around a homogeneous half-space reference model with velocity 3.8 km/s, allowing a wide range of velocity variations (±50%).

The resulting (pseudo) 3-D V_s model (Figure 3d) displays a channel of anomalously low shear-wave velocities (V_s = 3.6 km/s) at 70-km depth beneath the fast-velocity, high-density Ivrea body anomaly in the CIFALPS cross-section (IGA in Figure 3a). This low-velocity anomaly is located between the deep European Moho and the inverted Moho of the Ivrea body imaged by receiver functions of the CIFALPS experiment (Figure 3b). The transdimensional inversion of Zhao et al. [2020] was thus able to image the subduction of the European continental lithosphere beneath the Adriatic lithosphere with minimal a priori constraints.

2.2.3. *3-D tomography with transdimensional inversions*

The third methodological improvement carried out by Nouibat et al. [2022a] was to use the entire AASN dataset and apply a full transdimensional approach at both stages of the inversion, that is in the 2-D inversions for group velocity maps and in the 1-D inversions for V_s. At each period, a transdimensional inversion was carried out to obtain probabilistic Rayleigh-wave group-velocity maps following Bodin et al. [2012]. In the second stage, a full transdimensional approach was used to invert for V_s at each geographical location the dispersion curve obtained in the first stage.

The key benefit of the transdimensional inversion for group velocity maps is that spatial parameterization is treated as part of the inversion, allowing local resolution to adapt to data density. Another improvement introduced by Nouibat et al. [2022a] is the computation of uncertainties on group velocity estimates by transdimensional inversion; these uncertainties are then incorporated into the inversion for V_s (second stage). Young et al. [2013] and Pilia et al. [2015] were the first studies to use this two-step transdimensional procedure, with uncertainty computed in the first stage used to weight the input in the second.

In the first stage, to account for the strong lateral velocity contrasts of the Alpine crust, straight rays of the classical forward model were replaced by bent rays with the ray geometry updated at each iteration using the fast marching method of Rawlinson and Sambridge [2004]. Nouibat et al. [2022a] applied this new inversion scheme to four years of noise records from ~1440 permanent and temporary seismic stations, including the entire AlpArray network with its offshore component (Z3 network: AlpArray Seismic Network 2015), the two CIFALPS experiments [YP and XT networks: Zhao et al., 2016b, 2018], and the EASI experiment [XT network: AlpArray Seismic Network, 2014] (Figure 1). Data coverage is improved compared to Lu et al. [2018], and so to Zhao et al. [2020], especially in the Western Alps and the Ligurian Basin.

Figure 3e shows a depth section along the CIFALPS transect in the 3-D V_s model by Nouibat et al. [2022a], which may be compared to the models by Lu et al. [2018] shown in Figure 3c, and Zhao et al. [2020] shown in Figure 3d. Unlike Lu et al. [2018] and similar to Zhao et al. [2020], Nouibat et al. [2022a] image the dipping low-velocity layer beneath the Ivrea body high-density, high-velocity anomaly (IGA, x = 210–300 km in Figure 3), which is indicative of the continental subduction of Europe beneath Adria. As the Zhao et al. [2020] inversion for V_s was based on the same dispersion dataset as Lu et al. [2018], and as Nouibat et al. [2022a] used the same inversion method for V_s as Lu et al. [2018], but with a different set of four-layer models, we propose that the major difference between Figures 3c and 3e is related to the difference between the sets of velocity models explored in the probabilistic inversion for V_s: 130 million for Nouibat et al. [2022a], and 8 million for Lu et al. [2018]. In particular, the complex vertical velocity profiles of the subduction region with alternating high and low velocities were not explored by Lu et al. [2018]. Vertical velocity gradients are stronger in Nouibat et al. [2022a]'s model (Figure 3e) than in Zhao et al. [2020]'s model (Figure 3d), in particular at the crust-mantle boundary. Even

though the input data and the inversion schemes differ, the overall similarities between the two models of Figures 3e and 3f suggest that the differences in velocity gradient at the Moho may result from the parameterization of the inversions for V_s. While the probabilistic inversion of Nouibat et al. [2022a] assumes a four-layer starting model with a velocity jump at Moho, the reference velocity model in the transdimensional inversion of Zhao et al. [2020] is a homogeneous half-space with no discontinuity. This a priori uniform distribution of velocity may favor a smooth velocity gradient at the Moho. The V_s model by Nouibat et al. [2022a] with its a priori imposed sharp crust-to-mantle velocity contrast is more in line with previous controlled-source (ECORS-CROP in the north-western Alps) and receiver function profiles [CIFALPS: Figure 3b; CIFALPS-2, Paul et al., 2022], which display clear reflected and converted phases on the Moho. The impact of other refinements in the Nouibat et al. [2022a] inversion methodology (error estimates on group velocities, bent rays) is difficult to evaluate due to the differences in the input data coverage. It would be an interesting test to apply the fully transdimensional inversion for V_s of Zhao et al. [2020], with an a priori constraint on the velocity jump at the Moho, to the group velocity data with uncertainties of Nouibat et al. [2022a].

2.3. *Wave-equation tomography*

To compute shear-wave velocity models of the crust and uppermost mantle from Rayleigh-wave traveltime data between station pairs, Lu et al. [2018] and Nouibat et al. [2022a] have used a two-stage inversion scheme, which, in spite of improvements related to a probabilistic approach, is a standard strategy for ANT. The first stage, a series of 2-D inversions of traveltime data for group velocity maps at selected periods, is based on ray theory, which is only valid at infinite frequency. The second stage, a set of 1-D inversions of the local dispersion curves for S-wave velocity, results in 1-D models merged into a pseudo 3-D model. The strong crustal heterogeneity of the Alps and surrounding areas, including the Ligurian back-arc basin, makes the ray hypothesis particularly inadequate. This area therefore provides an excellent chance of testing a tomography procedure that better accounts for the physics of seismic wave propagation. In this section, we first describe a new wave-equation based approach of ambient noise tomography called wave equation tomography [WET, Lu et al., 2020] for the elastic case, using only land station recordings. We next present the extension of the WET method to include elastic–acoustic coupling at the sea bottom and OBS records [Nouibat et al., 2023].

2.3.1. *Wave-equation onshore tomography (elastic case)*

To calculate a truly three-dimensional V_s model consistent with wave propagation physics, Lu et al. [2020] derived a wave-equation based approach, hence called ambient noise wave-equation tomography. As in the ambient noise adjoint tomography of Chen et al. [2014], the observable is travel time (i.e. phase) of the Rayleigh wave reconstructed from noise correlation, while full-waveform inversion (FWI) would invert amplitude and time. Indeed, Rayleigh wave amplitudes are not correctly retrieved by the classical noise correlation procedure [e.g., Campillo, 2006]. FWI of ambient noise correlation signals probably has great potential for lithospheric imaging. It is not yet operational because it would require specific pre-processing of noise records for a better retrieval of amplitudes and, more importantly, an accurate estimate of noise source distributions and emitted waveforms [e.g., Fichtner, 2014, Sager et al., 2018].

The wave-equation tomography (WET) approach implemented by Lu et al. [2020] consists of iteratively updating an initial ambient noise tomography model (from the two-stage traditional method) by minimising frequency-dependent phase traveltime differences between the Rayleigh waveforms observed in noise correlations and the synthetic waveforms computed by 3-D numerical modeling of wave propagation. Synthetic waveforms are computed with the 3-D elastic wave equation solver of the SEM46 package [Trinh et al., 2019] based on the spectral element method [Komatitsch and Vilotte, 1998, Komatitsch and Tromp, 1999]. Of the 304 stations located in the study region, a subset of 64 suitably located stations were selected as virtual sources by Lu et al. [2020], and the signal bandwidth was limited to [10–50 s] to ensure acceptable computing time. The observed signal for a station pair is the Rayleigh wave part of the Green's function, estimated from the time derivative of the cross-correlation of seismic noise.

The synthetic signal is the convolution product of a bandpass filtered Dirac delta source function with the synthetic Green's function computed with SEM46 for a source–receiver pair, and a vertical force applied on the free surface at the source location. The misfit function is then computed from the frequency-dependent phase traveltime differences between observed and synthetic waveforms. The adjoint-state approach is used to compute the misfit gradients [e.g., Tromp et al., 2005], and the inversion is conducted as an iterative local optimization problem.

The final S-wave velocity model obtained by Lu et al. [2020] after 15 iterations of wave equation tomography has a 65% lower total misfit than the initial ANT model by Lu et al. [2018]. This strong misfit reduction is mostly due to periods larger than 25 s, where the WET has corrected for a strong and unexplained positive shift of the traveltime misfit histograms in the initial model. A direct consequence is that the final V_s model has significantly higher average velocities at lower crustal depth (30 km). Beyond this tuning of average velocities, the WET approach was able to retrieve finer scale heterogeneities than the ANT model, for example a high-velocity anomaly at 10 km depth, which is closer in shape to the well-known Ivrea positive Bouguer anomaly [see Figure 8 in Lu et al., 2020].

2.3.2. *Wave-equation onshore/offshore tomography (with acoustic–elastic coupling)*

As compared to Lu et al. [2018], a more accurate ANT model of the Alpine region and its surroundings was computed by Nouibat et al. [2022a] using a larger noise correlation dataset including recordings of sea-bottom seismometers in the Ligurian basin, and an improved inversion scheme (see Section 2.2). Like Lu et al. [2020], Nouibat et al. [2023] have performed a WET to improve the model of Nouibat et al. [2022a] by accounting for three-dimensional and finite-frequency effects of wave propagation. A major improvement achieved by Nouibat et al. [2023] is the inclusion of the water layer effect on wave propagation in the Ligurian basin. The vertical-component record of short-period (<20 s) surface waves at ocean-bottom stations is dominated by a fluid–solid interface wave named Rayleigh–Scholte wave that propagates at lower speed than the Rayleigh wave in the elastic medium. At periods >20 s, the effect of the water layer becomes negligible for the Ligurian basin (max. water depth 3 km) because the Rayleigh wavelength is large compared to water depth [Nouibat et al., 2023]. Accounting for the effect of the water layer in the forward simulation of surface-wave propagation and in the inversion of traveltime observations for shear-wave velocity is therefore required to enhance resolution in the shallow layers of the Ligurian basin.

For their wave-equation tomography with elastic–acoustic coupling, Nouibat et al. [2023] selected, from the dataset of Nouibat et al. [2022a], 600 stations as receivers, out of which 185 were selected as sources based on noise correlation signal quality. The initial model was the ANT V_s model computed by Nouibat et al. [2022a]. As in Lu et al. [2020], the inverse problem minimised the frequency-dependent phase traveltime differences between observed and synthetic vertical-component waveforms for considered source–receiver pairs. The inversion was conducted in the 5–85 s period range, considering elastic–acoustic coupling in the forward simulation in the 5–20 s band. Unlike Lu et al. [2020], the velocity model was updated progressively from long periods (40–85 s) to shorter ones, 20–40 s, 10–20 s then 5–10 s to avoid cycle skipping.

The final WET V_s model differs significantly from the initial ANT V_s model, particularly in shallow layers of the Ligurian Basin, and in the most heterogeneous parts of the Alpine crust. These discrepancies highlight the importance of accounting for the physics of wave propagation, i.e. elastic–acoustic coupling at the sea-bottom, finite-frequency effects and 3-D propagation. In the alpine crust (i.e. onland), velocity contrasts tend to be slightly enhanced, in particular at lower crustal depth [26 km, see Figure 6 in Nouibat et al. [2023]], while the location and shape of velocity changes are preserved with respect to the initial ANT model (Figures 3e–f). At depths shallower than ~10 km, S-wave velocities in the Ligurian basin are ~8% lower in the WET model than in the ANT model, in agreement with the lower velocities of the Rayleigh–Scholte wave. Accounting for the water layer in the Ligurian basin also leads to higher velocities in the crust of western (Variscan) Corsica.

Nouibat et al. [2023] conducted extensive evaluation of the robustness of their WET model. The quality of the S-wave velocity model was documented

by traveltime misfit maps at representative periods between 8 and 55 s. As expected, misfit is lower for the WET model than for the initial ANT model, except in the peripheral poorly illuminated regions [see Figure 12 in Nouibat et al., 2023]. The footprint of the broad geological structure has disappeared, whereas it was clearly visible for the ANT model at periods ≥20 s. Using the weak sensitivity of Rayleigh wave phase velocity to V_p, Nouibat et al. [2023] also inverted Rayleigh wave dispersion observations for P-wave velocity, starting from an initial V_p model computed from the initial (ANT) V_s model using an empirical formula. To document the robustness of their P and S-wave models, they computed synthetic waveforms for a regional earthquake in Switzerland and compared to observed waveforms in three frequency bands between 2 and 10 s. The fit between simulated and observed seismograms is striking for the travel times of the P and Rayleigh waves, but also for relative amplitudes between the wave trains. Such a high coherence in the short-period bands is a reliable indication that wave equation tomography is capable of imaging small-scale crustal structures. This synthetic test also demonstrates that the WET V_s and V_p models derived from ambient noise correlations would be a good initial model for a wave-equation tomography using earthquake records. As regional earthquake records include both body and surface waves, the resulting P-wave velocity model would be much more accurate than that obtained from Rayleigh wave travel time inversion alone, due to its weak sensitivity to V_p.

2.4. *Model validation: Moho depth*

Surface waves are weakly sensitive to velocity contrasts, but Bayesian inversions for V_s were shown to be very effective for imaging the crust-mantle boundary [Lu et al., 2018, Nouibat et al., 2022a]. Comparisons of Moho depths imaged by other geophysical methods such as DSS profiles (ECORS-CROP) and receiver function analyses have shown that selected iso-velocity surfaces in the ambient noise derived 3-D V_s models are reliable proxies of the Moho [Nouibat et al., 2022a, Paul et al., 2022, Nouibat et al., 2023]. For example, the velocity contour V_s = 4.3 km/s is a good proxy for the European Moho, and the Adriatic Moho outside the Ivrea body region, as shown by the coincidence of this surface with Moho conversions picked from CCP receiver function stacks along the CIFALPS and CIFALPS2 sections (see for example Figure 3e). In the Ivrea body region, the Moho imaged by the ECORS-CROP DSS profile and receiver function sections is better approximated by the 3.8 km/s velocity surface, probably because the external rim of the Ivrea body is made of serpentinized peridotites with lower velocities than dry peridotites [Figure 3e; see discussion in Malusà et al., 2021]. In the Ligurian basin, a comparison of the V_s model of Nouibat et al. [2022a] with a V_p model derived by Dannowski et al. [2020] from refraction and wide-angle reflection OBS data shows a striking coincidence of the V_p Moho (iso-velocity 7.2 km/s) with the 4.1 km/s V_s contour [see Figure 9 in Nouibat et al., 2022b]. A Moho depth map of much higher resolution than previous ones [e.g., Grad et al., 2009, Spada et al., 2013] can therefore be built by mapping iso-velocity contours of the V_s models by Nouibat et al. [2022a] and Nouibat et al. [2023].

3. Anisotropic ambient noise tomography

Surface waves in seismic noise correlations can potentially shed new light on anisotropy in the Earth's crust and upper mantle, overcoming the observational biases related to the uneven distribution of earthquakes, which leads to uneven azimuthal coverage [for a review, see Maupin and Park, 2015].

Our knowledge of azimuthal anisotropy beneath the Alps and Italy mostly comes from XKS splitting studies. Fast velocity directions are generally parallel to the mountain chain in the Western and Central Alps [Barruol et al., 2004, 2011, Lucente et al., 2006, Salimbeni et al., 2018], the Eastern Alps [Bokelmann et al., 2013, Qorbani et al., 2015] and the Apennines [Palano, 2015]. Teleseismic P wave travel time delays were used by Rappisi et al. [2022] to study anisotropy in the Central Mediterranean area, including the Alps. Both XKS and teleseismic P waves have too steep incidence angles to reliably constrain anisotropy in the crust, also because the cumulated travel time in the crust is much smaller than in the upper mantle. Studies using regional refracted Pn and Sn phases like Díaz et al. [2013] provide information about the uppermost mantle, as these waves are tied to the Moho interface and propagate with mantle velocities.

Long wavelength anisotropic structure beneath Europe is mostly known from large scale or global surface wave studies where the crust is not resolved [e.g., Kustowski et al., 2008, Weidle and Maupin, 2008, Boschi et al., 2009, Zhu et al., 2015, Nita et al., 2016, Schivardi and Morelli, 2011]. All these studies are constructed from long period observations, where the crust is not inverted for but set from a reference model such as LITHO1.0 [Pasyanos et al., 2014]. A few studies focussing on crustal anisotropy used surface waves from seismic noise correlations to characterise anisotropy at regional scale, such as Switzerland [Fry et al., 2010], the Vienna Basin [Schippkus et al., 2020], the Bohemian Massif [Kvapil et al., 2021], or the Eastern Alps [Kästle et al., 2024].

The dense station coverage (Figure 1) across the greater Alpine region during the AlpArray project provided a unique opportunity to further develop and understand the limitations of noise-based imaging methods aimed at characterising seismic anisotropy across a strongly heterogeneous structure. Since the Alpine region is heterogeneous at all scales, it is in particular crucial to reliably estimate uncertainties and identify locations and periods where systematic errors may affect azimuthal anisotropy measurements. These questions are the focus of Section 3.1.

Once uncertainties associated with surface wave velocities are estimated, they can be used in inversions for depth variations of anisotropic parameters. Reliable uncertainties are also crucial in the case of joint inversions, where different datasets are inverted simultaneously (e.g., earthquake based and noise-based observations). A Bayesian inversion framework in theory handles this question in a both intuitive and simple way, producing families of acceptable Earth models, over which it is possible to make posterior statistics. This ensemble solution can be exploited to give reliable and useful information on the Earth structure. Section 3.2 is dedicated to such strategies for both radial and azimuthal anisotropy.

3.1. *Improving observations of azimuthal anisotropy*

The effect of isotropic heterogeneities on the wavefield can map into anisotropic parameters. In this section, we give some insights into such effects through the now well-established Eikonal tomography method [Lin et al., 2009]. We present outcomes of Eikonal tomography across the Alps and show how beamforming can improve seismic noise-based observations of anisotropy. Both Eikonal tomography and beamforming naturally correct for deviations from great circle [e.g., Pedersen et al., 2015] and uneven distribution of noise sources [e.g., Froment et al., 2010, Harmon et al., 2010], so the only main bias to handle is the one from isotropic heterogeneities.

3.1.1. *Biases in measurements of azimuthal anisotropy: insights from Eikonal tomography*

Eikonal tomography makes use of dense station networks to reconstruct the wavefield propagating away from a source [Lin et al., 2009]. In ambient noise applications, any seismic station can act as a virtual source and the signals recorded at all other stations allow us to image the wavefield. When computing ambient noise correlations, amplitudes are lost due to filters such as spectral whitening. Only the travel-time field is recovered, therefore hindering the use of amplitudes to correct for bias from wave interference.

In Eikonal tomography [Lin et al., 2009], travel times recorded at receivers are interpolated onto a regular grid. The gradient of the travel-time field then gives the phase velocity and the propagation direction at each grid point. This highlights important strengths of Eikonal tomography: it is simple to calculate and the direction of the incoming wave is directly determined from the data. In order to get the full, azimuthal anisotropic phase velocity map, the process has to be repeated for all available virtual sources so that a set of phase velocity measurements and their propagation azimuths is obtained for each grid cell. The final phase-velocity field is obtained by averaging the measured phase velocities for all virtual sources. Different statistics of the estimated phase velocities (mean, median, mode and standard deviation) can be used as uncertainty estimates. Similarly, for the anisotropic part, the residual from the fitted function provides information on the reliability of parameter estimates.

Isotropic bias can be approximately modelled by a 360° variation of phase velocity with azimuth [Lin and Ritzwoller, 2011, Mauerberger et al., 2021]. We

refer to phase velocity variations with azimuth in the following form (applicable to weakly anisotropic media):

$$C(\phi) = C_0 \left(1 + A_1 \cos(\phi - \theta_1) + A_2 \cos(2(\phi - \theta_2)) + A_4 \cos(4(\phi - \theta_4))\right), \quad (1)$$

where $C(\phi)$ is the anisotropic phase velocity, dependent on the wave propagation azimuth ϕ. It is given by its isotropic component C_0 plus three anisotropy terms that describe the θ_1 anisotropy (360° symmetry), the θ_2 anisotropy (180° symmetry) and the θ_4 anisotropy (90° symmetry), where θ is the fast axis direction and A the fast axis amplitude in fractions of C_0 from zero to peak. The θ_2 anisotropy is the dominant component for Rayleigh anisotropy [e.g., Montagner and Nataf, 1986] while the non-physical θ_1 anisotropy can be used to check for potential measurement bias created by isotropic heterogeneities. The θ_4 component is not included in further discussions since it is mostly relevant for Love waves which are not taken into account in the methods described below.

Figure 4 shows systematic errors resulting from isotropic heterogeneities through synthetic data computed in a laterally heterogeneous model, onto which we apply Eikonal tomography. In Figure 4d (perfect sampling), we observe an undulating pattern in the isotropic velocities, which depends on the signal wavelength. This undulating pattern is due to the interference of waves that are refracted by the isotropic anomaly. Most of the bias, however, cancels out when averaging over sources from many directions (Figure 4e). This error can also be corrected when taking the amplitude information into account [e.g., Helmholtz tomography, Lin and Ritzwoller, 2011]. A more severe bias stems from under-sampling the wavefield (Figure 4b). To work properly, the Eikonal method requires approximately plane wavefront between adjacent receivers. If the medium is highly heterogeneous, this assumption is violated and only a smoothed version of the true wavefield can be reconstructed from the measurements at the receiver locations. The resulting error in the isotropic part mostly cancels out when signals from different azimuths are averaged (Figure 4c). In the anisotropic part, however, a systematic, azimuth-dependent error remains, resulting in spurious anisotropy around the edges of strong velocity heterogeneities.

The level of these spurious anisotropic measurements depends not only on the absolute velocity variation but also on the wavelength of the signal, the inter-station spacing and the velocity gradient at the edges of the anomalies. The controlling factor for the bias is the level of complexity of the wavefront between adjacent stations.

3.1.2. *Eikonal tomography in the Alps*

Kästle et al. [2022] presented an application of Eikonal tomography to the Alpine area, including data from the AlpArray network. They were able to resolve both the isotropic and the anisotropic parts at periods sensitive to different depth ranges from the shallow crust to the uppermost mantle. The three anisotropic components were obtained by taking the azimuthally dependent phase-velocity measurements and fitting them to Equation (1).

Kästle et al. [2022] tested for different observables that can be related to a bias in anisotropy measurements, such as the amplitude of the θ_1 component or the standard deviation from fitting the θ_2 anisotropy. They found that none of these observations are adequate to reliably identify biased measurements. More sophisticated approaches such as forward modelling the travel-time field from the isotropic velocities may be necessary. This could also be used iteratively to improve the accuracy of the interpolation for highly complex travel-time fields, at the cost of giving up the relative simplicity of the Eikonal approach. However, Kästle et al. [2022] inferred from synthetic tests that isotropic anomalies of up to 10% produce bias, which in most cases is smaller than what is identified as "true" anisotropy.

The θ_2 anisotropic component obtained by Kästle et al. [2022] is presented in Figure 5. The fast axis directions generally follow the curvature of the Alpine arc at 15 s period, representative of the upper crust. At 40 s period, the fast axis becomes more oblique to orogen-perpendicular within the central Alps. The eastern part of the Alps has more homogeneously E–W oriented fast axes from short to long period measurements. In most of the northern Alpine foreland, the anisotropic fast axis orientations are consistently following the Alpine curvature at periods between 10 and 50 s.

The uncertainties in the anisotropic measurements are largest at model boundaries, where the azimuthal coverage is non-optimal, as well as within

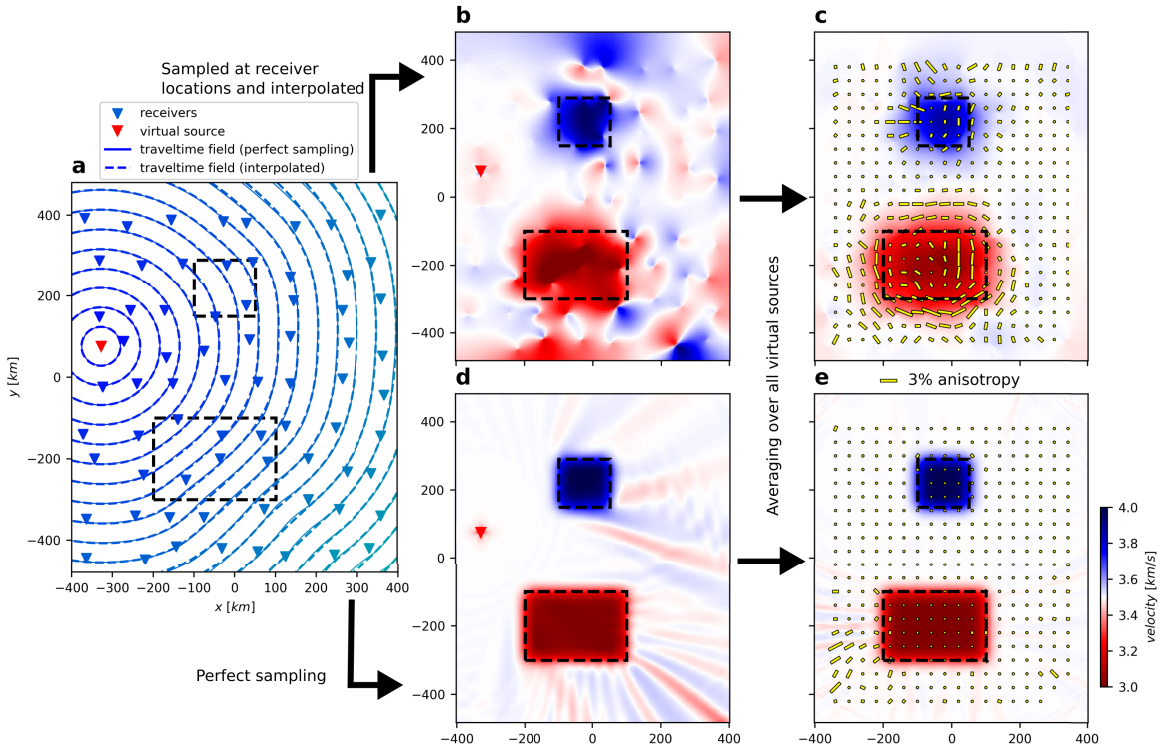

Figure 4. Example illustrating the bias in the anisotropic Eikonal tomography method. (a) 2-D wavefield propagating away from the virtual source station; black dashed lines indicate the locations of isotropic high and low velocity anomalies. (b) Isotropic phase velocities recovered by applying the Eikonal tomography method to the wavefield recorded at the receiver locations; anomalies outside the dashed lines are mainly caused by incomplete reconstruction of the true traveltime field. (d) Same as (b) for a perfectly sampled traveltime field; the striped velocity heterogeneities behind the anomalies are caused by wavelength-dependent wave interference effects. (c) and (e) Final models resulting from averaging the models for all virtual sources, i.e., swapping the position of the virtual source with all available receiver positions. The apparent anisotropy (yellow bars) is caused by velocity errors illustrated in (b) and (d) since the input model is purely isotropic.

and around the large sedimentary Po and Molasse basins north and south of the Alps. In the former, isotropic velocities indicate that velocities can be as low as −30% compared to the average velocity [Kästle et al., 2022]. These regions are therefore prone to the systematic bias mentioned above, particularly at short periods. In most of the other regions and at longer periods, the anomaly strength is usually within ±10% with smoothly varying isotropic velocities. Correspondingly, Kästle et al. [2022] found that the imaged pattern of anisotropies in the Alps is compatible with previous, more localised studies Fry et al. [2010], but also with the results from beamforming [Soergel et al., 2023; Section 3.1.3].

3.1.3. *Beamforming*

An alternative approach to Eikonal tomography is to use the phase information in a beamforming approach. Beamforming consists of, for a set of closely located seismic stations and at a given frequency, inferring the direction and local phase velocity of the incoming wave [for a review, see Rost and Thomas, 2002]]. Contrary to Eikonal tomography, the full waveform of the empirical Green function is used, as illustrated in Figure 6. The original waveforms (Figure 6a) are shifted in time using a grid search across many phase velocities and incoming directions. The final estimated phase velocity is the one

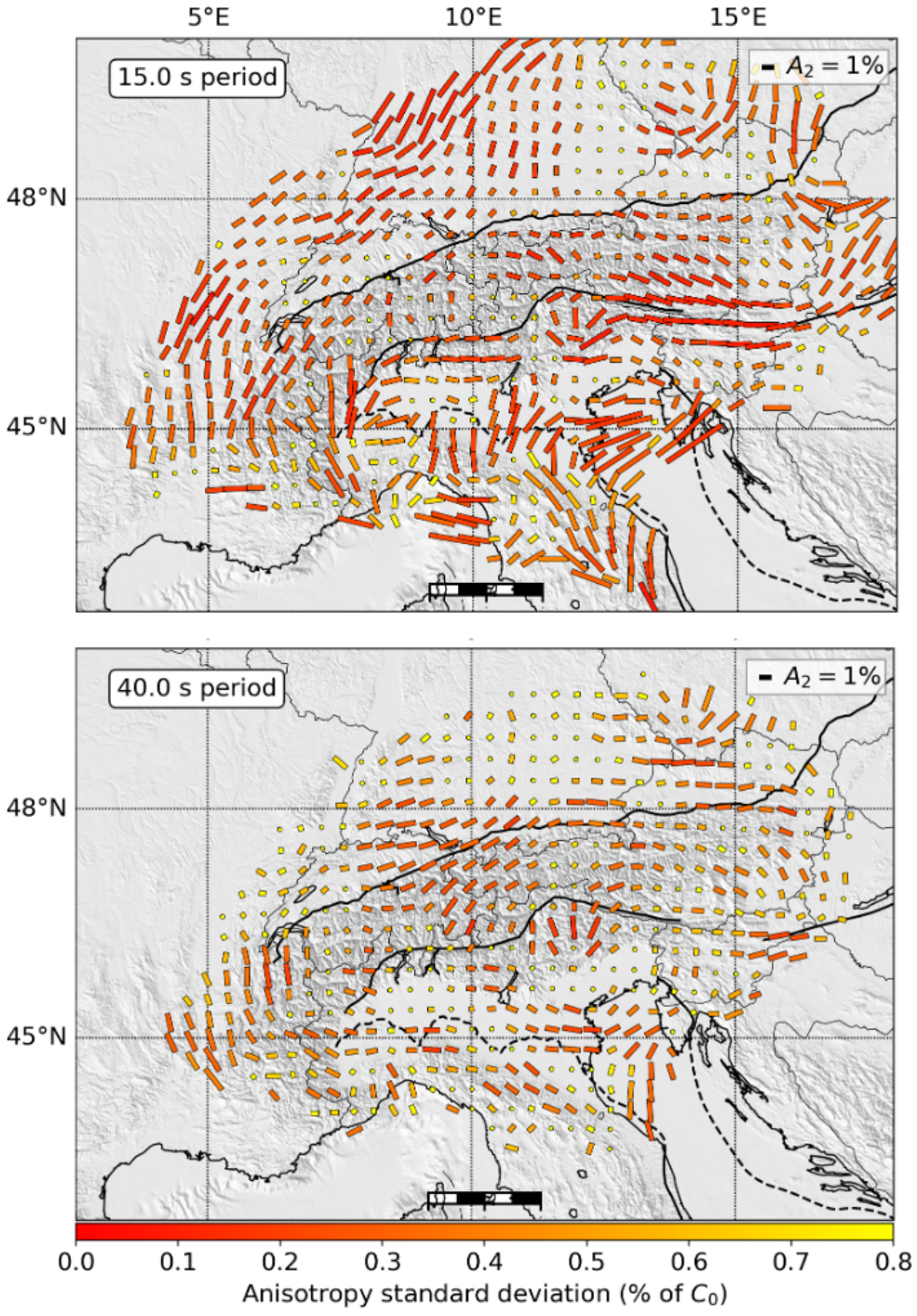

Figure 5. Maps of θ_2 azimuthal anisotropy at 15 and 40 s period resulting from Eikonal tomography in the Alps. The direction of each line shows the fast direction, and the length shows the amplitude (zero to peak). The colour of the lines gives the estimated uncertainty on the amplitude A_2 (in percent of C_0).

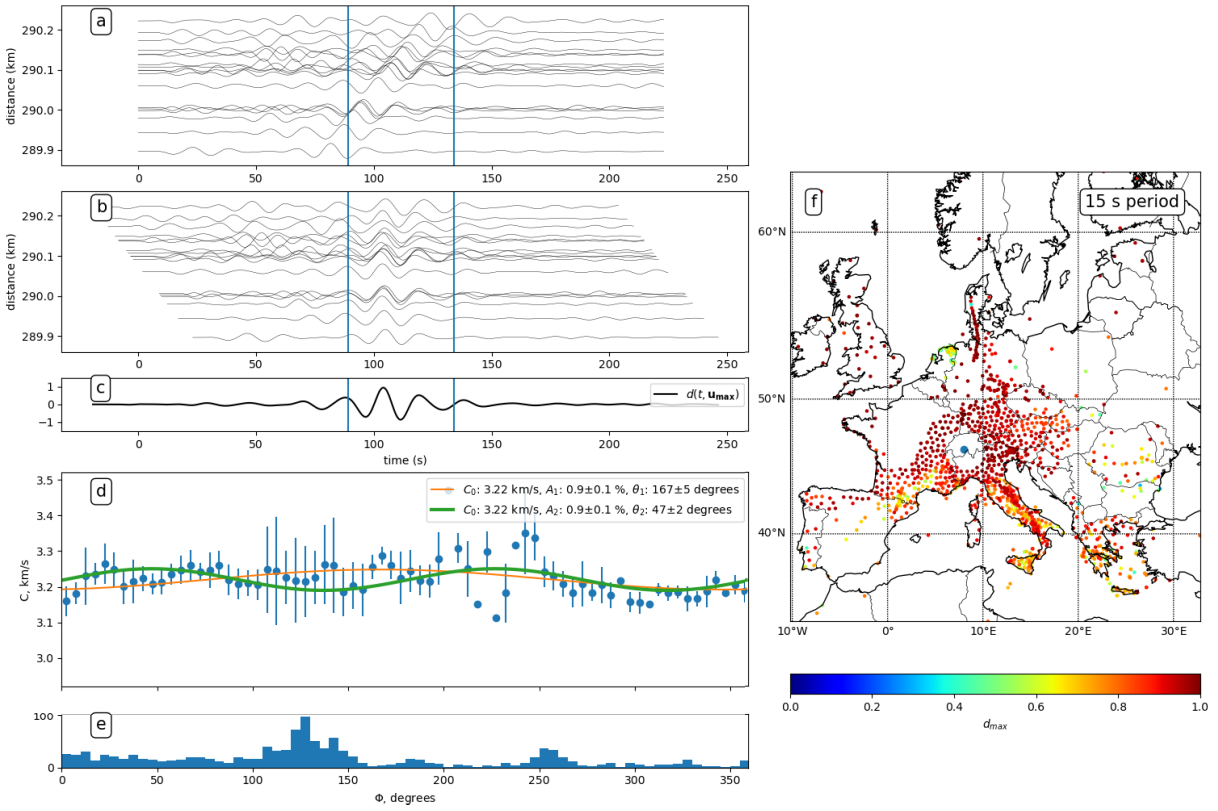

Figure 6. Illustration of data processing, and map of estimated azimuthal anisotropy at 15 s period for one seismic array. (a) Filtered traces before aligning. (b) Same traces as (a), aligned using the combination of azimuth and phase velocity for which the stack is optimal (maximum peak amplitude). (c) Stack at optimal parameters, normalised by the number of stations. The maximum of this stack is called $d_{\max}$. (d) Phase velocity as a function of azimuth, using all source stations. The orange and green curves correspond to the first two cosine terms of Equation (1). (e) Number of source stations (binned in 5° azimuth bins) as a function of azimuth. (f) Quality of stack $d_{\max}$ for all source stations. The seismic array is centered at the blue dot. It is surrounded by a blank area, because of the need to respect a minimum distance between source and receiver stations. The colour code shows $d_{\max}$, the maximum amplitude of the stack divided by the number of traces. Soergel et al. [2023] particularly focused on quality control and error estimates to be able to carry out inversions for anisotropic parameters with depth. Such quality control and error estimates are key input for subsequent transdimensional Bayesian inversion described in Section 3.2.

for which the traces are optimally aligned (Figure 6b), and for which the stack yields the highest maximum amplitude (Figure 6c).

Beamforming has been extensively used on seismic noise, in particular to characterise the noise field and infer the locations of origin of noise sources [for Europe, see for example Friedrich et al., 1998, Landès et al., 2010 or Juretzek and Hadziioannou, 2016]. Beamforming has also been used to quantify anisotropy on earthquake data [e.g., Pedersen et al., 2006, Alvizuri and Tanimoto, 2011] or directly on raw noise records [e.g., Riahi and Saenger, 2014].

To estimate surface wave azimuthal anisotropy, beamforming has to be carried out, for each source, across the range of target periods (Figure 6d).

This method was previously used on earthquake

data. Applying it to noise correlation is straightforward as seismic stations can be used as virtual sources. Here we present key elements of the implementation of Soergel et al. [2023] and the application to the Alps. A somewhat similar approach was taken at the same time by Wu et al. [2023] for the Northeastern Tibetan Plateau.

The specific choices made to adapt the beamforming included:

- Using seismic stations outside the study area as virtual sources, to improve azimuthal coverage at the edge of the study area.
- Taking into account the short distances between the array and the "source" station. This was done mainly by assuming circular wavefronts following Maupin [2011] rather than plane wavefronts, and imposing a minimum distance between array and "source" station. The implementation still allowed to take into account great-circle deviations, which can be significant across AlpArray.
- Propagating uncertainty of each data point (phase velocity at a given period for a given array and source stations, see example in Figure 6f). This is done by weighting each observed phase velocity for the estimate of the A_2 and θ_2 terms for a given array at a given period, with the normalised beam amplitude $d_{\max}$, and use of bootstrap to estimate the uncertainty on A_2 and θ_2.
- Exclusion of data points if the isotropic bias (estimated by A_1) is significant.
- Adapting array geometry to wavelength and noise levels.

Figure 7 shows two examples of surface wave azimuthal anisotropy measured with this method across the Alpine area, at 15 s and 40 s period. Points with risk of a strong isotropic bias (high value of A_1 as compared to A_2, see Equation (1)) are excluded from the maps. In many points, the bias was particularly strong at periods which are sensitive to changes in Moho depth, and was overall coherent with areas of strong isotropic velocity gradients. For further discussion, we refer to Soergel et al. [2023].

The beamforming yields spatially coherent patterns of azimuthal anisotropy across all of the study area. Overall, the beamforming is in good agreement with the Eikonal method (Figure 5) on key findings, such as (at 15 s period) lower amplitude anisotropy within the Alps as compared to surrounding areas, and the surrounding areas being dominated by chain parallel fast direction. There are main differences at the periphery of the study area, which can be explained by the lack of azimuthal coverage in the Eikonal tomography. Lateral smoothing effects are also different between the two methods. While the reliability of the beamforming is high due to the point by point (geographically, for each period) evaluation of quality and errors, it also leads to changing geographical distributions of reliable data with period, and the implementation would need to resolve this issue to be able to provide 3-D models of anisotropy.

Depth inversions for azimuthal anisotropy must be considered a priority in anisotropic studies because of the wide range of possible values of A_2. For example, if the upper crust is strongly anisotropic and neither lower crust or upper mantle are anisotropic, the observed anisotropy at, for example, 40 s period still has its origin in the upper crust. Similarly, changes in fast direction in layers with small anisotropy are not directly visible at any given period. Whether small amplitude anisotropy is resolved therefore strongly depends on the observation error. The strong control of errors provided by beamforming is consequently key for the depth inversions which are addressed in the following section.

3.2. *Transdimensional Bayesian inversions of anisotropic measurements*

Similar to isotropic inversions, once surface wave velocities have been estimated at different periods, they can be inverted to recover anisotropic shear wave velocity structure at depth. This is usually done in a second inversion step carried out at each geographical location. Rayleigh and Love dispersion curves can be jointly inverted for radial anisotropy parameters with depth. In the case of azimuthal anisotropy, Rayleigh and Love wave dispersion curves and their azimuthal dependency at each period can each be inverted to obtain azimuthal anisotropy parameters with depth.

Fortunately, this inverse problem is only weakly nonlinear, and many linearized approaches have been used, where data derivatives (sensitivity kernels) computed around a reference model are used. However, the solution is highly non-unique,

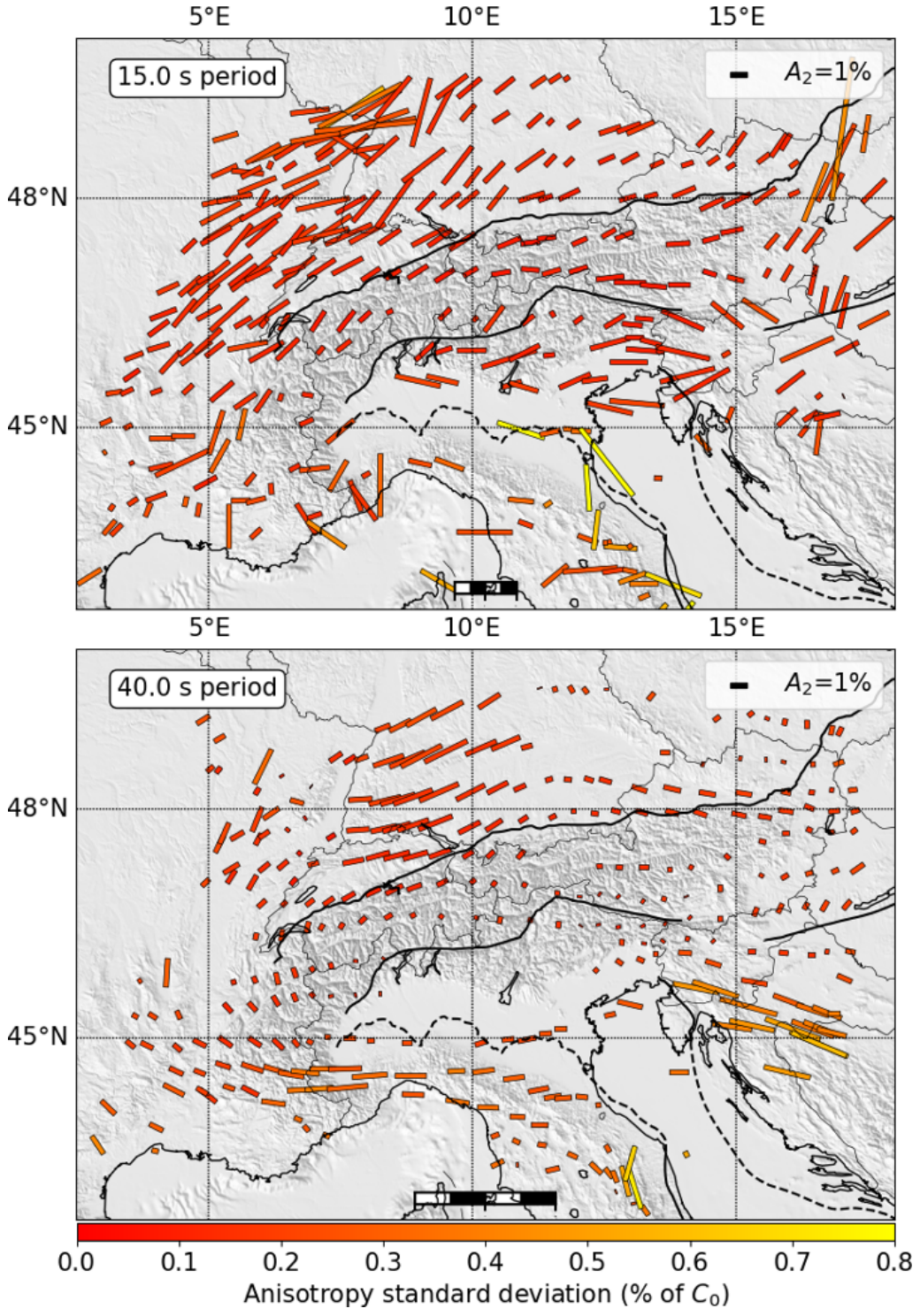

Figure 7. Maps of azimuthal anisotropy at 15 s and 40 s period resulting from the beamforming method. The direction of each line shows the fast direction, and the length shows the amplitude. The colour of the lines show the estimated uncertainty on the amplitude A_2 (in percent of C_0).

as surface waves are only sensitive to integrated velocities along a depth range. In the case where seismic anisotropy is inverted for, the non-uniqueness of the solution becomes particularly problematic as strong trade-offs emerge between different parameters. For example, the level of radial anisotropy trades off with V_p and with the level of heterogeneities in V_s [Bodin et al., 2015, Alder et al., 2017, Gao and Lekić, 2018], because of the equivalence of a stack of horizontal layers and a homogeneous anisotropic medium [Backus, 1962].

To add extra constraints on the solution, some regularisation can be used at the cost of biasing estimated uncertainties in the recovered model. In this way, linearized approaches only provide a unique velocity model that does not represent the range of potential solutions, and that is strongly dependent on the regularisation, the parameterization, or the reference model. For example, the V_p model is often set to a reference or arbitrarily scaled to V_s variations. The level of smoothness is also set in advance. Although these choices are based on geological or mineralogical arguments, they make the interpretation of results dependent on a priori choices.

Similar to isotropic inversions, these issues can be addressed by fully exploring the range of potential solutions with Monte Carlo methods (see Section 2.2.1). Since forward simulations are computationally cheap, a large number of 1-D models with variable parameterizations can be tested to sample complex posterior distributions. Adaptive parameterizations can be used to explore complex trade-offs between model parameters. For example, a transdimensional parameterization (where the number of model parameters is variable) can be used to explore the ambiguity between the level of spatial heterogeneity (horizontal layering) and the level of anisotropy created by the orientation of anisotropic minerals [Bodin et al., 2015, 2016, Alder et al., 2017]. In this case, the total number of layers in the inverted model as well as the presence of anisotropy in each layer are not constant parameters. Instead, they are adjusted by the inversion to fit the data to the degree required by their estimated noise. In this context, the Bayesian framework enables to propagate estimated uncertainties in the observed dispersion curves towards uncertainties in shear wave velocities at depth.

3.2.1. *Adaptive parameterizations: example with radial anisotropy*

To illustrate the benefit of such flexible parameterizations, we first show in Figure 8 an example of a synthetic test taken from Alder et al. [2021]. A target model is designed with a radially anisotropic layer in the crust and an isotropic upper crust and mantle. Noisy synthetic data are created and inverted with a transdimensional Monte Carlo algorithm, but with two different types of parameterizations (left and right panels). On the left, the number of layers is variable and each layer can be either isotropic and described solely by V_s and V_p (in this case, radial anisotropy in the form V_{SH}/V_{SV} takes a constant value of 1), or radially anisotropic and described by three parameters: V_{SV}, V_p and the level of radial anisotropy V_{SH}/V_{SV}. In this way, the number of inverted physical parameters in each layer is variable. On the right panel, the number of layers is also variable but all layers are radially anisotropic and described by three parameters. Everything else is equal in the two inversions.

Although the shear wave velocity is equally well resolved in both cases, the anisotropic layer in the crust is better recovered with the flexible scheme on the left. In the mantle, where the true model is isotropic, the ensemble solution produced on the left panel includes a large number of isotropic models, resulting in a narrower distribution for radial anisotropy and a median value of the distribution equal to unity. Conversely, in the case where anisotropy is imposed at all depths (right panels), a wider distribution of anisotropy is obtained, resulting in wider uncertainties.

This comparison shows that in the case of a true isotropic model, a flexible parameterization allows fitting data with simpler isotropic models that are described by fewer parameters. The result of the inversion is a distribution of models which is closer to the true model.

3.2.2. *Exploiting the full wealth of information in posterior distributions: example with azimuthal anisotropy*

The previous example shows the benefits of using complex adaptive parameterizations in Bayesian inversions. The solution is not a single model, but an ensemble of models with variable

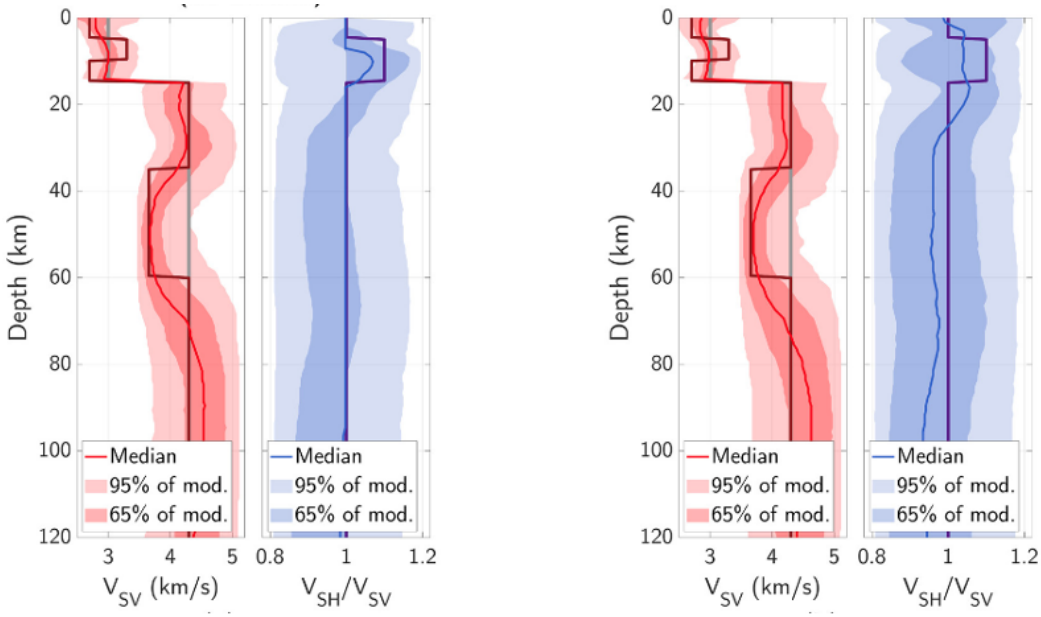

Figure 8. Joint inversion of Love and Rayleigh wave synthetic dispersion curves. The same data produced by the true model are inverted with two different procedures. Posterior distributions of V_{SV} (red), and V_{SH}/V_{SV} (blue). The true model used to create synthetic data is the thick solid line in every panel and the mean of the prior distribution used in the inversion is the grey line in the V_{SV} panel. Posterior distributions are depicted with their median (thin solid line) and likelihood intervals: for each parameter, the dark surface includes 65% of the models in the ensemble solution while the light area includes 95% of the models. Left panels: inversion used in Alder et al. [2021], where each layer can either be isotropic or anisotropic. Right panels: inversion where anisotropy is imposed as an unknown parameter at all depths. Modified from Alder et al. [2021].

parameterizations that approximates a probability distribution defined in a multiple dimensional space. As shown in Figure 8, one simple way to exploit this complex solution is to extract the mean or median value for a given parameter at each depth. Standard deviations can also be used, but more information is available about posterior covariances and trade-offs, and inference about these quantities can be hard to make. This wealth of information can be exploited through different angles of analysis and visualisation, each one giving additional insight to specific geophysical questions.

We illustrate this in Figure 9 where Rayleigh wave dispersion curves and their azimuthal variations measured from beamforming (see Section 3.1.3) are inverted at depth following the method of Bodin et al. [2016]. Here, the number of layers is variable and each layer is either isotropic and described solely by its isotropic shear-wave velocity, or azimuthally anisotropic and described by three parameters: (1) the isotropic shear-wave velocity; (2) the peak to peak level of azimuthal anisotropy, and (3) the direction of the horizontal fast axis relative to the north [Romanowicz and Yuan, 2012].

Figure 9 shows an example of inversion of a set of beamforming measurements below the Dinarides (location: ~45.3°N–16.3°E). The ensemble solution is shown in the left panels, where the probability of a given amplitude range and direction range for shear-wave anisotropy is shown at each depth. However, this way of displaying the posterior distribution does not show correlations and trade-offs between anisotropy amplitude and direction. Such plots do not show whether the sampled profiles contain thin isotropic layers, thin layers with strong anisotropy, or thick layers with small anisotropy.

To extract some key features from this complex probabilistic solution, Soergel et al. [2023] proposed

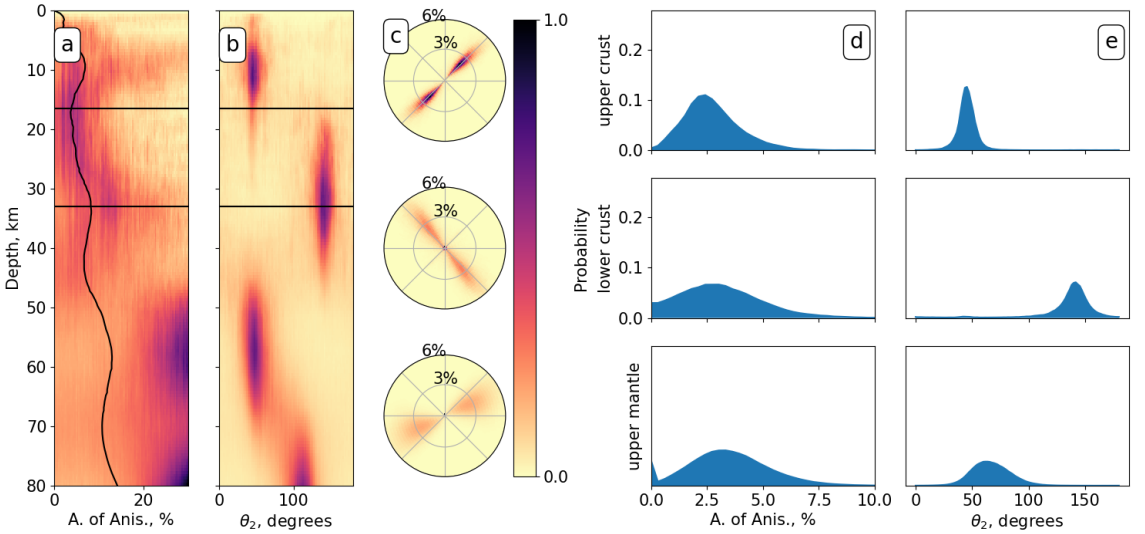

Figure 9. Depth inversion of Rayleigh wave surface wave dispersion curves with azimuthal variations for a subarray located in the Dinarides. The solution is a large ensemble of models with different parameterizations (different numbers of isotropic and anisotropic layers). (a) Probability distribution of the amplitude. (b) Probability distribution of the direction of the fast axis of anisotropy. The black line in (a) shows the average amplitude, and the horizontal black lines in (a) and (b) indicate the limits of the three layers over which we integrate anisotropy. (c) Density plot of anisotropy parameters integrated over the three different depth ranges. The radius in the polar plots indicate amplitude and the angle gives direction of the fast axis of anisotropy. The colour scale indicates the normalised probability of a given combination of amplitude and fast direction. Panels (d) and (e) show the marginal distributions of δV_S (d) and of θ_2 (e) for each of the three layers. The vertical scale is chosen such that the surface of the blue area is 1, that is the fraction of models with a given amplitude or (θ_2) range corresponds to the blue area within that range. Modified from Soergel et al. [2023].

to show the distribution of integrated anisotropy over a given depth range. The integration was defined as in Romanowicz and Yuan [2012], and carried out over three specific depth ranges with a meaningful sense (upper crust, lower crust, uppermost mantle). The distribution for the amplitude and direction of the anisotropy integrated over the three layers is shown in the right panels.

This visualisation makes it possible to see the correlations between fast direction and amplitude of anisotropy in each depth interval. Note that isotropic layers decrease the average level of anisotropy. Additionally, integrating anisotropy over several layers with different fast directions can also lead to anisotropy amplitudes smaller than expected. This explains the differences between the distribution of local anisotropy (left panels), and integrated anisotropy (right panels).

4. New information on the greater Alpine region

One of the main motivations behind the AlpArray initiative was to bring the resolution of seismic tomography closer to the spatial density of geological data over the entire Alpine belt, with the aim of increasing resolution of three-dimensional geological models at lithospheric scale. The methodological developments described in Section 2 have made a valuable contribution to this aim, in particular by providing new insights into the geometry of the crust-mantle boundary. A team of geologists and geophysicists is now working on exploiting the shear-wave velocity models derived by Nouibat et al. [2022a] and Nouibat et al. [2023] to build a 3-D structural model of the Western Alps [Bader et al., 2023]. All available geometrical (digital elevation model), geological (structural and geological maps) and geophysical

(3-D V_p and V_s models, DSS profiles, Moho models from seismic and gravity modeling/inversion, etc.) have been integrated and mixed in a geomodeling software, which provides a common framework and checks the geometrical coherence of geological interpretations of geophysical data [Calcagno et al., 2008]. The resolution of Nouibat et al. [2022a]'s model was sufficiently fine to allow Sonnet et al. [2023] to interpret a lateral V_s change in the subducted European lower crust as indication for the transition from amphibolite to granulite based on petrophysical data on Alpine rocks.

A depth map of the iso-velocity surface V_s = 4.2 km/s extracted from the model by Nouibat et al. [2023] is shown in Figure 10. As explained in Section 2.4, a composite depth map of velocity surfaces 3.8, 4.1 and 4.3 km/s would be a better proxy of the three Moho boundaries for the Ivrea body, the Ligurian basin, and Eurasia and Adria outside the Ivrea body region. The V_s = 4.2 km/s surface is therefore only an easy-to-calculate compromise. Since the velocity gradient is generally strong between 4.1 and 4.3 km/s, Figure 10 well illustrates lateral changes in Moho depth beneath the Alps revealed by our ambient noise tomography studies. The purple arrows highlight an ~8 km step in the European Moho with SSW–NNE orientation beneath the external crystalline massifs of the Western Alps, from Pelvoux to Mont Blanc. This orientation suggests that the Moho step might be a major lithospheric structure inherited from the Variscan orogeny. It had never been imaged before, even by the ECORS-CROP deep reflection profile, which showed reflections from the lower crust only west of the Belledonne external crystalline massif [e.g., Nicolas et al., 1990; see also Supplementary Figure S3 in Paul et al. [2022]]. The V_s models of Zhao et al. [2020], Nouibat et al. [2022a], and Nouibat et al. [2023] have confirmed the subduction of the European lithosphere beneath Adria, which is documented in Figure 10 by the dark blue areas (depth > 60 km). The CIFALPS cross-sections in Figures 3d–f document this continental subduction more precisely, with a European Moho reaching 75–80 km depth. Figure 10 also highlights the strong and rapid Moho depth changes along the belt strike, with maximum depths located right beneath the Insubric line (IL in Figure 10, also named Periadriatic fault further east) which marks the western and northern boundary of the undeformed Adria microplate [Handy et al., 2010]. The 3-D detailed geometry and internal structure of the Ivrea body are also important new findings of our ambient noise tomography studies. For example, the "inverted Moho" highlighted by receiver function sections (InvM in Figure 3b, dotted thick grey line in Figure 3e) is explained by the overthrusting of the Ivrea mantle slice of Adriatic origin onto the lower velocity European crust. This boundary was imaged a few tens of km north of the CIFALPS line by wide-angle reflections of the ECORS-CROP complementary experiment [ECORS-CROP Deep Seismic Sounding Group, 1989]. It was interpreted as the top of a second mantle slice beneath the Ivrea body, while the polarity of converted signals in receiver function studies and ambient noise tomography studies have proven that this reflector is the base of the Ivrea body (single) mantle slice [Zhao et al., 2015, Paul et al., 2022].

In the Ligurian basin, the wave-equation ANT model with elastic–acoustic coupling by Nouibat et al. [2023] has provided new images of the basin margins and new estimates of sediment thickness with potential inferences on tectonic models of basin formation. On Ligurian Moho depth, the recently published ANT V_s model by Magrini et al. [2022] exhibits significant differences from the V_s model by Nouibat et al. [2022b], with 15–18 km crustal thickness along the basin axis in Magrini et al. [2022]'s model and 12 km in Nouibat et al. [2023]'s. As explained in Section 2.4, the thinner crust of Nouibat et al. [2022b] is fully consistent with the P-wave velocity model derived from the refraction-reflection profile LOBSTER-P02 of Dannowski et al. [2020] along the Ligurian basin axis. The difference in Moho depth estimates between Nouibat et al. [2022b, 2023] and Magrini et al. [2022] may be due to different ray coverages in the Ligurian basin, as Magrini et al. [2022] did not use AlpArray OBS data.

Very little information was available on the anisotropy of the crust and upper mantle beneath the Alpine region prior to the works described in Section 3. Kästle et al. [2022] and Soergel et al. [2023] have mapped azimuthal anisotropy of Rayleigh wave phase velocity using ambient noise records of the AASN and permanent seismic stations, and two different methods, Eikonal and beamforming. Their azimuthal anisotropy maps are broadly similar at all periods, except at the periphery of the study area, probably due to differences in ray coverage

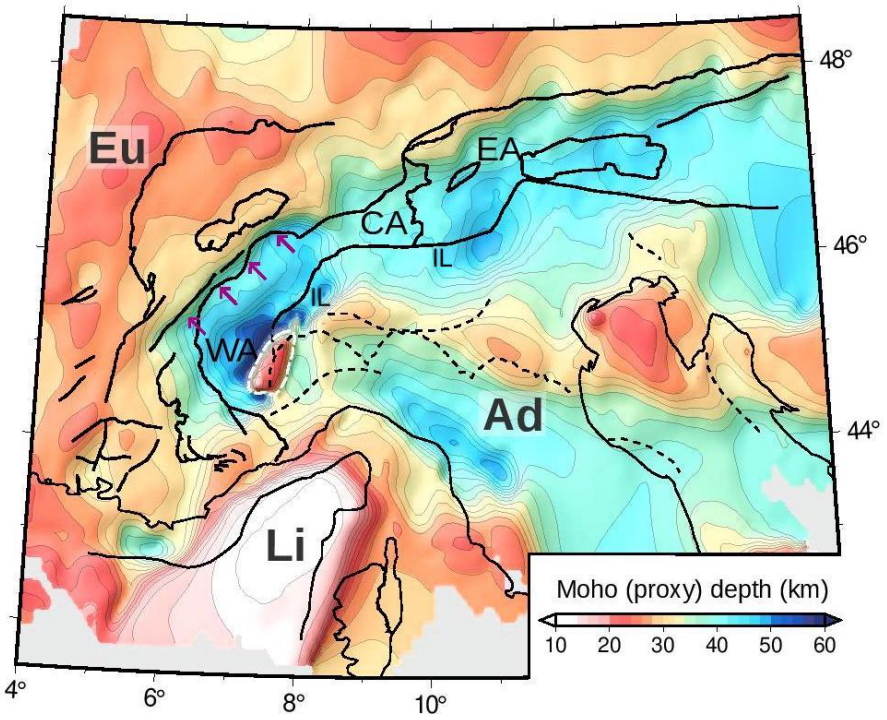

Figure 10. Depth map of the iso-velocity surface V_s = 4.2 km/s, extracted from the wave-equation ambient noise tomography model of Nouibat et al. [2023]. The continuous and dotted black lines are the main geological boundaries and faults, similar to Figure 1. The purple arrows highlight the Moho step located beneath the external crystalline massifs of the Western Alps. The dashed white line outlines the top of the high-velocity, peridotitic core of the Ivrea body, which appears as a dark blue spot in Figures 3d–f. Ad: Adria; CA: Central Alps; EA: Eastern Alps; Eu: Eurasia; IL: Insubric line; Li: Ligurian basin; WA: Western Alps. Modified from Nouibat et al. [2023].

(see examples at 15 and 40 s period in Figures 5 and 7). The Bayesian inversions for azimuthal anisotropy distribution with depth by Soergel et al. [2023] have shown that the anisotropic structure cannot be easily inferred from maps at individual periods. Spatially coherent anisotropy patterns are only visible in the upper half of the crust, with fast-velocity directions mostly parallel to the strike of the belt and amplitudes of 1–2% [see Figure 14 in Soergel et al., 2023]. By contrast, fast-velocity directions are mostly perpendicular to the belt in the lower half of the crust and uppermost mantle, with strongly varying amplitudes and no large-scale spatial pattern. This contrast between the shallow and deep layers suggests that Alpine deformation has only impacted the upper crust, through oriented crack and fractures, while the lower crust and upper mantle bear the imprint of more ancient processes. A single region located northwest of the Jura mountains displays coherent NE–SW fast velocity directions from the upper crust to the upper mantle, and rather strong amplitudes (~1%) in the lower crust. This orientation suggests that the observed anisotropy in that area outside the Alps may be of Variscan origin, and unaffected by the Alpine orogeny. Soergel et al. [2023] highlight the general disagreement between the fast-velocity directions they measured in the upper mantle and the fast directions measured from the splitting of core-refacted XKS teleseismic phases [e.g., Hein et al., 2021]. This may indicate that the source of XKS splitting is located deeper than the lithospheric mantle, either in the asthenosphere or in the subduction slabs.

When applied to Rayleigh and Love dispersion curves measured in the Alpine region, the flexible parameterization of Bayesian inversion allowed Alder et al. [2021] to produce maps of radial anisotropy differing from previous large-scale studies that suggested the presence of significant radial anisotropy everywhere in the European crust and shallow upper mantle [e.g., Zhu et al., 2015]. Instead, they observed that radial anisotropy is mostly localised beneath the Apennines while most of the crust and shallow upper mantle is isotropic in other parts of Europe. Thanks to synthetic tests, they attributed this difference to trade-offs between radial anisotropy and thin (hectometric) layering in previous studies based on least-squares inversions and long period data (>30 s). In contrast, Alder et al. [2021]'s approach involved a massive dataset of short period measurements and a Bayesian inversion that accounts for thin layering. They showed that the positive radial anisotropy ($V_{SH} > V_{SV}$) observed in the lower crust of the Apennines could not result from thin layering, but rather from ductile horizontal flow in response to the strong flexure of the Adriatic plate induced by doubly-vergent subduction.

5. Conclusions

The Alpine broadband seismic networks, including permanent stations and the temporary AlpArray seismic network have provided an optimal dataset for the development, improvement, and application of ambient-noise-based imaging methods. High station density and homogeneous coverage were key elements for these methodological improvements.

The overarching goals of our work were to improve observations when needed, move towards a probabilistic framework for inversion and interpretation, and adapting full waveform modelling in the forward problem. On the observational side, the work focused on (a) developing suitable techniques to combine OBS and land observations through higher order correlations, (b) improving our understanding of systematic errors made when measuring surface wave azimuthal anisotropy, and (c) applying and adapting beamforming techniques to seismic noise correlations to estimate surface wave anisotropy.

For the inversions, a Bayesian framework was applied both to 2-D inversions for group velocity maps [Nouibat et al., 2022a], and to 1-D depth inversions for elastic structure [Lu et al., 2018, Zhao et al., 2020, Alder et al., 2021, Soergel et al., 2023]. Particular efforts [Alder et al., 2021, Soergel et al., 2023] were made on the extraction of robust anisotropic parameters which are meaningful in a geologic/tectonic sense. Wave-equation ambient noise tomography studies by Lu et al. [2020] and Nouibat et al. [2023] have further improved ANT models by accounting for the physics of seismic wave propagation. The introduction of elastic–acoustic coupling at the seabed has enabled Nouibat et al. [2023] to improve the imaging of shallow layers below the sea. All of these developments led to improved models of the crust and uppermost mantle on the scale of the greater Alpine area (see Section 4).

The link between the overarching goals is naturally increasing because of the strong link between observational errors and the estimation of model resolution within a probabilistic inversion framework. In such a framework, the inversion provides not a single Earth model, but an ensemble of models obtained whilst taking into account uncertainties of inverted data. In this context, reliable error estimates of observables become objectively tied to the estimation of model uncertainties [Gallagher et al., 2009, Sambridge et al., 2013]. Also, the ensemble of models can be explored based on scientific questions (for example "What is the probability that the lower crust beneath the Apennines has significant radial anisotropy of crystallographic origin?") [Curtis, 1999, Meier et al., 2007, Zhang and Curtis, 2021].

Note also that the Bayesian framework allows to include independent information from geology, mineralogy, or other geophysical methods such as gravimetry. This can be done through the definition of the a priori distribution, or through the joint inversion of different datasets. Including other data types sensitive to P-wave structure (body waves) would be very useful for geological interpretation, as P and S waves have different sensitivities to different rock types, for example to hydrated minerals. In this context, full waveform inversion has the benefit to model the entire wavefield without having to preliminary extract and separate different data types (arrival times, phase velocities, splitting parameters, etc.), and three-dimensional variations of the entire elastic tensor can be directly reconstructed, including V_p, V_s and anisotropy. However, full waveform to-

mography in a fully non-linear Bayesian framework is still a prospect for the future, due to the computational cost of the forward model.

Within the framework of the AlpArray experiment, other noise-based methods were developed. For crustal imaging, it is becoming feasible to image coda-Q [Soergel et al., 2020], overcoming the difficulty of obtaining reliable amplitudes of noise correlations. This method makes it possible to estimate coda-Q at longer periods than those accessible through local earthquake estimates, but the method needs to be further developed to fully understand the meaning and reliability of the observed coda-Q values. The dense data coverage of the Alps also served the purpose of improving methods to extract body waves (reflections from mantle discontinuities) from seismic noise correlations [Pedersen et al., 2023, Lu et al., 2023].

The methods developed within the framework of the AlpArray experiment can naturally be applied and further improved within the framework of other dense and large-scale seismic arrays, such as the recently started AdriaArray experiment which significantly extends the area of high station density around the Adriatic plate, from the French Massif Central in the west to the Carpathians in the east [Kolínský et al., 2023; https://orfeus.readthedocs.io/en/latest/adria_array_main.html].

Declaration of interests

The authors do not work for, advise, own shares in, or receive funds from any organization that could benefit from this article, and have declared no affiliations other than their research organizations.

Funding

A large part of the studies described here were conducted within the AlpArray-FR project funded by Agence Nationale de la Recherche, France (contract ANR-15-CE31-0015), and Labex OSUG@2020 (Investissement d'Avenir, ANR-10-LABX-56). TB, CA and DS were funded by the European Research Council under the European Union Horizon 2020 research and innovation program (grant agreement 716542 – TRANSCALE). AP's work on the Alps is currently funded by project LisAlps (contract ANR-20-CE49-0007). EK is funded by the German Science Foundation DFG (SPP-2017, Project Ha 2403/21-1).

Acknowledgments

We are grateful to our colleagues, Laurent Stehly, Romain Brossier, and Eric Debayle who co-supervised YL's, CA's and AN's Ph-D theses with AP and TB, and have made major contributions to much of the work presented here. Liang Zhao (IGG-CAS Beijing) is also acknowledged for his decisive contributions to this work. This paper was partly conceived during the Cargèse 2022 school on "Passive imaging and monitoring in wave physics: from seismology to ultrasound", in which AP took part. We would therefore like to thank the organizers, in particular Michel Campillo and Nikolaï Shapiro for encouraging us to write it. We acknowledge detailed and constructive comments by two anonymous reviewers that helped improving the manuscript, and editorial handling by Andrew Curtis. Without high-quality, open data, such work is impossible. We therefore gratefully thank the operators of the European permanent seismic networks who make their data available through EIDA (http://www.orfeus-eu.org/eida), the AlpArray Seismic Network Team who operated the AASN (Z3-2015 network) and the CIFALPS Team who operated the CIFALPS experiments (YP-2012 and XT-2018 networks).

References

Aki, K., Christoffersson, A., and Husebye, E. S. (1977). Determination of the three-dimensional seismic structure of the lithosphere. *J. Geophys. Res.*, 82(2), 277–296.

Alder, C., Bodin, T., Ricard, Y., Capdeville, Y., Debayle, E., and Montagner, J. P. (2017). Quantifying seismic anisotropy induced by small-scale chemical heterogeneities. *Geophys. J. Int.*, 211(3), 1585–1600.

Alder, C., Debayle, E., Bodin, T., Paul, A., Stehly, L., Pedersen, H., and AlpArray Working Group (2021). Evidence for radial anisotropy in the lower crust of the Apennines from Bayesian ambient noise tomography in Europe. *Geophys. J. Int.*, 226(2), 941–967.

AlpArray Seismic Network (2014). Eastern Alpine Seismic Investigation (EASI)—AlpArray Complimentary Experiment [Data set]. AlpArray Working Group. https://doi.org/10.12686/alparray/xt_2014.

AlpArray Seismic Network (2015). AlpArray Seismic Network (AASN) temporary component [Data

set]. AlpArray Working Group. https://doi.org/10.12686/alparray/z3_2015.

Alvizuri, C. and Tanimoto, T. (2011). Azimuthal anisotropy from array analysis of Rayleigh waves in Southern California. *Geophys. J. Int.*, 186(3), 1135–1151.

Argand, E. (1922). La tectonique de l'Asie. In *Conference at the Geological International Congress XIII, Brussels (Belgium)*, pages 171–372. https://hal-insu.archives-ouvertes.fr/insu-00575289/.

Backus, G. E. (1962). Long-wave elastic anisotropy produced by horizontal layering. *J. Geophys. Res.*, 67(11), 4427–4440.

Bader, A. G., Calcagno, P., Bellahsen, N., and Paul, A. (2023). Towards a 3D crustal geomodel of the Western Alps in the French Geological Reference Platform (RGF). In *EGU General Assembly Conference Abstracts*, pages EGU–11633.

Bagagli, M., Molinari, I., Diehl, T., Kissling, E., and Giardini, D. (2022). The AlpArray research seismicity-catalogue. *Geophys. J. Int.*, 231(2), 921–943.

Barruol, G., Bonnin, M., Pedersen, H., Bokelmann, G. H., and Tiberi, C. (2011). Belt-parallel mantle flow beneath a halted continental collision: The Western Alps. *Earth Planet. Sci. Lett.*, 302(3–4), 429–438.

Barruol, G., Deschamps, A., and Coutant, O. (2004). Mapping upper mantle anisotropy beneath SE France by SKS splitting indicates Neogene asthenospheric flow induced by Apenninic slab roll-back and deflected by the deep Alpine roots. *Tectonophysics*, 394(1–2), 125–138.

Bodin, T., Capdeville, Y., Romanowicz, B., and Montagner, J. P. (2015). Interpreting radial anisotropy in global and regional tomographic models. In Khan, A. and Deschamps, F., editors, *The Earth's Heterogeneous Mantle*, Springer Geophysics, pages 105–144. Springer, Cham.

Bodin, T., Leiva, J., Romanowicz, B., Maupin, V., and Yuan, H. (2016). Imaging anisotropic layering with Bayesian inversion of multiple data types. *Geophys. J. Int.*, 206(1), 605–629.

Bodin, T., Sambridge, M., Rawlinson, N., and Arroucau, P. (2012). Transdimensional tomography with unknown data noise. *Geophys. J. Int.*, 189(3), 1536–1556.

Bokelmann, G., Qorbani, E., and Bianchi, I. (2013). Seismic anisotropy and large-scale deformation of the Eastern Alps. *Earth Planet. Sci. Lett.*, 383, 1–6.

Boschi, L. and Dziewonski, A. M. (1999). High- and low-resolution images of the Earth's mantle: Implications of different approaches to tomographic modeling. *J. Geophys. Res.: Solid Earth*, 104(B11), 25567–25594.

Boschi, L., Fry, B., Ekström, G., and Giardini, D. (2009). The European upper mantle as seen by surface waves. *Surv. Geophys.*, 30, 463–501.

Calcagno, P., Chilès, J. P., Courrioux, G., and Guillen, A. (2008). Geological modelling from field data and geological knowledge: Part I. Modelling method coupling 3d potential-field interpolation and geological rules. *Phys. Earth Planet. Inter.*, 171, 147–157.

Campillo, M. (2006). Phase and correlation in "random" seismic fields and the reconstruction of the green function. *Pure Appl. Geophys.*, 163, 475–502.

Campillo, M. and Paul, A. (2003). Long-range correlations in the diffuse seismic coda. *Science*, 299(5606), 547–549.

Chen, M., Huang, H., Yao, H., van der Hilst, R., and Niu, F. (2014). Low wave speed zones in the crust beneath SE Tibet revealed by ambient noise adjoint tomography. *Geophys. Res. Lett.*, 41(2), 334–340.

Chopin, C. (1984). Coesite and pure pyrope in high-grade blueschists of the Western Alps: A first record and some consequences. *Contrib. Mineral. Petrol.*, 86, 107–118.

Closs, H. and Labrouste, Y. (1963). *Recherches séismologiques dans les Alpes Occidentales au moyen des grandes explosions en 1956, 1958 et 1960: Année Géophysique Internationale*. CNRS. 12e série, fasc. II.

Crawford, W. C. and Webb, S. C. (2000). Identifying and removing tilt noise from low-frequency (<0.1 Hz) seafloor vertical seismic data. *Bull. Seismol. Soc. Am.*, 90(4), 952–963.

Crawford, W. C., Webb, S. C., and Hildebrand, J. A. (1998). Estimating shear velocities in the oceanic crust from compliance measurements by twodimensional finite difference modeling. *J. Geophys. Res.: Solid Earth*, 103(B5), 9895–9916.

Curtis, A. (1999). Optimal design of focused experiments and surveys. *Geophys. J. Int.*, 139(1), 205–215.

Dannowski, A., Kopp, H., Grevemeyer, I., Lange, D., Thorwart, M., Bialas, J., and Wollatz-Vogt, M. (2020). Seismic evidence for failed rifting in the Ligurian Basin, Western Alpine domain. *Solid Earth*,

11(3), 873–887.

Díaz, J., Gil, A., and Gallart, J. (2013). Uppermost mantle seismic velocity and anisotropy in the Euro-Mediterranean region from Pn and Sn tomography. *Geophys. J. Int.*, 192(1), 310–325.

Diehl, T., Husen, S., Kissling, E., and Deichmann, N. (2009). High-resolution 3-DP-wave model of the Alpine crust. *Geophys. J. Int.*, 179(2), 1133–1147.

ECORS-CROP Deep Seismic Sounding Group (1989). A new picture of the Moho under the western Alps. *Nature*, 337(6204), 249–251.

El-Sharkawy, A., Meier, T., Lebedev, S., Behrmann, J. H., Hamada, M., Cristiano, L., et al. (2020). The slab puzzle of the Alpine-Mediterranean region: Insights from a new, high-resolution, shear wave velocity model of the upper mantle. *Geochem. Geophys. Geosyst.*, 21(8), article no. e2020GC008993.

Eva, E., Malusà, M. G., and Solarino, S. (2015). A seismotectonic picture of the inner southern Western Alps based on the analysis of anomalously deep earthquakes. *Tectonophysics*, 661, 190–199.

Fichtner, A. (2014). Source and processing effects on noise correlations. *Geophys. J. Int.*, 197(3), 1527–1531.

Frei, W., Heitzmann, P., and Lehner, P. (1990). Swiss NFP-20 research program of the deep structure of the Alps. *Mémoires de la Société géologique de France (1833)*, 156, 29–46.

Friedrich, A., Krüger, F., and Klinge, K. (1998). Ocean-generated microseismic noise located with the Gräfenberg array. *J. Seismol.*, 2, 47–64.

Froment, B., Campillo, M., Roux, P., Gouedard, P., Verdel, A., and Weaver, R. L. (2010). Estimation of the effect of non-isotropically distributed energy on the apparent arrival time in correlations. *Geophysics*, 75(5), SA85–SA93.

Fry, B., Deschamps, F., Kissling, E., Stehly, L., and Giardini, D. (2010). Layered azimuthal anisotropy of Rayleigh wave phase velocities in the European Alpine lithosphere inferred from ambient noise. *Earth Planet. Sci. Lett.*, 297(1–2), 95–102.

Gallagher, K., Charvin, K., Nielsen, S., Sambridge, M., and Stephenson, J. (2009). Markov chain Monte Carlo (MCMC) sampling methods to determine optimal models, model resolution and model choice for Earth Science problems. *Mar. Pet. Geol.*, 26(4), 525–535.

Gao, C. and Lekić, V. (2018). Consequences of parametrization choices in surface wave inversion: Insights from transdimensional Bayesian methods. *Geophys. J. Int.*, 215(2), 1037–1063.

Grad, M., Tiira, T., and ESC Working Group (2009). The Moho depth map of the European Plate. *Geophys. J. Int.*, 176(1), 279–292.

Guerin, G., Rivet, D., Deschamps, A., Larroque, C., Mordret, A., Dessa, J. X., and Martin, X. (2020). High resolution ambient noise tomography of the Southwestern Alps and the Ligurian margin. *Geophys. J. Int.*, 220(2), 806–820.

Handy, M. R., Schmid, S. M., Bousquet, R., Kissling, E., and Bernoulli, D. (2010). Reconciling plate-tectonic reconstructions of Alpine Tethys with the geological–geophysical record of spreading and subduction in the Alps. *Earth-Sci. Rev.*, 102(3–4), 121–158.

Harmon, N., Rychert, C., and Gerstoft, P. (2010). Distribution of noise sources for seismic interferometry. *Geophys. J. Int.*, 183(3), 1470–1484.

Hein, G., Kolínský, P., Bianchi, I., and Bokelmann, G. (2021). Shear wave splitting in the Alpine region. *Geophys. J. Int.*, 227(3), 1996–2015.

Heit, B., Weber, M., Tilmann, F., Haberland, C., Jia, Y., Carraro, C., Walcher, G., Franceschini, A., and Pesaresi, D. (2017). The Swath-D Seismic Network in Italy and Austria [Data set]. GFZ Data Services. https://doi.org/10.14470/MF7562601148.

Hetényi, G., Molinari, I., Clinton, J., Bokelmann, G., Bondar, I., Crawford, W. C., et al. (2018a). The AlpArray seismic network: A large-scale European experiment to image the Alpine orogen. *Surv. Geophys.*, 39(5), 1009–1033.

Hetényi, G., Plomerová, J., Bianchi, I., Exnerová, H. K., Bokelmann, G., Handy, M. R., Babuška, V., and AlpArray-EASI Working Group (2018b). From mountain summits to roots: Crustal structure of the Eastern Alps and Bohemian Massif along longitude 13.3° E. *Tectonophysics*, 744, 239–255.

Juretzek, C. and Hadziioannou, C. (2016). Where do ocean microseisms come from? A study of Love-to-Rayleigh wave ratios. *J. Geophys. Res.: Solid Earth*, 121(9), 6741–6756.

Kästle, E. D., El-Sharkawy, A., Boschi, L., Meier, T., Rosenberg, C., Bellahsen, N., Cristiano, L., and Weidle, C. (2018). Surface wave tomography of the Alps using ambientnoise and earthquake phase velocity measurements. *J. Geophys. Res.: Solid Earth*, 123(2), 1770–1792.

Kästle, E. D., Molinari, I., Boschi, L., Kissling, E.,

and AlpArray Working Group (2022). Azimuthal anisotropy from eikonal tomography: example from ambient-noise measurements in the AlpArray network. *Geophys. J. Int.*, 229(1), 151–170.

Kästle, E. D., Soomro, R., Weemstra, C., Boschi, L., and Meier, T. (2016). Two-receiver measurements of phase velocity: cross-validation of ambient-noise and earthquake-based observations. *Geophys. J. Int.*, 207(3), 1493–1512.

Kästle, E. D., Tilmann, F., and AlpArray and SwathD Working Groups (2024). Anisotropic reversible-jump McMC shear-velocity tomography of the Eastern Alpine crust. *Geochem. Geophys. Geosyst.*, 25(3), article no. e2023GC011238.

Kolínský, P., Meier, T., and AdriaArray Seismology Group (2023). AdriaArray Seismic Network – status in April 2023. In *EGU General Assembly*, pages EGU23–12284.

Komatitsch, D. and Tromp, J. (1999). Introduction to the spectral element method for three-dimensional seismic wave propagation. *Geophys. J. Int.*, 139(3), 806–822.

Komatitsch, D. and Vilotte, J. P. (1998). The spectral element method: an efficient tool to simulate the seismic response of 2D and 3D geological structures. *Bull. Seismol. Soc. Am.*, 88(2), 368–392.

Kummerow, J., Kind, R., Oncken, O., Giese, P., Ryberg, T., Wylegalla, K., Scherbaum, F., and TRANSALP Working Group (2004). A natural and controlled source seismic profile through the Eastern Alps: TRANSALP. *Earth Planet. Sci. Lett.*, 225, 115–129.

Kustowski, B., Ekström, G., and Dziewoński, A. M. (2008). Anisotropic shearwave velocity structure of the Earth's mantle: A global model. *J. Geophys. Res.: Solid Earth*, 113(B6), article no. B06306.

Kvapil, J., Plomerová, J., Kampfová Exnerová, H., Babuška, V., Hetényi, G., and AlpArray Working Group (2021). Transversely isotropic lower crust of Variscan central Europe imaged by ambient noise tomography of the Bohemian Massif. *Solid Earth*, 12(5), 1051–1074.

Landès, M., Hubans, F., Shapiro, N. M., Paul, A., and Campillo, M. (2010). Origin of deep ocean microseisms by using teleseismic body waves. *J. Geophys. Res.: Solid Earth*, 115(B5), article no. B05302.

Lin, F. C. and Ritzwoller, M. H. (2011). Apparent anisotropy in inhomogeneous isotropic media. *Geophys. J. Int.*, 186(3), 1205–1219.

Lin, F. C., Ritzwoller, M. H., and Snieder, R. (2009). Eikonal tomography: surface wave tomography by phase front tracking across a regional broad-band seismic array. *Geophys. J. Int.*, 177(3), 1091–1110.

Lippitsch, R., Kissling, E., and Ansorge, J. (2003). Upper mantle structure beneath the Alpine orogen from high-resolution teleseismic tomography. *J. Geophys. Res.*, 108(B8), article no. 2376.

Lombardi, D., Braunmiller, J., Kissling, E., and Giardini, D. (2008). Moho depth and Poisson's ratio in the Western-Central Alps from receiver functions. *Geophys. J. Int.*, 173(1), 249–264.

Lu, Y., Schmid, S. M., Wang, Q. Y., and Bokelmann, G. (2023). Mapping the mantle transition zone discontinuities across South-Central Europe using body waves from seismic noise correlations. *Earth Planet. Sci. Lett.*, 624, article no. 118457.

Lu, Y., Stehly, L., Brossier, R., Paul, A., and AlpArray Working Group (2020). Imaging Alpine crust using ambient noise wave-equation tomography. *Geophys. J. Int.*, 222(1), 69–85.

Lu, Y., Stehly, L., Paul, A., and AlpArray Working Group (2018). High-resolution surface wave tomography of the European crust and uppermost mantle from ambient seismic noise. *Geophys. J. Int.*, 214(2), 1136–1150.

Lucente, F. P., Margheriti, L., Piromallo, C., and Barruol, G. (2006). Seismic anisotropy reveals the long route of the slab through the western-central Mediterranean mantle. *Earth Planet. Sci. Lett.*, 241(3–4), 517–529.

Lüschen, E., Borrini, D., Gebrande, H., Lammerer, B., Millahn, K., Neubauer, F., Nicolich, R., and TRANSALP Working Group (2006). TRANSALP—deep crustal Vibroseis and explosive seismic profiling in the Eastern Alps. *Tectonophysics*, 414, 9–38.

Macquet, M., Paul, A., Pedersen, H. A., Villaseñor, A., Chevrot, S., Sylvander, M., Wolyniec, D., and Pyrope Working Group (2014). Ambient noise tomography of the Pyrenees and the surrounding regions: inversion for a 3-D Vs model in the presence of a very heterogeneous crust. *Geophys. J. Int.*, 199(1), 402–415.

Magrini, F., Diaferia, G., El-Sharkawy, A., Cammarano, F., van Der Meijde, M., Meier, T., and Boschi, L. (2022). Surface-wave tomography of the central-western mediterranean: new insights into the liguro-provençal and tyrrhenian basins. *J. Geophys. Res.: Solid Earth*, 127(3), arti-

cle no. e2021JB023267.

Malusà, M. G., Guillot, S., Zhao, L., Paul, A., Solarino, S., Dumont, T., et al. (2021). The deep structure of the Alps based on the CIFALPS seismic experiment: A synthesis. *Geochem. Geophys. Geosyst.*, 22(3), article no. e2020GC009466.

Marchant, R. H. and Stampfli, G. M. (1997). Subduction of continental crust in the Western Alps. *Tectonophysics*, 269(3–4), 217–235.

Mauerberger, A., Maupin, V., Gudmundsson, Ó., and Tilmann, F. (2021). Anomalous azimuthal variations with 360° periodicity of Rayleigh phase velocities observed in Scandinavia. *Geophys. J. Int.*, 224(3), 1684–1704.

Maupin, V. (2011). Upper-mantle structure in southern Norway from beamforming of Rayleigh wave data presenting multipathing. *Geophys. J. Int.*, 185(2), 985–1002.

Maupin, V. and Park, J. (2015). 1.09—Theory and observations—Seismic anisotropy. In *Treatise on Geophysics*, volume 20, pages 277–305. Elsevier, Amsterdam.

Meier, U., Curtis, A., and Trampert, J. (2007). Global crustal thickness from neural network inversion of surface wave data. *Geophys. J. Int.*, 169(2), 706–722.

Michailos, K., Hetényi, G., Scarponi, M., Stipčević, J., Bianchi, I., Bonatto, L., others, and AlpArray-PACASE Working Group (2023). Moho depths beneath the European Alps: a homogeneously processed map and receiver functions database. *Earth Syst. Sci. Data*, 15(5), 2117–2138.

Molinari, I., Obermann, A., Kissling, E., Hetényi, G., Boschi, L., and AlpArray-Easi Working Group (2020). 3D crustal structure of the Eastern Alpine region from ambient noise tomography. *Results Geophys. Sci.*, 1, article no. 100006.

Molinari, I., Verbeke, J., Boschi, L., Kissling, E., and Morelli, A. (2015). Italian and Alpine three-dimensional crustal structure imaged by ambient-noise surface-wave dispersion. *Geochem. Geophys. Geosyst.*, 16(12), 4405–4421.

Montagner, J. P. and Nataf, H. C. (1986). A simple method for inverting the azimuthal anisotropy of surface waves. *J. Geophys. Res.: Solid Earth*, 91(B1), 511–520.

Nicolas, A., Hirn, A., Nicolich, R., Polino, R., and ECORS-CROP Working Group (1990). Lithospheric wedging in the western Alps inferred from the ECORS-CROP traverse. *Geology*, 18, 587–590.

Nita, B., Maurya, S., and Montagner, J. P. (2016). Anisotropic tomography of the European lithospheric structure from surface wave studies. *Geochem. Geophys. Geosyst.*, 17(6), 2015–2033.

Nouibat, A., Brossier, R., Stehly, L., Cao, J., Paul, A., and AlpArray Working Group (2023). Ambient-noise wave-equation tomography of the Alps and Ligurian-Provence basin. *J. Geophys. Res.: Solid Earth*, 128, article no. e2023JB026776.

Nouibat, A., Stehly, L., Paul, A., Schwartz, S., Bodin, T., Dumont, T., Rolland, Y., Brossier, R., and AlpArray Working Group (2022a). Lithospheric transdimensional ambient-noise tomography of W-Europe: implications for crustal-scale geometry of the W-Alps. *Geophys. J. Int.*, 229(2), 862–879.

Nouibat, A., Stehly, L., Paul, A., Schwartz, S., Rolland, Y., Dumont, T., Crawford, W. C., Brossier, R., and AlpArray Working Group (2022b). Ambientnoise tomography of the Ligurian-Provence Basin using the AlpArray onshore-offshore network: Insights for the oceanic domain structure. *J. Geophys. Res.: Solid Earth*, 127, article no. e2022JB024228.

Paffrath, M., Friederich, W., Schmid, S. M., Handy, M. R., and AlpArray and AlpArray-Swath D Working Group (2021). Imaging structure and geometry of slabs in the greater Alpine area–A P-wave traveltime tomography using AlpArray Seismic Network data. *Solid Earth*, 12(11), 2671–2702.

Palano, M. (2015). On the present-day crustal stress, strain-rate fields and mantle anisotropy pattern of Italy. *Geophys. J. Int.*, 200(2), 969–985.

Pasyanos, M. E., Masters, T. G., Laske, G., and Ma, Z. (2014). LITHO1. 0: An updated crust and lithospheric model of the Earth. *J. Geophys. Res.: Solid Earth*, 119(3), 2153–2173.

Paul, A., Cattaneo, M., Thouvenot, F., Spallarossa, D., Béthoux, N., and Fréchet, J. (2001). A three-dimensional crustal velocity model of the south-western Alps from local earthquake tomography. *J. Geophys. Res.: Solid Earth*, 106(B9), 19367–19389.

Paul, A., Malusà, M. G., Solarino, S., Salimbeni, S., Eva, E., Nouibat, A., et al. (2022). Along-strike variations in the fossil subduction zone of the Western Alps revealed by the CIFALPS seismic experiments and their implications for exhumation of (ultra-) high-pressure rocks. *Earth Planet. Sci. Lett.*, 598, article no. 117843.

Pedersen, H. A., Boué, P., Poli, P., and Colombi, A. (2015). Arrival angle anomalies of Rayleigh waves

observed at a broadband array: a systematic study based on earthquake data, full waveform simulations and noise correlations. *Geophys. J. Int.*, 203(3), 1626–1641.

Pedersen, H. A., Bruneton, M., Maupin, V., and SVEKALAPKO Seismic Tomography Working Group (2006). Lithospheric and sublithospheric anisotropy beneath the Baltic shield from surface-wave array analysis. *Earth Planet. Sci. Lett.*, 244(3–4), 590–605.

Pedersen, H. A., Mattern, F., Poli, P., and Stehly, L. (2023). Imaging with seismic noise: improving extraction of body wave phases from the deep Earth through selective stacking based on H/V ratios. *Geophys. J. Int.*, 232(2), 1455–1467.

Pilia, S., Rawlinson, N., Cayley, R. A., Bodin, T., Musgrave, R., Reading, A. M., Direen, N. G., and Young, M. K. (2015). Evidence of micro-continent entrainment during crustal accretion. *Sci. Rep.*, 5(1), article no. 8218.

Piromallo, C. and Morelli, A. (2003). P wave tomography of the mantle under the Alpine-Mediterranean area. *J. Geophys. Res.*, 108(B2), article no. 2065.

Qorbani, E., Bianchi, I., and Bokelmann, G. (2015). Slab detachment under the Eastern Alps seen by seismic anisotropy. *Earth Planet. Sci. Lett.*, 409, 96–108.

Rappisi, F., VanderBeek, B. P., Faccenda, M., Morelli, A., and Molinari, I. (2022). Slab geometry and upper mantle flow patterns in the central mediterranean from 3D anisotropic P-wave tomography. *J. Geophys. Res.: Solid Earth*, 127(5), article no. e2021JB023488.

Rawlinson, N. and Sambridge, M. (2004). Multiple reflection and transmission phases in complex layered media using a multistage fast marching method. *Geophysics*, 69(5), 1338–1350.

Riahi, N. and Saenger, E. H. (2014). Rayleigh and Love wave anisotropy in Southern California using seismic noise. *Geophys. Res. Lett.*, 41(2), 363–369.

Rollet, N., Déverchere, J., Beslier, M. O., Guennoc, P., Réhault, J. P., Sosson, M., and Truffert, C. (2002). Back arc extension, tectonic inheritance, and volcanism in the Ligurian Sea, Western Mediterranean. *Tectonics*, 21(3), 6–1–6–23.

Romanowicz, B. and Yuan, H. (2012). On the interpretation of SKS splitting measurements in the presence of several layers of anisotropy. *Geophys. J. Int.*, 188(3), 1129–1140.

Rost, S. and Thomas, C. (2002). Array seismology: Methods and applications. *Rev. Geophys.*, 40(3), 2–1–2–27.

Sadeghi-Bagherabadi, A., Vuan, A., Aoudia, A., Parolai, S., and AlpArray and AlpArray-Swath-D Working Group (2021). High-resolution crustal S-wave velocity model and Moho geometry beneath the Southeastern Alps: New insights from the SWATH-D experiment. *Front. Earth Sci.*, 9, article no. 641113.

Sager, K., Ermert, L., Boehm, C., and Fichtner, A. (2018). Towards full waveform ambient noise inversion. *Geophys. J. Int.*, 212(1), 566–590.

Salimbeni, S., Malusà, M. G., Zhao, L., Guillot, S., Pondrelli, S., Margheriti, L., et al. (2018). Active and fossil mantle flows in the western Alpine region unravelled by seismic anisotropy analysis and high-resolution P wave tomography. *Tectonophysics*, 731, 35–47.

Sambridge, M., Bodin, T., Gallagher, K., and Tkalčić, H. (2013). Transdimensional inference in the geosciences. *Phil. Trans. R. Soc. A*, 371(1984), article no. 20110547.

Schippkus, S., Zigone, D., and Bokelmann, G. (2020). Azimuthal anisotropy in the wider Vienna basin region: a proxy for the present-day stress field and deformation. *Geophys. J. Int.*, 220(3), 2056–2067.

Schippkus, S., Zigone, D., Bokelmann, G., and AlpArray Working Group (2018). Ambient-noise tomography of the wider Vienna Basin region. *Geophys. J. Int.*, 215(1), 102–117.

Schivardi, R. and Morelli, A. (2011). EPmantle: a 3-D transversely isotropic model of the upper mantle under the European Plate. *Geophys. J. Int.*, 185(1), 469–484.

Sénéchal, G. and Thouvenot, F. (1991). Geometrical migration of line-drawings: A simplified method applied to ECORS data. In *Continental Lithosphere: Deep Seismic Reflections*, volume 22 of *Geodynamics Series*, pages 401–407. American Geophysical Union, Washnigton DC.

Shapiro, N. M. and Campillo, M. (2004). Emergence of broadband Rayleigh waves from correlations of the ambient seismic noise. *Geophys. Res. Lett.*, 31(7), article no. L07614.

Shapiro, N. M., Campillo, M., Stehly, L., and Ritzwoller, M. H. (2005). High-resolution surface-wave tomography from ambient seismic noise. *Science*, 307(5715), 1615–1618.

Soergel, D., Pedersen, H. A., Stehly, L., Margerin, L., Paul, A., and AlpArray Working Group (2020). Coda-Q in the 2.5–20 s period band from seismic noise: application to the greater Alpine area. *Geophys. J. Int.*, 220(1), 202–217.

Soergel, S., Pedersen, H. A., Bodin, T., Paul, A., Stehly, L., and AlpArray Working Group (2023). Bayesian analysis of azimuthal anisotropy in the Alpine lithosphere from beamforming of ambient noise cross-correlations. *Geophys. J. Int.*, 232(1), 429–450.

Solarino, S., Kissling, E., Sellami, S., Smriglio, G., Thouvenot, F., Granet, M., Bonjer, K. P., and Sleijko, D. (1997). Compilation of a recent seismicity data base of the greater Alpine region from several seismological networks and preliminary 3D tomographic results. *Annali di Geofisica*, 40(1), 161–174.

Solarino, S., Malusà, M. G., Eva, E., Guillot, S., Paul, A., Schwartz, S., et al. (2018). Mantle wedge exhumation beneath the Dora-Maira (U)HP dome unravelled by local earthquake tomography (Western Alps). *Lithos*, 296, 623–636.

Sonnet, M., Labrousse, L., Bascou, J., Plunder, A., Nouibat, A., and Paul, A. (2023). Assessing chemical and mineralogical properties of the Alpine slab based on field analogues and ambient noise tomography. *Geochem. Geophys. Geosyst.*, 24, article no. e2022GC010784.

Spada, M., Bianchi, I., Kissling, E., Agostinetti, N. P., and Wiemer, S. (2013). Combining controlled-source seismology and receiver function information to derive 3-D Moho topography for Italy. *Geophys. J. Int.*, 194(2), 1050–1068.

Stehly, L., Fry, B., Campillo, M., Shapiro, N. M., Guilbert, J., Boschi, L., and Giardini, D. (2009). Tomography of the Alpine region from observations of seismic ambient noise. *Geophys. J. Int.*, 178(1), 338–350.

Szanyi, G., Gráczer, Z., Balázs, B., Kovács, I. J., and AlpArray Working Group (2021). The transition zone between the Eastern Alps and the Pannonian basin imaged by ambient noise tomography. *Tectonophysics*, 805, article no. 228770.

Trinh, P. T., Brossier, R., Métivier, L., Tavard, L., and Virieux, J. (2019). Efficient time-domain 3D elastic and viscoelastic full-waveform inversion using a spectral-element method on flexible Cartesian-based mesh. *Geophysics*, 84(1), R61–R83.

Tromp, J., Tape, C., and Liu, Q. (2005). Seismic tomography, adjoint methods, time reversal and banana-doughnut kernels. *Geophys. J. Int.*, 160(1), 195–216.

Verbeke, J., Boschi, L., Stehly, L., Kissling, E., and Michelini, A. (2012). High-resolution Rayleigh-wave velocity maps of central Europe from a dense ambient-noise data set. *Geophys. J. Int.*, 188(3), 1173–1187.

Virieux, J., Paul, A., Langlais, M., Janex, G., Guéguen, P., Helmstetter, A., and Stehly, L. (2024). Assessing the reliability of local earthquake tomography for crustal imaging: 30 years of records in the Western Alps as a case study. *Geophys. J. Int.*, 236(1), 99–118.

Waldhauser, F., Kissling, E., Ansorge, J., and Mueller, S. (1998). Three dimensional interface modelling with two-dimensional seismic data: the Alpine crust-mantle boundary. *Geophys. J. Int.*, 135(1), 264–278.

Waldhauser, F., Lippitsch, R., Kissling, E., and Ansorge, J. (2002). High-resolution teleseismic tomography of upper-mantle structure using an a priori three-dimensional crustal model. *Geophys. J. Int.*, 150(2), 403–414.

Weidle, C. and Maupin, V. (2008). An upper-mantle S-wave velocity model for Northern Europe from Love and Rayleigh group velocities. *Geophys. J. Int.*, 175(3), 1154–1168.

Wu, X., Guo, Z., Li, S., Yu, Y., Bai, Q., and Chen, Y. J. (2023). Seismic azimuthal anisotropy of northeastern Tibetan Plateau from ambient noise double beamforming tomography: Implication for crustal deformation. *J. Geophys. Res.: Solid Earth*, 128, article no. e2022JB026109.

Young, M. K., Rawlinson, N., and Bodin, T. (2013). Transdimensional inversion of ambient seismic noise for 3D shear velocity structure of the Tasmanian crust. *Geophysics*, 78(3), WB49–WB62.

Yuan, H. and Bodin, T. (2018). A probabilistic shear wave velocity model of the crust in the central West Australian craton constrained by transdimensional inversion of ambient noise dispersion. *Tectonics*, 37(7), 1994–2012.

Zahorec, P., Papčo, J., Pašteka, R., Bielik, M., Bonvalot, S., Braitenberg, C., et al. (2021). The first pan-Alpine surface-gravity database, a modern compilation that crosses frontiers. *Earth Syst. Sci. Data*, 13(5), 2165–2209.

Zhang, X. and Curtis, A. (2021). Bayesian geophysical inversion using invertible neural net-

works. *J. Geophys. Res.: Solid Earth*, 126(7), article no. e2021JB022320.

Zhao, L., Malusà, M. G., Yuan, H., Paul, A., Guillot, S., Lu, Y., et al. (2020). Evidence for a serpentinized plate interface favouring continental subduction. *Nat. Commun.*, 11(1), article no. 2171.

Zhao, L., Paul, A., Guillot, S., Solarino, S., Malusà, M. G., Zheng, T., Aubert, C., Salimbeni, S., Dumont, T., Schwartz, S., Zhu, R., and Wang, Q. (2015). First seismic evidence for continental subduction beneath the Western Alps. *Geology*, 43(9), 815–818.

Zhao, L., Paul, A., Malusà, M. G., Xu, X., Zheng, T., Solarino, S., et al. (2016a). Continuity of the Alpine slab unraveled by high-resolution P wave tomography. *J. Geophys. Res.: Solid Earth*, 121(12), 8720–8737.

Zhao, L., Paul, A., Solarino, S., and RESIF (2016b). Seismic network YP: CIFALPS temporary experiment (China-Italy-France Alps seismic transect) [Data set]. RESIF—Réseau Sismologique et géodésique Français. https://doi.org/10.15778/RESIF.YP2012.

Zhao, L., Paul, A., Solarino, S., and RESIF (2018). Seismic network XT: CIFALPS-2 temporary experiment (China-Italy-France Alps seismic transect #2) [Data set]. RESIF—Réseau Sismologique et géodésique Français. https://doi.org/10.15778/RESIF.XT2018.

Zhu, H., Bozdağ, E., and Tromp, J. (2015). Seismic structure of the European upper mantle based on adjoint tomography. *Geophys. J. Int.*, 201(1), 18–52.

ACADÉMIE DES SCIENCES
INSTITUT DE FRANCE

Comptes Rendus. Géoscience — Sciences de la Planète
2024, Vol. 356, Special issue S4, p. 41-57
https://doi.org/10.5802/crgeos.254

Research article

New Developments in Passive Seismic Imaging and Monitoring

Investigating the lateral resolution of the Rayleigh wave focal spot imaging technique using two-dimensional acoustic simulations

Bruno Giammarinaro [*, a], **Christina Tsarsitalidou** [a] **and Gregor Hillers** [a]

[a] Institute of Seismology, University of Helsinki, Helsinki, Finland

Current address: LabTAU, INSERM, Centre Léon Bérard, Université Lyon 1, Lyon, France (B. Giammarinaro)

E-mails: bruno.giammarinaro@inserm.fr (B. Giammarinaro), christina.tsarsitalidou@helsinki.fi (C. Tsarsitalidou), gregor.hillers@helsinki.fi (G. Hillers)

Abstract. We investigate the lateral resolution power of the seismic Rayleigh wave focal spot imaging technique. We use two-dimensional acoustics simulations in a closed cavity for the passive Green's function and focal spot reconstruction. Four different velocity distributions target different resolution aspects. The finite data range that is necessary to constrain the Bessel function model controls the lateral spreading of material contrasts, the distinction of two objects on sub-wavelength scales, and the image quality of complex random media. Good data quality from dense networks supports short range estimates and super-resolution.

Keywords. Numerical modeling, Wave propagation, Seismic noise, Cavity, Focal spot, Resolution, Seismic imaging.

Funding. Academy of Finland (decision number 322421).

Manuscript received 8 December 2022, revised 5 December 2023 and 9 February 2024, accepted 29 January 2024.

1. Introduction

Disadvantages of earthquake tomography associated with limited illumination can now be compensated by ambient noise tomography with its flexible virtual source and receiver configurations. Both approaches invert far-field observations of travel time differences, obtained from earthquake seismograms [Tromp et al., 2005, Liu and Gu, 2012] or from passive Green's function reconstructions [Shapiro and Campillo, 2004, Sabra et al., 2005], for a model of the velocity structure.

Modern dense seismic arrays support alternative local surface wave speed estimations from noise correlation functions [Lin et al., 2009, Lin and Ritzwoller, 2011], which includes the large scale application of the frequency domain spatial autocorrelation (SPAC) method [Aki, 1957, Ekström et al., 2009, Ekström, 2014] that is otherwise typically applied to local sparse array data [Asten, 2006]. Dense arrays can now contain on the order of 1000 sensors, which facilitates the proper sampling of the noise correlation amplitude distribution at near-field distances. At zero lag time, the time domain representation of the spatial autocorrelation field is referred to as focal spot, which contains the same information as SPAC

* Corresponding author

and can be analyzed using the same mathematical tools [Cox, 1973, Yokoi and Margaryan, 2008, Tsai and Moschetti, 2010, Haney et al., 2012, Haney and Nakahara, 2014].

Focal spot analysis is used in applications that work with a high sensor density. Focal spots have first been studied in time-reversal experiments in underwater acoustics and medical imaging [Fink, 1997]. Noise correlation medical imaging transferred the noise seismology approaches to passive elastography, first using far-field surface waves along muscle fibers [Sabra et al., 2007], later using refocusing shear waves. Different properties of the shear wave focal spot have been analyzed including its cross-section width [Catheline et al., 2008, Gallot et al., 2011], two-dimensional shape [Benech et al., 2013, Brum et al., 2015], and its tip curvature [Catheline et al., 2013], which can all be reconstructed using MRI [Zorgani et al., 2015] and ultrasound [Barrere et al., 2020] speckle tracking methods. Importantly, Zemzemi et al. [2020] demonstrated that the ability to discriminate two objects is not controlled and hence limited by the shear wavelength, but instead by the ultrasonic frequency and the pixel density. In seismology, this corresponds to the array station density.

Hillers et al. [2016] first applied Rayleigh wave focal spot imaging in seismology to image lateral velocity variations in a fault zone environment. As for SPAC, the phase velocity is estimated from the focal spot shape using Bessel function models. Using numerical time-reversal experiments based on a Green's function calculator for one-dimensional layered media [Cotton and Coutant, 1997], Giammarinaro et al. [2023] demonstrated the feasibility to accurately estimate phase velocity and dispersion from noisy focal spots. Results for non-isotropic surface wave illumination showed that the wave speed bias is negligible if the sensors are isotropically distributed, compatible with the SPAC results by Nakahara [2006]. Moreover, the effect of interfering P waves can be mitigated using a data or fitting range around one wavelength. Whereas these results from Giammarinaro et al. [2023] suggest the overall robustness and utility of the focal spot method for seismic imaging applications, most notably because of the increase in depth resolution, the study could not address lateral resolution. Considering that super-resolution can be obtained with tip-curvature measurements [Zemzemi et al., 2020], it is important to assess the effect of the data range on speed estimates from densely sampled seismic focal spots.

Here we study systematically the lateral focal spot resolution using numerical experiments. We perform two-dimensional acoustics simulations to reconstruct the Green's function from reverberating wave fields (Section 2). The ambient field generated in a chaotic closed cavity [Draeger and Fink, 1999] yields results that are equivalent to results from open media noise correlation [Derode et al., 2003]. The obtained Green's function is identical and is here therefore taken as a proxy for seismic vertical–vertical component Rayleigh wave correlations [Sanchez-Sesma, 2006, Haney et al., 2012]. We work with a constant number of grid points and a fixed reference frequency. We implement four test cases and vary the data range or fitting distance r_{fit} to investigate the effect on the resolution of the velocity structure. These cases include a homogeneous control experiment (Section 3.1), an interface between two half-spaces (Section 3.2), circular inclusions (Section 3.3), and heterogeneous or random velocity distributions (Section 3.4). In Section 4 we discuss the different resolution aspects that are investigated with the variable configurations for a comprehensive evaluation of the seismic Rayleigh wave focal spot imaging performance.

2. Method

2.1. *Synthetic experiments*

This study is based on synthetic diffuse wave fields generated in a closed cavity. The resulting correlation functions are equivalent to noise correlations in open media [Derode et al., 2003]. Simulations are performed using the function *kspaceFirstOrder2D* from the MATLAB toolbox *kWave* [Treeby et al., 2018]. This function solves a system of first-order acoustic equations for the conservation of mass and momentum using a wavenumber k-space pseudospectral method. The two-dimensional medium is composed of 500×500 grid points that are spaced in the x and y direction by $\mathrm{d}x = \mathrm{d}y = 0.1$ km (Figure 1a). The background wave speed in the cavity is $V_0 = 2$ km/s. The closed cavity is implemented using different densities outside ($\rho_{\text{out}} = 59$ kg/m^3) and inside ($\rho_{\text{in}} = 2950$ kg/m^3) the cavity. Choosing ρ_{out} to be 2% of ρ_{in} creates strongly reflecting boundaries from

impedance contrast. It supports a homogeneous stability regime of the *kWave* simulations through a constant Courant–Friedrichs–Lewy number. This number depends on the wave speed, hence varying only the density mitigates potentially problematic stability conditions associated with a large change in wave speed. We cannot exclude the occurrence of weak numerical dispersion in some of the heterogeneous case studies, but the overall consistency of the synthesized Green's functions and focal spots in the different experiments suggests that this effect does not govern our results. Inside the cavity we select a square target domain consisting of 151×151 grid points where we record the solution. In this region we define the different velocity distributions introduced in Section 2.2. Results for each of the four cases discussed in Section 3 are obtained by averaging 11 independent wave field simulations. Each simulation starts with a point source at a different position inside the cavity (Figure 1a). The source term is defined as a time-varying mass source (Figures 1b, c) emitting a 1 s long pulse. The pressure is a differentiation of this signal with the frequency range centered at 1 Hz. The wave field is recorded for 300 s inside the square sub-domain with a 100 Hz sampling frequency.

2.2. *The acoustic medium in the target domain*

The acoustic wave speed distribution $V(\mathbf{x})$ is defined as a spatial function in the square target domain

$$V(\mathbf{x}) = V_0(1 + \xi(\mathbf{x})), \tag{1}$$

where $V_0 = 2$ km/s is the background wave speed in the cavity, $\mathbf{x}$ is the position, and ξ is the relative change in wave speed, i.e., the parameter that controls the medium heterogeneity. In the following sections, the 2 km background wavelength at 1 Hz is denoted λ_0. In Section 3 we begin with a control experiment of a homogeneous medium with $\xi = 0$ to study the overall system response.

2.3. *Lateral spreading across two welded half-spaces*

We modify the homogeneous control experiment and replace the 2 km/s velocity in the left half of the target domain by an increased 2.2 km/s value. This creates two half-spaces and allows us to investigate the lateral resolution as the imaging method induces spreading or averaging across the sharp interface. Such sharp lateral velocity contrasts can occur across bimaterial interfaces in fault zone environments [Weertman, 1980, Ben-Zion, 1989], or in the contact region of intrusions with the host rock [Chamarczuk et al., 2019].

2.4. *Resolution of circular inclusions*

Next we perform a classic resolution test and study the power of the method to separate two individual entities in an image. For this we impose three pairs of circular inclusions separated by $0.25\lambda_0$, $0.5\lambda_0$ and $1\lambda_0$. The inclusions have a diameter of $1\lambda_0$. We test two different sets, where one set of inclusions is stiffer than the background with $\xi = 25\%$, and the other set has more compliant inclusions compared to the background with $\xi = -25\%$. Such a "two-body problem" is typically studied in gel phantom experiments performed in medical ultrasound imaging or medical imaging for tumor detection [Catheline et al., 2013, Zemzemi et al., 2020]. It is a less common configuration in seismology where so-called checkerboard tests are typically employed to quantify the resolution of a tomography configuration. Circular cross-section features can occur in the context of magmatic intrusions or conduits. However, as said, with this configuration we can study the lateral resolution defined as the minimum distance between objects that the method allows to discriminate in an image. This and the other cases are studied using different data ranges r_{fit} discussed in Section 2.6.

2.5. *Randomly distributed wave speeds*

Last we consider random media using a functional form that is often used to parameterize the heterogeneous distributions of variables such as wave speed, stress, or frictional properties in Earth materials [Frankel and Clayton, 1986, Holliger and Levander, 1992, Mai and Beroza, 2002, Ripperger et al., 2007, Hillers et al., 2007, Sato et al., 2012, Obermann et al., 2016]. We define $\xi(\mathbf{x})$ through a spatial 2D inverse Fourier transform as

$$\xi(\mathbf{x}) = \mathrm{FT}^{-1}\left[\sqrt{P(\mathbf{k})}\mathrm{e}^{\mathrm{i}\phi(\mathbf{k})}\right], \tag{2}$$

where $\mathbf{k}$ is the spatial wavenumber of the 2D distribution, $P(\mathbf{k})$ is the power spectral density, and $\phi(\mathbf{k})$ is a random distribution of the phase between 0 and 2π. The random distribution is calculated using

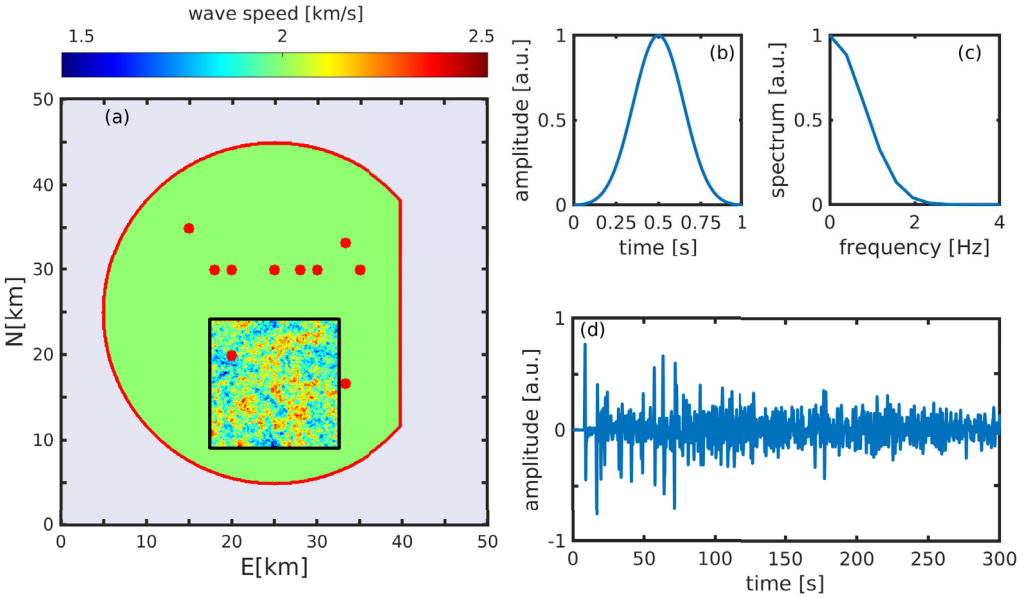

Figure 1. Configuration of the numerical experiments. (a) Representation of the closed cavity with a background velocity $V_0 = 2$ km/s. The gray area represents the outer part of the medium with the same velocity but with an impedance contrast to trap the waves in the cavity. The red line is the boundary of the closed cavity. The black square indicates the target area where the results are recorded. Inside the cavity the color corresponds to the input wave speed. Red dots indicate the source positions for the 11 realizations. (b) Times series and (c) normalized power spectrum of the emitted pulse used for each simulation. (d) Example of a full time-series recorded in the cavity.

the Python *randn* function coupled with a seed fixed to 3. Fixing the seed allows to randomly generate the phase and to keep the same distribution to observe the effect of the control parameters. The power spectral density $P(\mathbf{k})$ follows the von Karman probability function [Sato et al., 2012]

$$P(\mathbf{k}) = \frac{4\pi\Gamma[\kappa+1]\varepsilon^2 a^2}{\Gamma[\kappa](1+a^2\|\mathbf{k}\|^2)^{\kappa+1}}. \quad (3)$$

The correlation length of the modeled parameter is a, ε governs the contrast in the medium, κ defines the sharpness of the spectral decay, and Γ is the Gamma function. We use Equation (3) to generate nine different media with variable a and κ (Table 1), and constant $\varepsilon = 150$ km^{-1}.

2.6. *Data processing and wave speed estimation*

Data processing is performed in a Python3.8 environment. For each simulation, we analyze the diffusive parts of the wave field (Figure 2a) by focusing on simulated time series data between 100 s and 300 s (Figure 1d). Considering the distances between the sources and chaotic cavity borders, this corresponds to a range between 10 and 30 mean-free times. We follow Giammarinaro et al. [2023] and filter the traces with a Gaussian filter centered at 1 Hz and with a width of 3.2% to estimate the central frequency dependent phase velocity. In the limit, the analysis could be performed for a harmonic case, however, the narrow filter stabilizes the results. As demonstrated by Giammarinaro et al. [2023], a wider frequency-band filter leads to group velocity estimates, and it biases the focal spot reconstruction by averaging over frequencies which leads to an apparent attenuation. We compute the normalized cross-correlation between each sensor pair to extract the spatial autocorrelation amplitude fields at zero lag time. Results are stacked over the 11 realizations for each case. This yields at short distances around a reference station the large-amplitude feature referred to as focal spot (Figure 2c). The shape is linked to the wave speed through the imaginary part of the Green's function. From each focal spot we estimate the free parameter wave speed $V = \omega/k$ by fitting

Table 1. Parameters for the generation of different heterogeneous media using Equation (3)

Medium	1	2	3	4	5	6	7	8	9
a (km)	1	1	1	2	2	2	3	3	3
κ	0.1	0.3	0.6	0.1	0.3	0.6	0.1	0.3	0.6

Where a is the correlation length and κ governs the sharpness of the spectral decay. The corresponding wave speed distributions are displayed in the top row of Figure 8.

the azimuthal averaged and normalized data to the $J_0(kr)$ model using a nonlinear least squares regression algorithm [Hillers et al., 2016, Giammarinaro and Hillers, 2022, Giammarinaro et al., 2023]. Again, the 2D acoustic configuration yields results that are equivalent to the lateral propagation of Rayleigh surface waves. The $J_0(kr)$ model equally describes the vertical–vertical component of the Rayleigh wave focal spot [Haney et al., 2012, Haney and Nakahara, 2014], and V is thus equivalent to the Rayleigh wave phase velocity c_R.

This process is performed for the 22,801 focal spots, and each obtained V estimate is associated with the location of the reference station. This imaging concept thus compiles velocity distributions across dense arrays without solving a tomography inverse problem. Importantly, we choose two different data ranges r_{fit} of 1 km and 2 km associated with $0.5\lambda_0$ and $1\lambda_0$ at 1 Hz (Figure 2d). Away from edges, this corresponds to 80 and 314 samples, respectively. We vary r_{fit} because it is a critical tuning parameter, and values around one wavelength yield overall stable results [Giammarinaro et al., 2023]. Larger values can stabilize a regression for noisy signals, but the short distance focal spot imaging concept essentially invites the limitation of r_{fit} for improved resolution. This refers to improved depth resolution as c_R values can be estimated at wavelengths that cannot be studied with tomography [Tsarsitalidou et al., 2021, Giammarinaro et al., 2023], but also to the lateral resolution investigated here.

2.7. *Error estimation*

An important advantage of the focal spot approach is the local assessment of the measurement uncertainty ϵ that is estimated following Aster et al. [2019]

$$\epsilon_k = \sqrt{\frac{RSS}{N-2} C_k}, \tag{4}$$

where RSS is the residual sum of squares, N is the number of samples, and C_k is the diagonal element of the parameter covariance matrix C associated with the wavenumber k. Rules of error propagation apply to yield the wave speed error ϵ_V

$$\epsilon_V = V\epsilon_k / k. \tag{5}$$

In addition to this estimate we can compare imaged with ground truth input values to discuss resolution.

3. Results

3.1. *The homogeneous reference case*

The first test is the homogeneous control experiment which illustrates basic features of the approach. The simulations yield diffuse wave fields that can be used for focal spot imaging. Figure 2(a) shows a snapshot of a diffuse wave field, Figure 2(b) a time-space representation of the time-reversed correlation wave field, Figure 2(c) shows a focal spot of one realization, and Figure 2(d) shows the results of the nonlinear regression following the data processing described in Section 2.6. In Figure 2(b) we can see the refocusing and diverging waves of the Green's function after cross-correlation. However, the reconstruction is not perfect which is indicated by the small-amplitude fluctuations. The time domain autocorrelation field shows the focal spot at small distances around the origin (Figure 2c). The irregularity of the white zero-crossing contours again illustrates fluctuations and imperfect reconstruction after stacking over 11 realizations. We attribute this to non-perfectly diffuse wave fields associated with the modes in the cavity. However, studies of non-diffuse wave fields [Nakahara, 2006, Giammarinaro et al., 2023] demonstrate that isotropically distributed sensors yield unbiased wave speed estimates. This condition is not met along the boundaries of the domain which yields

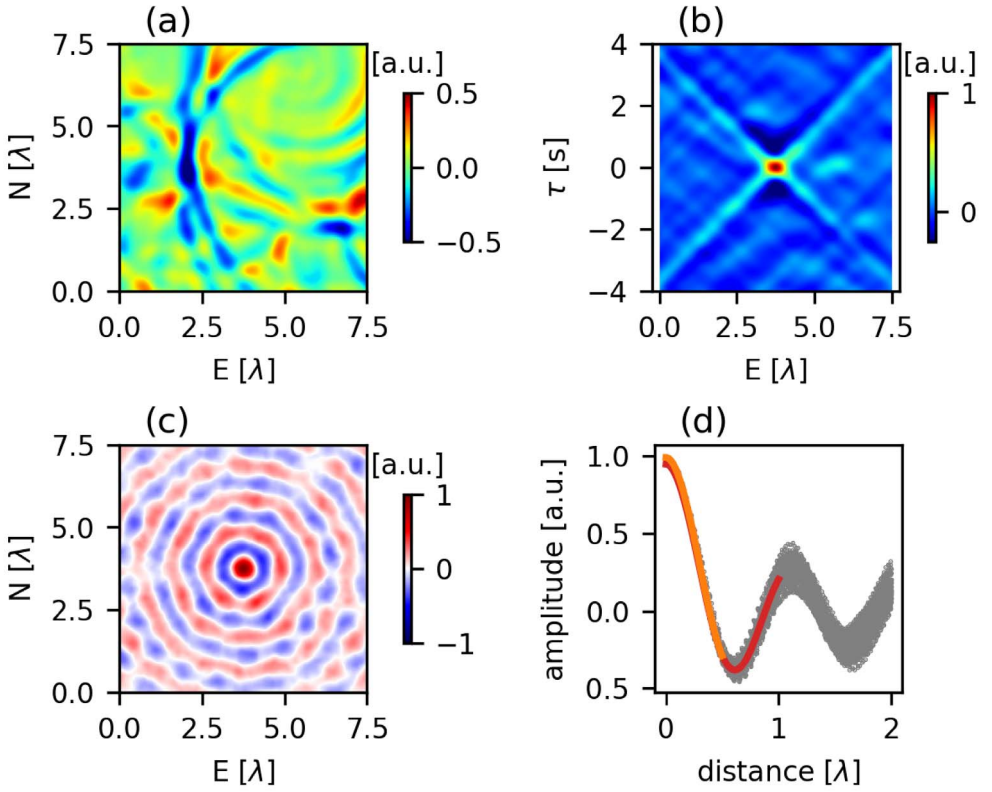

Figure 2. Workflow stage examples for the homogeneous medium in the target area. (a) Snapshot of a diffuse wave field. (b) Time-reversed space-time wave field obtained by cross-correlation. (c) Spatial autocorrelation with the focal spot at the center obtained at 1 Hz after stacking over 11 realizations. (d) Simulated 1 Hz focal spot data (gray) and nonlinear regression results for $r_{\text{fit}} = 0.5\lambda_0$ (orange) and $r_{\text{fit}} = 1\lambda_0$ (red). In this and all subsequent figures the unit λ is equal to the 1 Hz wavelength λ_0 for the reference $V_0 = 2$ km/s.

larger fluctuations in the estimates. Figure 2(d) displays results from the nonlinear regression using the two data distances $r_{\text{fit}} = 0.5\lambda_0$ and $r_{\text{fit}} = 1\lambda_0$. The spread in the data with increasing distance corresponds to the fluctuations from Figure 2(c).

The 2D velocity distributions obtained with $r_{\text{fit}} = 0.5\lambda_0$ and $r_{\text{fit}} = 1\lambda_0$ are displayed in Figures 3(a) and (b), respectively. The key feature in these images are the speckle patterns. They illustrate that the imperfect reconstruction affects the measurement process to produce these fluctuations around the average reference value. Using $r_{\text{fit}} = 0.5\lambda_0$ and $r_{\text{fit}} = 1\lambda_0$ leads to $V = 2.014 \pm 0.034$ km/s and $V = 2.008 \pm 0.021$ km/s, respectively, so the $V_0 = 2$ km/s reference value is well recovered with an uncertainty level of 1.5% and 1%. Figures 3(c) and (d) display the spatial error distribution obtained from Equation (5), where the values indicate a similar error range. Both illustrations demonstrate that an increasing data range improves accuracy and precision. Another strong feature are the boundary effects in Figures 3(a) and (b). Recall that we only use observations inside the square target area, similar to an array deployment. The estimation error increases towards the boundaries and the affected area appears to depend on the r_{fit} length. However, the biasing effects are not homogeneously distributed along the boundaries but are largest along the southern edge. This is likely explained by the centered, low position of the target area in the cavity, together with the excitation of specific modes in the cavity that sustain a non-isotropic energy flux in the scattered wave field. This also explains the corresponding pattern of larger uncertainties in the lower half of Figure 3(c).

The boundary effects emerge in all our discussed cases but do not affect our conclusions. These effects can be mitigated by a different configuration or geometry, or by averaging over more sources located at more diverse locations.

3.2. *Resolution of the interface between half-spaces*

Figure 4 displays the input wave speed distribution (Figure 4a) and the focal spot-based images of two homogeneous half-space media for the data ranges $r_{\text{fit}} = 0.5\lambda_0$ (Figure 4c) and $r_{\text{fit}} = 1\lambda_0$ (Figure 4d). As for the control experiment, the distributions show small residual fluctuations around the well resolved input values (the distributions in the left half in panels (c) and (d) yield $V = 2.200 \pm 0.099$ km/s and $V = 2.196 \pm 0.095$ km/s, respectively), and again larger edge effects along the lower boundary.

More interesting are the profiles across the domain shown in Figure 4(b). These profiles are averages along the N-axis. The imaged distributions across the interface do not follow the blue input step function but are spread out. To quantify the resolution we estimate the width ΔL of the transition. This is the distance between the samples where the amplitude of the estimated profile equals the 5% and 95% values of the 0.2 km/s velocity jump, i.e., when the values are 2.01 km/s and 2.19 km/s. Figure 5(a) enlarges the area around the interface located at $3.75\lambda_0$. It shows four profiles obtained with r_{fit} values ranging from $0.5\lambda_0$ to $2\lambda_0$ in $0.5\lambda_0$ intervals. It confirms the previous observation that the overall velocity in each half-space is correctly estimated for every data range. As for the results in Figures 3 and 4 we can perhaps discern a weak trend to overestimate the reference values. We attribute this to the imperfect simulation configuration since similar effects are not observed in numerical time-reversal experiments, even in the presence of noise [Giammarinaro et al., 2023]. The width ΔL is shown in Figure 5(a) as dotted lines at the bottom, with the vertical dashed lines being the 5% and 95% boundaries of the transition zone. The calculated widths are compiled in Figure 5(b). For $r_{\text{fit}} = 0.5\lambda_0$, the transition zone has a width of $\Delta L = 0.4\lambda_0$. For $r_{\text{fit}} = 1\lambda_0$ we obtain $\Delta L = 1.2\lambda_0$, and for $r_{\text{fit}} = 2\lambda_0$, it is $\Delta L = 2.2\lambda_0$. The spreading effect quantified as the transition width between the two media can hence well be approximated to scale with the data range, $\Delta L \approx r_{\text{fit}}$. Figure 5(c) shows the average r_{fit} dependent ϵ_V profiles. The lack of features at the position of the interface indicates that the 10% velocity contrast does not influence the reconstruction. The profiles indicate the tendency of an overall better reconstruction in the right slower domain. This is likely controlled by the proportionally smaller data range in the left faster domain, which is a consequence of the constant r_{fit} value tied to the reference wavelength in the right domain. As expected, this trend weakens with increasing r_{fit}. Figures 5(a) and (c) together show that an increasing r_{fit} leads to a generally increased precision as ϵ_V decreases, but to a loss in accuracy around the position of the interface.

3.3. *Resolution and contrast of circular inclusions*

We now examine the resolution of pairs of $1\lambda_0$-wide circular inclusions separated by variable distances. The velocity in the inclusions increases and decreases by 0.5 km/s with respect to the background reference $V_0 = 2$ km/s. Nonlinear regression of the focal spot data are performed using data ranges $r_{\text{fit}} = 0.5\lambda_0$ and $r_{\text{fit}} = 1\lambda_0$. Figure 6 collects in the left two columns the input wave speed distributions, and the focal spot obtained images for $r_{\text{fit}} = 0.5\lambda_0$ and $r_{\text{fit}} = 1\lambda_0$. As a general observation, every inclusion is visible on the images for both data ranges, and for the three different distances separating the inclusions. This highlights the effectiveness of the Rayleigh wave focal spot method for "discovery mode" applications [Tsai, 2023]. However, the contrast—the difference in "velocity amplitude"—depends on the data range. Using $r_{\text{fit}} = 1\lambda_0$ increases the area of the biased velocity estimates. The quantitative aspect of the method decreases with an increase of the data range, which appears as an averaging effect, consistent with the observations across the interface in the half-space case. Panels in the right two columns in Figure 6 show the data from Figures 6(a) to (f) normalized by the input wave speed maps (Figures 6a, b). The overall neutral or white backgrounds illustrate the well resolved reference value. The fact that circular features are visible in Figures 6(i) to (l) demonstrates that the velocity estimates around the edges are biased. The width of the halo or ΔL scales again with the data distance,

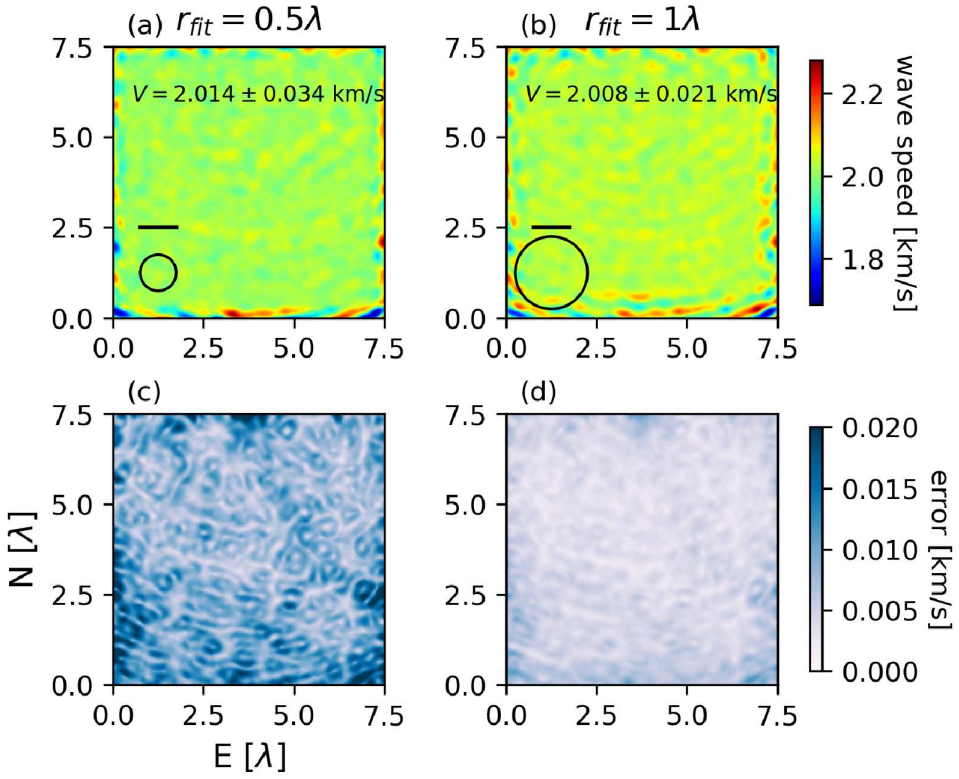

Figure 3. The control experiment. Focal spot obtained images for (a) $r_{\text{fit}} = 0.5\lambda_0$ and (b) $r_{\text{fit}} = 1\lambda_0$ for a homogeneous medium with wave speed $V = 2$ km/s. The reference wavelength λ_0 is indicated by the black line and the r_{fit} range used for the nonlinear regression is the radius of the black circle. The indicated wave speeds V are the domain average values and the standard deviation quantify the fluctuations across the domain. Panels (c) and (d) illustrate the spatial distribution of wave speed errors obtained with Equation (5) for $r_{\text{fit}} = 0.5\lambda_0$ and $r_{\text{fit}} = 1\lambda_0$, respectively.

the reconstruction benefits from smaller r_{fit} values (Figures 6i, j).

These interpretations are supported by wave speed profiles across the inclusions (Figure 7), which demonstrate again that the focal spot image quality, i.e., resolution and contrast, depends on the data range. Inclusions separated by $0.25\lambda_0$ (Figures 7a, b) are well imaged for small $r_{\text{fit}} = 0.5\lambda_0$. The wave speed value away from an interface is well approximated. This applies to the stiff and the compliant inclusions. For $r_{\text{fit}} = 1\lambda_0$ the contrast cannot be recovered, which is linked to the data range dependent transition zone width that is here similar to the inclusion diameter. The same mechanism applies to the results obtained with $r_{\text{fit}} = 1.5\lambda_0$. Importantly, two inclusions can always be discriminated when the separation distance is $0.25\lambda_0$, which is yet more obvious from Figure 6. For a separation distance of $0.5\lambda_0$ this quality of the imaging approach increases, and inclusions are completely discriminated for a distance of $1\lambda_0$. Taken together, the data range dependent sensitivity of the resolution mostly affects the contrast estimate, but less so the ability to discriminate two objects. The power to discriminate inclusions separated by only $0.25\lambda_0$ suggests that the property of super-resolution applies, similar to focal spot medical imaging results obtained with ultrasound wavelengths [Zemzemi et al., 2020]. Focal spot imaging resolution thus benefits from high station density across short data ranges. The wave speed estimates are, however, sensitive to noisy data at short distances. In turn, longer data distances reduce fluctuations, which leads to a trade-off between accuracy or contrast and resolution or discrimination [Giammarinaro et al., 2023].

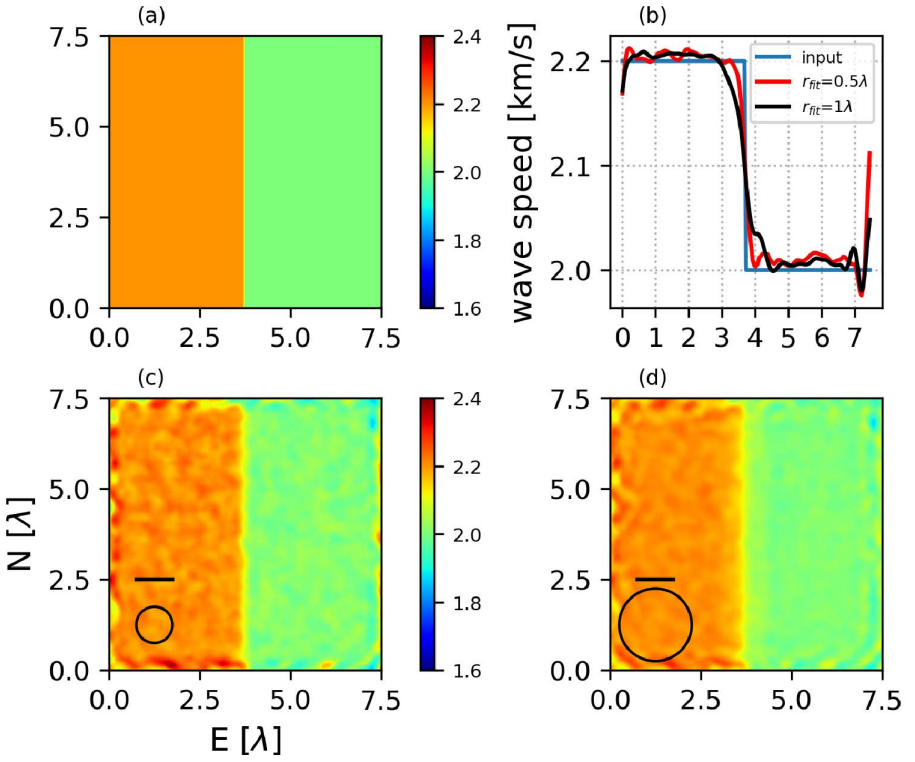

Figure 4. Results for the two half-spaces. (a) The input model. (b) Reference (blue) and focal spot based velocity profiles obtained with two data ranges (red, black) that are averaged along the N-axis. Panels (c) and (d) show focal spot based images of the velocity. The reference wavelength λ_0 is indicated by the black line and the r_{fit} range used for the nonlinear regression is the diameter of the black circle.

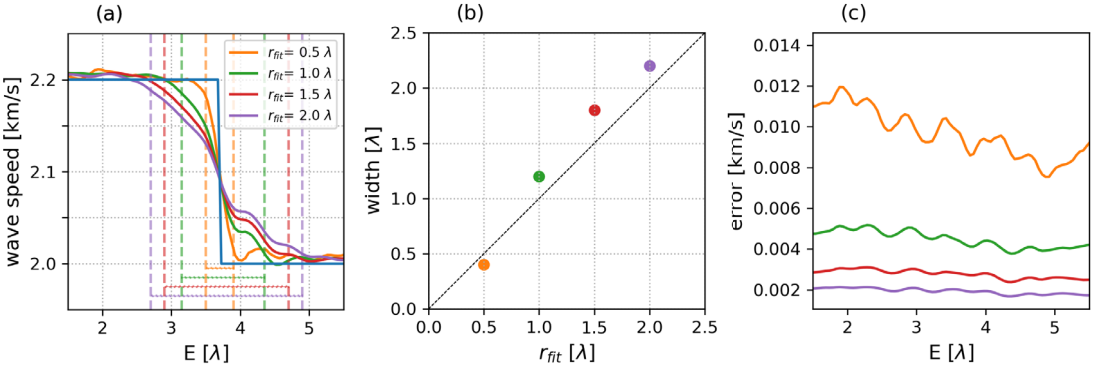

Figure 5. The dependence of the transition width ΔL on the data range r_{fit}. (a) Averaged input and imaged wave speed profiles using four different data ranges. Averaging is performed along the N-axis. The vertical dashed lines indicate the location where the amplitudes of the empirical profiles equal the 5% and 95% values of the 0.2 km/s velocity jump. The dotted lines indicate the estimates of the transition width ΔL. (b) The transition width ΔL as a function of the data distance. (c) The averaged error estimate ϵ_V. Colors in all panels correspond to the same r_{fit} values.

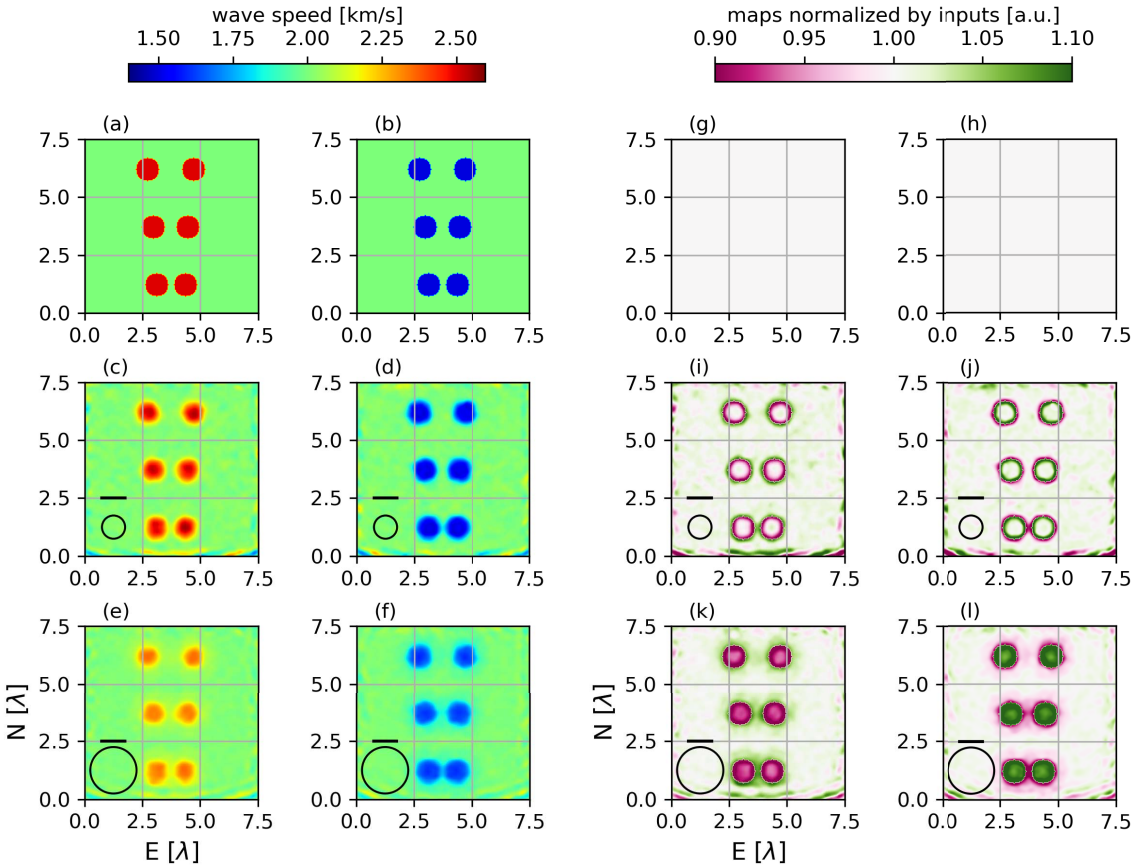

Figure 6. Results of the circular inclusion resolution test. The left two columns panels (a–f) show absolute values, the right two columns panels (g–l) show scaled values. (a,b) Input models of the three circular inclusion pairs separated by $1\lambda_0$, $0.5\lambda_0$, and $0.25\lambda_0$. The inclusion diameter is $1\lambda_0$. Focal spot images obtained with (c,d) $r_{\text{fit}} = 0.5\lambda_0$ and (e,f) $r_{\text{fit}} = 1\lambda_0$. (g,h) Normalized input wave speed map. (i,j) Images in panels (c,d) scaled by the corresponding input distributions in panels (a,b). (k,l) Images in panels (e,f) scaled by the corresponding input distributions in panels (a,b). In the lower two rows, the reference wavelength λ_0 is indicated by the black line and the r_{fit} range used for the nonlinear regression is the diameter of the black circle.

3.4. *Imaging random media*

The last experiment explores focal spot imaging results of heterogeneous media that are characterized by a von Karman spectral density probability function (Equations (2), (3)). Figure 8 shows input wave speed distributions and the images obtained with data ranges $r_{\text{fit}} = 0.5\lambda_0$ and $r_{\text{fit}} = 1\lambda_0$ together with the input-normalized images and the formal uncertainties obtained with Equation (5). For each case, we calculate a coefficient of correlation R between the input distribution and the image. As in the previous experimental configurations, the overall pattern of the velocity variations is well retrieved. Peak R correlation values are obtained at zero-lag, which implies no systematic phase change and hence the effectiveness of focal spot "inference-mode" imaging [Tsai, 2023]. The smallest coefficient of correlation is $R = 0.66$ for the small scale, high contrast wave speed variation Medium 1 ($a = 0.5\lambda_0$, $\kappa = 0.1$) and the longer data range $r_{\text{fit}} = 1\lambda_0$. The best estimation is obtained for Medium 9 ($a = 2\lambda_0$, $\kappa = 0.6$) imaged with $r_{\text{fit}} = 0.5\lambda_0$, which corresponds to analysis using shorter ranges than the correlation length a. This leads to a high coefficient of correlation $R = 0.97$. Increasing r_{fit} to $1\lambda_0$ yields $R = 0.95$. This again

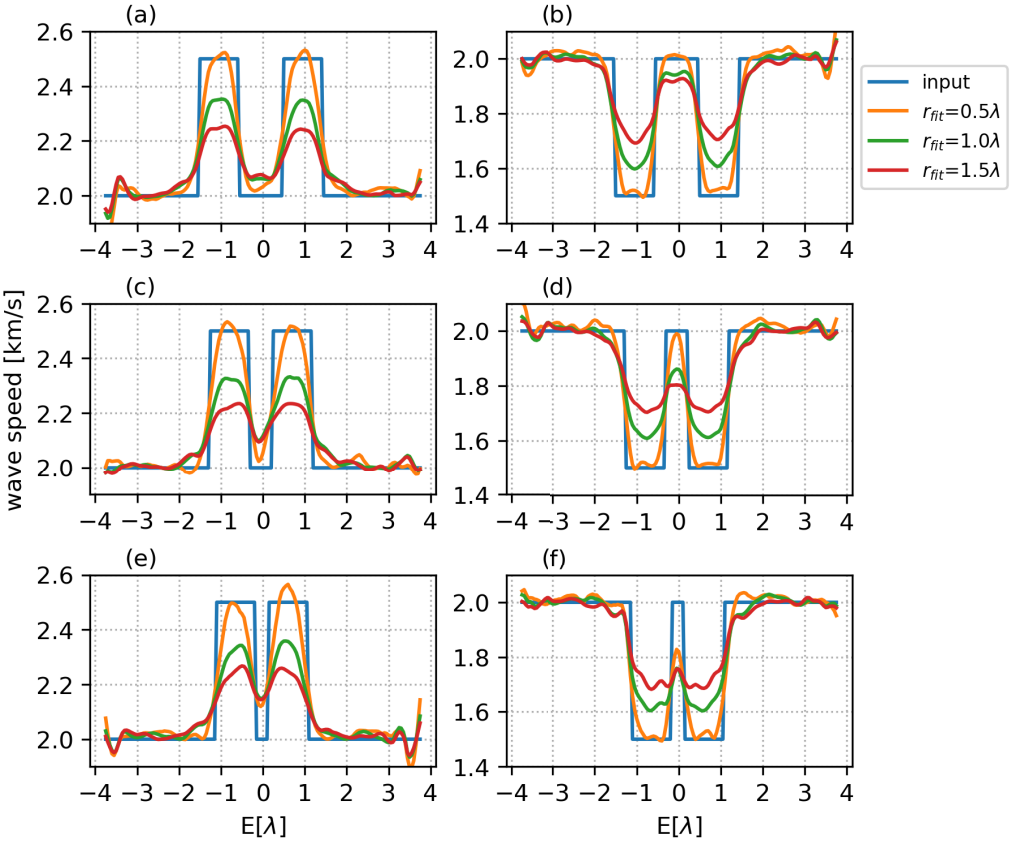

Figure 7. Cross-sections through the circular inclusions. Profiles of input (blue) and estimated wave speeds for $r_{\text{fit}} = 0.5\lambda_0$ (orange), $r_{\text{fit}} = 1\lambda_0$ (green), and $r_{\text{fit}} = 1.5\lambda_0$ (red) for each pair of the circular inclusions. Results are obtained along the E-axis passing through the center of the inclusions. (a,b) Inclusions separated by $1\lambda_0$. (c,d) Inclusions separated by $0.5\lambda_0$. (e,f) Inclusions separated by $0.25\lambda_0$.

confirms our previous results, the images become smoother with increasing r_{fit}, which is synonymous with a loss in contrast and hence details. As an example, in row 6, the green 45-degree trending feature around position $x = 3\lambda$, $y = 2.5\lambda$ illustrates a narrow low-velocity zone that is overestimated by the averaging, longer $r_{\text{fit}} = 1\lambda_0$. The other way around, the smoother the input distribution for larger a and κ (Medium 3, 6, 9), the better is the estimate. The corresponding normalized results in rows 3 and 6 illustrate the imaging quality in a complementary style. Predominantly neutral distributions indicate overall good reconstructions, the red-green pattern amplitude range indicates the loss in accuracy, and the color-speckle size is related to r_{fit}. As an example, in row 6, the green 45-degree trending feature around position $x = 3\lambda$, $y = 2.5\lambda$ illustrates a narrow low-velocity zone that is overestimated by the averaging, longer $r_{\text{fit}} = 1\lambda_0$. The spatial variations of the formal uncertainty estimates in row 4 indicate a medium and wave field dependence. As for the control experiment (Figure 3c) the generally larger error in the lower region is governed by the configuration (Figure 1). The resolution of the comparatively large error spot at $x \approx 6\lambda$, $y \approx 3\lambda$ in the short correlation length media 1 to 6 highlight the advantage of the local error estimation. Again as for the control experiment, the larger data range in row 7 reduces the uncertainty associated with fluctuations significantly.

We estimate the relative wave speed change ξ from the wave speed images by inverting Equation (1)

$$\xi(\mathbf{x}) = V/V_0 - 1, \tag{6}$$

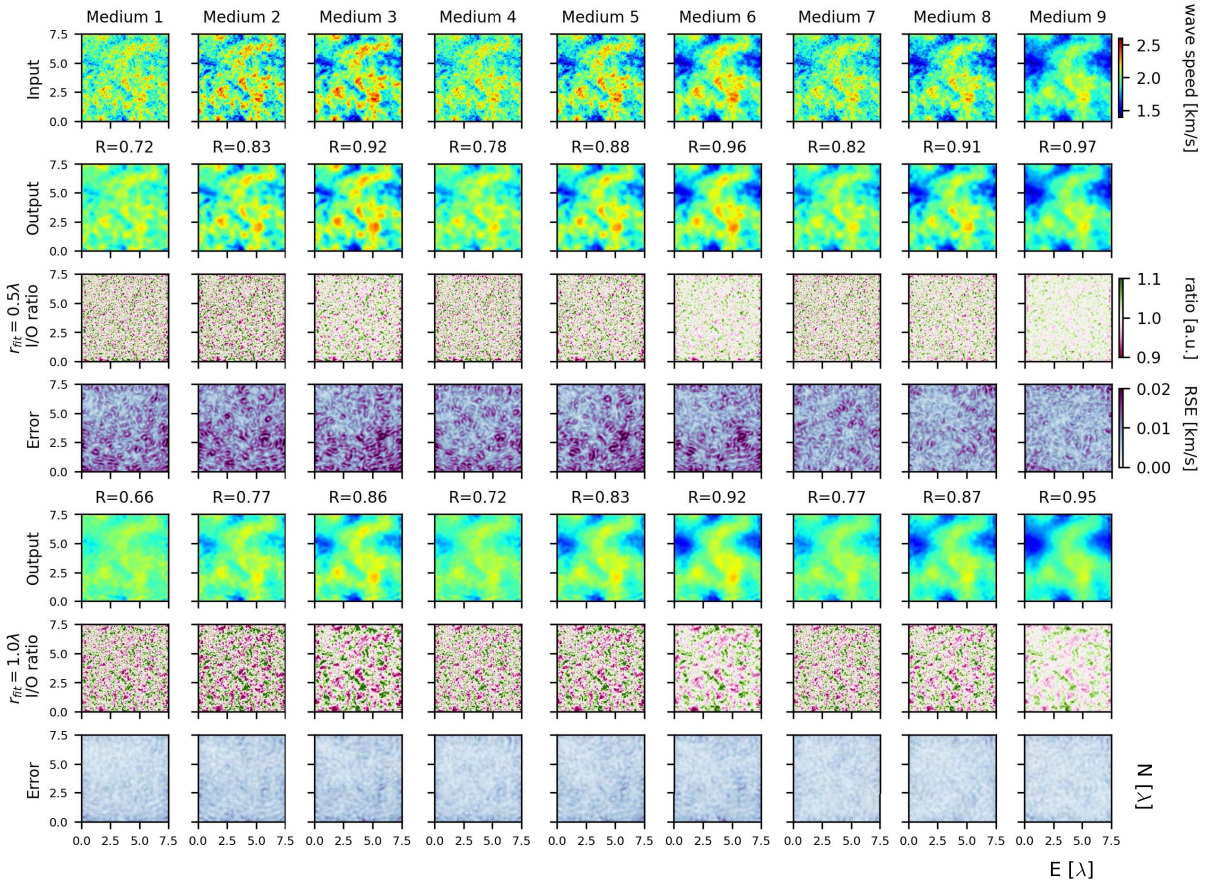

Figure 8. Results from the random media case. The top row shows the heterogeneous velocity distributions that are synthesized using Equations (2) and (3). Values of the corresponding tuning parameters are given in Table 1. Rows 2–4 and rows 5–7 show focal spot based results obtained with $r_{\text{fit}} = 0.5\lambda_0$ and $r_{\text{fit}} = 1\lambda_0$, respectively. For each case, the top rows 2 and 5 show the estimated wave speed distributions, the center rows 3 and 6 show the ratio between the estimated and the input wave speed, and the bottom rows 4 and 7 show the local wave speed error estimates. For each panel, the vertical axis and the horizontal axis correspond respectively to the North and East axis, scaled by the mean input wavelength. The R coefficient is the correlation between the input and the estimated map.

with $V_0 = 2$ km/s. We compile histograms of the ξ distributions to compare properties of the reference input distributions and of the obtained images. Figure 9 collects the ξ histograms from the input and from the estimates for $r_{\text{fit}} = 0.5\lambda_0$ and $r_{\text{fit}} = 1\lambda_0$. The similarity between reference and image is better for $r_{\text{fit}} = 0.5\lambda_0$ than $r_{\text{fit}} = 1\lambda_0$. The best result is obtained for the smoothest Medium 9. The green histograms obtained with $r_{\text{fit}} = 1\lambda_0$ are more narrow and have a higher peak value around small ξ values compared to the orange $r_{\text{fit}} = 0.5\lambda_0$ results. This indicates again the low-pass filter property of larger data ranges observed in the previous experiments.

4. Discussion

Resolution can mean different things in different imaging contexts, including the number or density of measuring points, the spectral sensitivity of an imaging device or method, the ability to detect or discriminate features and to accurately estimate their properties, contrast in brightness or color, or phase

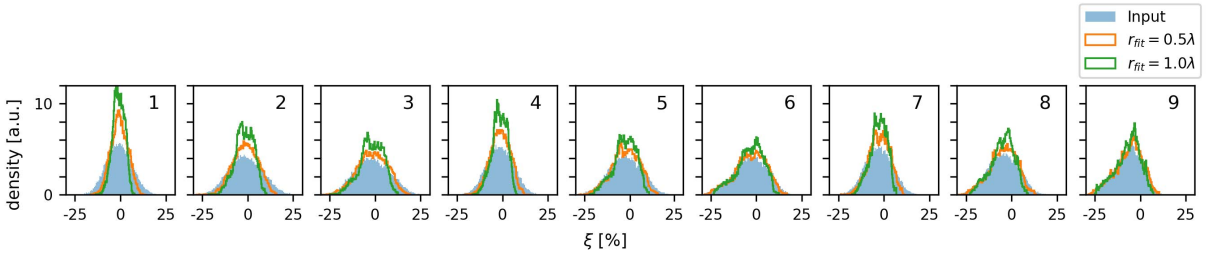

Figure 9. Histograms of the relative wave speed change ξ for the nine media imaged in Figure 8. Blue data correspond to the input reference values, and orange and green data correspond to images obtained with $r_{\text{fit}} = 0.5\lambda_0$ and $r_{\text{fit}} = 1\lambda_0$, respectively.

fidelity [e.g., Smith, 2003]. We use numerical simulations of two-dimensional acoustic wave propagation in a cavity (Figures 1, 2) to investigate the lateral resolution of the focal spot imaging technique for a fixed acquisition system with a constant number of grid points. The increase in depth resolution for such a compact dense array configuration compared to measurements made on traveling seismic Rayleigh surface waves is established by Giammarinaro et al. [2023]. We implement four test cases that together allow us to study the lateral resolution power of Rayleigh wave focal spots reconstructed from vertical–vertical component noise correlation data. Lateral resolution is discussed as the ability to resolve a step function in the material properties, to discriminate and characterize two closely spaced objects, and to measure position, amplitude, and phase of random distributions.

In a first homogeneous control experiment (Figures 2, 3) the reference wave speed is estimated with an error below 2% on average, which includes, however, areas of larger bias associated with edge effects. This average error is larger compared to the focal spot results based on numerical time-reversal experiments, where noise-free synthetics lead to errors in the 0.01% range for vertical–vertical component records and data ranges of $r_{\text{fit}} = 0.5\lambda_0$ and $r_{\text{fit}} = 1\lambda_0$, and where anisotropic surface wave incidence results in biases in the 0.1% range [Giammarinaro et al., 2023]. The different error levels are associated with the different methods used to synthesize Green's functions and focal spots. In time-reversal experiments, the wave field and hence the ballistic wave correlations are fully controlled by the mirror properties. More mirror elements lead to better refocusing results. Controlled lab experiments can stack over different space realizations. In seismic data applications an improved Green's function and refocusing reconstruction is achieved by time averaging to better conform with the decorrelated noise source assumption. Here, the focal spots are retrieved from cross-correlation of the reverberating cavity wave field, where the quality of the Green's function is controlled by the ability to excite and average a sufficiently large number of modes in the cavity [Draeger and Fink, 1999]. Hence we stack over different realizations using different source positions. This increases the number of independent modes to enhance the narrow-band refocusing, which is equivalent to using more time reversal mirror elements in a time-reversal experiment. Our approach converges towards the theoretical focal spot, but it remains sensitive to details of the implementation such as the source positions of the relatively few realizations. This explains the observed fluctuations in the focal spot reconstructions, which indicate the imperfect Green's function synthesis, even for the homogeneous case. This means that our imperfect cavity results are comparable to focal spots obtained from noisy data.

The second half-spaces experiment (Figures 4, 5) shows the feasibility to resolve the contrast between two media that have a 10% difference in wave speed. However, the interface is not perfectly resolved. Whereas the wave speed is correctly estimated away from the interface, the finite data or fitting range creates an averaging or low-pass filter effect that depends on r_{fit}. Tests with different r_{fit} values indicate that the transition width ΔL scales with good approximation linearly with the data range, $\Delta L \approx r_{\text{fit}}$.

The third circular inclusion configuration (Figures 6, 7) shows the possibility to discriminate two

separate objects separated by $0.25\lambda_0$, even for data ranges of one wavelength. However, the data range dependent low-pass filter properties lead to averaged amplitude values at edges. We have not observed situations where the focal spot method yields biased phase properties, so the inclusion positions are accurate. This suggests that the super-resolution property demonstrated with passive elastography in soft tissues [Zemzemi et al., 2020] also applies to 2D Rayleigh surface wave propagation. Again this means that for good data quality and high station density the method has the potential to meet the formal criterion of super-resolution, i.e., the sensitivity at small scales is sufficient to discriminate objects or features that are separated by distances that are much shorter than the wavelength.

The fourth test case considers random media (Figures 8, 9, Table 1) which show the highest similarity to distributions of Earth material properties. The quality of the focal spot reconstruction as quantified by the correlation coefficient R between reference and image depends on the roughness or smoothness of the distribution in relation to wavelength and data range. R is small when the distributions are rough, have small-scale fluctuations compared to the probing wavelength, and the data range is large. The reconstruction is almost perfect when the distributions are smooth, have large-scale fluctuations, and the data range is small. These conclusions are further corroborated comparing histogram properties of the velocity variation parameter ξ (Equation (2), Figure 9), which again demonstrate the low-pass filtering effect of large r_{fit} values. Thus, positions are well estimated but the amplitudes diverge for small-scale heterogeneities. The best estimates are obtained for variations on scales larger than r_{fit}. Deblurring methods can potentially be developed to further improve the lateral resolution of the method considering that the focal spot Bessel function shape acts as a spatial convolution filter. If resources permit, an imaging campaign could be optimized by first detecting target features with low contrast before then a sensor re-configuration helps to improve the quantitative estimate by increasing the signal-to-noise ratio through network densification.

The present study employs two-dimensional acoustic simulations. These scalar simulations yield the same Green's function as for vertical–vertical component Rayleigh wave propagation. Our main conclusions thus hold for seismic Rayleigh wave imaging, including the advantageous estimation of the local error that can help improve the uncertainty management of shear wave inversions. However, this set-up does not allow to study the biasing effect of interfering body wave energy. Giammarinaro et al. [2023] shows that the error on the vertical–vertical component increases in the presence of P waves, but this can be compensated for by increasing the data range. Together with our observations here this implies that an increase in r_{fit} improves the results if refocusing P wave energy distorts the surface wave focal spot, but that this remedy negatively affects lateral resolution power. This trade-off situation would benefit from efficient focal spot filters. Alternatively, Rayleigh wave phase speed estimates obtained from radial-vertical component data are much less sensitive to P waves [Giammarinaro et al., 2023], which offers independent constraints for the improvement of vertical–vertical results. The application of radial–radial and transversal–transversal component focal spots requires first an efficient separation of the combined Rayleigh and Love wave energy [Haney and Nakahara, 2014]. Spatial autocorrelations of surface wave strain and rotational data can further provide additional constraints on the local velocity structure [Nakahara et al., 2021, Nakahara and Haney, 2022].

5. Conclusion

We investigate the lateral resolution power of the Rayleigh surface wave focal spot imaging method using two-dimensional numerical experiments of reverberating wave fields in a cavity. Most importantly the resolution depends on the data range. This means that focal spot imaging exhibits super-resolution properties provided the data quality supports sub-wavelength data ranges. Longer data ranges still allow imaging of small-scale features at super-resolution albeit with a loss in contrast. Seismic Rayleigh wave focal spot imaging shows convincing resolution properties that make it suitable for a wide range of imaging applications ranging from feature detection to accurate wave speed estimates. There are hence no fundamental disadvantages compared to established passive surface wave tomography methods. Here as there, the station configuration can be tuned to support image quality and properties

for different goals, and in both cases the data quality or signal-to-noise ratio ultimately has the largest impact on the resolution.

Declaration of interests

The authors do not work for, advise, own shares in, or receive funds from any organization that could benefit from this article, and have declared no affiliations other than their research organizations.

Open research/data availability

No observational data were used in this study.

Dedication

The manuscript was written with contributions from all authors. All authors have given approval to the final version of the manuscript.

Funding

This work was sponsored by a research grant from the Academy of Finland (decision number 322421).

Acknowledgments

We thank Julien de Rosny, Stefan Catheline, Michel Campillo, Léonard Seydoux, Laurent Stehly, Alexander Meaney, and Markus Juvonen for helpful discussions. We thank the editor N. Shapiro and two anonymous reviewers for comments that helped to improve the manuscript.

References

Aki, K. (1957). Space and time spectra of stationary stochastic waves, with special reference to microtremors. *Bull. Earthq. Res. Inst.*, 35, 415–456.

Asten, M. W. (2006). On bias and noise in passive seismic data from finite circular array data processed using SPAC methods. *Geophysics*, 71(6), V153–V162.

Aster, R. C., Borchers, B., and Thurber, C. H. (2019). *Parameter Estimation and Inverse Problems*. Elsevier,Amsterdam, Oxford, Cambridge, 3rd edition.

Barrere, V., Melodelima, D., Catheline, S., and Giammarinaro, B. (2020). Imaging of thermal effects during high-intensity ultrasound treatment in liver by passive elastography: a preliminary feasibility in vitro study. *Ultrasound Med. Biol.*, 46, 1968–1977.

Ben-Zion, Y. (1989). The response of two joined quarter spaces to *SH* line sources located at the material discontinuity interface. *Geophys. J. Int.*, 98(2), 213–222.

Benech, N., Brum, J., Catheline, S., Gallot, T., and Negreira, C. (2013). Near-field effects in Green's function retrieval from cross-correlation of elastic fields: experimental study with application to elastography. *J. Acoust. Soc. Am.*, 133, 2755–2766.

Brum, J., Catheline, S., Benech, N., and Negreira, C. (2015). Quantitative shear elasticity imaging from a complex elastic wavefield in soft solids with application to passive elastography. *IEEE Trans. Ultrason. Ferroelectr. Freq. Control*, 62(4), 673–685.

Catheline, S., Benech, N., Brum, J., and Negreira, C. (2008). Time reversal of elastic waves in soft solids. *Phys. Rev. Lett.*, 100(6), article no. 064301.

Catheline, S., Souchon, R., Rupin, M., Brum, J., Dinh, A. H., and Chapelon, J.-Y. (2013). Tomography from diffuse waves: Passive shear wave imaging using low frame rate scanners. *Appl. Phys. Lett.*, 103(1), article no. 014101.

Chamarczuk, M., Malinowski, M., Nishitsuji, Y., Thorbecke, J., Koivisto, E., Heinonen, S., Juurela, S., Mężyk, M., and Draganov, D. (2019). Automatic 3D illumination-diagnosis method for large-N arrays: Robust data scanner and machine-learning feature provider. *Geophysics*, 84(3), Q13–Q25.

Cotton, F. and Coutant, O. (1997). Dynamic stress variations due to shear faults in a plane-layered medium. *Geophys. J. Int.*, 128, 676–688.

Cox, H. (1973). Spatial correlation in arbitrary noise fields with application to ambient sea noise. *J. Acoust. Soc. Am.*, 54, 1289–1301.

Derode, A., Larose, E., Tanter, M., de Rosny, J., Tourin, A., Campillo, M., and Fink, M. (2003). Recovering the Green's function from field–field correlations in an open scattering medium (L). *J. Acoust. Soc. Am.*, 113(6), 2973–2976.

Draeger, C. and Fink, M. (1999). One-channel time-reversal in chaotic cavities: Theoretical limits. *J. Acoust. Soc. Am.*, 105(2), 611–617.

Ekström, G. (2014). Love and Rayleigh phase-velocity maps, 5–40 s, of the western and central USA from

USArray data. *Earth Planet. Sci. Lett.*, 402(C), 42–49.

Ekström, G., Abers, G. A., and Webb, S. C. (2009). Determination of surface-wave phase velocities across USArray from noise and Aki's spectral formulation. *Geophys. Res. Lett.*, 36(18), 5–9.

Fink, M. (1997). Time reversed acoustics. *Phys. Today*, 50(3), 34–40.

Frankel, A. and Clayton, R. W. (1986). Finite difference simulations of seismic scattering: Implications for the propagation of short-period seismic waves in the crust and models of crustal heterogeneity. *J. Geophy. Res.*, 91(B6), 6465–6489.

Gallot, T., Catheline, S., Roux, P., Brum, J., Benech, N., and Negreira, C. (2011). Passive elastography: shear-wave tomography from physiological-noise correlation in soft tissues. *IEEE Trans. Ultrason. Ferroelectr. Freq. Control*, 58(6), 1122–1126.

Giammarinaro, B. and Hillers, G. (2022). Resources for "Seismic surface wave focal spot imaging: numerical resolution experiments. University of Helsinki.

Giammarinaro, B., Tsarsitalidou, C., Hillers, G., de Rosny, J., Seydoux, L., Catheline, S., Campillo, M., and Roux, P. (2023). Seismic surface wave focal spot imaging: numerical resolution experiments. *Geophys. J. Int.*, 232(1), 201–222.

Haney, M. M., Mikesell, T. D., van Wijk, K., and Nakahara, H. (2012). Extension of the spatial autocorrelation (SPAC) method to mixed-component correlations of surface waves. *Geophys. J. Int.*, 191(1), 189–206.

Haney, M. M. and Nakahara, H. (2014). Surface-wave Green's tensors in the near field. *Bull. Seism. Soc. Am.*, 104(3), 1578–1586.

Hillers, G., Mai, P. M., Ben-Zion, Y., and Ampuero, J.-P. (2007). Statistical properties of seismicity of fault zones at different evolutionary stages. *Geophys. J. Int.*, 169, 515–533.

Hillers, G., Roux, P., Campillo, M., and Ben-Zion, Y. (2016). Focal spot imaging based on zero lag cross-correlation amplitude fields: Application to dense array data at the San Jacinto fault zone. *J. Geophy. Res. Solid Earth*, 121(11), 8048–8067.

Holliger, K. and Levander, A. R. (1992). A stochastic view of lower crustal fabric based on evidence from the Ivrea Zone. *Geophys. Res. Lett.*, 19(11), 1153–1156.

Lin, F.-C. and Ritzwoller, M. H. (2011). Helmholtz surface wave tomography for isotropic and azimuthally anisotropic structure. *Geophys. J. Int.*, 186(3), 1104–1120.

Lin, F.-C., Ritzwoller, M. H., and Snieder, R. (2009). Eikonal tomography: surface wave tomography by phase front tracking across a regional broad-band seismic array. *Geophys. J. Int.*, 177(3), 1091–1110.

Liu, Q. and Gu, Y. (2012). Seismic imaging: From classical to adjoint tomography. *Tectonophysics*, 566–567, 31–66.

Mai, P. M. and Beroza, G. C. (2002). A spatial random field model to characterize complexity in earthquake slip. *J. Geophy. Res. Solid Earth*, 107(B11), ESE 10–1–ESE 10–21.

Nakahara, H. (2006). A systematic study of theoretical relations between spatial correlation and Green's function in one-, two- and three-dimensional random scalar wavefields. *Geophys. J. Int.*, 167, 1097–1105.

Nakahara, H., Emoto, K., and Nishimura, T. (2021). Extending the formulation of the spatial autocorrelation (SPAC) method to strain, rotation and tilt. *Geophys. J. Int.*, 227(1), 287–302.

Nakahara, H. and Haney, M. M. (2022). Connection between the cross correlation and the Green's function: strain and rotation of surface waves. *Geophys. J. Int.*, 230(2), 1166–1180.

Obermann, A., Planès, T., Hadziioannou, C., and Campillo, M. (2016). Lapse-time-dependent coda-wave depth sensitivity to local velocity perturbations in 3-D heterogeneous elastic media. *Geophys. J. Int.*, 207(1), 59–66.

Ripperger, J., Ampuero, J.-P., Mai, P. M., and Giardini, D. (2007). Earthquake source characteristics from dynamic rupture with constrained stochastic fault stress. *J. Geophys. Res.*, 112(B4), article no. B04311.

Sabra, K. G., Conti, S., Roux, P., and Kuperman, W. A. (2007). Passive in vivo elastography from skeletal muscle noise. *Appl. Phys. Lett.*, 90(19), article no. 194101.

Sabra, K. G., Gerstoft, P., Roux, P., Kuperman, W. A., and Fehler, M. C. (2005). Surface wave tomography from microseisms in Southern California. *Geophys. Res. Lett.*, 32(14), 1–4.

Sanchez-Sesma, F. J. (2006). Retrieval of the Green's function from cross correlation: the canonical elastic problem. *Bull. Seism. Soc. Am.*, 96(3), 1182–1191.

Sato, H., Fehler, M. C., and Maeda, T. (2012). *Seis-*

mic Wave Propagation and Scattering in the Heterogeneous Earth: Second Edition. SpringerLink. Springer, Berlin, Heidelberg, 2nd edition.

Shapiro, N. M. and Campillo, M. (2004). Emergence of broadband Rayleigh waves from correlations of the seismic ambient noise. *Geophys. Res. Lett.*, 31, article no. L07614.

Smith, S. W. (2003). *Digital Signal Processing: A Practical Guide for Engineers and Scientists*. Demystifying Technology Series. Newnes, Amsterdam, Boston.

Treeby, B. E., Budisky, J., Wise, E. S., Jaros, J., and Cox, B. T. (2018). Rapid calculation of acoustic fields from arbitrary continuous-wave sources. *J. Acoust. Soc. Am.*, 143(1), 529–537.

Tromp, J., Tape, C., and Liu, Q. (2005). Seismic tomography, adjoint methods, time reversal and banana-doughnut kernels. *Geophys. J. Int.*, 160(1), 195–216.

Tsai, V. C. (2023). The future of Earth imaging. *Seismol. Res. Lett.*, 94(5), 2119–2128.

Tsai, V. C. and Moschetti, M. P. (2010). An explicit relationship between time-domain noise correlation and spatial autocorrelation (SPAC) results. *Geophys. J. Int.*, 182(1), 454–460.

Tsarsitalidou, C., Boué, P., Hillers, G., Giammarinaro, B., Campillo, M., Seydoux, L., and Stehly, L. (2021). Seismic imaging with focusing surface waves obtained from USArray noise correlation functions. In *EGU General Assembly Conference Abstracts*, pages EGU21–9045. EGU.

Weertman, J. (1980). Unstable slippage across a fault that separates elastic media of different elastic constants. *J. Geophy. Res. Solid Earth*, 85(B3), 1455–1461.

Yokoi, T. and Margaryan, S. (2008). Consistency of the spatial autocorrelation method with seismic interferometry and its consequence. *Geophys. Prospect.*, 56, 435–451.

Zemzemi, C., Zorgani, A., Daunizeau, L., Belabhar, S., Souchon, R., and Catheline, S. (2020). Super-resolution limit of shear-wave elastography. *Europhys. Lett.*, 129(3), article no. 34002.

Zorgani, A., Souchon, R., Dinh, A.-H., Chapelon, J.-Y., Ménager, J.-M., Lounis, S., Rouvière, O., and Catheline, S. (2015). Brain palpation from physiological vibrations using MRI. *Proc. Natl. Acad. Sci. USA*, 112, 12917–12921.

ACADÉMIE DES SCIENCES
INSTITUT DE FRANCE

Comptes Rendus. Géoscience — Sciences de la Planète
2024, Vol. 356, Special issue S4, p. 59-84
https://doi.org/10.5802/crgeos.243

Research article

New Developments in Passive Seismic Imaging and Monitoring

Potential and limitations of noise-based surface-wave tomography for numerical site effect estimation: a case study in the French Rhône valley

François Lavoué [a,*,a,b], Bérénice Froment [a,a], Céline Gélis [a,a], Pierre Boué [b,b], Emmanuel Chaljub [b,b], Laurent Stehly [b,b], Sophie Beauprêtre [c], Florent De Martin [d,d], Loïc Gisselbrecht [a,a,b], Marco Pilz [e,e], Denis Moiriat [a,a] and Edward Marc Cushing [a,a]

[a] Institut de Radioprotection et Sûreté Nucléaire (IRSN), PSE-ENV, SCAN, BERSSIN/BEHRIG, Fontenay-aux-Roses, France

[b] Univ. Grenoble Alpes, Univ. Savoie Mont Blanc, CNRS, IRD, UGE, ISTerre, Grenoble, France

[c] Sisprobe/EGIS, 3 rue du Dr Schweitzer, 38180 Seyssins, France

[d] BRGM (French Geological Survey), Risks and Prevention Division, Orléans, France

[e] GFZ, German Research Center for Geosciences, Potsdam, Germany

E-mail: francois.lavoue@univ-grenoble-alpes.fr (F. Lavoué)

Abstract. In certain geological settings such as sedimentary basins, the ground motion induced by an earthquake may be amplified by local site conditions. Estimating these site effects is important for seismic hazard assessment but can be difficult to do empirically due to the scarcity of site-specific field data in time and space, especially in low-to-moderate seismicity regions where the earthquakes needed for measuring the site effects have long return periods. In this study, we try to overcome these limitations and investigate an alternative approach based on ambient seismic noise and numerical simulations. More specifically, we use a 3D numerical model of seismic properties derived from Ambient Noise Surface-Wave Tomography (ANSWT) for 3D numerical simulations of seismic wave propagation, and consequently for a numerical estimation of seismic amplification in the basin. We illustrate the approach on a target site located in the French Rhône valley, where the Messinian salinity crisis has dug a paleo-canyon which is now filled by soft sediments in direct contact with a harder substratum, thereby providing typical conditions for significant site effects, as also observed by previous studies in the area. This work makes use of two dedicated datasets. On one hand, we use earthquake recordings acquired by a network of broadband stations deployed over the target site over 8 months, in order to estimate seismic amplification in the basin with respect to a rock-site reference via Standard Spectral Ratios (SSR), which we consider as our reference for evaluating our numerical results. On the other hand, we exploit one-month-long ambient noise recordings acquired by a dense array of 400 3C sensors. Prior to this work, this noise data was used to build a 3D shear-wave velocity (V_S) model of the target site via ANSWT, and also to estimate seismic amplification via noise-based Standard Spectral Ratios (SSRn). The obtained ANSWT model well reproduces the main geological structures of the basin, with lateral variations of velocities at depth depicting the deeper parts of the basin. However, our simulation results also show that some of its limitations related to surface wave

*Corresponding author

sensitivity and resolution capability have an impact on the numerical amplification predicted in the basin. In particular, this ANSWT model lacks clear basin edges in order to efficiently trap seismic waves in the basin and to generate significant 3D wave propagation effects (diffractions, reflections, and generation of laterally propagating surface waves at the edges of the basin). As a result, the numerical amplification predicted in the ANSWT model remains dominated by a 1D response and does not reproduce the broadband character of the observed amplification at locations affected by significant 3D propagation effects. On the other hand, the numerical amplification predicted in the ANSWT model shows a good agreement with the observations at locations that seem less affected by 3D propagation effects, including in complex regions of the model where lateral variations must be taken into account. Our results therefore contribute to identify and better understand the potential and limitations of using ANSWT models for numerical site effect estimation. This study allows us to propose perspectives for future work to improve the approach, which remains promising for site effect assessment in low- to moderate-seismicity contexts.

Keywords. Seismology, Seismic hazard, Site effects, Passive seismic imaging, Numerical simulations.

Funding. French National Research Agency (Agence Nationale pour la Recherche, ANR, grant number ANR19-CE31-0029), German Research Foundation (Deutsche Forschungsgemeinschaft, DFG, project number 431362334), HPC resources of TGCC under the allocation 2022-gen13461 made by GENCI, GRICAD infrastructure.

Manuscript received 10 August 2023, revised 29 March 2024, accepted 27 May 2024.

1. Introduction

In sedimentary basins, the impedance contrast at the interface between soft sedimentary layers and the underlying bedrock leads to the trapping of seismic waves within the sedimentary in-filling. This gives rise to complex wave phenomena (body wave resonance, generation and diffraction of surface waves at the edges of the basin, vertical and lateral reverberations, focusing effects) which highly depend on the three-dimensional (3D) geometry of the basin and often result in an increased amplitude (or "amplification") and duration of the ground motion (or "duration lengthening"). This modification of ground motion due to local geology is referred to as *site effects*. Site effects have been the subject of many studies, especially since the devastating 1985 Mexico earthquake that brought to light the influence of local soil conditions on the strong amplification of ground motion observed in Mexico City, despite the long distance to the seismic source [e.g., Campillo et al., 1989]. This example, along with many other observations around the world [e.g., Kawase, 1996, Graves et al., 1998, Lebrun et al., 2001, Roten et al., 2008, Bindi et al., 2011, Ktenidou et al., 2016], makes it clear that the quantification of these site effects is essential for seismic hazard assessment (SHA). Because they are related to local soil conditions, site effects can be highly variable from one site to another, and therefore require site-specific studies for a robust estimation that accounts for the whole complexity of wave phenomena, in particular in 3D geological structures.

The French-German DARE project (*Dense ARray for site effect Estimation*) has been conceived and designed in this line. The idea is to implement various and complementary approaches to perform a detailed study of site effects at a target site located in the French Rhône valley. The area hosts critical facilities including nuclear installations, thereby motivating the need for robust SHA studies locally. This site is located on the deep and elongated Messinian Rhône Canyon, whose geometry and lithological characteristics make it a good candidate for generating multidimensional site effects. DARE is centred on the exploitation of dense and complementary datasets acquired in the area [Froment et al., 2022b]. The project proposes to investigate the interest of using such datasets for a robust estimation of site effects, especially in low-to-moderate seismicity areas such as metropolitan France.

One first, standard approach considered in DARE relies on earthquake recordings through the calculation of so-called site/reference Standard Spectral Ratios [SSR, Borcherdt, 1970]. SSR estimate the local seismic amplification by direct comparison between earthquake seismograms simultaneously recorded at a given *site* station laying on a sedimentary basin (subject to *site effects)* with respect to a nearby *reference* station (typically on a bedrock outcrop, considered free of site effects). This empirical method has proven to be efficient for a robust quantification of

site effects in various configurations. The implementation of this method may however show some difficulties in low-to-moderate seismicity areas, such as mainland France [Traversa et al., 2020], where moderate to large earthquakes ($M_w > 5.0$) have long return periods, therefore requiring long deployments. Alternative approaches may thus be considered to complement such seismicity-based analysis of site effects. To this end, the DARE project investigates two main research tracks in order to explore the potential of using weak but ubiquitous vibrations—known as ambient seismic noise—as an alternative source of data for estimating site effects due to complex wave propagation in sedimentary basins [e.g., Boué et al., 2016]. On one hand, seismic noise can be used directly for empirical estimations of site effects, via H/V analysis [e.g., Bonnefoy-Claudet et al., 2006, Spica et al., 2017, van Ginkel et al., 2019] or noise-based SSR estimations [e.g., Perron et al., 2018, Gisselbrecht et al., 2023]. On the other hand, ambient noise could also be used in a more indirect way as the initial ingredient to build seismic models of the target site that could then be used for numerical prediction of the ground motion and thus of seismic amplification. The present paper focuses on this numerical aspect.

By giving access to the complete wavefield, simulations help to evaluate the spatial variability of site effects and more importantly to understand the underlying physical parameters to which they are sensitive [e.g., De Martin et al., 2021]. 1D modelling of body-wave resonance phenomena is a first way to calculate the response of a sedimentary layer overlaying a rigid bedrock [e.g., Thomson, 1950, Haskell, 1953]. However, in the presence of complex geological structures, several studies have shown the limitation of 1D numerical simulations, and the necessity of 2D or 3D simulations of seismic wave propagation to reproduce the observed amplifications [e.g., Kawase, 1996, Smerzini et al., 2011, Matsushima et al., 2014, Ktenidou et al., 2016]. Gélis et al. [2022] reach the same conclusions for our target site, as they observe that 1D simulations do not reproduce the amplification measured in the Tricastin basin, in particular regarding its maximum amplitude (up to a factor 8) and its broadband spectral character, typical of 3D wave propagation effects [Chávez-García et al., 2000, Cornou and Bard, 2003, Bindi et al., 2009, Michel et al., 2014]. The conclusions of this previous study by Gélis et al. [2022] form the motivation for the use of 3D numerical simulations in our work. 3D simulations have become more affordable lately thanks to the rapid increase of computational resources and to the development of dedicated software, using in particular spectral-element methods [SEM, e.g., Komatitsch and Vilotte, 1998, De Martin, 2011, Trinh et al., 2019]. These developments led to many applications, notably in sedimentary basins with complex geometries that require detailed simulations [e.g., Komatitsch et al., 2004, Maufroy et al., 2015, 2016, Chaljub et al., 2010, 2015, Paolucci et al., 2015, Thompson et al., 2020, De Martin et al., 2021, Panzera et al., 2022]. These simulations however require an accurate knowledge of the subsurface, both in terms of geometry and of seismic properties (S-wave velocity V_S, P-wave velocity V_P, density ρ, and S- and P-wave attenuation factors Q_S and Q_P). As a consequence, these numerical approaches also rely on field data and geophysical surveys in order to constrain numerical models and define reliable input parameters for the simulations. On the other hand, seismic data (earthquake and noise recordings) are also essential to provide observations which the outputs of the simulations can be compared and calibrated with.

Most studies involving 3D numerical simulations for site effect estimation rely on layered models [e.g., Taborda and Bielak, 2013, Maufroy et al., 2016, De Martin et al., 2021, Panzera et al., 2022]. In these models, layers are separated by interfaces associated to sharp impedance contrasts, and seismic properties are usually assumed either homogeneous or varying only vertically within each layer. The geometry of the interfaces is often derived from geological knowledge (borehole data, field campaigns, surface mapping or interpreted cross-sections), from the interpretation of active seismic migrated images, or from H/V spectral ratio analysis, while seismic properties are often estimated from a limited number of local measurements such as Ambient Vibration Analysis (AVA) and extrapolated to the entire layers, assuming vertical but no lateral variations within the layers [e.g., Manakou et al., 2010, Molinari et al., 2015, Cushing et al., 2020, Panzera et al., 2022].

In the present paper, we propose an alternative approach that uses ambient-noise surface-wave tomography (ANSWT) for building 3D seismic models of the target area. ANSWT is a tomographic method

that has proven very successful for imaging shear-wave velocities (V_S) at the crustal and lithospheric scales [e.g., Shapiro et al., 2005] and more recently at smaller, basin scales [e.g., Boué et al., 2016, Chmiel et al., 2019]. Taking full advantage of the deployment of dense seismic networks, this passive seismic imaging technique is particularly attractive. ANSWT has the advantage to provide a quantitative model of shear-wave velocity structure in 3D, including both vertical and lateral variations, at relatively low cost. However, ANSWT provides smoother models compared to active seismics and to the geology-based layered models usually considered in numerical simulations. The aim of this paper is to investigate the use of standard ANSWT models for the numerical estimation of seismic amplification and for site effect assessment. More precisely, the question we address here is the following: what are the potential and limitations of 3D numerical simulations based on standard ANSWT models to assess seismic amplification in complex sedimentary basins?

The paper is organized as follows. Section 2 presents the target zone, its geological context, and the seismic data acquired in the frame of the DARE project. Section 3 reminds the steps of the standard ANSWT workflow used to build a 3D V_S model of the target site, and explains how we derive other seismic properties (V_P, ρ, Q_S, Q_P) in order to build a full 3D seismic model. In Section 4, we present our numerical results and the seismic amplification predicted in the 3D model, which we compare with observed, earthquake-based SSR, as well as with noise-based SSRn and with 1D approximations. Finally, we discuss the results in Section 6, highlighting the potential of using ANSWT models for the seismic characterization of sedimentary basins, but also underlining some limitations in their use for the numerical estimation of site effects, which leads us to propose perspectives for future work.

2. Target site and data

The DARE project targets the area of the Tricastin Nuclear Site (TNS) in the French Rhône Valley (Figure 1). The TNS is located on the Messinian Rhône canyon that was dug about 6 million years ago during the Messinian Salinity Crisis (MSC) by the paleo-Rhône river in older geological formations. In this area, the geological basement is mainly constituted by hard and thick (several hundreds of meters) lower Cretaceous limestones (Barremian), so-called "Urgonian" limestones, which we consider to be the reference *bedrock* unit in the region. These Urgonian limestones are overlain by more detrital lower to upper Cretaceous (Aptian to Turonian) formations (sands, sandstones, and marls), and then by Tertiary marine and continental detrital formations. These units are called hereafter "post-Urgonian Cretaceous (and/or Tertiary) formations" in order to distinguish them both from the Urgonian bedrock and from post-Messinian sediments. Indeed, after the MSC, the canyon has been filled with Pliocene sediments of marine (sands and clays) and continental (fluviatile conglomerates) origins, nowadays covered by the Rhône lower-to-recent Quaternary terraces. In 2019, when the DARE project was initiated, the local geology of the Messinian canyon remained poorly documented in the region of Tricastin. Gélis et al. [2022] provide some first insights about the canyon rims and the local subsurface characteristics based on borehole data, geological study, and local 1D geophysical characterization campaigns (H/V and AVA measurements). This first study provided local knowledge about the characteristics (thickness and V_S velocities) of the sedimentary canyon infilling and of the underlying bedrock at two sites in the area. A first site is located 2–3 km south of the TNS (seismic station E1/BOLL in Figure 1), on top of the sedimentary basin. At this site, Gélis et al. [2022] show that the base of the canyon reaches a depth of at least 500 m, incising—or, at least, lying directly on top of—high-velocity Urgonian limestones. The 2nd site is station G6/ADHE on a nearby outcrop of Urgonian limestones, which Gélis et al. [2022] characterize as a hard rock site with an estimated V_S30 (the average shear-wave velocity in the first 30 m) of about 2000 m/s. At larger depth, the 1D V_S profiles show velocity rapidly increasing with depth and reaching about 3000 m/s beyond 50 m depth. Gélis et al. [2022] present the various criteria for considering G6/ADHE as a good reference for SSR calculations. It is worth noting that V_S profiles obtained at ADHE and BOLL are consistent (i) with available geological data [e.g., Bagayoko, 2021, Do Couto et al., 2024] and (ii) with each other in terms of mean velocities at depth, therefore giving a reference velocity of $V_S \cong 3000$ m/s for the deep Urgonian substratum.

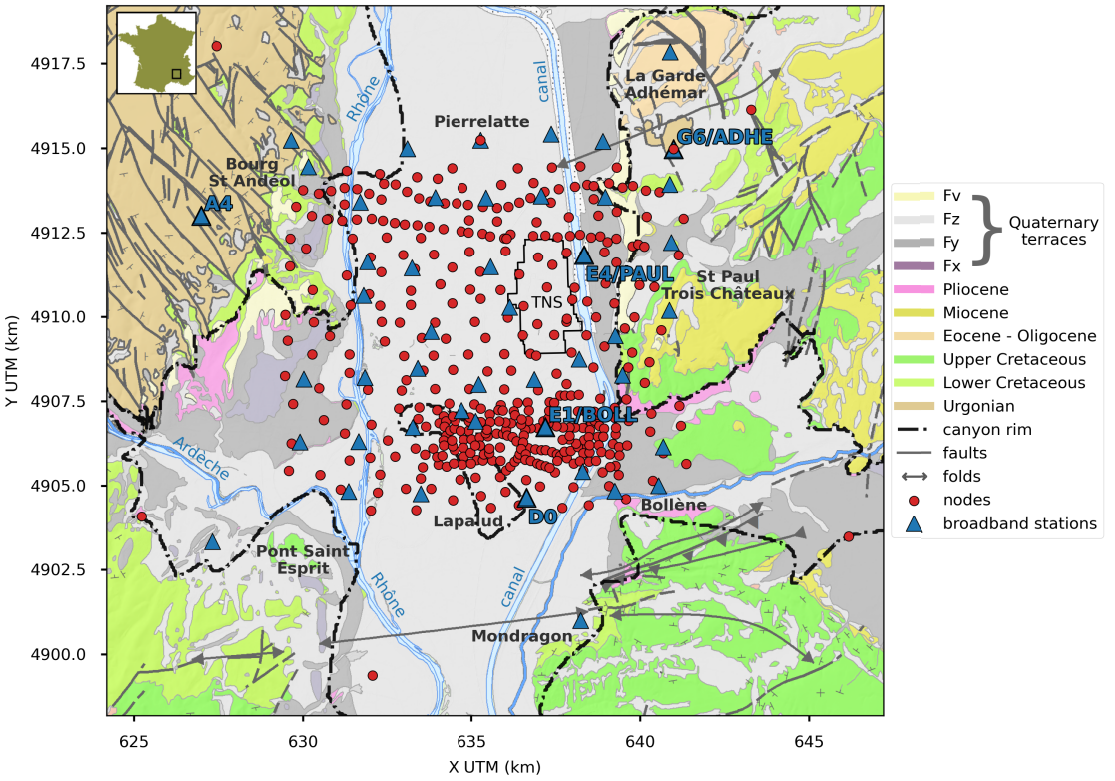

Figure 1. Simplified geological map of the target zone and localisation of the two deployments (red circles: nodal array, blue triangles: broadband network). Background colors correspond to main geological units (see legend). The extent of the map corresponds to the domain of interest for numerical simulations (excluding 15-km-wide margins).

From this first knowledge of the canyon, a 10 km × 10 km area surrounding the imprint of Pliocene and Quaternary sediment deposits around the TNS (Figure 1) was targeted. This extension allows us to embed the edges of nearby outcrops of Cretaceous series incised by the canyon, that constitute the basement of the canyon sedimentary in-filling. Most of this target zone is located in a heavily industrialized area, including the widespread TNS, a hydroelectric dam, towns, several railroads and a highway. The associated anthropogenic activity controls the distribution of high-frequency noise sources locally [Gisselbrecht et al., 2023].

Two complementary seismic campaigns were carried out in the framework of the DARE project [Froment et al., 2022b]. The first campaign consisted of deploying 400 3-component seismic nodes over a 10 km × 10 km area for one month (red dots in Figure 1). This campaign targeted the recording of seismic ambient noise. A second campaign consisted of deploying about 50 broadband stations over the same target area for more than eight months and targeted the recording of seismicity (including teleseismic events, regional, and local seismicity). These two datasets [Pilz et al., 2021, Froment et al., 2023b] are presented in detail in a data paper [Froment et al., 2022b] and are publicly available (see section *Data and software availability*).

The present study exploits the ambient noise data recorded by the 400-node network. In the methodological approach adopted in this work, seismicity data recorded by the 50-station network will only be used here to compare our numerical estimations of seismic amplification with observations. Three-component Geospace GSX nodes have been used for the dense nodal experiment whose design is shown in Figure 1. The average inter-node distance is about 800 m over the area. About half of the stations

spaced 200–250 m apart are used to form a denser grid located south of the TNS. Similarly, two dense east–west lines following two roads are located north of the TNS. Information about data completeness, noise levels, and overall data quality is available in Froment et al. [2022b]. A detailed characterization of seismic noise sources recorded by the nodal network is given in Gisselbrecht et al. [2023].

3. Soil model from noise-based medium characterization

3.1. *3D V_S model from ANSWT*

As mentioned in the introduction, the dataset of continuous seismic noise recorded by the nodal array was processed using a standard ANSWT workflow to obtain a 3D model of shear-wave velocity, as presented in Froment et al. [2022a]. In order to bring elements for the discussion of the results obtained by using this model, we detail the workflow used in this previous work hereafter:

(1) Cross-correlations of seismic signals between all pairs of stations of the nodal array (except 6 nodes located outside the dense 10×10 km grid, and 24 nodes with unusable data, resulting in 69,192 valid cross-correlations). Continuous signals were cross-correlated over 30-min-long time windows after spectral whitening, and stacked over the one-month duration of the acquisition. The cross-correlations of all three components (N,E,Z) provided the full cross-correlation tensor. Inter-station cross-correlations were then rotated in terms of radial (RR) and transverse (TT) components assuming straight inter-station paths. The vertical components (ZZ) of the cross-correlations were used for exploiting Rayleigh waves and the transverse (TT) for exploiting Love waves.

(2) Semi-automatic picking of fundamental-mode group-velocity dispersion curves using frequency-time analysis [FTAN, Dziewonski et al., 1969, Levshin et al., 1989]. A statistical quality control of the picked dispersion curves was used to reject outliers falling outside two standard deviations of the distribution of picked values. After this quality control, a total of 17,031 Love dispersion curves between 0.4 and 3 Hz and 29,719 Rayleigh dispersion curves between 0.35 and 6.5 Hz were kept for tomography (i.e., 25% and 43% of the full dataset, respectively). The tomography is therefore considered to be well constrained up to 3 Hz (by both Love and Rayleigh data) and partially constrained up to 5–6 Hz (only by Rayleigh data).

(3) Frequency-dependent 2D traveltime tomography [Barmin et al., 2001] in order to convert inter-station dispersion curves into local dispersion curves, i.e. build group velocity maps. This step was performed via a linearized inversion involving regularization in the form of norm damping and lateral smoothing. The choice of these regularization parameters plays a role in the resolution of the final model.

(4) Inversion of local group-velocity dispersion curves into local 1D V_S profiles using a Neighbourhood Algorithm [Sambridge, 1999, Mordret et al., 2014]. Here the use of a global optimization scheme allowed for a statistical exploration of the model space and provided an average of best-fitting models for each 1D V_S profiles, which were then linearly interpolated into a 3D V_S model.

The tomographic process was guided by assumptions derived from the geological knowledge at the time of this first imaging. In particular, for the 1D depth inversion (step 4), the expectation of a strong velocity contrast between sediments and bedrock led to a parameterization of the 1D profiles consisting in two smooth layers (represented by splines functions) potentially separated by a velocity discontinuity (if required by the data). This parameterization was adapted locally within sub-areas defined by clustering the local dispersion curves after the 2D tomography stage (step 3), using a data-driven *K-means* algorithm [MacQueen, 1967]. The resulting four sub-areas are shown in Figure 2 and turn out to well coincide with previous geological knowledge. Area #1 (in blue in Figure 2) corresponds to the deepest parts of the basin. Area #2 (in green) corresponds to the shallower northwestern edge of the basin, including the northwesternmost corner where Urgonian limestones are outcropping. Area #3 (in yellow) corresponds to the eastern edge and its outcrops of post-Urgonian/pre-Messinian formations (limestones, sands, sandstones, and marls of

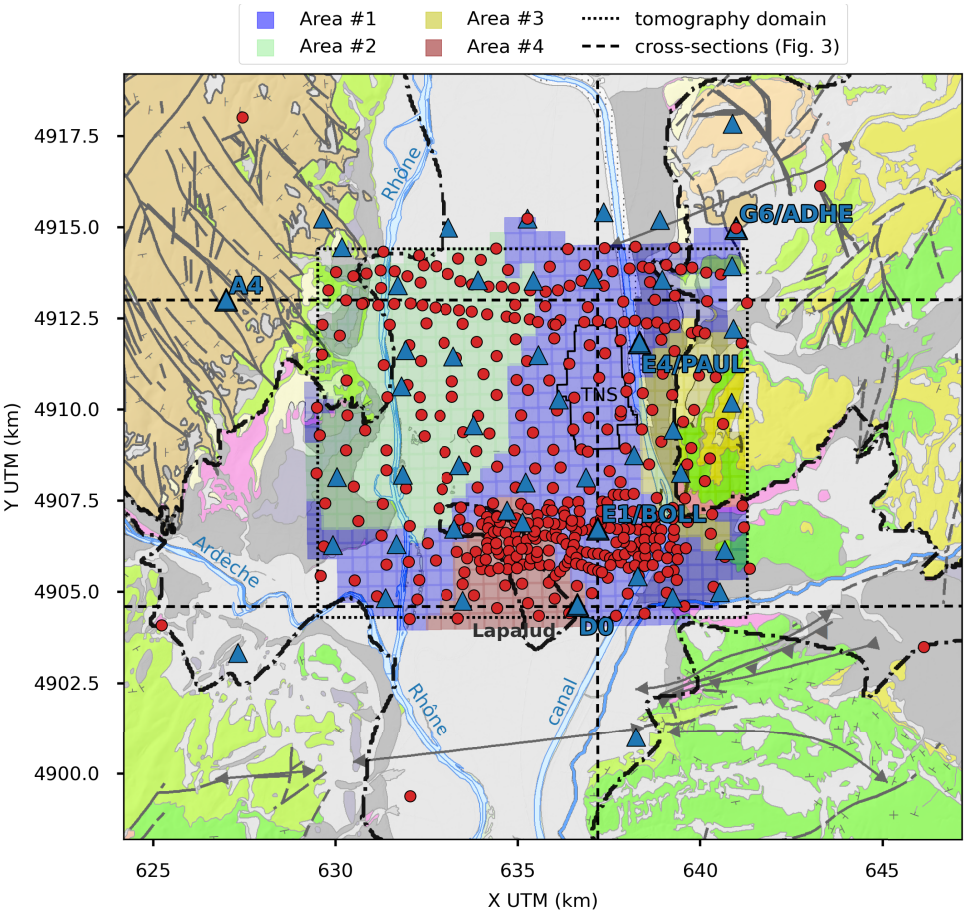

Figure 2. Regionalization of the tomographic domain in sub-areas based on the clustering of local dispersion curves.

Aptian to Miocene ages). Finally, Area #4 corresponds to a complex zone, including the so-called Lapalud island, formed by post-Urgonian Cretaceous units (limestones, sandstones and marls of Aptian to Turonian ages) expected to have lower seismic velocities than the hard Urgonian limestones [e.g., Bagayoko, 2021, Do Couto et al., 2024]. In addition to adapting the parameterization of the 1D inversion in these sub-areas, the sub-arrays were also used to perform FK analysis and estimate an average phase velocity curve that was used to constrain the 1D depth inversion of local group velocity curves within each sub-area.

Besides the assumption of a two-layer model with smooth velocity variations within each layer, we did not impose any strong constraint to the inversion. This preliminary 3D V_S model is therefore mainly data driven, its purpose being precisely to investigate how such a model, based on seismic noise only via a *blind* ANSWT workflow, can be used to predict seismic amplification in the basin. This remains a fairly open question, considering that the ANSWT procedure uses phase information only (amplitudes are discarded by spectral whitening in the cross-correlations).

In order to use the ANSWT model for numerical simulations, the 3D V_S volume is extrapolated outside the tomographic domain, both laterally and vertically, to define seismic properties in the full simulation domain, which extends laterally by 15 km from the limits of the domain of interest (*SEM domain* in Figure 2), and vertically down to 30 km depth. Because, in a first time, we want to rely on our data-driven ANSWT model and avoid making strong

assumptions about the subsurface, lateral extrapolation is performed invariantly at a given depth. Downward vertical extrapolation consists in a smooth transition from the bottom of the tomographic model (1000 m below ground surface) to a constant velocity of 3000 m/s at 1500 m depth. This value of V_S = 3000 m/s is chosen for consistency with prior measurements in the area [Gélis et al., 2022]. It also roughly corresponds to the maximum velocity of the tomographic model at 1 km depth, and therefore ensures a positive velocity gradient with respect to depth. Outside the basin, we also perform a vertically invariant extrapolation upwards in order to assign seismic properties to topographical heights above basin level.

Figure 3 gives several views of the obtained 3D V_S model. Figure 3a gives a 3D view that includes N–S and E–W vertical cross-sections through the V_S model (left and back panels, first colorbar), as well as the 1200-m/s iso-velocity surface that can be associated to the interface between sediments and bedrock (second colorbar). Figure 3b gives a 3D view of the numerical model, after extrapolation of the ANSWT model outside the tomographic domain over the full domain of interest (but excluding 15-km-wide margins, which just consist of further extrapolation). Figure 3c shows a vertical N–S cross-section along the expected axis of the Rhône paleo-canyon [Gélis et al., 2022, Froment et al., 2022a], passing through the TNS and through station E1/BOLL [on which we will focus later on to illustrate our results, and compare them with those of Gélis et al., 2022]. Figure 3d shows a vertical E–W cross-section in the south of the tomographic domain, through the Lapalud island and station D0 (on which we will also focus later on to illustrate our results).

As already described by Froment et al. [2022a], the ANSWT V_S model agrees well with the main geological structures expected in the area. In particular, the range of estimated shear-wave velocity values are consistent with previous studies [e.g., Gélis et al., 2022], with values ranging from 500 to about 1200–1400 m/s in the sediments, and from about 1700–2000 to 3000 m/s in the underlying bedrock. Moreover, the velocity discontinuity between the two layers (which roughly corresponds to the 1200-m/s iso-velocity surface shown in Figure 3a) coincides well with the expected depth of the paleo-canyon, at least for its deeper parts, with a north–south axis corresponding to the paleo-Rhône and a southwestern branch corresponding to the paleo-Ardèche (Figure 3a). Between these two branches, the model also depicts the so-called Lapalud island with higher velocities reaching shallower depths, representing post-Urgonian Cretaceous units (Figures 3a,c).

However, when looking in more detail, we notice that some features of the model are questionable. In particular, the model does not display high velocities reaching the surface, even in regions where we expect surface outcrops of Cretaceous formations (especially in the northwestern corner and on the eastern edge of the basin, Figures 3a, b). Instead, the model exhibits a lower-velocity layer ($500 < V_s <$ 1000 m/s) with a thickness of at least 200 m over the entire domain (Figures 3b–d). This low-velocity layer is not restricted to the basin, which is therefore not well delimited laterally. We will see in the following that this lack of basin edges will have consequences in terms of seismic amplification.

In spite of these limitations, the fact that the 3D V_S model derived from ANSWT well depicts the expected large-scale geometry of the Messinian paleo-valley at depth, including some complex structures such as the Lapalud island, motivates us to use this model for numerical simulations, in order to look at the seismic amplification that it may generate. This, however, first requires the definition of other seismic properties in the considered 3D volume. We will now present how we define these properties, and we will distinguish between properties that are constrained by the same seismic noise data as the V_S model (namely Q_S) and other properties that are estimated by other means (V_P, density, Q_P).

3.2. *Estimation of shear-wave quality factors Q_S*

Besides ANSWT, the seismic noise recorded by the dense array is processed via Q-SPAC analysis [Prieto et al., 2009] to estimate seismic attenuation parameters (Q_S), following the methodology of Boxberger et al. [2017]. To this end, the study area is subdivided into 15 sub-arrays, each of them containing 15 to 25 seismic nodes.

In a first step, the Extended Spatial AutoCorrelation (ESAC) method is adapted to first obtain mean 1D V_S profiles below each sub-array by joint inversion of Rayleigh wave dispersion and H/V spectral

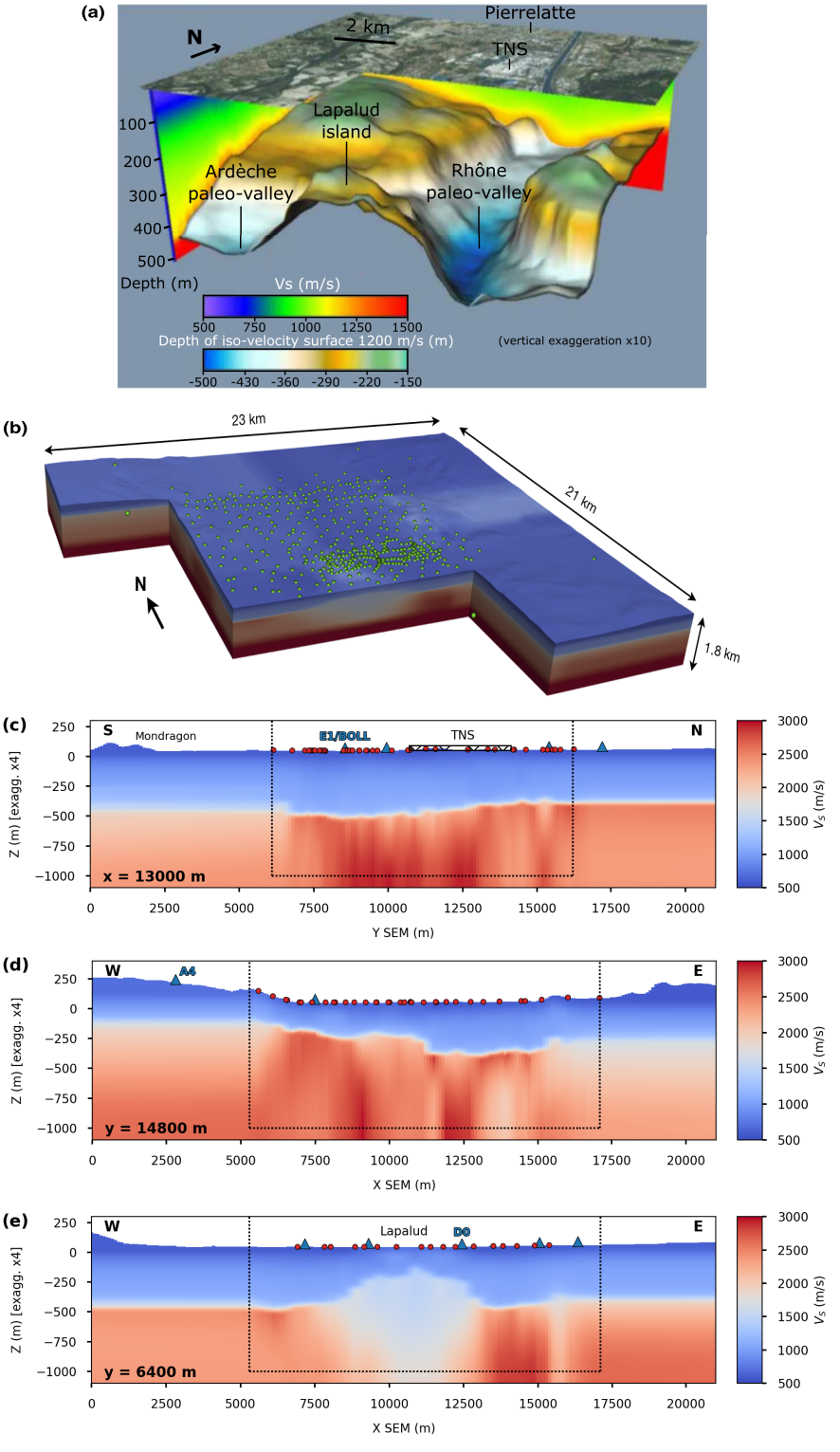

Figure 3. Caption continued on next page.

Figure 3. (**cont.**) 3D Vs model. (a) 3D view showing the interface between sediments and bedrock [adapted from Froment et al., 2022a]. (b) 3D view of the numerical model after extrapolation outside the tomography domain (excluding 15-km-wide margins). Green dots represent nodes and broadband stations. (c) South–north vertical cross-section along the axis of the paleo-Rhône canyon. (d) West–east vertical cross-section through the northern part of the array and station A4. (e) West–east vertical cross-section through the southern part of the array and the Lapalud island. In (c–e), the dashed box corresponds to the tomography domain. Red dots and blue triangles represent nodes and broadband stations located within 500 m of the sections (see Figure 2 for the location of the sections).

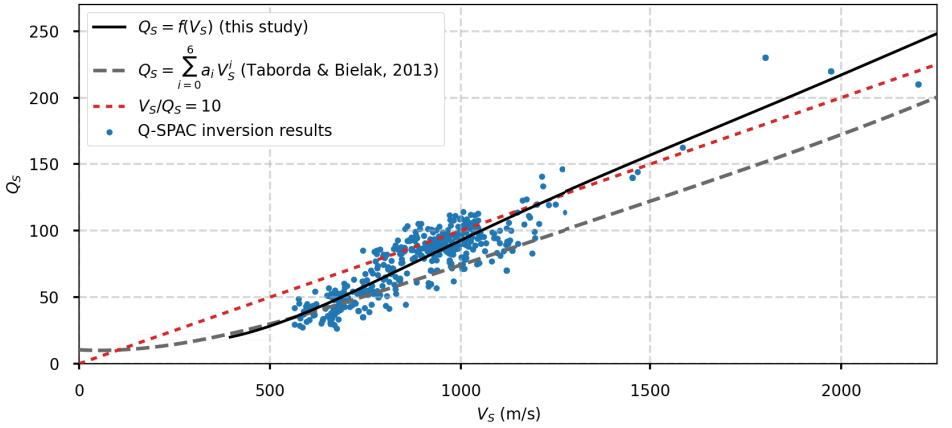

Figure 4. Calibration of a site-specific V_S/Q_S relationship using Q-SPAC inversion results.

ratios, and then estimate frequency-dependent Rayleigh-wave attenuation factors from the mean 1D V_S profiles [Ohori et al., 2002, Boxberger et al., 2011]. In a second step, individual 1D Q_S profiles are obtained from the inversion of the Rayleigh-wave attenuation coefficients by constraining the V_S profiles to the values obtained in the first step, following Xia [2014]. It is worth noting that the seismic attenuation discussed here does not distinguish between intrinsic and scattering attenuation. Furthermore, while the Rayleigh-wave attenuation factors of the input data depend on frequency, the Q_S parameter of the obtained layered model is assumed to be frequency-independent. Finally, following Xia et al. [2002], we disregard the contributions of P waves on the Rayleigh-wave attenuation factors.

In the end, 15 layered 1D profiles representative of average V_S and Q_S values as a function of depth are derived, one for each of the 15 sub-arrays of the nodal network. V_S profiles are found to be in general agreement with the ANSWT model (with deviations smaller than 15%). These profiles are used to calibrate a relationship between V_S and Q_S values in the form of a 6-order polynom [after Taborda and Bielak, 2013, see Figure 4] which is then used to derive a 3D Q_S model from the 3D ANSWT V_S model. This is expected to provide more realistic and site-specific Q_S values than assuming generic relationships (e.g., V_S/Q_S = 10), or other relationships from the literature calibrated for other sites [e.g., Taborda and Bielak, 2013, see Figure 4]. The Q_S values obtained from our site-specific relationship range from 21 for small V_S values in shallow sediments to 360 for high V_S values in the deep substratum (Table 1).

3.3. *Other seismic parameters (V_P, Q_P, density)*

Unlike V_S and Q_S properties, P-wave velocity V_P and quality factor Q_P, and density parameters are not (or poorly) constrained by our ambient noise data, which are typically dominated by surface waves.

In situ geotechnical measurements performed in the vicinity of the TNS down to approximately 30 m depth provide us with local estimations of V_P, V_S,

Table 1. Ranges of seismic properties in the two layers of the 3D V_S model

	V_S (m/s)		V_P (m/s)		Density (kg/m^3)		Q_S		Q_P	
	min	max	min	max	min	max	min	max	min	max
1st layer (sediments)	500	1400	2000	2675	2075	2225	21	130	260	350
2nd layer (bedrock)	1700	3070	3075	5300	2300	2640	170	340	420	760

and density [Moiriat, 2019]. These measurements show V_P/V_S ratios of up to 8 in very shallow sediments (Quaternary limons and alluvions forming thin (<20 m) layers and lenses, which are not included in the ANSWT due to its lack of sensitivity to these shallow layers), and of about 4 for values of $V_S \approx 500$ m/s in the blue marls encountered below 15 to 20 m depth. It is worth noting that these values of $V_S \approx 500$ m/s are in very good agreement with the V_S values of the shallow part of the basin in the ANSWT model which, according to the smallest wavelength considered in the tomography (≈100 m), we can regard as effective V_S values for the basin sediments in the first 30 to 50 m.

Based on these geotechnical measurements, we calibrate a site-specific V_P/V_S relationship of the form

$$\frac{V_P}{V_S} = 1.73 + a\,\mathrm{e}^{-bV_S}, \tag{1}$$

with $a = 9.46$ and $b = -2.82 \times 10^{-3}$. This *ad hoc* relationship is designed such as to yield a V_P/V_S ratio of 1.73 for large V_S values (deep bedrock), corresponding to the usual assumption of a Poisson's solid, while the calibration yields V_P/V_S ratios of about 4 for $V_S \approx 500$ m/s, as indicated by *in situ* geotechnical data.

In lack of sufficient density measurements, we use Gardner's empirical law [Gardner et al., 1974, equation (7); Brocher, 2005, equation (2)] in order to relate density to P-wave velocity V_P. This law is supposed to be valid for sedimentary rocks such as limestones. We verify that the density values obtained for the range of seismic velocities encountered in our ANSWT model roughly coincide with expected values for the known lithologies in the area (limestones, sandstones, and marls), as well as with the above-mentioned geotechnical measurements.

Finally, we must define values for the P-wave quality factor Q_P in our 3D model, although this parameter is expected to have very little impact on the amplification of the SH excitation that we will simulate. In lack of any constraint on these Q_P values, we derive them from Q_S, V_S, and V_P values, under the assumption that the compressibility quality factor is much larger than the shear quality factor [$Q_\kappa \gg Q_\mu$, Dahlen and Tromp, 1998, equation (9.59), p. 350].

Table 1 summarizes the ranges of values of the different seismic properties in the final 3D seismic model.

4. Numerical estimation of seismic amplification

4.1. *Simulation of seismic wave propagation*

Simulations of seismic wave propagation in the constructed 3D model are performed using the EFISPEC software [De Martin, 2011], which makes use of a time-domain spectral-element method (SEM) solving the 3D equation of motion in visco-elastic media. A hexahedral mesh is designed for simulations valid up to 5 Hz, which is about the maximum frequency used to constrain the ANSWT model (at least with Rayleigh data, see Section 3.1). The simulation domain extends laterally 15 km further than our domain of interest (Figures 1 and 2) and vertically down to 30 km, in order to mitigate parasite reflections on domain boundaries, where the absorbing condition is based on a paraxial approximation [Stacey, 1988]. This leads to a total of 6.5 M elements, with an element size that varies between 100 m and 300 m from the shallow to the deeper parts of the model. In order to reproduce the assumptions underlying SSR calculations, the simulated source is a vertically-incident plane wave with SH polarization in the X- (east–west) or Y- (north–south) direction, injected at 5 km depth. We perform two simulations, one for each polarization of the plane wave, for a duration of 60 s. Each simulation costs 3500 CPUh and is parallelized on 480 cores. The source time function is a low-pass-filtered Dirac delta function, filtered

below 5 Hz, such as to remain in the domain of validity of the simulation (and of the ANSWT model) and to be able to visualize and exploit simulated outputs directly, without filtering them at the post-processing stage.

Figure 5 shows snapshots of the simulated wavefield on the free surface at different times. The vertically-incident plane wave first arrives after approximately 2.2 s of simulation in the northwestern corner, which has slightly higher velocities than the rest of the domain (Figure 5a). At 2.5 s, amplitudes are saturated over the entire domain while the plane wave is reflecting on the free surface (Figure 5b). At 3.5 and 4 s (Figures 5c, d), high amplitudes are visible in the deepest parts of the basin, reflecting 1D basin amplification due to vertical body-wave resonance, but also outside the tomographic domain, due to topographic effects, in particular on the margins that are not constrained by the tomography. After 4.5 s (Figures 5e, f), late reverberations are slightly visible in the basin (likely due to reflections on the edges of the basin), but also in the margins of the model outside the tomographic domain (due to topographic effects). These snapshots show that waves are not efficiently trapped in the basin, as we would expect in a well-delimited basin [e.g., Chaljub et al., 2015, De Martin et al., 2021]. Instead, waves escape in the low-velocity shallow layer, resulting in an amplification over the entire domain, in particular in the margins of the simulation domain that are not constrained by the tomography.

Based on these first observations and despite some limitations, we will now continue to analyse our simulation results, especially in terms of predicted amplification, with the objective to better understand the limitations of our ANSWT model, which we just started to point out, and thus to draw perspectives about how such ANSWT models could be improved to better reproduce basin amplification. We propose to start by looking into the seismograms simulated at the locations of known stations, including E1/BOLL that has been investigated by Gélis et al. [2022], as well as A4 that serves as a reference station for the calculation of our empirical, earthquake-based SSR (see Supplementary Material for more details). We shall specify here that station A4 is located on the same kind of Urgonian outcrop and presents similar H/V characteristics as station G6/ADHE that was used as a reference station by Gélis et al. [2022].

Figure 6 shows seismograms (Figure 6a) simulated at stations E1/BOLL (in blue) and A4 (in orange) and their amplitude spectra (Figure 6b). In Figure 6b, thin lines represent raw spectra and thick lines represent spectra smoothed using Konno-Omachi smoothing with a bandwidth $b = 40$ [Konno and Ohmachi, 1998] which are then used to compute spectral ratios (Figure 6c). As expected, the signal simulated at station E1/BOLL has a long duration because of wave reverberations in the basin (only the first 11 s of the signals are shown in Figure 6, but reverberations generate non-negligible amplitudes—of the order of about 10% of the maximum peak amplitude—over the entire 60-s duration of the simulation). The signal simulated at station A4, on the other hand, does not correspond to our expectations for a reference rock site precisely because it also contains late reverberations of similar, non-negligible amplitudes as station E1. Apart from a high-amplitude arrival at about 4 s, probably due to a vertical body-wave reflection in the basin, the ground motion in E1 does not seem much amplified compared to the one in A4. In the Fourier domain (Figure 6b), the amplitude spectra at stations E1 and A4 differ mostly by the frequencies of their respective peaks at low frequencies: around 0.5 Hz for E1 (blue line in Figure 6b), which corresponds well to the 1D resonance of the basin [Gélis et al., 2022], and around 1 Hz for A4 (orange line in Figure 6b), which rather corresponds to the 1D resonance of the shallow low-velocity layer extrapolated outside the actual extent of the basin (if we consider a relation between resonance frequency f_{res} and layer thickness h of the form $f_{\text{res}} = V_S^{\text{avg}}/(4h)$, with V_S^{avg} the average V_S velocity in the layer).

As a consequence, we cannot consider the signal simulated at A4 as a reference for estimating amplification via spectral ratios: the resulting amplification would be dramatically underestimated, especially at frequencies corresponding to the 1D resonance of the shallow low-velocity layer (e.g., 1 Hz, see red curve in Figure 6c). Instead, we consider a deep reference point, located at 10.050 km depth, i.e., at the same distance from the depth at which the plane wave source is injected (5 km) as the free surface in the basin (which has an average elevation of 50 m asl). The seismogram extracted from this deep reference point is time-windowed, such as to retain only the incident plane wave, which has travelled in a homogeneous medium between its injection

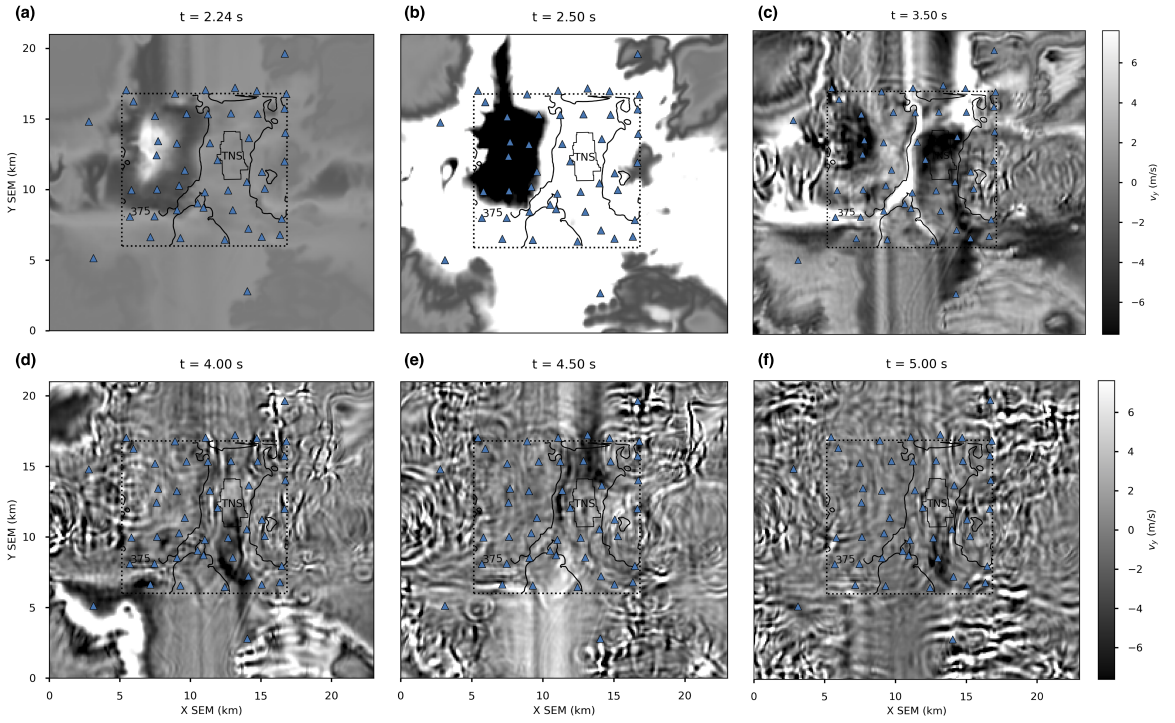

Figure 5. Snapshots of the simulated wavefield (v_y component excited by a vertically-incident SH plane wave polarized in the Y direction) on the free surface at different times. The black contour corresponds to the iso-depth 375 m of the velocity discontinuity between sediments and bedrock, delineating the deepest part of the basin. The dashed line corresponds to the tomographic domain. The full movie of wave propagation is provided in Supplementary Material.

point at 5 km depth and this reference point at 10.050 km depth, therefore yielding a clean signal (green curves in Figure 6). The amplitude spectrum of this windowed signal is then multiplied by 2, which corresponds to the amplitude spectrum of a point that would be located on the free surface. In doing so, we therefore define a reference amplitude spectrum that is equivalent to the theoretical response of a point on the free surface above a homogeneous halfspace that would have the same seismic properties as the deep part of our 3D numerical model (including visco-elastic attenuation, which makes this deep reference spectrum different from the spectrum of the injected source time function) and that is consistent with the wavefield simulated at the free surface (since it is extracted from the simulated wavefields, and not computed separately). We refer to the spectral ratio computed with this deep reference as the amplification function (AF), as opposed to the standard spectral ratio (SSR) computed with a reference point located on the free surface. We have verified that AF and SSR are identical in the case of a surface reference point located above a homogeneous subsurface, and far away from basin edges (clean numerical reference). As a consequence, our numerical amplification functions remain comparable to empirical SSRs computed with respect to a clean empirical reference on the field, which is the case of station A4. Figure 6c shows the resulting amplification functions for station E1 (in blue), with a clear peak around 0.55 Hz corresponding to basin resonance, and for station A4 (in orange), with a peak at 1 Hz, related to the resonance of the artificially extrapolated low-velocity layer. In the following, we will now analyse in more detail these numerical amplification functions, with a particular focus on points located in the basin (since we know that rock sites outside the basin are misrepresented in our model, and therefore may provide less relevant amplification results).

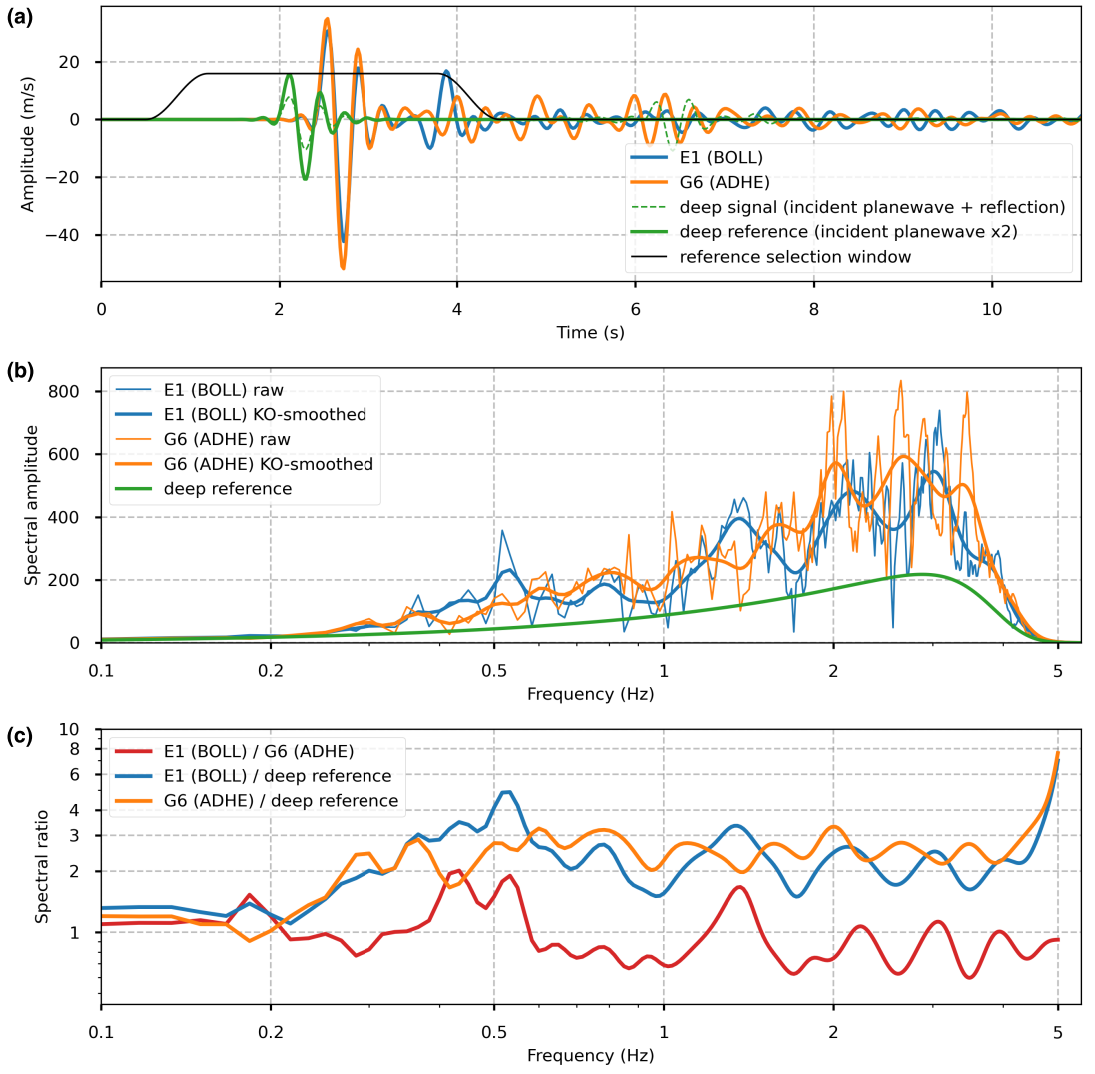

Figure 6. (a) Seismograms simulated at stations E1/BOLL (in blue) and A4 (in orange) and their amplitude spectra (b), for a vertically-incident plane wave source polarized in the Y direction (v_y components are shown). Green curves show the reference signal considered for computing amplification, which corresponds to the recording of the incident plane wave at 10 km depth. (c) Spectral ratios.

4.2. *Numerical amplification*

In this section, we will analyse in three different ways the numerical amplification simulated in our ANSWT model. First, we will compare our numerical amplification functions and their spectral characteristics to empirical SSR measurements based on earthquake data recorded during the deployment of the DARE broadband network. We will exemplify this comparison at two specific locations in the basin, which we have identified as representative of two different signatures that we find of particular interest for our scope, especially when compared to a 1D SH response approximation, which we will also provide as another point of comparison. Second, we will comment on the spatial variability of the numerical amplification predicted in our model, for a few example frequencies. Third, we will have a closer look

at this spatial variability at low frequency, and more precisely at the spatial pattern of the (mis)match between our numerical amplification and two empirical amplification estimations based on earthquake and noise data.

4.2.1. *Local comparison of numerical amplification with earthquake-based SSR and 1D amplification*

Figure 7 shows the amplification at stations E1 (a) and D0 (b) as a function of frequency (see Figure 1 for the location of these two stations). Purple lines represent the empirical, earthquake-based SSR computed with respect to reference station A4 and their uncertainties (purple dashed lines). A catalog of these empirical SSR for all stations of the DARE broadband network is provided in Supplementary Material, together with details on the computation of these SSR. The green line corresponds to the SH amplification computed in a 1D model extracted from the 3D model below the station of interest (right panels), using the *gpsh* function of the Geopsy software [Wathelet et al., 2020]. The numerical amplification of the horizontal component (AF_H) computed in the 3D tomographic model is shown as dark blue and red dashed lines for vertically-incident plane wave sources polarized in the E–W (PW_X) and N–S (PW_Y) directions, respectively. The set of grey curves corresponds to the amplification of the horizontal component for plane wave sources polarized in different directions (PW_θ, with θ the polarization azimuth), showing the variability of the amplification with respect to source polarization. These curves are obtained by a linear combination of the two wavefields simulated for plane wave sources polarized in the X and Y directions, in order to reproduce, by linearity of the wave equation with respect to the source, the wavefield generated by a plane wave source polarized in any given direction.

The two stations considered in Figure 7, E1 and D0, exhibit two different amplification patterns that can be linked to their respective locations in the basin, and eventually to the corresponding subsurface structures. Below station E1, we know from previous studies that the paleo-canyon is quite deep [about 560 m according to Gélis et al., 2022], and that a thick pile of Pliocene sediments probably lies directly on top of the hard substratum of Urgonian limestones. This results in a significant observed amplification (up to 7 ± 2) above the main resonance frequency of the canyon (about 0.5 Hz for this location/depth, according to Gélis et al. [2022]. Here it is worth noting that the numerical results do not retrieve this observed level of amplification (with a maximum of about 4 ± 1), nor its broadband character: while the observed amplification exhibits a plateau above 0.55 Hz, which is commonly interpreted as the signature of 3D wave propagation effects [due, in particular, to laterally propagating surface waves generated at the edges of the basin, see e.g. Cornou and Bard, 2003, Bindi et al., 2009], the numerical amplification computed from 3D numerical simulations (envelope of gray curves) remains quite close from the 1D resonance peaks predicted in a local 1D model extracted below the considered station (green curve). This suggests that the ANSWT model does not generate significant amounts of laterally propagating surface waves within the basin, which can be easily understood from our observations of the model (Figure 3) and of the wavefield (Figure 4), where we already noted the lack of clear lateral basin edges, resulting in a lack of wave trapping within the basin. Nevertheless, the numerical amplification computed in the 3D ANSWT model is not strictly identical to a 1D amplification. In particular, it exhibits non-negligible variations with respect to source polarization for some frequencies, including in the vicinity of the main resonance frequency (0.45–0.55 Hz). While this source-related variability would probably deserve a more detailed investigation [e.g., Maufroy et al., 2017], it is a clear indication that the ANSWT model well includes some 3D characteristics of the basin that cannot be captured by purely 1D approximations. Moreover, it should also be noted that the local 1D profile extracted from the 3D ANSWT model below station E1 and the associated 1D amplification (green curves in Figure 7a) are very similar to the results obtained by Gélis et al. [2022, their figure 8d] for this location. This suggests that the ANSWT well played its role in terms of local V_S estimation, just as well as the local Ambient Vibration Analysis performed by Gélis et al. [2022], but with the added value of imaging the lateral variations of the 1D V_S structure in the basin.

Regarding station D0, it is located at the border of the Lapalud island, where the subsurface has a complex structure due to the presence of the late lower Cretaceous units in between the Pliocene

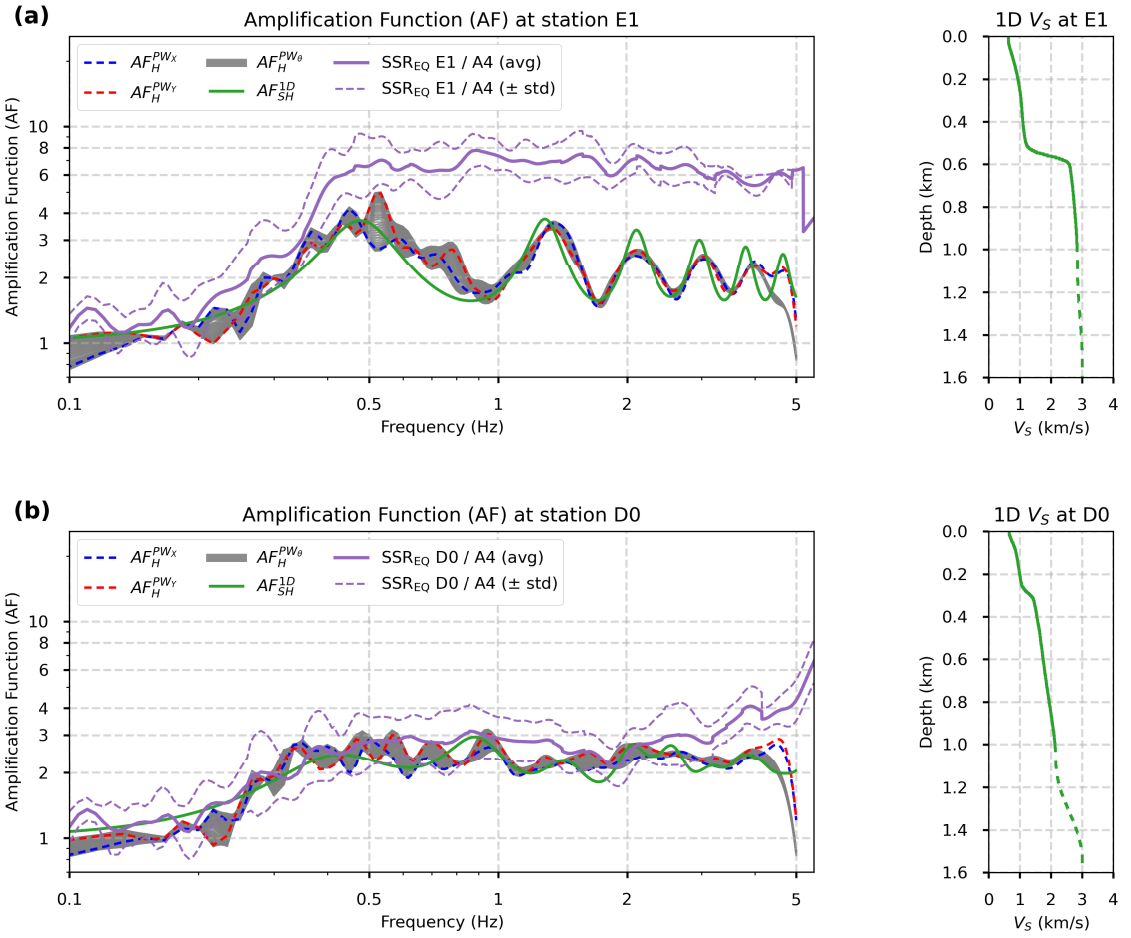

Figure 7. Amplification spectra at stations E1 (a) and D0 (b). Dark blue and red dashed lines: numerical amplification of the horizontal component (AF_H) in the 3D tomographic model, for vertically-incident plane wave sources polarized in the E–W (PW_X) and N–S (PW_Y) directions, respectively. Grey curves: amplification of the horizontal component for plane wave sources polarized in different directions (PW_θ). Green line: 1D SH amplification (AF_{SH}^{1D}) computed in a 1D model extracted from the 3D model below the station of interest (right panels, where the dashed line below 1 km depth corresponds to the part of the model that is not constrained by ANSWT and is extrapolated to a constant V_S = 3000 m/s). Purple lines: empirical, earthquake-based SSR_EQ computed with respect to reference station A4, and their uncertainties (purple dashed lines). Note that uncertainties do not appear for high frequencies where the SSR is often constrained by a single event, which does not enable to compute a standard deviation (see Supplementary Material for details).

sediments and the Urgonian bedrock [Bagayoko, 2021, Do Couto et al., 2024]. These units are made of sandstones and marls, and have intermediary seismic velocities compared to the Pliocene and Urgonian lithologies, which in the V_S profiles is represented by a smooth gradient of velocity progressively increasing with depth. This results in a lower level of observed amplification (up to 3 ± 0.5). This amplification also displays a broadband character as a function of frequency, but for a different reason as previously: in this case, the amplification plateau above 0.5 Hz is due to the smooth gradient of increasing

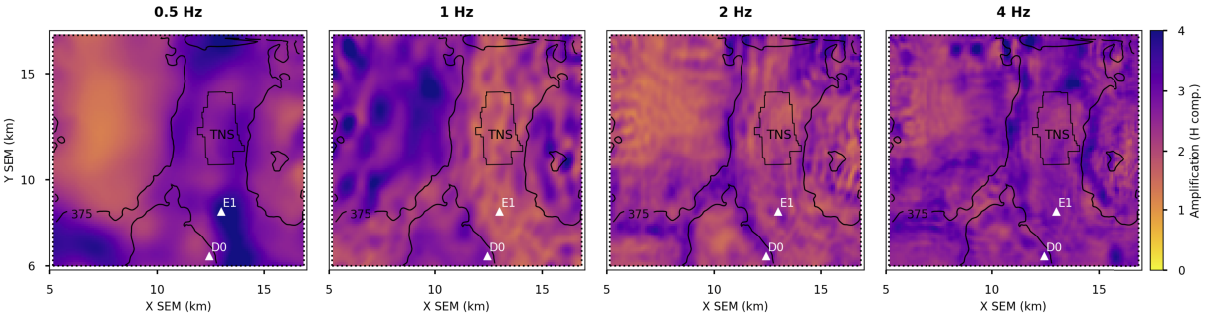

Figure 8. Maps of the amplification of the horizontal component at 0.5, 1, 2, and 4 Hz, for a vertically-incident SH plane wave polarized in the Y direction (N–S). The black line represents the iso-375-m depth contour of the interface between the two layers considered in the 1D depth inversion. Margins outside the tomographic domain have been masked.

velocity with depth, and not to 3D wave propagation effects (since 1D amplification also shows this broadband character). Interestingly, both 3D and 1D numerical results show a good agreement with the observations in this case, which again suggests that the amplification is not dominated by 3D propagation effects at this location, but by 1D vertical resonance, so that the 1D approximation is sufficient to explain the observations. It should be noted, however, that this agreement is only possible because the tomography well played its role in terms of (3D) characterization of the local (1D) velocity structure.

4.2.2. *Spatial variability of the numerical amplification*

One of the interests of numerical simulations is to provide access to the spatial variability of the amplification in the basin. Figure 8 shows amplification maps at different frequencies. At 0.5 Hz, most of the amplification corresponds to the deepest part of the basin (delineated by the iso-375-m depth contour of the interface between sediments and bedrock), as expected. At higher frequencies, however, amplification does not behave as expected. At 1 Hz, amplification is larger outside the basin than inside, which is likely due to the resonance of the shallow 200-m-thick low-velocity layer at this frequency. At 2 Hz, the amplification pattern is less clear but seems to concern mainly the slopes of the basin. At 4 Hz, results simply do not seem to be relevant, and are probably dominated by the topographic effects identified in the wavefield snapshots (Figure 5). In the following, we focus our analysis to the low-frequency part of the amplification, in the frequency range 0.3–0.7 Hz, related to the deepest parts of the basin (note however that this frequency range is wide enough to cover a relatively wide range of canyon depths, from about 300 m to 700 m). More specifically, we propose to look at the ratio between our numerical amplification and the observed amplification in this frequency range, for all broadband stations (earthquake-based SSR_{EQ}, Figure 9) and all nodes (noise-based SSRn, Figure 10).

4.2.3. *Spatial variability of the misfit between numerical amplification and observed SSR*

Comparison to earthquake-based SSR_{EQ}. Figure 9 shows the spatial distribution, for all broadband stations, of the mean ratio between our numerical amplification AF_{num} (log-average of the gray curves in Figure 7) and the observed earthquake-based amplification SSR_{EQ} with respect to reference station A4 in the frequency range 0.3–0.7 Hz. According to the logarithmic color scale, dark red and dark blue colors represent stations where the numerical amplification underestimate and overestimate the observations by a factor of 4, respectively. Empty triangles correspond to stations for which we could not estimate empirical SSR_{EQ}, due to an insufficient signal-to-noise ratio of the earthquake recordings or to a lack of data (see Supplementary Material for details). The dashed-dotted line represents the surface imprint of the canyon rim, as interpreted from geological mapping (Figure 1), which provides a visual

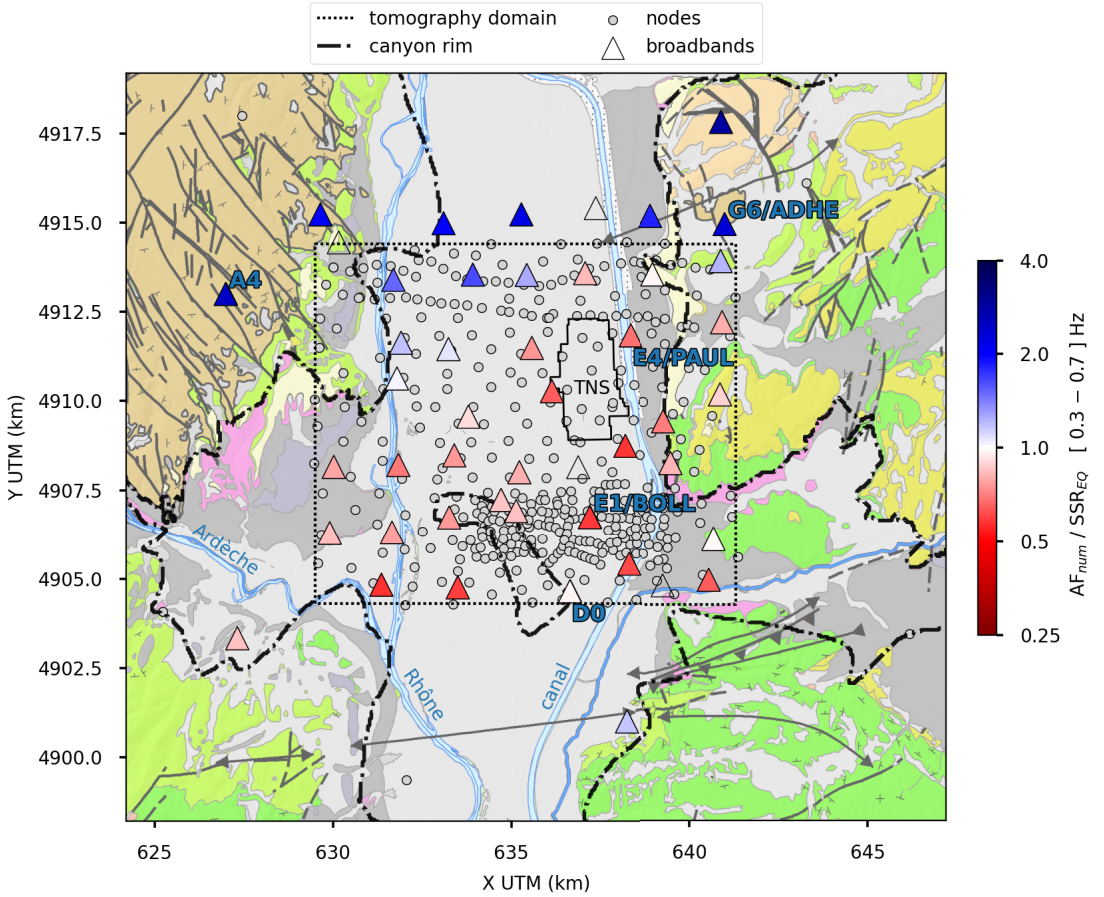

Figure 9. Mean ratio between numerical amplification and earthquake-based SSR_{EQ} between 0.3 and 0.7 Hz (note the logarithmic color scale).

guide to locate the results with respect to the basin. The dotted line delimits the domain constrained by the tomography, outside which laterally-invariant extrapolation is performed (Figure 3) and makes the results hardly interpretable, in particular at rock sites (e.g., A4, G6/ADHE). Within the tomography domain, however, the ratio between numerical and observed amplification is always comprised between 0.5 and 2, and is close to 1 for some stations. This suggests that the ANSWT model, although not perfect and still improvable, is able to explain, in some extent, the amplification observed in this low-frequency range, and in various parts of the basin (where, incidentally, the frequency range 0.3–0.7 Hz may include different amplification phenomena depending on the location in the basin and on the underlying/surrounding geological structures). In order to look in more detail at the spatial pattern of the (mis)match between numerical and observed amplification, we now propose to look at the ratio between numerical and noise-based amplification.

Comparison to noise-based SSRn. Similarly to Figure 9, Figure 10 shows the spatial distribution, for all nodes, of the mean ratio between our numerical amplification AF_{num} and the observed noised-based amplification SSRn in the frequency range 0.3–0.7 Hz, in which we consider SSRn estimations to be reliable [Gisselbrecht et al., 2023]. Indeed, several studies have reported a good agreement between noise-based SSRn and earthquake-based SSR in this frequency band [e.g., Lermo and Chávez-García, 1994, Bard, 1999], mostly because distant sources dominate the ambient noise wavefield at these frequencies [e.g., Bonnefoy-Claudet et al., 2006]. In order to further mitigate undesired effects of local

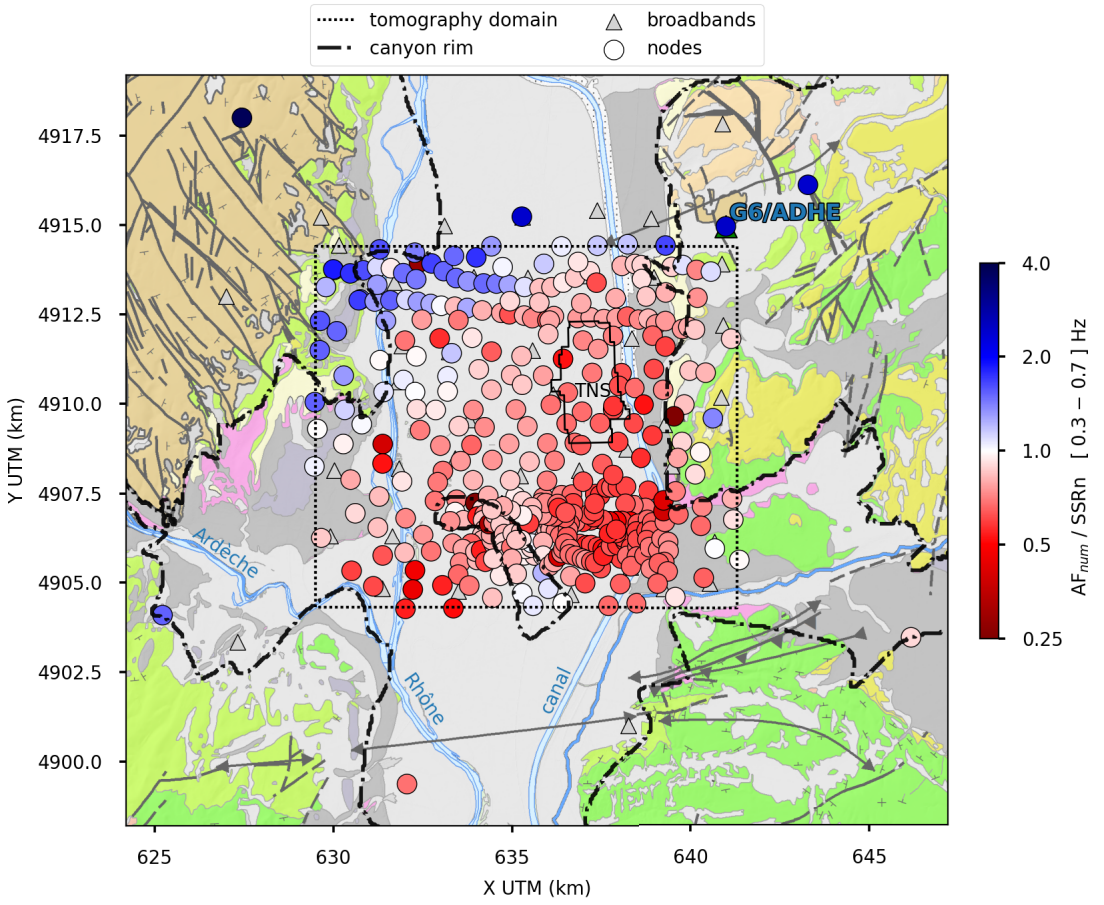

Figure 10. Mean ratio between numerical amplification and noise-based SSRn [Gisselbrecht et al., 2023] between 0.3 and 0.7 Hz (note the logarithmic color scale).

and transient low-frequency sources (such as wind), Gisselbrecht et al. [2023] computed these SSRn using short time windows (1 min) restricted to quieter nighttime recordings. Note also that these empirical SSRn have been estimated with respect to a node co-located with reference station G6/ADHE. The similarities between Figures 9 and 10 in the vicinity of broadband stations suggests that the two empirical estimations, based on earthquake and ambient noise, are overall consistent, and that the choice of the reference station, A4 or G6/ADHE, has very little effect on the results in this low-frequency band, as also suggested by the SSR $\cong$ 1 between the two stations (see Supplementary Material). Thanks to the density of the nodal array, Figure 10 gives a nice spatial view of the (mis)match between empirical and numerical amplification, and enables to look at its spatial pattern in more detail.

In particular, we see again that our numerical amplification over-estimates the observations in the northwesternmost corner of the domain, including at rock sites where we know that Urgonian limestones are outcropping, but also in the north-west of the basin (south-west of Pierrelatte), suggesting that the ANSWT model might over-estimate sediment thickness in this area. In contrast, amplification seems under-estimated in the deepest part of the basin, along the north–south axis of the paleo-Rhône canyon, as well as along the paleo-Ardèche in the south-west of the domain. Knowing that ANSWT provides a similar estimate of the canyon depth at station E1 as AVA [Gélis et al., 2022], this

underestimation could suggest a lack of 3D wave propagation effects in these parts of the model, all the more that they also correspond to regions susceptible to be affected by laterally propagating surface waves generated at basin edges.

Interestingly, one of the areas where the match between numerical and empirical amplification seems the most satisfying corresponds to the Lapalud island in the South of the domain. Again, this suggests that the ANSWT model is successful in estimating the subsurface velocity structure in this region, despite its relative complexity due to the presence of heterogeneous post-Urgonian Cretaceous units. It also suggests that local 1D effects may be dominant in the amplification at this location, which may be intuitively understood as the fact that the top of the island itself is not affected by waves that are diffracted by (/away from) the island. The ratio between numerical and noise-based amplification is also quite satisfying north-west from Lapalud, where the basin is shallower [Do Couto et al., 2024], as well as on its eastern margin, which suggests that the post-Urgonian Cretaceous and Tertiary units that form this margin do not have the same properties as the rock sites located on Urgonian outcrops (A4, G6/ADHE), and experience some amplification compared to these hard rock sites. These lateral variations of bedrock properties, rarely taken into account in numerical studies, are important to consider, as they affect not only the local response, and thus the choice of a reference for SSR calculation [Steidl et al., 1996], but also the impedance contrast at the sediment/bedrock interface.

5. Discussion

The aim of this paper was to investigate if and how a standard ANSWT model could be used for the numerical estimation of seismic amplification in sedimentary basins. In light of our results, we can state that ANSWT is surely a method of choice for depicting the large-scale velocity structure of the subsurface, but that a standard, purely data-driven, ANSWT workflow alone is visibly not sufficient to generate seismic models that well reproduce the observed amplification in complex sedimentary basins where 3D wave propagation effects are significant.

In particular, we clearly saw the consequences of the lack of well-marked lateral basin edges, and thus of laterally propagating surface waves in the basin. There are several reasons for this lack of shallow lateral contrasts in the model, in relation to the sensitivity and resolution capacity of the surface wave data used for tomography. First, the upper layers of the subsurface (first 50 m in the basin, where the minimum wavelength is about 100 m; first 200 m outside the basin, where the minimum wavelength is about 400 m) are poorly constrained by our measurements of the dispersion of fundamental Love and Rayleigh modes in the considered frequency range (0.3–5 Hz). Second, due to this weak data sensitivity and to the relative weight of regularization (smoothing), there is a smearing of low-velocity anomalies from the center to the edges of the basin at the 2D tomography stage, all the more that the edges of the model are less well constrained by data coverage, given the imprint of the array. This understanding is important because it gives precise clues about how to improve future ANSWT applications for site effect assessment in sedimentary basins. In terms of acquisition design, it suggests that the seismic array should probably extend more outside the basin, in order to better constrain basin edges and surrounding bedrock properties. More generally, it suggests that we should seek more information about basin edges, either in the seismic data themselves or elsewhere.

In this preliminary study, indeed, we deliberately adopted a purely data-driven ANSWT approach, in order to assess its potential and limitations. But if surface wave data alone are not sufficient to generate sharp lateral variations, then we should turn to other sources of information which we first need to collect and then to integrate in the tomographic process in order to constrain our models. In our case, the surface imprint of the Messinian paleo-canyon is known from geological mapping (Figure 1), field campaigns, and borehole data. Besides, active seismic profiles are also available in the area. The interpretation of these profiles (time-domain migrated sections), together with geological field campaigns and borehole data, allows for a high-resolution identification of geological horizons [Bagayoko, 2021, Do Couto et al., 2024]. These horizons, however, cannot be considered as a strict ground truth, because the inference of their depth depends on P-wave velocity values assumed for time-to-depth conversion. Moreover, these geological horizons do not necessarily correspond to seismic impedance contrasts, as discussed

in Froment et al. [2022a], and need to be interpolated over the entire domain of interest. Nevertheless, these horizons could be used as prior information in order to constrain the geometry of subsurface layers in the tomographic process. This will be the subject of further work following directly from this study, which enables us to pinpoint more precisely where this prior information should be introduced: namely both at the 2D tomography stage, where lateral coherency could be enforced using these geological constraints rather than blind smoothing, and at the 1D inversion stage, where interface depths could be constrained directly.

Finally, the computation of H/V ratios from the ambient noise data recorded by the dense nodal array also results in the estimation of an interface related to an impedance contrast that controls seismic amplification, and this information could also be worth taken into account in the tomography and in our simulations. In practice, however, how to take this interface into account is not completely obvious, given that (i) the interpretation of this interface in terms of depth also implies some assumption about V_S values in the sediments, (ii) this interface may not correspond to geological stratigraphic horizons, or not always to the same horizons, and may even not be continuous [Froment et al., 2022a].

In all these cases, the consideration of such prior information in the tomographic process would be best handled in the frame of probabilistic methods, such as trans-dimensional tomography [e.g., Bodin et al., 2012, Galetti et al., 2017] or Bayesian approaches [e.g., Lu et al., 2020, Nouibat et al., 2022]. This would at least require the use of state-of-the-art imaging techniques, and probably some dedicated methodological developments as well, in particular to properly evaluate and propagate uncertainties throughout the whole ANSWT workflow, starting from reliable prior data uncertainty related to dispersion curve picking, and ending with robust posterior uncertainties on model parameters, which could then be used in our numerical simulations to explore the variability of the predicted amplification within the range of model uncertainties. As a direct perspective of this work, we are currently investigating such probabilistic methods in order to improve our tomographic model of the Tricastin basin, and explore the sensitivity of our numerical amplification to input data and model features, within realistic uncertainty ranges. Another important—and yet open—question related to data and model uncertainties concerns the frequency range in which we can reliably predict seismic amplification, based on a certain set of informations to design our numerical models.

Finally, the lack of 3D characteristics in the ANSWT model likely comes in part from the 1D approximation which the standard 2-step ANSWT procedure relies on for interpreting surface-wave dispersion in terms of velocity structure as a function of depth. This assumption could be overcome by using other imaging techniques, such as 1-step 3D ANSWT [e.g., Zhang et al., 2018] or full waveform inversion [FWI, e.g., Virieux and Operto, 2009, Lu et al., 2020]. FWI, in particular, would enable one to fully consider 3D wave propagation, as well as higher-mode surface waves, and eventually body waves (if present in the cross-correlations), that would bring additional information on the impedance contrast between sediments and bedrock, and potentially provide higher-resolution models with sharper lateral variations associated to basin edges. We would recommend the investigation of such waveform tomography techniques for building seismic models for site effect assessment as a long-term research track, keeping in mind that FWI applications in complex subsurface settings are always challenging, and that noise-based FWI is still the subject of current developments and raises challenges of its own, in particular regarding the effect of noise sources on parameter estimation [e.g., Tromp et al., 2010, Säger et al., 2018]. Standard ANSWT models such as the one considered in this study could be used as initial models for further waveform inversion approaches.

6. Conclusion

In this paper, we have used a 3D V_S model of a complex sedimentary basin built via a standard ANSWT workflow to perform numerical simulations of seismic wave propagation, and compute ground motion amplification within the basin. The tomographic model well depicts the main geological structures of the basin via its lateral variations of seismic velocities at depth, but it also suffers from limitations related to surface wave sensitivity and resolution capabilities, especially in its shallow part. In particular, this ANSWT model lacks of clear basin edges in order to efficiently trap seismic waves and generate significant

amounts of surface waves susceptible to propagate laterally in the basin. As a result, the numerical amplification predicted in this ANSWT model presents some 3D characteristics, such as non-negligible variations with respect to the polarization of the incident seismic wave, but also lacks of other expected 3D features, such as the broadband signature of observed amplification at locations affected by laterally propagating surface waves coming from basin edges. On the other hand, in basin sites where a 1D response is sufficient to explain the local amplification, the numerical amplification predicted in the ANSWT model show a good agreement with the observations, including in complex regions of the basin where lateral variations of the deeper subsurface velocity structure must be taken into account in order to reproduce the local 1D response. The tomography also enables one to image lateral variations of bedrock properties which are rarely taken into account in numerical site effect estimations. These observations still concur in considering noise-based tomography as a promising method for building seismic models for site effect assessment in sedimentary basins, provided we can compensate the lack of data sensitivity to shallow and sharp lateral variations, and improve the reconstruction of basin edges.

Our results therefore show the potential of the approach, while identifying its limitations and giving perspectives for future work, which should aim at considering other imaging paradigms (e.g., noise-based waveform inversion) and at including prior information from other sources of geological and geophysical data into the tomographic process, in order to better constrain the geometry of the basin, in particular its surface boundaries in the shallow subsurface which is poorly constrained by surface-wave data alone.

Declaration of interests

The authors do not work for, advise, own shares in, or receive funds from any organization that could benefit from this article, and have declared no affiliations other than their research organizations.

Data and software availability

The datasets acquired in the frame of the DARE project are freely available via their doi: 10.14470/L27575187372 [Pilz et al., 2021], 10.15778/RESIF.3T2019 [Froment et al., 2023a], and 10.15778/RESIF.XG2020 [Froment et al., 2023b, see also Froment et al., 2022b, for details]. The EFISPEC software [De Martin, 2011] is freely available at https://gitlab.brgm.fr/brgm/efispec3d (last accessed 25 January 2024).

Funding

This work is part of the DARE project (*Dense ARray for site effect Estimation*, https://anr.fr/Projet-ANR-19-CE31-0029, last accessed 25 January 2024), funded by the French National Research Agency (*Agence Nationale pour la Recherche*, ANR, grant number ANR19-CE31-0029) and by the German Research Foundation (*Deutsche Forschungsgemeinschaft*, DFG, project number 431362334). ISTerre is part of Labex OSUG@2020 (ANR10 LABX56).

Numerical simulations have been performed with the EFISPEC software developed at BRGM [De Martin, 2011, https://gitlab.brgm.fr/brgm/efispec3d, last accessed 25 January 2024]. This work was granted access to the HPC resources of TGCC under the allocation 2022-gen13461 made by GENCI, and of the GRICAD infrastructure (https://gricad.univ-grenoble-alpes.fr, last accessed 25 January 2024), which is supported by Grenoble research communities.

Acknowledgements

The geological context of the studied area was discussed and completed with the help of Damien Do Couto, Nanaba Bagayoko, Ludovic Mocochain and Jean-Loup Rubino. We warmly acknowledge them.

Supplementary data

Supporting information for this article is available on the journals website under https://doi.org/10.5802/crgeos.243 or from the author.

References

Bagayoko, N. (2021). *Intégration de données de sismiques réflexion et de données géologiques dans un modèle structural 3D du canyon messinien du Rhône : Etude du site du Tricastin*. Master's thesis, Sorbonne Université.

Bard, P.-Y. (1999). Microtremor measurements: A tool for site effect estimation? In Irikura, Kudo, Okada, and Sasatani, editors, *Second International Symposium on the Effects of Surface Geology on Seismic Motion, Yokohama, Japan*, volume 3, pages 1251–1279. Balkema, Rotterdam.

Barmin, M. P., Ritzwoller, M. H., and Levshin, A. L. (2001). A fast and reliable method for surface wave tomography. In Levshin, A. L. and Ritzwoller, M. H., editors, *Monitoring the Comprehensive Nuclear-Test-Ban Treaty: Surface Waves*, Pageoph Topical Volumes, pages 1351–1375. Birkhäuser, Basel.

Bindi, D., Luzi, L., Parolai, S., Di Giacomo, D., and Monachesi, G. (2011). Site effects observed in alluvial basins: the case of Norcia (Central Italy). *Bull. Earthq. Eng.*, 9(6), 1941–1959.

Bindi, D., Parolai, S., Cara, F., Di Giulio, G., Ferretti, G., Luzi, L., Monachesi, G., Pacor, F., and Rovelli, A. (2009). Site amplifications observed in the Gubbio Basin, Central Italy: Hints for lateral propagation effects. *Bull. Seismol. Soc. Am.*, 99(2A), 741–760.

Bodin, T., Sambridge, M., Tkalcic, H., Arroucau, P., Gallagher, K., and Rawlinson, N. (2012). Transdimensional inversion of receiver functions and surface wave dispersion. *J. Geophys. Res.: Solid Earth*, 117(B2), article no. B02301.

Bonnefoy-Claudet, S., Cotton, F., and Bard, P.-Y. (2006). The nature of noise wavefield and its applications for site effects studies: a literature review. *Earth-Sci. Rev.*, 79(3), 205–227.

Borcherdt, R. D. (1970). Effects of local geology on ground motion near San Francisco Bay. *Bull. Seismol. Soc. Am.*, 60(1), 29–61.

Boué, P., Denolle, M., Hirata, N., Nakagawa, S., and Beroza, G. C. (2016). Beyond basin resonance: characterizing wave propagation using a dense array and the ambient seismic field. *Geophys. J. Int.*, 206(2), 1261–1272.

Boxberger, T., Picozzi, M., and Parolai, S. (2011). Shallow geology characterization using Rayleigh and Love wave dispersion curves derived from seismic noise array measurements. *J. Appl. Geophys.*, 75(2), 345–354.

Boxberger, T., Pilz, M., and Parolai, S. (2017). Shear wave velocity versus quality factor: results from seismic noise recordings. *Geophys. J. Int.*, 210(2), 660–670.

Brocher, T. M. (2005). Empirical relations between elastic wavespeeds and density in the Earth's crust. *Bull. Seismol. Soc. Am.*, 95(6), 2081–2092.

Campillo, M., Gariel, J. C., Aki, K., and Sánchez-Sesma, F. J. (1989). Destructive strong ground motion in Mexico city: source, path, and site effects during great 1985 Michoacán earthquake. *Bull. Seismol. Soc. Am.*, 79(6), 1718–1735.

Chaljub, E., Maufroy, E., Moczo, P., Kristek, J., Hollender, F., Bard, P.-Y., Priolo, E., Klin, P., De Martin, F., Zhang, Z., Zhang, W., and Chen, X. (2015). 3-D numerical simulations of earthquake ground motion in sedimentary basins: testing accuracy through stringent models. *Geophys. J. Int.*, 201(1), 90–111.

Chaljub, E., Moczo, P., Tsuno, S., Bard, P.-Y., Kristek, J., Käser, M., Stupazzini, M., and Kristeková, M. (2010). Quantitative comparison of four numerical predictions of 3D ground motion in the Grenoble valley, France. *Bull. Seismol. Soc. Am.*, 100(4), 1427–1455.

Chávez-García, F., Raptakis, D., Makra, K., and Pitilakis, K. (2000). Site effects at Euroseistest–II. Results from 2D numerical modeling and comparison with observations. *Soil Dyn. Earthq. Eng.*, 19(1), 23–39.

Chmiel, M., Mordret, A., Boué, P., Brenguier, F., Lecocq, T., Courbis, R., Hollis, D., Campman, X., Romijn, R., and Van der Veen, W. (2019). Ambient noise multimode Rayleigh and love wave tomography to determine the shear velocity structure above the Groningen gas field. *Geophys. J. Int.*, 218(3), 1781–1795.

Cornou, C. and Bard, P.-Y. (2003). Site-to-bedrock over 1D transfer function ratio: an indicator of the proportion of edge-generated surface waves? *Geophys. Res. Lett.*, 30(9), article no. 1453.

Cushing, E. M., Hollender, F., Moiriat, D., Guyonnet-Benaize, C., Theodoulidis, N., Pons-Branchu, E., Sépulcre, S., Bard, P.-Y., Cornou, C., Dechamp, A., Mariscal, A., and Roumelioti, Z. (2020). Building a three dimensional model of the active Plio-Quaternary basin of Argostoli (Cephalonia Island, Greece): an integrated geophysical and geological approach. *Eng. Geol.*, 265, article no. 105441.

Dahlen, F. A. and Tromp, J. (1998). *Theoretical Global Seismology*. Princeton University Press, Princeton, NJ.

De Martin, F. (2011). Verification of a spectral-element method code for the Southern California earthquake center LOH.3 viscoelastic case. *Bull. Seismol. Soc. Am.*, 101(6), 2855–2865.

De Martin, F., Chaljub, E., Thierry, P., Sochala, P., Dupros, F., Maufroy, E., Hadri, B., Benaichouche, A., and Hollender, F. (2021). Influential parameters on 3-D synthetic ground motions in a sedimentary basin derived from global sensitivity analysis. *Geophys. J. Int.*, 227(3), 1795–1817.

Do Couto, D., Cushing, E. M., Mocochain, L., Rubino, J.-L., Miquelis, F., Hanot, F., Froment, B., Gélis, C., Camus, H., Bagayoko, N., and Bellier, O. (2024). Messinian canyons morphology of the Rhône and Ardèche rivers (south-east France): new insights from seismic profiles. *Bull. Soc. Géol. Fr.*, 195.

Dziewonski, A., Bloch, S., and Landisman, M. (1969). A technique for the analysis of transient seismic signals. *Bull. Seismol. Soc. Am.*, 59(1), 427–444.

Froment, B., Cushing, E. M., Gélis, C., Bagayoko, N., Beauprêtre, S., Boué, P., Do Couto, D., Magnin, O., Mocochain, L., Mordret, A., Rubino, J.-L., and Tourette, A. (2022a). First 3D characterization of the Rhône Messinian Canyon in the Tricastin area from complementary geophysical approaches. In *3rd European Conference on Earthquake Engineering & Seismology, Bucharest (Romania)*. HAL-Id: irsn-03962474.

Froment, B., Cushing, E. M., Gélis, C., Gisselbrecht, L., Beauprêtre, S., Tourette, A., and RESIF (2023a). France 2019, Nodal seismic array in the Rhône Valley, DARE project - Preliminary campaign [Data set]. RESIF - Réseau Sismologique et géodésique Français.

Froment, B., Cushing, E. M., Gélis, C., Gisselbrecht, L., Beauprêtre, S., Tourette, A., and RESIF (2023b). France 2020, Dense nodal seismic array in the Rhône Valley, DARE project [Data set]. RESIF - Réseau Sismologique et géodésique Français.

Froment, B., Olivar-Castaño, A., Ohrnberger, M., Gisselbrecht, L., Hannemann, K., Cushing, E. M., Boué, P., Gélis, C., Haendel, A., Pilz, M., Hillmann, L., Barbaux, O., Beauprêtre, S., Bouzat, G., Chaljub, E., Cotton, F., Lavoué, F., Stehly, L., Zhu, C., Magnin, O., Métral, L., Mordret, A., Richet, Y., and Tourette, A. (2022b). Complementary dense datasets acquired in a low-to-moderate seismicity area for characterizing site effects: application in the French Rhône valley. *Seismol. Res. Lett.*, 94(1), 531–547.

Galetti, E., Curtis, A., Baptie, B., Jenkins, D., and Nicolson, H. (2017). Transdimensional love-wave tomography of the British Isles and shear-velocity structure of the East Irish Sea Basin from ambient-noise interferometry. *Geophys. J. Int.*, 208(1), 36–58.

Gardner, G., Gardner, L., and Gregory, A. (1974). Formation velocity and density—the diagnostic basics for stratigraphic traps. *Geophysics*, 39(6), 770–780.

Gélis, C., Cauchie, L., Cushing, E. M., Froment, B., Franco, S., Jomard, H., Moiriat, D., Provost, L., Sariguzel, B., and Tebib, H. (2022). Estimation of the local seismic amplification on an industrialized site in the French Rhône valley. *Pure Appl. Geophys.*, 179(6), 2119–2145.

Gisselbrecht, L., Froment, B., Boué, P., and Gélis, C. (2023). Insights into the conditions of application of noise-based spectral ratios in a highly industrialized area: a case study in the French Rhône Valley. *Geophys. J. Int.*, 234(2), 985–997.

Graves, R. W., Pitarka, A., and Somerville, P. G. (1998). Ground-motion amplification in the Santa Monica area: Effects of shallow basin-edge structure. *Bull. Seismol. Soc. Am.*, 88(5), 1224–1242.

Haskell, N. A. (1953). The dispersion of surface waves on multilayered media. *Bull. Seismol. Soc. Am.*, 43(1), 17–34.

Kawase, H. (1996). The cause of the damage belt in Kobe: "the basin-edge effect," constructive interference of the direct S-wave with the basin-induced diffracted/Rayleigh waves. *Seismol. Res. Lett.*, 67, 25–34.

Komatitsch, D., Liu, Q., Tromp, J., Süss, P., Stidham, C., and Shaw, J. H. (2004). Simulations of ground motion in the Los Angeles basin based upon the spectral-element method. *Bull. Seismol. Soc. Am.*, 94(1), 187–206.

Komatitsch, D. and Vilotte, J. P. (1998). The spectral element method: an efficient tool to simulate the seismic response of 2D and 3D geological structures. *Bull. Seismol. Soc. Am.*, 88, 368–392.

Konno, K. and Ohmachi, T. (1998). Ground-motion characteristics estimated from spectral ratio between horizontal and vertical components of microtremor. *Bull. Seismol. Soc. Am.*, 88(1), 228–241.

Ktenidou, O.-J., Chávez-García, F.-J., Raptakis, D., and Pitilakis, K. D. (2016). Directional dependence of site effects observed near a basin edge at Aegion, Greece. *Bull. Earthq. Eng.*, 14(3), 623–645.

Lebrun, B., Hatzfeld, D., and Bard, P. Y. (2001). Site effect study in urban area: Experimental results in

Grenoble (France). *Pure Appl. Geophys.*, 158, 2543–2557.

Lermo, J. and Chávez-García, F. J. (1994). Are microtremors useful in site response evaluation? *Bull. Seismol. Soc. Am.*, 84(5), 1350–1364.

Levshin, A. L., Yanovskaya, T. B., Lander, A. V., Bukchin, B. G., Barmin, M. P., Ratnikova, L. I., and Its, E. N. (1989). *Seismic Surface Waves in a Laterally Inhomogeneous Earth*, volume 149. Springer Netherlands, Dordrecht.

Lu, Y., Stehly, L., Brossier, R., Paul, A., and the AlpArray Working Group (2020). Imaging Alpine crust using ambient noise wave-equation tomography. *Geophys. J. Int.*, 222(1), 69–85.

MacQueen, J. (1967). Some methods for classification and analysis of multivariate observations. In *Proceedings of the Fifth Berkeley Symposium on Mathematical Statistics and Probability, Oakland, CA, USA*, volume 1, pages 281–297.

Manakou, M., Raptakis, D., Chávez-García, F., Apostolidis, P., and Pitilakis, K. (2010). 3D soil structure of the Mygdonian basin for site response analysis. *Soil Dyn. Earthq. Eng.*, 30(11), 1198–1211.

Matsushima, S., Hirokawa, T., De Martin, F., Kawase, H., and Sánchez-Sesma, F. J. (2014). The effect of lateral heterogeneity on horizontal-to-vertical spectral ratio of microtremors inferred from observation and synthetics. *Bull. Seismol. Soc. Am.*, 104(1), 381–393.

Maufroy, E., Chaljub, E., Hollender, F., Bard, P. Y., Kristek, J., Moczo, P., De Martin, F., Theodoulidis, N., Manakou, M., Guyonnet-Benaize, C., Hollard, N., and Pitilakis, K. (2016). 3D numerical simulation and ground motion prediction: verification, validation and beyond–Lessons from the E2VP project. *Soil Dyn. Earthq. Eng.*, 91, 53–71.

Maufroy, E., Chaljub, E., Hollender, F., Kristek, J., Moczo, P., Klin, P., Priolo, E., Iwaki, A., Iwata, T., Etienne, V., De Martin, F., Theodoulidis, N. P., Manakou, M., GuyonnetBenaize, C., Pitilakis, K., and Bard, P. Y. (2015). Earthquake ground motion in the Mygdonian basin, Greece: The E2VP verification and validation of 3D numerical simulation up to 4 Hz. *Bull. Seismol. Soc. Am.*, 105(3), 1398–1418.

Maufroy, E., Chaljub, E., Theodoulidis, N. P., Roumelioti, Z., Hollender, F., Bard, P.-Y., de Martin, F., Guyonnet-Benaize, C., and Margerin, L. (2017). Source-related variability of site response in the Mygdonian Basin (Greece) from accelerometric recordings and 3D numerical simulations. *Bull. Seismol. Soc. Am.*, 107(2), 787–808.

Michel, C., Edwards, B., Poggi, V., Burjánek, J., Roten, D., Cauzzi, C., and Fäh, D. (2014). Assessment of site effects in alpine regions through systematic site characterization of seismic stations. *Bull. Seismol. Soc. Am.*, 104(6), 2809–2826.

Moiriat, D. (2019). Etude sommaire des propriétés des sols du site de Tricastin. Internal Report 2019-00378, IRSN.

Molinari, I., Argnani, A., Morelli, A., and Basini, P. (2015). Development and testing of a 3D seismic velocity model of the Po Plain sedimentary basin, Italy. *Bull. Seismol. Soc. Am.*, 105(2A), 753–764.

Mordret, A., Landès, M., Shapiro, N. M., Singh, S. C., and Roux, P. (2014). Ambient noise surface wave tomography to determine the shallow shear velocity structure at Valhall: depth inversion with a Neighbourhood Algorithm. *Geophys. J. Int.*, 198(3), 1514–1525.

Nouibat, A., Stehly, L., Paul, A., Schwartz, S., Bodin, T., Dumont, T., Rolland, Y., Brossier, R., Cifalps Team, and AlpArray Working Group (2022). Lithospheric transdimensional ambient-noise tomography of W-Europe: implications for crustal-scale geometry of the W-Alps. *Geophys. J. Int.*, 229(2), 862–879.

Ohori, M., Nobata, A., and Wakamatsu, K. (2002). A comparison of ESAC and FK methods of estimating phase velocity using arbitrarily shaped microtremor arrays. *Bull. Seismol. Soc. Am.*, 92(6), 2323–2332.

Panzera, F., Alber, J., Imperatori, W., Bergamo, P., and Fäh, D. (2022). Reconstructing a 3D model from geophysical data for local amplification modelling: The study case of the upper Rhône valley, Switzerland. *Soil Dyn. Earthq. Eng.*, 155, article no. 107163.

Paolucci, R., Mazzieri, I., and Smerzini, C. (2015). Anatomy of strong ground motion: near-source records and three-dimensional physics-based numerical simulations of the Mw 6.0 2012 May 29 Po Plain earthquake, Italy. *Geophys. J. Int.*, 203(3), 2001–2020.

Perron, V., Gélis, C., Froment, B., Hollender, F., Bard, P.-Y., Cultrera, G., and Cushing, E. M. (2018). Can broad-band earthquake site responses be predicted by the ambient noise spectral ratio? Insight from observations at two sedimentary basins. *Geophys. J. Int.*, 215(2), 1442–1454.

Pilz, M., Cotton, F., Ohrnberger, M., and Froment, B. (2021). DARE: Dense ARray for seismic site effect Estimation. GFZ Data Services. Seismic Network.

Prieto, G. A., Lawrence, J. F., and Beroza, G. C. (2009). Anelastic Earth structure from the coherency of the ambient seismic field. *J. Geophys. Res.: Solid Earth*, 114(B7), article no. B07303.

Roten, D., Fäh, D., Olsen, K. B., and Giardini, D. (2008). A comparison of observed and simulated site response in the Rhône valley. *Geophys. J. Int.*, 173(3), 958–978.

Säger, K., Ermert, L., Boehm, C., and Fichtner, A. (2018). Towards full waveform ambient noise inversion. *Geophys. J. Int.*, 212(1), 566–590.

Sambridge, M. (1999). Geophysical inversion with a Neighbourhood Algorithm–I. Searching for a parameter space. *Geophys. J. Int.*, 138, 479–494.

Shapiro, N. M., Campillo, M., Stehly, L., and Ritzwoller, M. H. (2005). High-resolution surface-wave tomography from ambient seismic noise. *Science*, 307(5715), 1615–1618.

Smerzini, C., Paolucci, R., and Stupazzini, M. (2011). Comparison of 3D, 2D and 1D numerical approaches to predict long period earthquake ground motion in the Gubbio plain, Central Italy. *Bull. Earthq. Eng.*, 9(6), 2007–2029.

Spica, Z., Perton, M., Nakata, N., Liu, X., and Beroza, G. (2017). Site characterization at Groningen gas field area through joint surface-borehole H/V analysis. *Geophys. J. Int.*, 212(1), 412–421.

Stacey, R. (1988). Improved transparent boundary formulations for the elastic-wave equation. *Bull. Seismol. Soc. Am.*, 78(6), 2089–2097.

Steidl, J. H., Tumarkin, A. G., and Archuleta, R. J. (1996). What is a reference site? *Bull. Seismol. Soc. Am.*, 86(6), 1733–1748.

Taborda, R. and Bielak, J. (2013). Ground-motion simulation and validation of the 2008 Chino Hills, California, earthquake. *Bull. Seismol. Soc. Am.*, 103(1), 131–156.

Thompson, M., Wirth, E. A., Frankel, A. D., Renate, H. J., and Vidale, J. E. (2020). Basin amplification effects in the Puget Lowland, Washington, from strong-motion recordings and 3D simulations. *Bull. Seismol. Soc. Am.*, 110(2), 534–555.

Thomson, W. T. (1950). Transmission of elastic waves through a stratified solid medium. *J. Appl. Phys.*, 21(2), 89–93.

Traversa, P., Maufroy, E., Hollender, F., Perron, V., Bremaud, V., Shible, H., Drouet, S., Guéguen, P., Langlais, M., Wolyniec, D., Péquegnat, C., and DousteBacque, I. (2020). RESIF RAP and RLBP dataset of earthquake ground motion in mainland France. *Seismol. Res. Lett.*, 91(4), 2409–2424.

Trinh, P.-T., Brossier, R., Métivier, L., Tavard, L., and Virieux, J. (2019). Efficient time-domain 3D elastic and viscoelastic full-waveform inversion using a spectral-element method on flexible Cartesian-based mesh. *Geophysics*, 84(1), R75–R97.

Tromp, J., Peter, D., Luo, Y., and Hanasoge, S. (2010). Noise cross-correlation sensitivity kernels. *Geophys. J. Int.*, 183(2), 791–819.

van Ginkel, J., Ruigrok, E., and Herber, R. (2019). Assessing soil amplifications in Groningen, the Netherlands. *First Break*, 37(10), 33–38.

Virieux, J. and Operto, S. (2009). An overview of full-waveform inversion in exploration geophysics. *Geophysics*, 74(6), WCC127–WCC152.

Wathelet, M., Chatelain, J.-L., Cornou, C., Di Giulio, G., Guillier, B., Ohrnberger, M., and Savvaidis, A. (2020). Geopsy: a user-friendly open-source tool set for ambient vibration processing. *Seismol. Res. Lett.*, 91(3), 1878–1889.

Xia, J. (2014). Estimation of near-surface shear-wave velocities and quality factors using multichannel analysis of surface-wave methods. *J. Appl. Geophys.*, 103, 140–151.

Xia, J., Miller, R. D., Park, C. B., and Tian, G. (2002). Determining Q of near-surface materials from Rayleigh waves. *J. Appl. Geophys.*, 51(2–4), 121–129.

Zhang, X., Curtis, A., Galetti, E., and de Ridder, S. (2018). 3-D Monte Carlo surface wave tomography. *Geophys. J. Int.*, 215(3), 1644–1658.

ACADÉMIE DES SCIENCES
INSTITUT DE FRANCE

Comptes Rendus. Géoscience — Sciences de la Planète
2024, Vol. 356, Special issue S4, p. 85-100
https://doi.org/10.5802/crgeos.222

Research article

New Developments in Passive Seismic Imaging and Monitoring

Opportune detections of global P-wave propagation from microseisms interferometry

Pierre Boué [*, a] **and Lisa Tomasetto** [a]

[a] Univ. Grenoble Alpes, Univ. Savoie Mont Blanc, CNRS, IRD, Univ. Gustave Eiffel, ISTerre, 38000 Grenoble, France

E-mails: pierre.boue@univ-grenoble-alpes.fr (P. Boué), lisa.tomasetto@univ-grenoble-alpes.fr (L. Tomasetto)

Abstract. Global seismological observations are sensitive to oceanic forcings, namely microseisms. In addition to dominant surface waves, these sources generate body waves that travel through the deep structures of our planet. Despite these sources' inherent complexity, interferometric methods allow isolating coherent waves for imaging applications. For a given station pair, only specific microseism events contribute to the illumination of a specific target. We propose an opportune workflow based on ocean sea state models to extract robust interferences. This approach is illustrated with a strong microseism source in the North Atlantic Ocean, occurring around December 9, 2014.

Keywords. Global seismology, Secondary microseisms, Seismic interferometry, Data processing, Body waves.

Manuscript received 20 September 2022, revised 13 April 2023, accepted 31 May 2023.

1. Introduction

Part of our knowledge about the Earth's deep interior is deduced from seismological observations. Seismologists derive Earth models from their measurements of the elastodynamic response between sources and sensors. Earthquakes and/or controlled sources are classically used as an impulsive elastic perturbation for this purpose, but other forcings are known to produce seismic waves. Signal processing techniques make it possible to use what can be considered unconventional sources, insofar as they are not directly exploitable because of their broad and complex temporal and/or spatial signature.

The so-called ambient-noise correlation approach (i.e., for surface waves tomography or structural monitoring applications) relies on the fundamental idea that cross-correlation functions (CCF) of the background seismic wavefield observed at two stations (e.g., A and A′) converges toward the elastodynamic Green's functions (GF) between these two locations. A good convergence here means that, under some assumptions, CCF can be considered to be an empirical approximation of a band-limited GF and can be readily used for many applications. Putting aside the particularities of the ubiquitous seismic noise, and focusing on the foundations of seismic interferometry (SI), this idea was proposed and broadly studied within different domains related to acoustic and elastic wavefields; we can here refer to seismic exploration with the pioneered work on daylight imaging from Claerbout [1968], ultrasonic experiments [Lobkis and Weaver, 2001], helioseismology [Duvall et al., 1993], underwater acoustic

* Corresponding author

[Roux et al., 2004] and seismology [Campillo and Paul, 2003].

In short, and explained using a ray theory approximation, a perfect convergence would ultimately require the illumination of all possible eigenrays between two sensors with the right partition of energy between them. This could be achieved by multiple-scattering or reverberations within a chaotic cavity [e.g., Weaver and Lobkis, 2001, Sánchez-Sesma and Campillo, 2006], or an isotropic wavefield produced by an even source distribution within a volume or on a surrounding surface [e.g., Wapenaar, 2004, van Manen et al., 2006]. In practice, the background wavefield recorded on the Earth never enables a perfect convergence, but its characteristics are often sufficient for many imaging and monitoring applications. These applications range from local to regional scale, mostly using surface waves [e.g., Shapiro et al., 2005], but also body waves [e.g., Nakata et al., 2015]. A usual processing step to enhance CCF convergence and mitigate measurement biases is to average over many source distribution realizations by stacking CCF computed over long time series [from months to years, e.g., Bensen et al., 2007].

Global seismology did not benefit from the new source of information produced by SI in the early years of the development of these methods. Studies focused on targets ranging from the near-surface to the lithospheric scale [e.g., Wapenaar et al., 2010, Campillo and Roux, 2014]. To probe the deep Earth, other methods that use earthquakes ballistic, scattered wavefields, and associated normal modes remain the standard and most efficient ways. Using any other non-impulsive tremor-like sources (i.e., with long duration or stationary source time functions) requires an interferometric approach to decipher and identify different seismic phases (i.e., wave packets) mixed by the inherent convolution between source and propagation terms. Although helioseismologists quickly produced promising imaging applications based on SI, transposition to the Earth and its deep interior is not straightforward; "if it works on the Sun, can it work on the Earth?" questioned Rickett and Claerbout [1999]. The main difference is the background wavefield itself. Even if its observation itself is very challenging, a chaotic acoustic wavefield emanating from stochastic sources resulting from turbulent convection of hot plasma in a star is a perfect ingredient for GF estimation from SI. On our solid Earth, a few effective sources can produce a significant enough field (meaning above other fluctuations) to probe the mantle and the core: significant earthquakes, large volcanic eruptions, large impacts, significant explosions, and finally ocean microseisms. But all these sources are mostly located at or close to the Earth's surface, and most problematically for imaging purposes they are unevenly distributed. The distribution of sources surrounding a target is not a theoretical limitation of SI (if attenuation is not critical), but a discontinuous source distribution, if not balanced by sufficient scattering, can significantly lower our ability to evaluate, at least partly, an accurate empirical GF. Nevertheless, a theoretical validation of the interferometric relations for a full Earth has been derived by Ruigrok et al. [2008]. In that work, they also validated their findings with purely acoustic modeling which already shows some of the main possibilities and challenges of implementing with SI at that scale.

In parallel, the community of seismologists working on teleseismic signals also developed and used an interferometric approach to extract crustal reflections from earthquake signals [e.g., Bostock et al., 2001]. Interestingly, these approaches were quickly extended to less conventional sources such as non-volcanic tremors [Chaput and Bostock, 2007] and ocean microseisms [Ruigrok et al., 2011]. At that stage, the connection with noise-based SI was evident for deeper targets. After several demonstrations of the possibility to extract body wave signals at the crustal scale from conventional ambient noise correlations [e.g., Roux et al., 2005], Poli et al. [2012] show evidence of reflections on the 410 and 660 km upper mantle discontinuities which demonstrated for the first time the potential of SI for deep Earth seismology. Several studies have then quickly proven that this approach can be further extended to the global scale, detecting phases at teleseismic distances that probe the Earth's deep mantle and core [e.g., Nishida, 2013, Boué et al., 2013]. While a significant contribution of observed interferences comes from earthquakes that remain dominant after several hours [Lin et al., 2013, Boué et al., 2014, Phạm et al., 2018], it is also evident that secondary microseisms play a dominant role in the 3 to 10 s period band [e.g., Li et al., 2020a,b]. Alongside, the so-called Earth's correlation wavefield based on earthquakes' long-lasting and longer period coda waves emerged as a very ef-

fective approach for probing the deepest part of the Earth [e.g., Wang and Tkalčić, 2020, Tkalčić et al., 2020].

Regarding the processing strategy, it should be also noted that the idea of using a selective stacking to improve the detectability of low-amplitude body waves from SI has been proposed at various scales. Draganov et al. [2013] took advantage of the density of geophones available in a seismic exploration survey to detect and take into account only particular "events" in the background wavefield with significant body wave content. Similarly, but at a continental scale, Pedersen et al. [2023] assessed the most favorable period for observing body waves by detecting a low amplitude ratio between the horizontal plane and the vertical component (H/V) at seismic stations.

In this manuscript, our efforts focus on secondary microseism sources. Our interest in this source is motivated mainly by three arguments:

- This mechanism is known to be very efficient at producing body waves detectable at a global scale [e.g., Vinnik, 1973, Gerstoft et al., 2008, Landès et al., 2010, Nishida and Takagi, 2016].
- There is much evidence that noise correlations carry valuable information in the corresponding frequency range. For instance, several observations of P waves in the lower mantle and core were reported with a conventional (noise) processing workflow [e.g., Poli et al., 2015, Xia et al., 2016].
- The secondary microseism peak is a well-constrained mechanism [Longuet-Higgins, 1950, Hasselmann, 1963, Ardhuin et al., 2011]. Ocean-induced pressure field derived from hindcast models (WAVEWATCH III), combined with proper bathymetric amplification coefficients [e.g., for body waves, Gualtieri et al., 2014], produces a good prediction of the actual seismic wavefield [e.g., Farra et al., 2016, Retailleau and Gualtieri, 2021]. In other words, we have a good model of source time and spatial distribution to rely on.

Helped by our knowledge of source spatiotemporal properties, we propose to use an adaptive approach to avoid conventional "blind" correlation stacking over continuous time series. This study explores the possibility of measuring reliable P-wave interferences for a specific target by correlating signals from a single microseism event and adapting receiver pairs to specific phase interferences.

In the first section of this manuscript, we explain the main limitations of classical noise-based approach for deep Earth applications and for a realistic secondary microseism source distribution. We then introduce a simple microseism event-based approach that allows measuring relative phases from a single source. An example is shown for an already well-studied and significant microseism event. Finally, we discuss the possible implications of this research for deep Earth seismology and highlight future challenges.

2. On the limitations of the noise-based approach

Seismic rays emanating from a source located on the Earth's surface and propagating as P-waves are illustrated in Figure 1A as a reference. For simplicity, only main (first) phases are indicated. In global seismology, a P phase refers to propagation within the crust and the mantle; PcP corresponds to arrivals that reflect on the Core-Mantle Boundary (CMB). Both phases are detected up to about 90° of epicentral distance. In the source's antipodal region, first arrivals correspond to phases that propagate through the outer core (PKP) and both the outer and inner core (PKIKP). Interferometric methods aim to capture all these (well-known) seismic phases, among many others, in situations where source E is not impulsive enough to allow direct observation.

For instance, Retailleau et al. [2020] reported clear observations of both P and PcP phases between seismic stations deployed in Europe and the USA after correlating one year of continuous data. These signals were interpreted as partial GF retrieval and used to produce a lower mantle image through migration techniques. Besides the obvious first-order time match with a 1D reference model, these two phases exhibited clear symmetry between the two propagation directions (respectively on both causal and

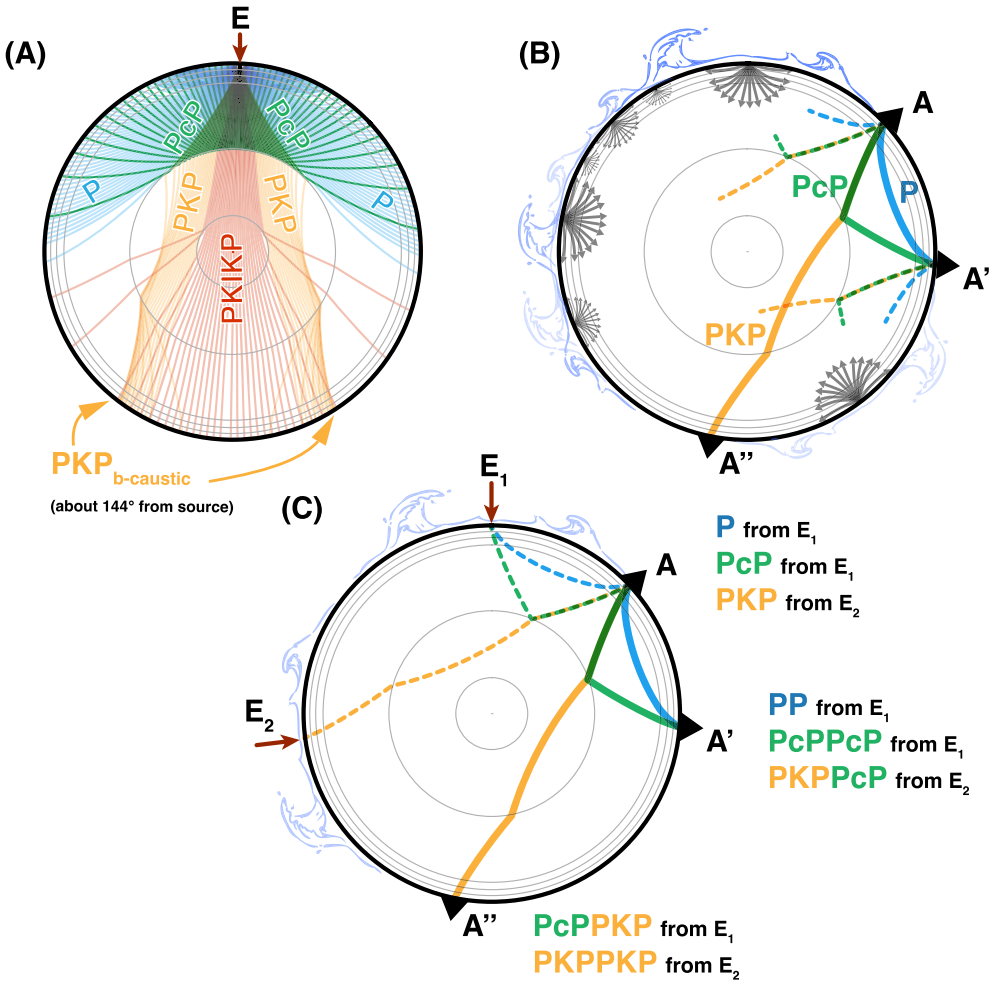

Figure 1. (A) Representation of ray paths for P, PcP, and PKP-type phases emanating from a source E located at the surface and computed within a radial Earth model for a regularly sampled take-off angle. (B) Schematic representation of the noise-based approach where multiple unknown sources are acting (also helped with a possible stacking procedure along continuous recordings). Under favorable conditions, the correlation between two stations could reveal GF-compatible phases like P, PcP between A and A′ or PKP between A and A″. (C) Schematic representation of the proposed approach which relies on a careful data selection. Here, particular phases (like P, PcP, or PKP) are retrieved by specific interferences made from specific and known sources like E_1 or E_2 in this example. On all panels, the different types of seismic phases are organized by color. Dotted lines represent the incoming rays while solid lines correspond to the expected/targeted paths.

acausal parts of the CCF). This symmetry of the correlation function was argued to be proof of CCF convergence toward the GF, thus justifying a direct application of migration technics. Such a noise correlation approach, illustrated in Figure 1B and initially developed for surface wave applications [Bensen et al., 2007], relies on the idea that for a given station pair (e.g., AA′), a sufficient stacking over continuous data will average the contributions from many sources. This idea is represented schematically in Figure 1B where many sources give rise to a ("noise") field that contains P and PcP phases between A and A′, and PKP between A and A″. The corresponding processing workflow is shown in Figure 2 (left panel). The

resulting correlation wavefield will then contain GF-compatible ray paths, also producing symmetrical CCF. For instance, van Manen et al. [2006] showed and discussed at a smaller scale how the surrounding distribution of sources enables CCF convergence toward GF based on constructive stacking produced by the stationarity (over source integral) of travel-time difference (or phase) between two interfering seismic phases. At a large scale, this was further explored and discussed in the context of the so-called Earth's correlation wavefield based on the coda of large earthquakes [Phạm et al., 2018]. In that study, the stationarity was explicitly associated with shared ray parameters for which Earth's major discontinuities play the role of secondary (i.e., virtual) sources. This was also discussed in Li et al. [2020a] for microseism sources.

In the context of secondary microseisms, the distribution of sources located on the Earth's surface is far from being even. Also, strong isolated sources, usually associated with significant cyclonic events [e.g., Farra et al., 2016, Retailleau and Gualtieri, 2021] dominate continuous seismic recordings [e.g., Nishida and Takagi, 2022]. Dominant sources are responsible for an unbalanced partition of energy between eigenrays reaching the two stations, which can lead to ambiguous phase measurements. As a result, final images are biased, if not erroneous. A non-symmetrical CCF will be the first obvious sign of such source effects, hence the argument of Retailleau et al. [2020] that symmetry is an indicator of CCF quality. But more subtle ambiguities also exist.

An example is shown in Figure 3 to illustrate the problem in a case that conforms to the observation of PcP phase, as in Retailleau et al. [2020]. We here use PcP as a target phase between station A and A′ (red path in Figure 3A). The reflection mid-point at the CMB between A and A′ is considered here as a target region. Following the idea and vocabulary introduced by Wang and Tkalčić [2020] in the context of long-lasting reverberations, a correlation "feature" (labeled PcP* in this case) is made from numerous constitutive interferences or "constituents"; each constituent being an interference between two coherent seismic phases, which can be reduced to a ray path difference under the ray approximation. Thus, constituents are named by simply associating the two interfering phases with a minus sign, the corresponding lag-time being the subtraction between the two initial phases. For example, PcPPcP-PcP (Figure 3A) refers to an interference matching a PcP phase between the two stations. Assuming that microseisms generate weak body waves which quickly drop below incoherent noise level, and contrary to the late coda of the large earthquakes [e.g., Tkalčić et al., 2020], only the direct wavefield and a limited number of reverberations (e.g., PP, PcPPcP, PKPPKP, PKPPcP, as illustrated in Figure 1C) are involved in the correlation wavefield. Note that no long-lasting reverberation is observed in the microseism frequency range due to both weak sources and rapid attenuation. It means that correlations are mostly sensitive to source dynamics (and primarily all their appearance and disappearance) and the same goes for ambiguities they contain as illustrated in Figure 3.

The most intuitive constituents of a PcP* feature are PcPPcP-PcP and PKPPcP-PKP differential travel paths. These interferences are only possible in the case where sources are located at E_1 and E_2 respectively. If these two sources are contributing to the CCF, the resulting PcP* between A and A′ will be made from, at least, these two constituents. Because a reflection at the CMB is generally weak relative to the corresponding transmission into the core, we expect PKPPcP-PKP to be more effective to produce a PcP* feature. Several studies reported the major influence of PKP branches emanating from secondary microseism events [e.g., Li et al., 2020a]. For instance, PKKPPcP-PKKP can also contribute in the same way for a source located in E_3. For these 3 constituents, the PcP* travel path is corresponding to the actual PcP between A and A′ (Figure 3A), meaning that these constituents are at least partly sensitive to the targeted path (discussion on spatial sensitivity in the last section).

As explained by Phạm et al. [2018] in a more generalized framework, a correlation feature is made from all possible constituents that are formed by seismic phases reaching A and A′ with the same ray parameter (condition of phases stationarity). Consequently, a constituent can be formed by two seismic phases that do not intrinsically contain a PcP between A and A′. This is for instance the case of PcPPKP-PKP from source point E_2 or PKPPKP-PKKP from E_3 (Figure 3B). Note that PKPPKP-PKKP does not include a PcP branch by itself, but rather a reflection of a "cP" branch on the surface, which by symmetry shares the same travel time as a PcP, thus contributing to the PcP* feature. This could of course be extended to

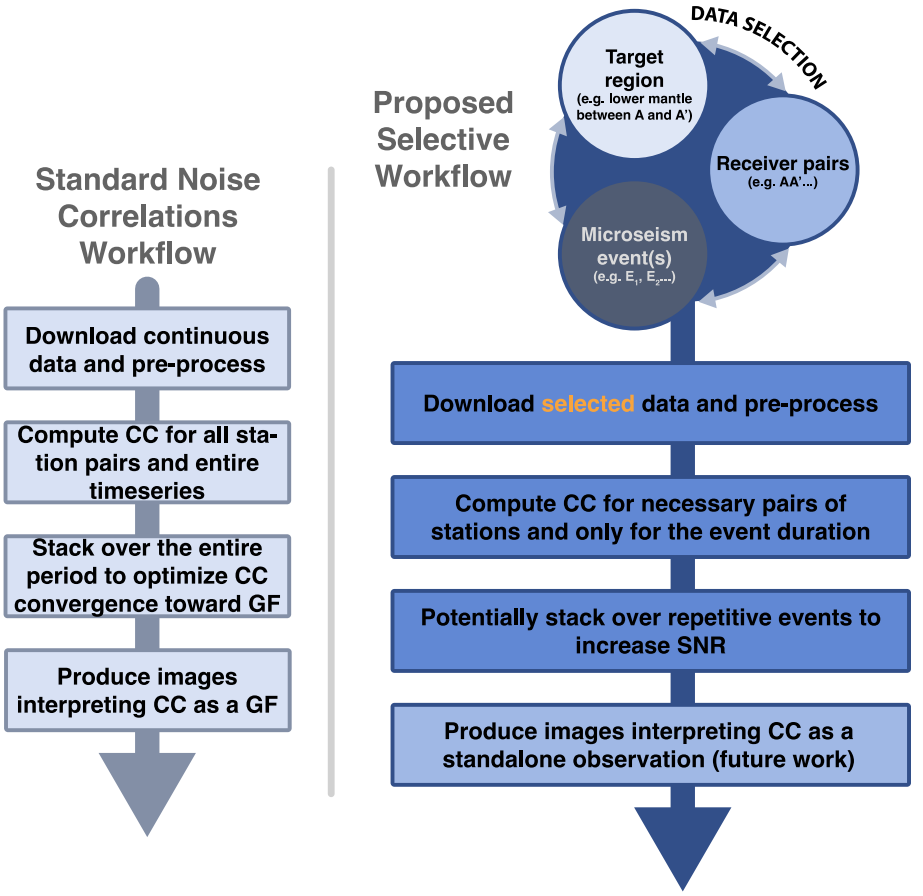

Figure 2. Schematic comparison between the standard noise correlation approach (left column) and the proposed selective workflow (right column). CC and GF stand for cross-correlation and Green's function respectively, SNR for signal to noise ratio. The proposed approach relies on a data selection using the 3 main parameters: microseism events (date, location, strength), structural target and associated seismic phases (e.g., CMB/PcP), and corresponding receiver pairs that will support the necessary interference.

any other correlation features such as P* and PKP*. It is important to note that this decomposition into constituent interferences underpins the classical GF retrieval from noise correlation for a closed system such as the Earth. Ruigrok et al. [2008] already proposed some pre-processing (multiple removals) to properly satisfy interferometric relations. Problems could be critical when CCF is blindly used from an initial source distribution that is dominated by some specific events. In that case, some constituents may become dominant and generate misinterpretation of the observed travel times and waveforms in terms of structural information: in other words, observations are not sensitive to the expected structure/location within the Earth.

To come back to the case of Retailleau et al. [2020], it is most likely that the observed PcP* between the US and Europe is dominated by a PKPPcP-PKP constituent that is formed by sources in the southern oceans. A single oceanic event following a prevailing Eastward trajectory south of Tasmania can indeed produce a PcP branch traveling in both directions below the North Atlantic. In other words, a source (E) transiting near E_2 in Figure 3A could produce a PKPPcP-PKP constituent for the geometry E–A–A′ and then, depending on its trajectory and dynamic, for the reversed direction E–A′–A. This is by itself not a problem for imaging applications, the symmetry of the correlation is simply produced by a transit of the "same" source into the stationary zone

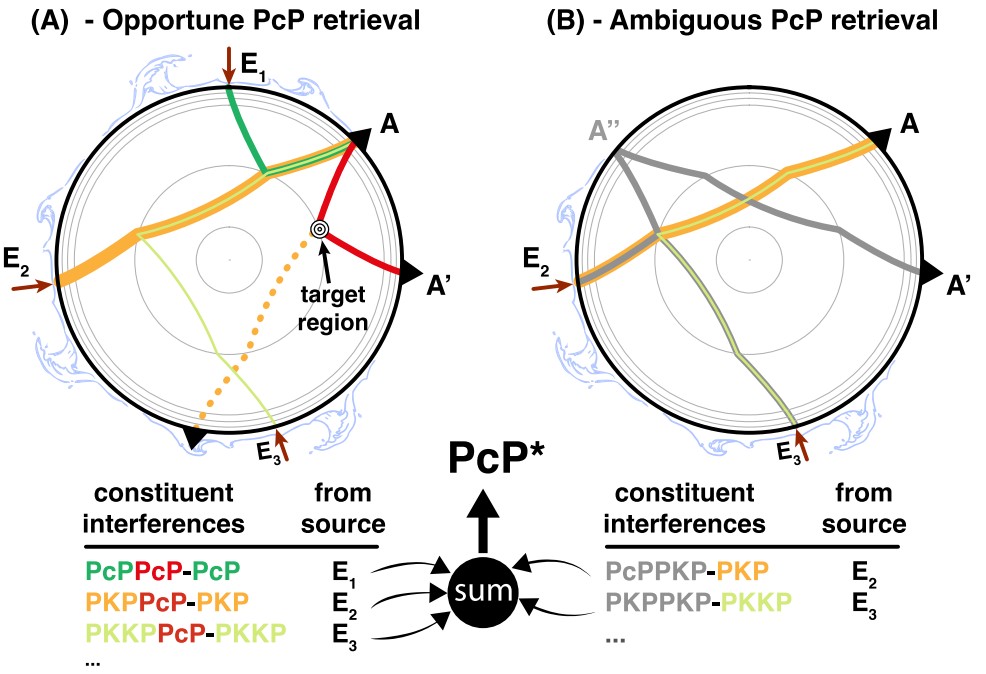

Figure 3. Illustration of possible ambiguities for a PcP* feature. Microseism sources are labeled from E_1 to E_3. A and A′ are the two considered stations. The targeted phase here corresponds to a PcP between A and A′. (A) Illustration of the main constituents of PcP* which indeed include the targeted PcP branch (in red). (B) Ambiguous constituents as they do not include the targeted PcP branch. Note that the same kind of ambiguities exists for any correlation features, such as PKP*, shown as a dotted yellow ray in (A).

(a.k.a. Fresnel zone, the area formed by the stationary condition of the phase difference for a given interference) of this constituent. Finally, the convergence of the PcP* observed by Retailleau et al. [2020] is probably not as complete as expected and very few oceanic events contribute to it over the entire year.

To avoid these complications, we here propose to restrict the number of constituents by only correlating localized events. Following the synthetic experiment proposed by Ruigrok et al. [2008] where they correlate wavefields produced by patches of sources, we show in the following sections that a single microseism event is sufficient to produce robust features in the correlation between distant stations.

3. Proposed workflow

Figures 1C and 2 illustrate the proposed workflow as a comparison with the classical noise-based approach, the latter being similar to surface wave applications. The main steps remain the same: downloading necessary data and correlating after some pre-processing. Differences are mostly in data selection. Where one could download continuous seismic data to facilitate, through stacking, the convergence of CCF to a more robust GF estimate, we here propose to only use a limited amount of data that we preselect both in time and space according to three ingredients:

- a target structure (e.g., CMB in a given area) or a seismic phase (P, PcP, PKP . . .)
- the worldwide distribution of seismic stations
- our knowledge of the secondary microseisms (strength, date, location, spatial spread)

From here, it depends on the objective. Whereas a usual approach is to target a specific area, we here start from a particular microseism event to demon-

strate the applicability of our workflow. One could easily adapt this workflow to other goals.

Knowledge of the source dynamics is critical to design an efficient strategy for data processing and avoiding ambiguous phase retrieval by adding unwanted constituents into the final correlograms, as discussed in the previous section. Numerous studies reported direct seismic observations of significant secondary microseism events, usually associated with major atmospheric depressions and oceanic storms. For instance, the seismic coupling of the super typhoon Ioke, which occurred in the late summer of 2006 in the western Pacific was detailed by several authors [e.g., Zhang et al., 2010, Retailleau and Gualtieri, 2021, among others]. Such a significant event was proved to be very well predicted from sea state models. The source mechanism associated with secondary microseisms can be numerically computed from ocean sea state hindcast datasets when considering azimuthally dependent oceanic wave spectrum [Ardhuin et al., 2011, Ardhuin and Herbers, 2013]. These numerical models usually show a good match with global seismic observations [e.g., Nishida and Takagi, 2022]. Besides the state of the ocean swells, bathymetry plays an important role in the coupling between the ocean-generated pressure field and seismic waves [Longuet-Higgins, 1950]. This amplification factor depends on several parameters other than the bathymetry itself: wave type and local velocity, considered frequency range and ray parameters (and thus local apparent wavelength). We follow derivations from Gualtieri et al. [2014] and use a P-wave amplification factor integrated over all possible ray parameters and computed at 6 s of period for this preliminary work. Finally, we focus on a single major event occurring in the North Atlantic on December 2014 that is already known to be seismically significant [Nishida and Takagi, 2016]. In terms of secondary microseisms, the particularity of this northern Atlantic active area is linked to the combination of two factors: (1) an often adequate and very energetic sea state and (2) a good seismic coupling due to a complex bathymetry that produces a significant amplification factor over a large area overlapping storms' trajectories.

Figure 4 shows the strategy to characterize source parameters from the ocean model. Figure 4A illustrates a portion of the sea state input model. Here, only the significant (ocean) wave height is shown at a given date (with a 3 h resolution). We can see the major impact of the storm between Iceland and Greenland where ocean swells reach values higher than 12 m on a very broad surface. The pressure field at the ocean surface is computed from the azimuthally dependent oceanic wave spectrum [Figure 4B, Ardhuin et al., 2011]. P-wave amplification coefficients are computed from local bathymetry (Figure 4C) and following Gualtieri et al. [2014]. Iso-values follow isobathymetry. Figure 4E shows modulation of the pressure field at the ocean surface by bathymetric amplification; this is interpreted as the actual pressure acting at the ocean bottom that applies to the crust and generates P-waves. On December 9, 2014, at 12:00 UTC, we can locate a very energetic source at about −33° E and 63° N (green star). We can also verify from our model that this location remains very active for the entire day. A better source characterization could be considered, but we rely on this first estimate to conduct our tests. Our modeling of this microseism event follows previous results from Nishida and Takagi [2016].

Now that a source location and timing are known, we can select pairs of operational seismic stations worldwide depending on the targeted seismic phase (or constituent). For instance, let us again consider a pair of stations AA′ aligned on the great circle that includes source E and that would be spaced by the same distance that separates source E from the closest station A (e.g., the configuration of E_1–A–A′ on Figure 1C). Such a combination would be perfectly suited for measuring constituents that are made by simple phase multiples reflecting at the Earth's free surface such as PP-P, PcPPcP-PcP, or even PKPPKP-PKP when the inter-station distance gets long enough (Figure 1C). This geometry matches a stationary phase condition in the sense that the ray parameter of each phase reaching the sensors are similar. Since we work in a finite frequency range, the stationarity of the phase difference also allows the incorporation of some tolerance in the station selection: for a given source and a first station, a second station is searched in a small circle centered on the optimal point with a radius corresponding to 5% of the interstation distance. This simple criterion accounts for the expected aperture of the stationary phase area on the source regions [see for instance Sager et al., 2022].

It is slightly more complicated for some other kinds of interferences. Let us consider a PKPPcP-PKP

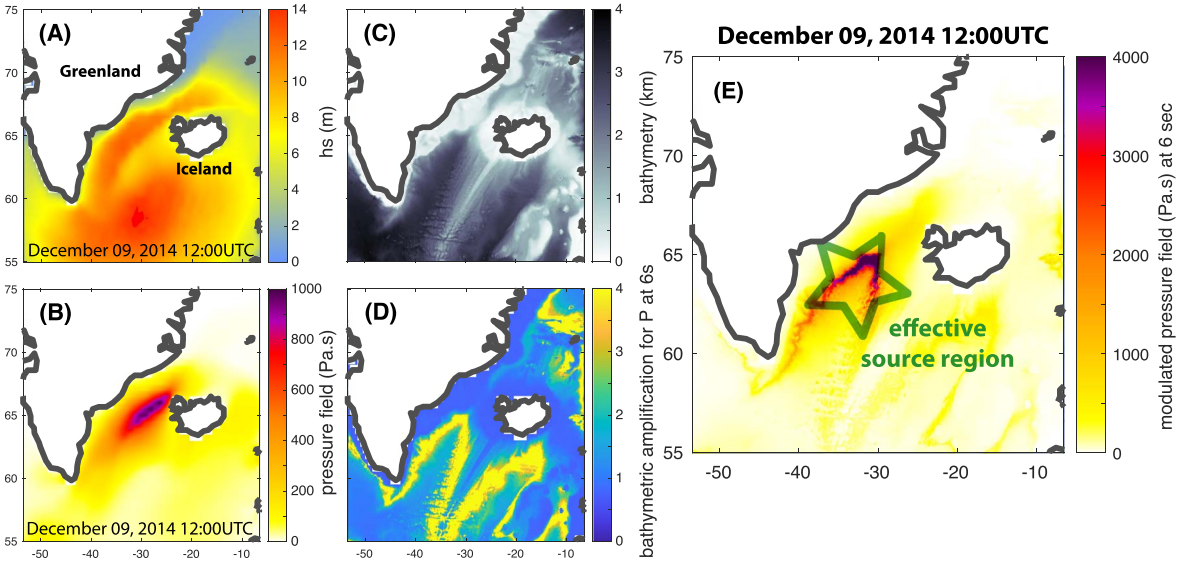

Figure 4. Illustration of the source characterization in the North Atlantic Ocean from the sea state model. (A) Significant wave height in the region on December 9, 2014 (12:00UTC). (B) Pre-computed pressure field from wave-wave interaction in open ocean derived from directional wave spectrum [Ardhuin et al., 2011]. (C) Local bathymetry (ETOPOv2). (D) The bathymetric amplification factor is computed for P waves at 6 s of period and intergrated over ray parameters following Gualtieri et al. [2014]. (E) Result of the effective source region from the modulation of panel (B) with (D). The green star corresponds to the most energetic area which we identify as the epicenter of this event at that date.

constituent (see E_3–A–A′ configuration in Figure 1C). In that case, ray tracing is required. The ray parameter of PKP reaching the first station is used to compute the propagation distance of the PcP (with the same ray parameter) between the two stations. Using this distance, a forward geodetic arc is computed from the first station and following a great-circle direction to locate the optimal point to search a terminus station A′. As before, a tolerance area is kept when searching for a possible A′ station according to the expected stationary zone aperture. This ray-based data selection can be generalized to any others constituents. The sensitivity of final measurements to such a station pair selection according to the spatiotemporal properties of the source is outside of the scope of this study and will be further explored in future work.

Finally, seismic data are downloaded for the duration of a microseism event (typically from a few hours to a few days) and then correlated according to the previous selection. In the following section, all possible vertical components of high-sensitivity sensors (*HZ) are considered based on the International Federation of Digital Seismograph Networks (FDSN) archive. No particular processing is performed before correlation except for (1) an instrument response deconvolution and a resampling to 4 Hz after the application of an anti-aliasing pre-filter, to account for variability in instrument sensitivity; and (2) a spectral whitening in the period range of interest (from 3 to 12 s), to only measure the coherency of the phases and reduce the impact of relative amplitudes. Correlations are computed on an hourly time series and phase-weighted stacked [Schimmel and Paulssen, 1997]. Since our selection of station pairs is oriented, only the causal part of the CCF is considered. Bathymetry plays an important role in the spatial distribution of sources. Some locations in the ocean with favorable bathymetry may produce redundant events over time even though the ocean sea state has a complex dynamic. In that case, a stacking procedure could be performed to enhance the signal-to-noise ratio (SNR). In the following, a single event is used as it is strong enough to show good SNR and validate the workflow. This workflow is summarized in the right panel of Figure 2.

4. Application and results

To illustrate the workflow, we choose a time window of 24 h starting on December 9, 2014, at 9:00 UTC, also knowing that such a significant ocean storm is seismically active for more than a day [Nishida and Takagi, 2016]. Taking into account a longer time window could require re-evaluating the epicenter of the event, hence re-evaluating the optimal pairs of stations following the method described above.

Figure 5A illustrates our selection of station pairs considered to measure constituents involving a simple reflection at the Earth's surface such as PP-P and PKPPKP-PKP (see Figure 1C). Because of this data selection, station pairs align naturally along great circle arcs including the source region (green star). Inter-station distances are color-coded from short, in black, to long, in light yellow. Red points are starting points (e.g., station A for event E_1 in Figure 1C), and purple ones are terminus points (e.g., station A′ for event E_1 in Figure 1C). At longer distances, for which we expect detection of PKPPKP-PKP (e.g., E_2–A–A″ in Figure 1C), terminus points can be close to the source region. Since surface waves are dominant close to the source, this geometry decreases our capability to detect weak body waves.

Figure 5B shows a very coherent PP-P constituent that matches the prediction of a ballistic mantle P wave travel-time computed in a reference model [PREM, Dziewonski and Anderson, 1981] using ray tracing from TauP toolkit for a corresponding inter-station distance [Crotwell et al., 1999]. Interestingly, no significant PcPPcP-PcP constituent is visible, despite the strength of this major source. As explained earlier in the context of the preliminary work of Retailleau et al. [2020], this is probably related to a relatively weak CMB reflectivity. In other words, observing both P and PcP in noise cross-correlation wavefield computed between two stations most probably corresponds to two different source regions. Some other coherent branches are visible. Before the PP-P branch, a significant arrival shows up (see at about 8.5 min, 80°). This matches a PKP_{ab}-P quasi-stationary constituent discussed by Li et al. [2020a]. A coherent signal at about 13 min, between 60° and 65° of distance may correspond to other constituents related to P-wave multiples. This composite seismic section shows a discontinuous coherency along the expected arrival times, which cannot be explained only by the stacking order within each bin. Complex local geology as well as other local sources in the vicinity of some stations, or simply non-isotropic source radiation in the far field may explain such differences in the coherency of the expected constituent for some pairs. This would require investigations and a quality check before any further exploitation of such signals for imaging applications. It is important to note that stacking pairs of stations according to inter-station distance is done for representation purposes, but a single pair of stations can show a very strong signal for a single ocean event already. Being able to detect a wavelet on a single station pair (or by using a local array) is critical for any 3D imaging application.

Figure 5C shows CCF for the same kind of station pair selection, but simply at larger distances where PKPPKP-PKP constituent is expected. Some significant coherency can be seen from 145° to 148°, which corresponds to the $PKP_{b\text{-caustic}}$. At this frequency, it is difficult to decipher the different PKP branches' contributions, but the caustic seems to play a significant role here as discussed by Snieder and Sens-Schönfelder [2015]. Some finite-frequency propagation modeling could help to see to what extent PKP-related constituents could constrain Earth's structure. Again, it is worth reminding that only 24 h-long signals are used here, and stacking multiple events could help improve SNR.

Finally, we explore the feasibility of measuring PcP travel time based on a station selection that corresponds to a PKPPcP-PKP constituent (e.g., E_2–A–A′ in Figures 1C and 3A). Figure 6A shows our data selection with a map projection that is centered at the sources' antipode. A large number of temporary and permanent stations were initially present on a purely geometric selection, but a first-order quality check based on the SNR of the CCF left us with most station pairs between Australia and Antarctica. Local conditions of observations (southern oceans sea state), as well as the Antarctica ice cap, may explain the relatively low quality of observed signals. Figure 6B shows the PKPPcP-PKP constituent, zoomed over a portion of the available distant range. Our observation matches the expected PcP travel time, thus validating our station pairs selection. Again here, the quality of this composite seismic section does not seem to be correlated to the number of pairs stacked for building this section.

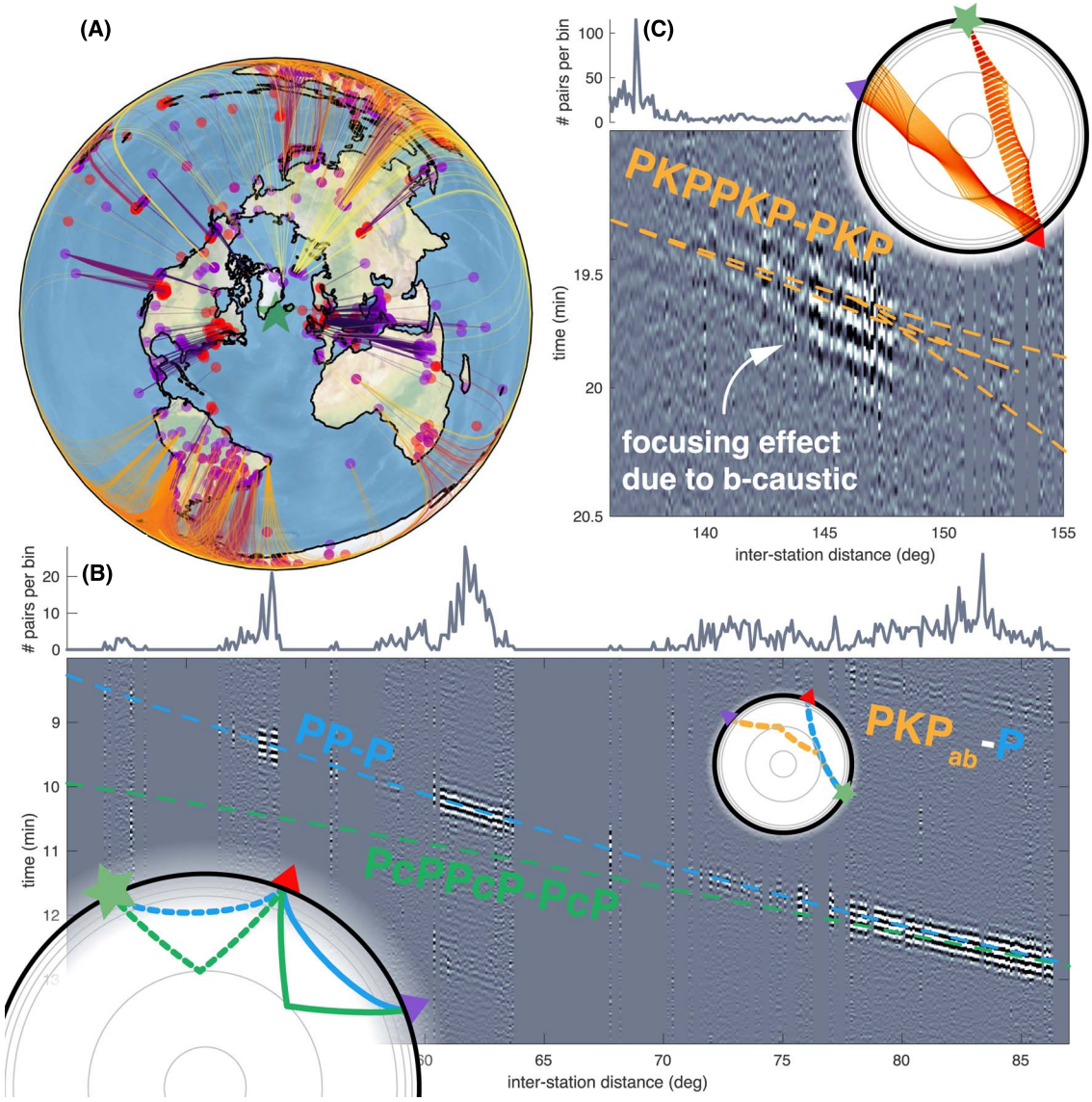

Figure 5. Results for station pairs selected based on their alignment with the source and an inter-station spacing matching single-phase multiples at the Earth's surface. (A) Map of the effective station pairs selection centered on the source region (green star); inter-station distance is color-coded from black to light yellow. Red and purple dots are departure and terminus station locations respectively. (B, C) Seismic sections from cross-correlations stacked over a 0.1° distance bin. Ray tracing results matching each constituent are shown as dashed lines on both sections. Inserts showing slices of the Earth recall the ray path of each constituent as in Figure 1C. (B) Zoom on PP-P constituent. (C) Zoom on PKPPKP-PKP constituent.

5. Discussions and conclusions

The proposed workflow revisits the idea of seismic daylight imaging [Rickett and Claerbout, 1999, Schuster et al., 2004] and is also motivated by more recent successes of a noise-based correlation approach for the detection of teleseismic body waves in the secondary microseism frequency band. Here,

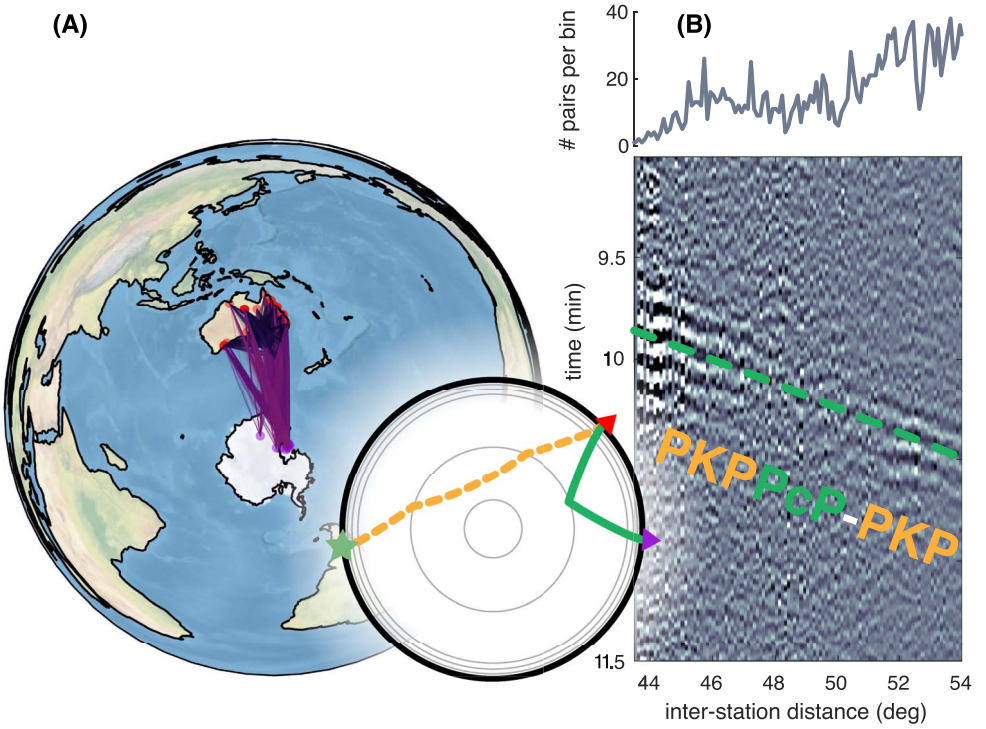

Figure 6. Same as Figure 5 but for a station pairs selection that corresponds to PKPPcP-PKP constituent which corresponds to PcP travel time. (A) Map of station pair selection centered on the antipode of the source location. (B) Seismic section from cross-correlations stacked over 0.1° distance bin zoomed on PKPPcP-PKP. Ray tracing results corresponding to a PcP arrival is shown as a green dashed line.

cross-correlations are computed on carefully selected seismic station pairs for a given date and duration adapted to our knowledge of source patterns. Source parameters are derived from secondary microseisms computed from sea state models. The main goal of the proposed approach is to overcome some limitations of the noise-based correlation approach. Noise-based CCF can be biased and ambiguous because of the non-completeness of the necessary hypothesis of an isotropic incoming wavefield or source distribution. This is particularly important when teleseismic body waves are targeted. Misinterpretations emerge when a correlation feature with a travel time matching a known seismic phase (e.g., PcP) between the two stations is "blindly" interpreted as such. Following the decomposition of CCF features into constitutive interferences [Wang and Tkalčić, 2020], we proposed an adaptative workflow to mitigate ambiguities for microseism event-based correlations.

A major microseism hitting North Atlantic Ocean on December 9, 2014, is used for illustrating the proposed approach. Pairs of stations are assembled according to various constituents: PP-P, PKPPKP-PKP, and PKPPcP-PKP. While such a large event is, by itself, sufficient to produce clear evidence of these constituents, multiple events could be stacked to improve SNR. Smaller events could then be used, helped by the fact that some areas are very prone to secondary microseisms over years, due to both storm periodicity and the dominant role of bathymetry for seismic coupling [e.g., Nishida and Takagi, 2022].

Since different constituents can be measured independently, their interpretation is less ambiguous. The approximation of the GF between seismic stations is not an objective here, hence connecting measurements to the Earth's structure is less straightforward. Since a single constituent is made from interference between two seismic phases, one needs to measure sensitivity to the structure of this differen-

tial path for imaging applications. Sager et al. [2022] estimated the sensitivity of such constituents in the context of fault monitoring, where crustal P-waves emanating from freight trains were correlated in California. Structural sensitivity of travel times measured from PP-P and P-P interferences were computed. This computationally intensive approach also enables a sensitivity evaluation of such measurements to source patterns. Similar evaluations should be performed at a global scale to make use of teleseismic constituents for imaging purposes. We can also emphasize the similarity of the microseism event-based SI approach discussed here with previous works on imaging and monitoring at smaller scales using timely passages of freight trains [Brenguier et al., 2019, Pinzon-Rincon et al., 2021].

It is important to note that even if an empirical evaluation of the GF between stations is not an objective, considering constituents based on a phase difference stationarity is critical because of the spatial extension of microseism sources. Again, stationarity appears when the constituent is made from seismic phases sharing the same ray parameters (e.g., P and PP when doubling the propagation distance), thus defining a possible finite frequency Fresnel zone. By definition, constructive interference happens for any source lying in (the main lobe of) this Fresnel zone. In a first approximation, the relatively large aperture of the stationary area in the secondary microseism frequency range (e.g., several hundreds of kilometers for PP-P at 50° inter-station distance and 6 s period) allows us to take advantage of each source spatial extent and time evolution. On the opposite, a spatially extended source outside the Fresnel zone would interfere destructively with itself due to the oscillatory nature of the interference for a finite frequency wavefield. Further work needs to be done to compare, for a given constituent, observed travel times with a prediction made from a combination of modeled sources and expected Fresnel zones. This is somehow related to the definition of microseism events themselves, which would also need some further investigations (time, space, strength, radiation . . .). We can also question the feasibility of inverting the interferometric scheme using its reciprocal form, following the idea introduced by Curtis et al. [2009]. The objective could then be to recover correlation features between two events by interfering them at a single seismic station aligned with these sources; but in this case, the (a priori) low correlation between the two source time functions of the two events will most likely be an obstacle for making significant detections.

Finally, this study shows that it is possible to observe teleseismic phases propagating from a single strong microseism source by correlating only a few hours of continuous recordings between station pairs selected for particular body-wave interferences (constituents). In other words, it is possible to turn a few hours of ocean-related non-impulsive tremors-like signals into a clear ballistic pulse in the far field. The limited frequency range of secondary microseisms as well as a dominant impact of some particular regions acting as significant microseism events (e.g., North Atlantic Ocean) are the main and foreseen limitations of this approach. Moreover, we noticed the lack of S-wave-related constituents in these preliminary results, despite the possibility to observe S waves in ballistic wavefields emanating from the same source [Nishida and Takagi, 2016]. Horizontal components need to be explored to further conclude. Direct comparison with earthquake data is not straightforward because of the sensitivity of the constituents that are different from the GF between the two stations [Sager et al., 2022], but we expect these two datasets to be complementary. An opportune station pair selection could fill in some of the inherent lack of illumination produced by uneven source–receiver geometries when using earthquakes as sources for deep Earth imaging applications.

Conflicts of interest

Authors have no conflict of interest to declare.

Acknowledgments

We acknowledge the two anonymous reviewers and the editor Andrew Curtis for their thorough reading and useful comments. We also acknowledge the support from the French National Research Agency (ANR) under the project TERRACORR (ANR-20-CE49-0003). Maps are produced using the Cartopy package (doi:10.5281/zenodo.1182735). Bathymetry is taken from ETOPOv2c (doi:10.7289/V5J1012Q). Authors used subfunctions from Obspy within their processing workflow [Beyreuther et al., 2010]. The output of the ocean wave model can be found at

http://ftp.ifremer.fr/ifremer/ww3/HINDCAST. We thank Fabrice Ardhuin and Mickaël Accensi for making this dataset available. We acknowledge all the people involved in seismic station deployment, maintenance, and data distribution worldwide. The list of all network codes used in the work is provided in supplementary material, as well as associated DOI.

Supplementary data

Supporting information for this article is available on the journal's website under https://doi.org/10.5802/crgeos.222 or from the author.

References

Ardhuin, F. and Herbers, T. H. (2013). Noise generation in the solid Earth, oceans, and atmosphere, from nonlinear interacting surface gravity waves in finite depth. *J. Fluid Mech.*, 716, 316–348.

Ardhuin, F., Stutzmann, E., Schimmel, M., and Mangeney, A. (2011). Ocean wave sources of seismic noise. *J. Geophys. Res. Oceans*, 116, article no. C09004.

Bensen, G. D., Ritzwoller, M. H., Barmin, M. P., Levshin, A. L., Lin, F., Moschetti, M. P., and Yang, Y. (2007). Processing seismic ambient noise data to obtain reliable broad-band surface wave dispersion measurements. *Geophys. J. Int.*, 169(3), 1239–1260.

Beyreuther, M., Barsch, R., Krischer, L., Megies, T., Behr, Y., and Wassermann, J. (2010). ObsPy: A Python toolbox for seismology. *Seismol. Res. Lett.*, 81(3), 530–533.

Bostock, M. G., Rondenay, S., and Shragge, J. (2001). Multiparameter two-dimensional inversion of scattered teleseismic body waves 1. Theory for oblique incidence. *J. Geophys. Res. Solid Earth*, 106(B12), 30771–30782.

Boué, P., Poli, P., Campillo, M., Pedersen, H., Briand, X., and Roux, P. (2013). Teleseismic correlations of ambient seismic noise for deep global imaging of the Earth. *Geophys. J. Int.*, 194(2), 844–848.

Boué, P., Roux, P., Campillo, M., and Briand, X. (2014). Phase velocity tomography of surface waves using ambient noise cross correlation and array processing. *J. Geophys. Res. Solid Earth*, 119(1), 519–529.

Brenguier, F., Boué, P., Ben-Zion, Y., Vernon, F., Johnson, C. W., Mordret, A., et al. (2019). Train traffic as a powerful noise source for monitoring active faults with seismic interferometry. *Geophys. Res. Lett.*, 46(16), 9529–9536.

Campillo, M. and Paul, A. (2003). Long-range correlations in the diffuse seismic coda. *Science*, 299(5606), 547–549.

Campillo, M. and Roux, P. (2014). Seismic imaging and monitoring with ambient noise correlations. *Treatise Geophys.*, 1, 256–271.

Chaput, J. A. and Bostock, M. G. (2007). Seismic interferometry using non-volcanic tremor in Cascadia. *Geophys. Res. Lett.*, 34, article no. L07304.

Claerbout, J. F. (1968). Synthesis of a layered medium from its acoustic transmission response. *Geophysics*, 33(2), 264–269.

Crotwell, H. P., Owens, T. J., and Ritsema, J. (1999). The TauP Toolkit: Flexible seismic travel-time and ray-path utilities. *Seismol. Res. Lett.*, 70, 154–160.

Curtis, A., Nicolson, H., Halliday, D., Trampert, J., and Baptie, B. (2009). Virtual seismometers in the subsurface of the Earth from seismic interferometry. *Nat. Geosci.*, 2(10), 700–704.

Draganov, D., Campman, X., Thorbecke, J., Verdel, A., and Wapenaar, K. (2013). Seismic exploration-scale velocities and structure from ambient seismic noise (>1 Hz). *J. Geophys. Res. Solid Earth*, 118(8), 4345–4360.

Duvall, T. L., Jeffferies, S. M., Harvey, J. W., and Pomerantz, M. A. (1993). Time–distance helioseismology. *Nature*, 362(6419), 430–432.

Dziewonski, A. M. and Anderson, D. L. (1981). Preliminary reference Earth model. *Phys. Earth Planet Inter.*, 25(4), 297–356.

Farra, V., Stutzmann, E., Gualtieri, L., Schimmel, M., and Ardhuin, F. (2016). Ray-theoretical modeling of secondary microseism P waves. *Geophys. J. Int.*, 206(3), 1730–1739.

Gerstoft, P., Shearer, P. M., Harmon, N., and Zhang, J. (2008). Global P, PP, and PKP wave microseisms observed from distant storms. *Geophys. Res. Lett.*, 35, article no. L23306.

Gualtieri, L., Stutzmann, É., Farra, V., Capdeville, Y., Schimmel, M., Ardhuin, F., and Morelli, A. (2014). Modelling the ocean site effect on seismic noise body waves. *Geophys. J. Int.*, 197(2), 1096–1106.

Hasselmann, K. (1963). A statistical analysis of the generation of microseisms. *Rev. Geophys.*, 1(2),

177–210.

Landès, M., Hubans, F., Shapiro, N. M., Paul, A., and Campillo, M. (2010). Origin of deep ocean microseisms by using teleseismic body waves. *J. Geophys. Res. Solid Earth*, 115, article no. B05302.

Li, L., Boué, P., and Campillo, M. (2020a). Observation and explanation of spurious seismic signals emerging in teleseismic noise correlations. *Solid Earth*, 11(1), 173–184.

Li, L., Boué, P., Retailleau, L., and Campillo, M. (2020b). Spatiotemporal correlation analysis of noise-derived seismic body waves with ocean wave climate and microseism sources. *Geochem. Geophys. Geosyst.*, 21(9), article no. e2020GC009112.

Lin, F. C., Tsai, V. C., Schmandt, B., Duputel, Z., and Zhan, Z. (2013). Extracting seismic core phases with array interferometry. *Geophys. Res. Lett.*, 40(6), 1049–1053.

Lobkis, O. I. and Weaver, R. L. (2001). On the emergence of the Green's function in the correlations of a diffuse field. *J. Acoust. Soc. Am.*, 110(6), 3011–3017.

Longuet-Higgins, M. S. (1950). A theory of the origin of microseisms. *Philos. Trans. Royal Soc. Lond. Ser. A*, 243(857), 1–35.

Nakata, N., Chang, J. P., Lawrence, J. F., and Boué, P. (2015). Body wave extraction and tomography at Long Beach, California, with ambient-noise interferometry. *J. Geophys. Res. Solid Earth*, 120(2), 1159–1173.

Nishida, K. (2013). Global propagation of body waves revealed by cross-correlation analysis of seismic hum. *Geophys. Res. Lett.*, 40(9), 1691–1696.

Nishida, K. and Takagi, R. (2016). Teleseismic S wave microseisms. *Science*, 353(6302), 919–921.

Nishida, K. and Takagi, R. (2022). A global centroid single force catalog of P-wave microseisms. *J. Geophys. Res. Solid Earth*, 127(4), article no. e2021JB023484.

Pedersen, H. A., Mattern, F., Poli, P., and Stehly, L. (2023). Imaging with seismic noise: improving extraction of body wave phases from the deep Earth through selective stacking based on H/V ratios. *Geophys. J. Int.*, 232(2), 1455–1467.

Phạm, T. S., Tkalčić, H., Sambridge, M., and Kennett, B. L. (2018). Earth's correlation wavefield: Late coda correlation. *Geophys. Res. Lett.*, 45(7), 3035–3042.

Pinzon-Rincon, L., Lavoué, F., Mordret, A., Boué, P., Brenguier, F., Dales, P., et al. (2021). Humming trains in seismology: an opportune source for probing the shallow crust. *Seismol. Soc. Am.*, 92(2A), 623–635.

Poli, P., Campillo, M., Pedersen, H., and LAPNET Working Group (2012). Body-wave imaging of Earth's mantle discontinuities from ambient seismic noise. *Science*, 338(6110), 1063–1065.

Poli, P., Thomas, C., Campillo, M., and Pedersen, H. A. (2015). Imaging the D′′ reflector with noise correlations. *Geophys. Res. Lett.*, 42(1), 60–65.

Retailleau, L., Boué, P., Li, L., and Campillo, M. (2020). Ambient seismic noise imaging of the lowermost mantle beneath the North Atlantic Ocean. *Geophys. J. Int.*, 222(2), 1339–1351.

Retailleau, L. and Gualtieri, L. (2021). Multi-phase seismic source imprint of tropical cyclones. *Nat. Commun.*, 12(1), 1–8.

Rickett, J. and Claerbout, J. (1999). Acoustic daylight imaging via spectral factorization: Helioseismology and reservoir monitoring. *Lead. Edge*, 18(8), 957–960.

Roux, P., Kuperman, W. A., and NPAL group (2004). Extracting coherent wave fronts from acoustic ambient noise in the ocean. *J. Acoust. Soc. Am.*, 116(4), 1995–2003.

Roux, P., Sabra, K. G., Gerstoft, P., Kuperman, W. A., and Fehler, M. C. (2005). P-waves from cross-correlation of seismic noise. *Geophys. Res. Lett.*, 32, article no. L19303.

Ruigrok, E., Campman, X., and Wapenaar, K. (2011). Extraction of P-wave reflections from microseisms. *C. R. Geosci.*, 343(8–9), 512–525.

Ruigrok, E., Draganov, D., and Wapenaar, K. (2008). Global-scale seismic interferometry: theory and numerical examples. *Geophys. Prospect.*, 56(3), 395–417.

Sager, K., Tsai, V. C., Sheng, Y., Brenguier, F., Boué, P., Mordret, A., and Igel, H. (2022). Modelling P waves in seismic noise correlations: advancing fault monitoring using train traffic sources. *Geophys. J. Int.*, 228(3), 1556–1567.

Sánchez-Sesma, F. J. and Campillo, M. (2006). Retrieval of the Green's function from cross correlation: the canonical elastic problem. *Bull. Seismol. Soc. Am.*, 96(3), 1182–1191.

Schimmel, M. and Paulssen, H. (1997). Noise reduction and detection of weak, coherent signals through phase-weighted stacks. *Geophys. J. Int.*,

130(2), 497–505.

Schuster, G. T., Yu, J., Sheng, J., and Rickett, J. (2004). Interferometric/daylight seismic imaging. *Geophys. J. Int.*, 157(2), 838–852.

Shapiro, N. M., Campillo, M., Stehly, L., and Ritzwoller, M. H. (2005). High-resolution surface-wave tomography from ambient seismic noise. *Science*, 307(5715), 1615–1618.

Snieder, R. and Sens-Schönfelder, C. (2015). Seismic interferometry and stationary phase at caustics. *J. Geophys. Res. Solid Earth*, 120(6), 4333–4343.

Tkalčić, H., Phạm, T. S., and Wang, S. (2020). The Earth's coda correlation wavefield: Rise of the new paradigm and recent advances. *Earth Sci. Rev.*, 208, article no. 103285.

van Manen, D. J., Curtis, A., and Robertsson, J. O. (2006). Interferometric modeling of wave propagation in inhomogeneous elastic media using time reversal and reciprocity. *Geophysics*, 71(4), SI47–SI60.

Vinnik, L. P. (1973). Sources of microseismic P waves. *Pure Appl. Geophys.*, 103(1), 282–289.

Wang, S. and Tkalčić, H. (2020). Seismic event coda-correlation's formation: implications for global seismology. *Geophys. J. Int.*, 222(2), 1283–1294.

Wapenaar, K. (2004). Retrieving the elastodynamic Green's function of an arbitrary inhomogeneous medium by cross correlation. *Phys. Rev. Lett.*, 93(25), article no. 254301.

Wapenaar, K., Draganov, D., Snieder, R., Campman, X., and Verdel, A. (2010). Tutorial on seismic interferometry: Part 1—Basic principles and applications. *Geophysics*, 75(5), 75A195–75A209.

Weaver, R. L. and Lobkis, O. I. (2001). Ultrasonics without a source: Thermal fluctuation correlations at MHz frequencies. *Phys. Rev. Lett.*, 87(13), article no. 134301.

Xia, H. H., Song, X., and Wang, T. (2016). Extraction of triplicated PKP phases from noise correlations. *Geophys. Suppl. Mon. Notices Royal Astron. Soc.*, 205(1), 499–508.

Zhang, J., Gerstoft, P., and Shearer, P. M. (2010). Resolving P-wave travel-time anomalies using seismic array observations of oceanic storms. *Earth Planet. Sci. Lett.*, 292(3–4), 419–427.

ACADÉMIE DES SCIENCES
INSTITUT DE FRANCE

Comptes Rendus. Géoscience — Sciences de la Planète
2024, Vol. 356, Special issue S4, p. 101-124
https://doi.org/10.5802/crgeos.241

Research article

New Developments in Passive Seismic Imaging and Monitoring

Dynamic of seismic noise sources in the Mediterranean Sea: implication for monitoring using noise correlations

Laurent Stehly[*,a], **Estelle Delouche**[a], **Lisa Tomasetto**[a] **and Pratul Ranjan**[a]

[a] Univ. Grenoble Alpes, Univ. Savoie Mont Blanc, CNRS, IRD, UGE, ISTerre, 38000 Grenoble, France

E-mails: laurent.stehly@univ-grenoble-alpes.fr (L. Stehly), estelle.delouche@univ-grenoble-alpes.fr (E. Delouche), lisa.tomasetto@univ-grenoble-alpes.fr (L. Tomasetto), patrul.ranjan@univ-grenoble-alpes.fr (P. Ranjan)

Abstract. We study the dynamics of short-period (1–3 s) seismic noise across Europe and its implication on the convergence speed of noise auto-correlation coda waves. Our aim is not to describe the source of the seismic noise with high spatial resolution, since this has already been done by a number of previous studies. Instead, the goal of this work is to study how the dynamics of the seismic noise affect the possibility of monitoring the evolution of the crust, in particular the temporal resolution and accuracy of the velocity change that can be detected.

To that end, we perform a single station analysis at all available European broadband stations in 2021 using a proxy that quantifies the extent to which the frequency content of the noise wavefield is stationary over time, independently of its amplitude variations. We show that at short periods (<3 s), the noise field in Europe is dominated by surface waves coming from the north Atlantic ocean, with also a significant contribution from the Adriatic and Aegean Seas in southern Europe. The relative contribution of these two source regions depends on the season, with the influence of the Adriatic and Aegean Sea increasing in summer.

The interplay of these two sources regions creates lateral variations in the properties of the seismic noise. Thus, the noise field is more stable in northern Europe where the influence of the Atlantic Ocean predominates, while along the Adriatic coast and around the Aegean Sea, micro-seismic events lasting several hours are regularly detected, especially in summer. This leads to strong lateral variation in the convergence velocity of the coda waves, and thus in the accuracy and temporal resolution of the velocity changes that can be detected in Europe.

Keywords. Seismic noise, Microseisms, Autocorrelation, Monitoring.

Funding. Real-time Earthquake Risk Reduction for a Resilient Europe (RISE) (Grant agreement number 821115).

Manuscript received 27 January 2023, revised 31 July 2023 and 14 February 2024, accepted 12 October 2023.

[*] Corresponding author

1. Introduction

In the last two decades, the advent of dense networks of seismic stations and the use of seismic noise to reconstruct Green's functions between station pairs have opened up new possibilities for studying the internal structure of the Earth and its temporal evolution. Indeed, several theoretical studies have established that the correlations of random wavefields between two receivers yields the Green's function of the medium between these two receivers, assuming that the wavefield is equipartitioned (see for instance Weaver and Lobkis [2001], Wapenaar [2004], Roux et al. [2005], Colin de Verdière [2006a,b], Sánchez-Sesma and Campillo [2006], Campillo [2006], Margerin and Sato [2011]).

This has led to a new interest in the study of seismic ambient noise. Indeed, the possibility to recover the Green's function between (ideally) any pair of stations has been widely and successfully used to image the Earth's structure [Shapiro and Campillo, 2004, Shapiro et al., 2005, Sabra et al., 2005], and to monitor changes in seismic wave velocity resulting from the response of the Earth's crust to seismicity and tectonic processes [Brenguier et al., 2008, Chen et al., 2010, Rivet et al., 2011, Zaccarelli et al., 2011, Froment et al., 2013, Soldati et al., 2015, Wang et al., 2019], as well as to environmental changes such as thermoelastic stress and precipitation [Sens-Schönfelder and Wegler, 2006, Meier et al., 2010, Lecocq et al., 2017, Clements and Denolle, 2018, Taira et al., 2018, Poli et al., 2020, Barajas et al., 2021, Vidal et al., 2021, Berbellini et al., 2021, Hillers et al., 2015, Wang et al., 2017, Mao et al., 2022].

The ideal case for retrieving Green's functions would be to have a spatially homogeneous distribution of stationary noise sources and to average the noise correlations over a sufficiently long time interval. However, in practice, the long-period seismic noise comes from discrete locations and the noise field is neither isotropic nor fully equipartitioned. In other words, the ambient seismic noise does not fully satisfy the assumptions of the theory. Indeed, at periods greater than 1 s, the seismic noise is mainly generated by the interaction between the atmosphere, the ocean and the solid Earth by different mechanisms depending on the period considered, and it consists mainly of surface waves with a smaller amount of body waves [Toksoz and Lacoss, 1968, Ekström, 2001, Landès et al., 2010, Boué et al., 2013, Gualtieri et al., 2014].

In the 1–20 s period band, the seismic noise is dominated by two distinct energy peaks, the primary and secondary microseisms, which are observed globally. The primary microseism has periods similar to the main swell (10–20 s) with a maximum energy at about 14 s. It results from a direct interaction between the swell and the sea floor in shallow water [Hasselmann, 1963]. The secondary microseism peak is more energetic and has -on average- a dominant period around 7 s. It is generated by the non-linear interaction of swell reflections near the coast or by swells propagating in opposite directions in the deep ocean that cause half-period (5–10 s) pressure variations [Longuet-Higgins and Jeffreys, 1950, Hasselmann, 1963, Ardhuin and Herbers, 2013]. In this particular case, the pressure fluctuation in the water column does not present an exponential decay with depth, making it possible to generate seismic noise in deep water. For primary and secondary microseisms, the complexity of the noise field is increased by lateral variations in seafloor bathymetry and in the scattering properties of the crust that affect the ocean-solid earth coupling and tend to randomise the wavefield [Saito, 2010, Ardhuin, 2018, Lu et al., 2022].

In Europe, the use of seismic noise correlations for tomographic and monitoring studies has been supported by the development of permanent networks of stations across the continent complemented by the deployment of large and dense temporary networks such as IberArray and Pyrope in the Pyrenees, Cifalps I&II and AlpArray in the greater Alpine region [Díaz et al., 2010, Chevrot et al., 2014, Zhao et al., 2015, Hetényi et al., 2018, Paul et al., 2022].

Many authors have studied the origin of seismic noise in Europe in the 3–20 s period band. Several approaches have been used to investigate the sources of seismic noise on a continental scale using either distant arrays distributed across Europe [Essen et al., 2003, Chevrot et al., 2007, Juretzek and Hadziioannou, 2016] or even seismic arrays on different continents [Friedrich et al., 1998, Stehly et al., 2006, Retailleau et al., 2017]. Other studies have instead focused on the origin of the noise at specific networks and locations [Pedersen and Krüger, 2007, Beucler et al., 2015, Tanimoto et al., 2015, Craig et al., 2016, Lepore and Grad, 2020, Guerin et al., 2022].

On the other hand, Lu et al. [2020] used a decade (2011–2019) of data collected at all European broadband stations to map lateral variations of the noise field properties. All these studies indicate that the north Atlantic ocean, in particular south of Greenland and off the coast of the British Isles and Norway, are the main sources of surface waves in the 3–20 s period band, with additional contributions from the Mediterranean coast (see for example Evangelidis and Melis [2012], Lu et al. [2022]).

Further development of imaging and monitoring methods based on noise correlations can be supported by a better understanding of the noise field and its variations in time and space. In particular, most studies to date have focused on the origin of microseisms at 3–20 s, and little is known about the generation of seismic noise at shorter periods (1–3 s). Gimbert and Tsai [2015] and Gal et al. [2015] have shown that seismic noise in the 0.5–2 s period band is mostly caused by local wind-waves occuring less than 2000 km of the seismic station rather than by the ocean swell like at periods greater that 3 s. Using three components array analysis at a dense array located in Pilbara, Autralia Gal et al. [2017] found that Rayleigh waves are more energetic than Love waves between 1.5–3 s, Rayleigh waves coming from convex coastlines, and Love waves from seafloor sedimentary basins. In addition to allowing the study of velocity changes associated with earthquakes [Maeda et al., 2010, Zaccarelli et al., 2011, Soldati et al., 2015], the 1–3 s period band is of particular interest for tracking changes in groundwater levels, providing a unique opportunity to monitor the response of the crust to the hydrological cycle [Poli et al., 2020, Barajas et al., 2021].

Unlike previous studies of the seismic noise in Europe, we do not aim at investigating the origin of the seismic noise per se. Instead, our aim is to study how lateral variations of the noise field affect the speed of convergence of the noise auto-correlations coda waves and thus the possibility of monitoring velocity changes in the Earth's crust. Indeed, we may wonder how the temporal resolution of monitoring studies is affected by the dynamics of seismic noise sources? In particular, at the European scale, do autocorrelation coda waves converge everywhere at a similar rate, or are there lateral variations that are due either to different scattering properties of the crust or to the dynamics of the seismic noise sources?

To answer these questions, we first study the origin of the seismic noise and its seasonal variations around 2 and 7 s of periods. We then introduce a proxy to quantify whether the seismic noise is stationary (Section 3). This allows us to characterise the dynamics of the short-period seismic noise at the European scale. This makes it then possible to study the relationship between the dynamics of the seismic noise and the convergence speed of the autocorrelations coda waves (Section 4). We highlight the influence of seasonal variations of the contribution of the Atlantic Ocean and of the particular dynamics of the Adriatic and Aegean seas that influence the reconstruction of coda waves. Finally, this allows us to show that the temporal resolution and the accuracy with which it is possible to measure velocity changes at short periods exhibit lateral variations across Europe. Our results shows that there is a strong contrast between southern and northern Europe, depending on whether the influence of the Adriatic/Aegean Sea or the Atlantic Ocean dominates.

2. Average noise wavefield in Europe

2.1. *Data used*

We use all broadband stations with publicly available data in Europe in 2021 located between −5 and 31 degrees of longitude and between 34 and 53 degrees of latitude. To complete the stations coverage in the Pyrenees, we included the temporary networks Pyrope (X7, 2011–2013) and IberArray (IB, 2009–2011). We thus use data from 47 European networks and 1960 stations for which we have at least 300 days of data. The stations map is presented in Figure 1. We represent with red triangles the stations with data in 2021, with blue triangles the IberArray network and with yellow triangles the Pyrope network.

2.2. *Median level in Europe*

To study the average noise level across Europe and its seasonal variations, we use an approach inspired by McNamara and Buland [2004] by analysing continuous waveform data without removing any signal such as earthquakes or instrumental glitches. We processed the vertical records of each station day by day. Each daily record was band pass filtered between 0.5 s and 300 s, corrected from the instrumental response, decimated to a sampling frequency of

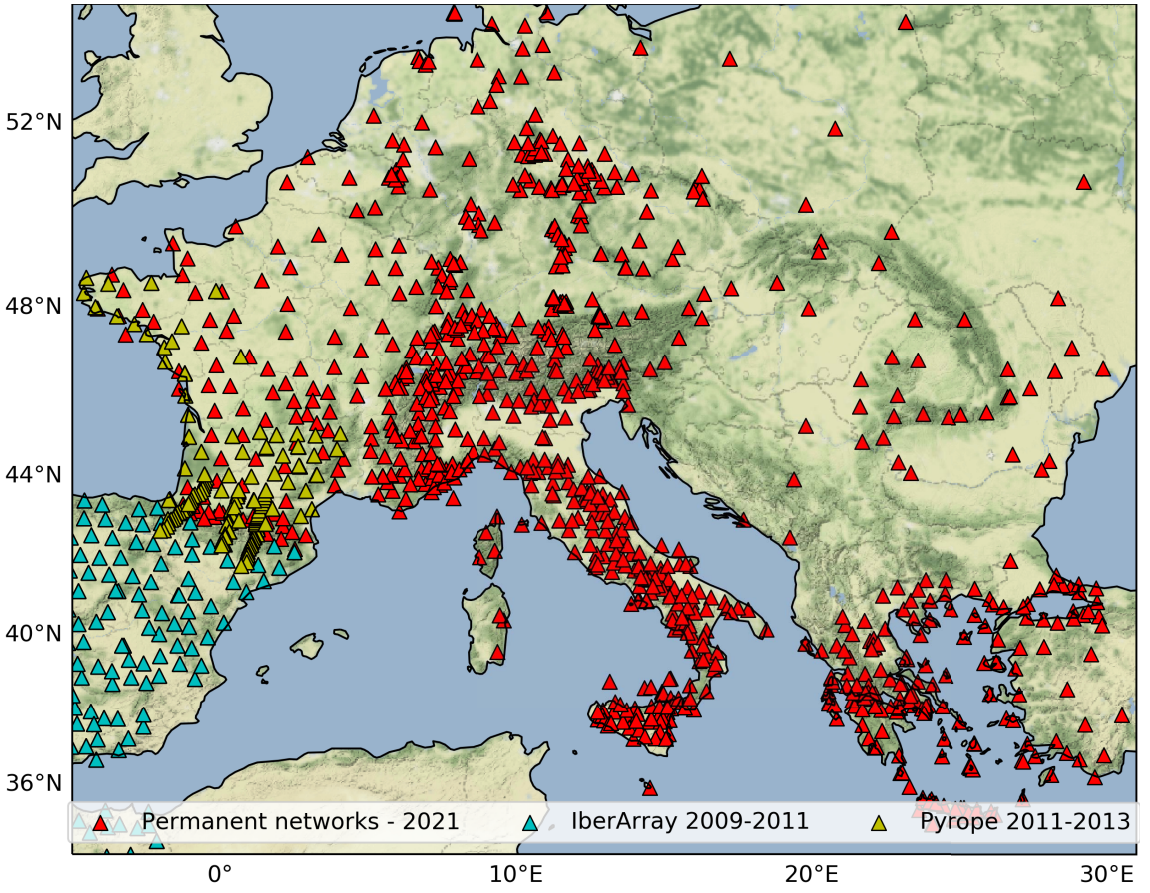

Figure 1. Map of the broadband seismic networks used in this study including permanent networks for which we use continuous noise records from 2021 (red triangles), the IberArray network (2009–2011, blue triangles) and the Pyrope network (2011–2013, yellow triangles).

5 Hz. For each station and for each day of data we compute Power Spectral Densities (PSD) with a sliding window of one hour with no overlap. A 10% cosine taper is applied to both ends of each 1 h segment to suppress the effect of side lobes in the Fast Fourier Transform. The PSD of each 1 h segment is obtained from the FFT of the seismic data. Finally the PSDs are converted into decibels with respect to velocities.

To obtain the median noise level at each station as a function of the season, we compute for each station the median noise level for January–February (winter) and July–August (summer). We remind the reader that we used data from 2009–2013 from the IBerArray and the Pyrope temporary network in the Pyrenees, and from 2021 elsewhere (see Figure 1). We use specifically the median rather than mean to reduce the contribution of large amplitude events such as earthquakes and glitches. The median noise level obtained during the winter and the summer at 2 s and 7 s of periods are presented in Figure 2. The noise level depends mainly on the distribution and energy of noise sources and on the attenuation of seismic wave during their propagation. It is also influenced by the scattering of waves by crustal heterogeneities and topography [Wu and Aki, 1985, Snieder, 1986, Levander, 1990]. In addition, sedimentary basins affect the wave field in complex ways, amplifying certain frequency ranges [Sánchez-Sesma et al., 1988, Boué et al., 2016, Gisselbrecht et al., 2023].

As shown on the lower panels in Figure 2, at 7 s in January we observe a large-scale variation of the median seismic noise level across Europe. The

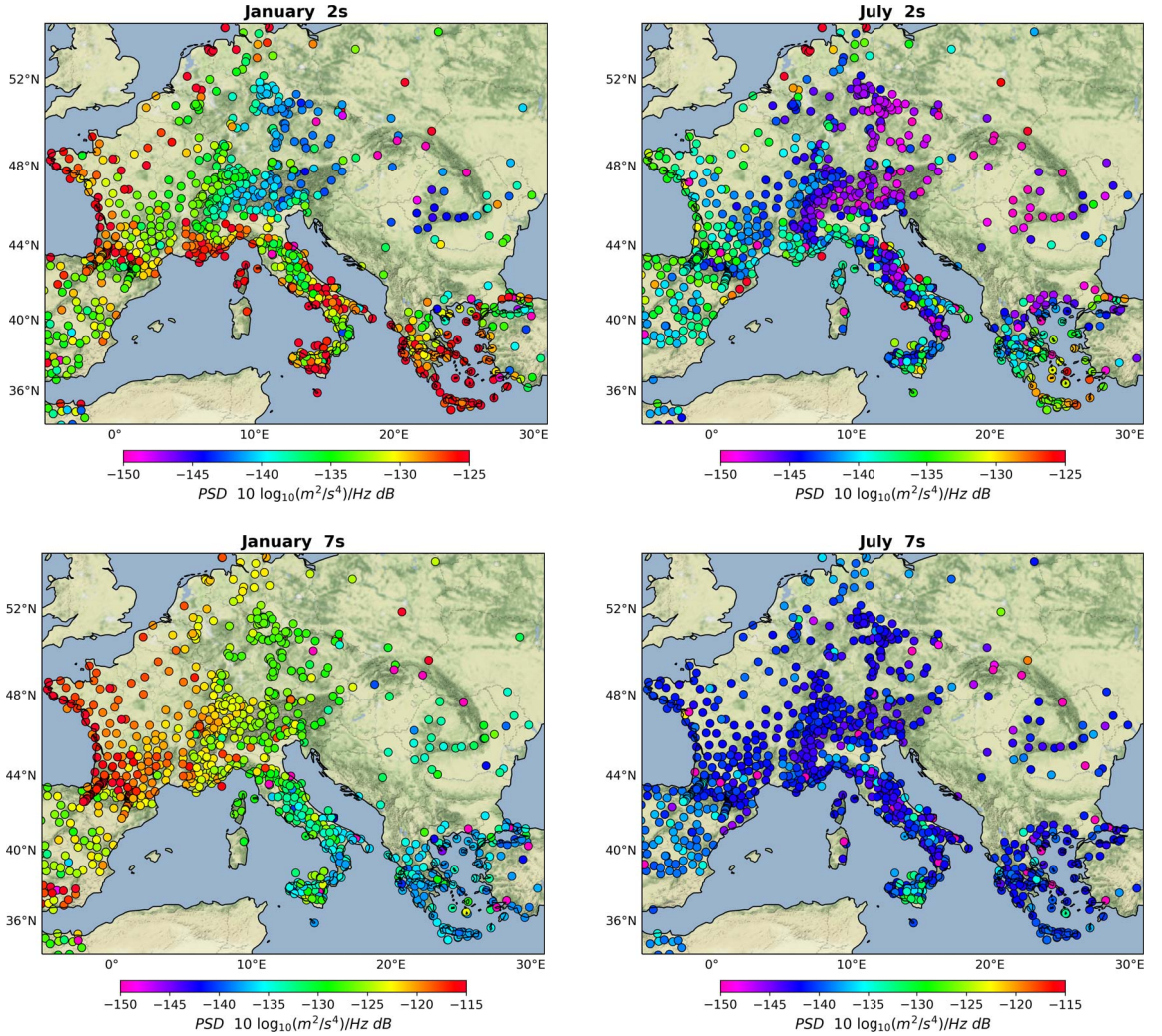

Figure 2. Spatial distribution of the median noise level at 2 s and 7 s of period in January (left) and July (right).

noise level is maximum on the west coast of France (−115 dB) and it decreases progressively towards the southeast, the minimum being reached in Greece (−140 dB). This noise level gradient is consistent with a dominant noise source located in the north Atlantic ocean as it was previously observed by various studies [Friedrich et al., 1998, Stehly et al., 2006, Chevrot et al., 2007, Kedar et al., 2008, Retailleau et al., 2017].

On the other hand, during the month of July we observe an almost homogeneous noise level in Europe, with a median level of −140 dB. This illustrates that at 7 s of period the noise level in Europe varies strongly depending on the season, the noise level being higher during the winter in the northern hemisphere when the wave height is larger in the north Atlantic ocean.

We observe that the seismic noise level differs strongly at 2 s period, indicating that the distribution of seismic noise source is not the same at 2 s and 7 s of period (Figure 2). In January at 2 s of period, the noise level is maximum on the coast reaching −125 dB on the west coast of France, southeast France, and in southern Greece. Conversely, the noise level decreases towards the East (and not towards the southeast as it was the case at 7 s of period) when moving away from the Mediterranean and Atlantic coasts.

Thus, the minimum median noise level is reached in Romania (−145 dB). This indicates that the seismic noise is mainly generated locally near the Atlantic and Mediterranean coasts.

Just as at 7 s of period, the median noise level at 2 s exhibits clear seasonal variations, the noise level decreasing in the summer. However the lateral variation of the seismic noise level remains similar during the summer and the winter. Thus in July the median noise level range reaches −135 dB in the west part of France and Spain and decreases towards the East becoming less than −145 dB past Switzerland.

In addition to this West–East gradient, we note that in Italy the noise level is larger towards the Mediterranean and the Adriatic coast (about −140 dB) than in the Apennines (−147 dB). This observation is compatible with a generation of seismic noise along the coasts. Similarly, high noise levels are also observed in Greece (for example, the Cyclades).

To summarise, the noise level maps show that the origin and the seasonal variations of the microseismic noise differ at 2 s and 7 s of period. At 7 s, the median noise level is consistent with a dominant noise source located in the north Atlantic ocean, while in the summer the homogeneity of the noise level indicates a distant origin, probably with a significant contribution of the southern hemisphere. On the other hand, there is no clear local maximum near the coasts that would indicate a local coupling. This seasonal variation implies that the quality of the Green function retrieved from cross-correlation may differ during the summer and the winter. Hence for tomographic studies, simultaneously using data recorded during winter and summer is a common way to improve the quality of the traveltime measurements performed on noise correlations. For monitoring applications, it implies that the precision of the $\delta v/v$ measurements may depend on the season.

Conversely, at 2 s of period, the lateral variations of the seismic noise are similar in January and July suggesting that the sources are always located in the same areas. In January as well as in July the maximum noise levels are reached in specific regions along the coasts, hence indicating local coastal noise sources. This is consistent with theoretical expectations: at 2 s of period the primary and secondary mechanism can generate seismic noise in shallower water than at 7 s [Longuet-Higgins and Jeffreys, 1950].

2.3. *Dominant periods in the 2–10 s period band*

Figure 3 shows a spatial map of the dominant period of the seismic noise measured in the 2–10 s period band corresponding to the secondary microseism. It represents the period at which the median PSD of the seismic noise record is maximum. The median PSD is defined as the median of the PSDs computed with a one-hour sliding window. If the noise originated from a single region, and assuming a constant quality factor across Europe, the dominant period of the noise should increase smoothly with distance from the source [Lu et al., 2022]. However, this is not what we observe in either January or July (Figure 3) between 2–10 s, the seismic noise is influenced by two distinct source regions located in the north Atlantic and in the south-east Mediterranean. Thus the spatial distribution of the dominant period results from the interaction between these two source areas. This interaction is itself dependent on the season.

In January (Figure 3a), the dominant period is 6 s in northern Europe (France, Germany, Switzerland). It decreases progressively towards the south-east to about 5 s in northern Italy. This would be consistent with a dominant source located in southeastern Europe. However, we note an abrupt change between northern Italy and southern Italy where the dominant period is less than 3.5 s. In Greece values lower than 3 s are observed around the Aegean Sea. These observations are consistent with a dominant noise source in the south-east Mediterranean explaining the north-west/south-east gradient of the dominant period, with moreover a short-period noise source close to the southern Italy coastline explaining the abrupt change observed in Italy.

In July, the spatial distribution of the dominant period is completely different (Figure 3b). We observe a shift toward shorter periods, with a dominant period of 5 s throughout Europe with 3 exceptions: in southern Greece, near Galicia (Spain) and at several stations on the Italian, French and Spanish coasts, the dominant period is less than 3.5 s. This suggests that short period microseismic noise is generated locally close to in these areas.

These observations have two implications for monitoring studies: the seasonal behaviour of the seismic noise does not guarantee that noise correlations coda waves converge to a similar waveform in summer and winter and as we will see in the next

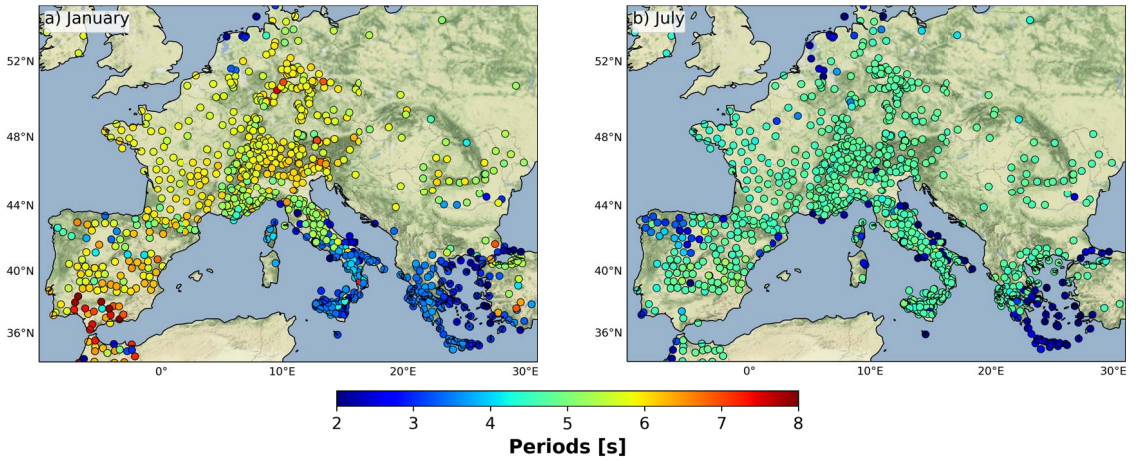

Figure 3. Spatial distribution of the dominant period of seismic noise: period at which the median PSD of the seismic noise is maximum in (a) January and (b) July. The median PSD is defined as the median of PSDs computed with a sliding window of one hour that is shifted by 5 min.

sections the coda of correlations in coastal regions dominated by a 2 s period in summer converges more slowly.

3. Dynamic of the noise wavefield in Europe in the 0.5–0.7 Hz frequency band

In the previous section we presented the noise level in Europe at 2 s and 7 s and the dominant period of seismic noise records. In the present section we study the dynamics of the seismic noise and its temporal evolution specifically in the 0.5–0.7 Hz frequency band. We choose specifically to focus on this frequency band since it is often used to monitor the temporal evolution of the crust using seismic noise correlations in particular for tracking groundwater level change [Poli et al., 2020, Barajas et al., 2021]. Moreover, little is known about the generation of seismic noise in the period band, since previous studies on the secondary micro-seismic noise tend to focus on the 3–20 s period band. We use only European networks for which we have continuous record in 2021, and we thus discard the data of the IberArray and Pyrope experiments.

3.1. *Quantifying the stationarity of the wavefield*

Our goal is to quantify the impact of the dynamic of the seismic ambient noise on the convergence of coda waves obtained from noise correlations. To that end, in this section we define a proxy to quantify whether the seismic noise is stationary or not. We look for a proxy that does not depend on the amplitude of the seismic noise, since a change of noise level per se does not modify the waveform of the correlations. Instead, we design a proxy which depends only on the temporal evolution of the frequency content of the seismic noise.

To define this proxy, we first compute at each station PSDs with a 30 min sliding window which is shifted by 5 min. These 30-min PSDs are then used to quantify the temporal evolution of the frequency content of the seismic noise over several time scales ranging from 1 day to 30 days, independently of the amplitude of the seismic noise. We thus define a stationarity coefficient (SC) obtained in the following way:

- Each 30 min PSD is smoothed over frequency using a moving average gaussian filter having a width of 0.05 Hz. We thus study specifically the first order variations of the frequency content of the noise.
- Each 30 min PSD is then normalised by its energy in the target frequency band, i.e. 0.5–0.7 Hz.
- At each date, we define the current PSD as the PSD computed with a 30 min window that ends at the current date, and the N-days PSD

as the PSDs averaged over the previous N-days, with N ranging from 1 day to 30 days. We then compute the normalised correlation coefficients of the current PSD and each N-days PSD. We note that this correlation coefficient is independent of the noise level and depends only on temporal evolution of the frequency content of the noise.

- Finally, we define the stationarity coefficient for each 30 min window as the lowest coefficient of correlation between the current and the N-days PSDs. A stationarity coefficient close to 1, indicates that the current 30 min PSD is similar to the PSDs averaged over the previous N days, i.e. that the noise is stationary over all time scales. A value close to 0 indicates that the current PSD differs strongly from at least one of the PSD averaged over the N previous days, i.e. that the frequency content of the noise is not stationary on at least one time scale.

3.2. *Stationarity coefficient at a single station in Italy*

Figure 4 shows as an example the stationarity coefficient measured in the 0.5–0.7 Hz frequency band at the station NRCA located close to Norcia in Italy from June 6th to June 30th. As shown on the upper panel, the stationarity coefficient typically varies between 0.96 and 1 which reflects the usual variability of the frequency content of the seismic noise. In addition to these variations, we observe several events on June 14, 15, 18 and 30 during which the stationarity coefficient drops to values below 0.94 for a few hours.

Looking at the spectrogram presented on the lower panel in Figure 4, we can correlate changes in the stationarity coefficient with changes of the frequency contents of the noise. We first observe that in central Italy, the seismic noise has a maximum of energy between 0.2 and 0.4 Hz which corresponds to the secondary microseismic peak. This peak of energy is continuous in time. Above 0.4 Hz,—apart from particular events—the energy of the noise decreases continuously with frequency. In addition to this average behavior, we observe two kinds of microseismic events:

- The first type of events are characterised by a clear increase (~5–10 dB) of the noise level above 0.4 Hz. This occurs on June 14, 15, 22, and 30. These events modify the decay of the noise level with frequency measured between 0.5 and 0.7 Hz, and are thus associated with a drop of the stationarity coefficient which become less than 0.94 (Figure 4 upper panel).
- On June 18th we observe a second kind of event: a local maximum of energy appears between 0.5 and 0.8 Hz, the noise level remaining in the usual range. This type of event, characterized by a first order change in the shape of the spectrum but without a significant change in noise level, is associated with a sharp drop in stationarity coefficient which become less than 0.9.

This example illustrates that the stationarity coefficient computed in the 0.5–0.7 Hz allows us to distinguish the usual fluctuations of the frequency content of the seismic noise ($SC > 0.96$) from discrete events lasting a few hours ($SC < 0.94$) corresponding to either (1) microseismic events characterized by a sharp increase in the noise level between 0.4–0.6 Hz, or (2) to a first order change in the shape of the spectrum.

3.3. *Stationarity coefficient maps for two particular events*

In this section we quantify the spatial extent of the noise wavefield perturbations that were introduced in the previous section. We would like to know if they are detected at the scale of Europe, or if on the contrary they are located in a particular region. To that end, we look at the spatial distribution of the stationarity coefficient for the events of June 30th and June 18th that were discussed in the previous section.

3.3.1. *Stationarity coefficient map for the June 30 event*

The first event that occurred on June 30th was detected along the Adriatic coastline as shown in Figure 5. The lower panel in Figure 5 shows the seismic noise recorded at the station IV.NRCA located in central Italy (see Figure 4) filtered in the 0.5–0.7 Hz frequency band. The time series runs from June 29

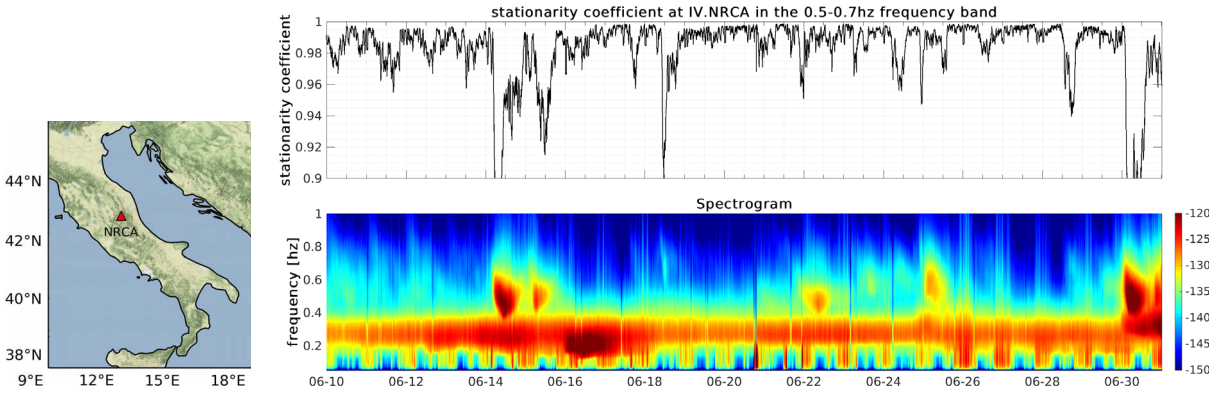

Figure 4. (Left) Map showing the location of the NRCA station located in Norcia, Italy. (Right, upper panel) Stationarity coefficient measured at the station NRCA in the 0.5–0.7 Hz from june 6th to June 30th. (Right, lower panel) Spectrogram in dB measured at the station NRCA in the 0.05–1 Hz frequency band on the same date. The 0.5–0.7 Hz frequency band where the stationarity coefficient is measured is shaded in gray. The dates of type I and type II events are indicated by red and white marks.

to July 2. The amplitude of the seismic noise increases by a factor of 3 from June 30 to July 1 compared to the noise level of June 29th. This change in amplitude observed in the time domain is also visible in the spectrogram computed at the same station (Figure 5, third panel): in addition to the secondary microseismic peak visible at 0.2–0.4 Hz, an increase in energy is observed between 0.4 and 0.7 Hz from June 30 to July 2.

In order to see which European stations are affected by this event, we present in Figure 5a, the value of the stationarity coefficient of June 30, 2021 averaged between 3 to 9 a.m. We note that over the whole of Europe the stationarity coefficient is greater than 0.97 except around the Adriatic Sea, in particular in Italy and Slovenia where we obtain values lower than 0.95. This indicates that this event originates from the Adriatic Sea.

This event is also associated with an increase in noise level between 0.4 and 0.7 Hz. Figure 5b shows the difference between the measured noise level measured on June 30, 2021 between 3:00–9:00 a.m. and the noise level averaged over the past 10 days. This difference is expressed as a percentage. Across Europe the noise level is similar on June 30 and the previous 10 days, with the exception of the stations located around the Adriatic Sea in Italy and Slovenia where the noise level increases by more than 3%.

To summarize, this microseismic event lasted almost 2 days and induced a change in noise level and in the frequency content of the noise detectable locally around the Adriatic Sea in Italy and Slovenia, but not elsewhere in Europe.

3.3.2. *Stationarity coefficient map for the June 18 event*

The second event occurred on June 18th around 4 p.m. In contrast to the previous example, it is not associated with a significant change in the amplitude of the noise level at station IV.NRCA (Figure 6, bottom panel). As shown in the spectrogram in Figure 6, usually between 0.6 and 0.8 Hz, the noise energy decreases with frequency, except on June 18 when a local maximum of energy is observed. However, the absolute noise level varies little, the noise level being about −135 dB on June 18 compared to −140 dB on the other days.

This change in the shape of the noise spectrum, induces a decrease in the stationarity coefficient measured on the Adriatic coast of Italy as shown in Figure 6a. Elsewhere in Europe, the noise is stationary, the stationarity coefficient remaining above 0.96 except around the Aegean Sea. However, this event is not associated with a significant change in noise levels, so that at the European stations the noise level is similar on June 18 and during the previous 10 days (Figure 6b). This illustrates the

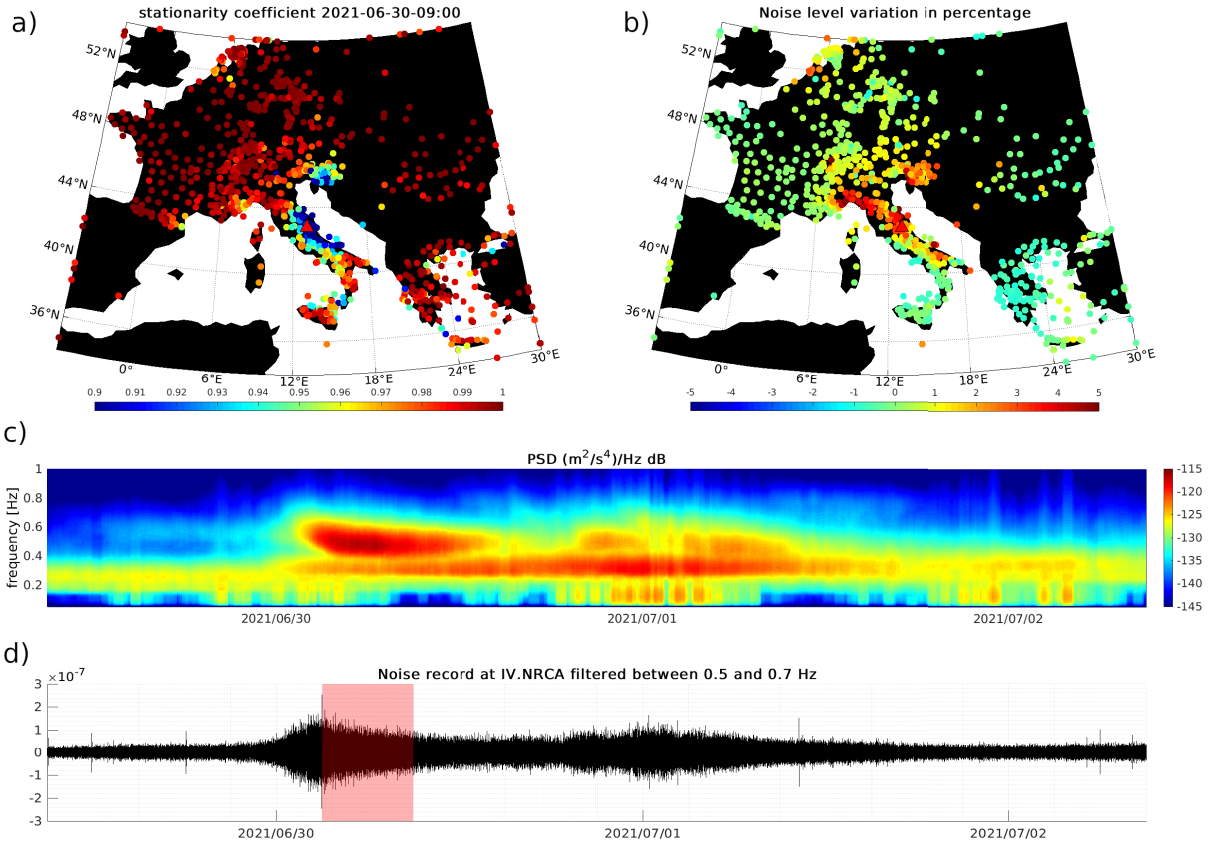

Figure 5. Detail of the June 30 microseismic event. (a) The spatial distribution of the stationarity coefficient measured between 0.5 and 0.7 Hz on June 30, averaged from 6:00 a.m. to 9:00 a.m. (b) Map of the relative change in the percentage of the average noise level on June 30 between 3:00 a.m. and 9:00 a.m. compared to the average noise level of the last 10 days. (c) Spectrogram in dB computed at the station NRCA located in central Italy from June 29 to July 2 with a sliding window of 30 min shifted by 5 min. (d) Vertical noise record at the station NRCA filtered between 0.5 and 0.7 Hz from June 29 to July 2.

stationary coefficient allows detecting events that are not clearly visible on the absolute noise level but that are nevertheless likely to affect the noise correlations waveform.

3.4. *Stationarity of the noise field at the scale of Europe*

In this section, we seek to quantify whether the noise wavefield is stationary at the scale of Europe. In particular, we wish to identify lateral variations in the dynamics of the seismic noise wavefield that could affect seismic waves velocity variations measurements ($\delta v/v$) obtained from seismic noise correlations.

On Figure 7, we present the percentage of time when the stationarity coefficient is less than 0.98 in the 0.5–0.7 Hz frequency band during the months of January (left panel) and July (right panel). First of all, we observe larger values in July than in January indicating the seismic noise is more unstable in summer than in winter. In January the wavefield is extremely stable in the north of the Alps, especially in France, Germany, Holland and Romania. On the contrary, the stationarity coefficient is lower than 0.98 more than 20% of the time around the Aegean Sea and in Italy along the Mediterranean and Adriatic coasts. This means that there is a particular dynamic in the Aegean and Adriatic seas generating microseismic

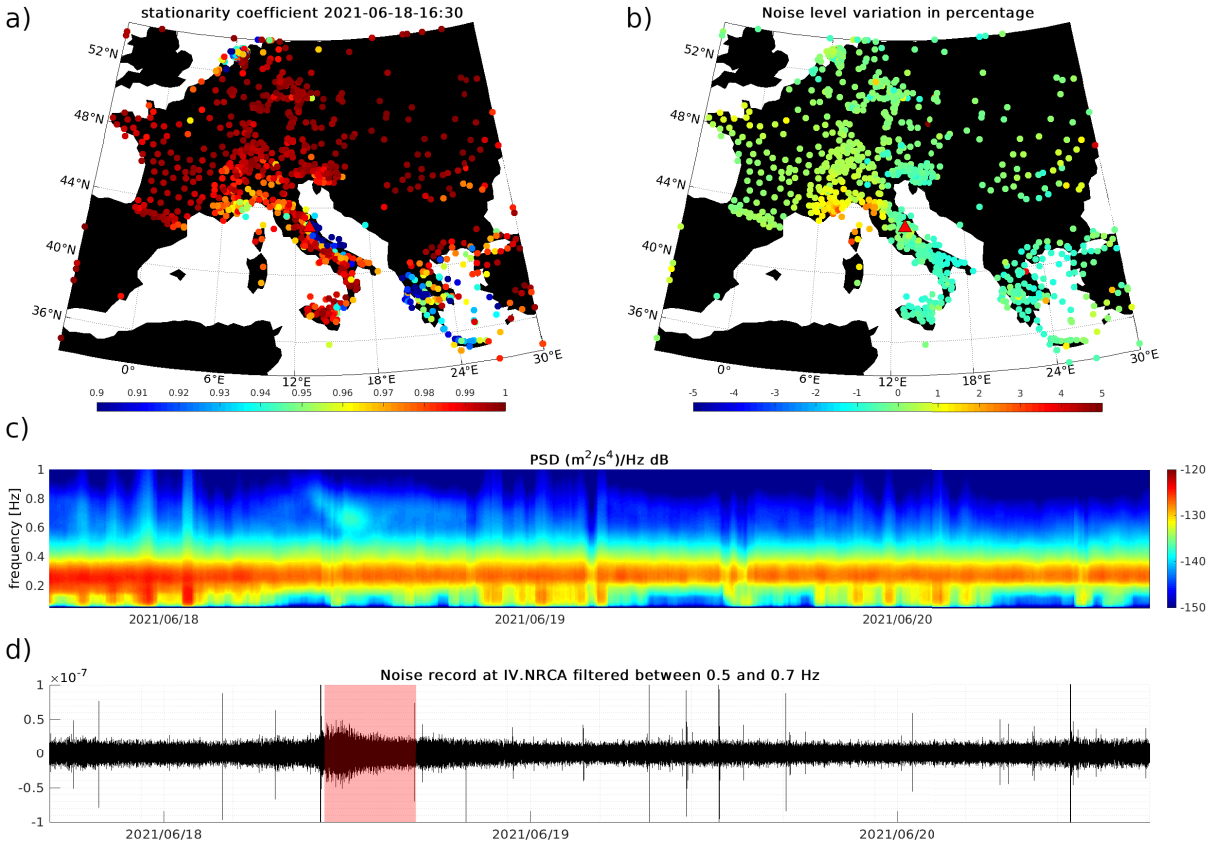

Figure 6. Detail of the June 18 microseismic event. (a) The spatial distribution of the stationarity coefficient measured between 0.5 and 0.7 Hz on June 18, averaged from 13:30 to 16:30 a.m. (b) Map of the relative change in the percentage of the average noise level on June 30 between 10:30 and 16:30 a.m. compared to the average noise level of the last 10 days. (c) Spectrogram in dB computed at the station NRCA located in central Italy from June 17 to June 20 with a sliding window of 30 min shifted by 5 min. (d) Vertical noise record at the station NRCA filtered between 0.5 and 0.7 Hz from June 17 to June 20.

events that are detected between 0.5 and 0.7 Hz. The fact that these two seas are almost closed areas may explain this particular dynamic by favouring coastal reflections.

This contrast between Italy, Greece and the rest of Europe is more significant in July (Figure 7, right panel). The stationarity coefficient is below 0.98, more than 30% of the time around the Aegean Sea, the Adriatic Sea and in the south of France along the Mediterranean coast. Conversely, few events are detected elsewhere in Europe.

This indicates that there is a particular dynamic off the southern coast of Europe that generate high frequency (>0.4 Hz) microseismic noise, especially in the Adriatic and Agean seas that are enclosed spaces. These high-frequency events are visible mainly along the southern coastline of Europe, and attenuate rapidly so that they are not detected further away on the continent. The number of detected events is larger during the summer than during the winter (Figure 7). It is difficult to say whether this is because microseismic noise coming from the north Atlantic has less energy in summer than in winter (Figure 2) which reveals the dynamics of the Mediterranean, or whether the Mediterranean is indeed more active in summer than in winter.

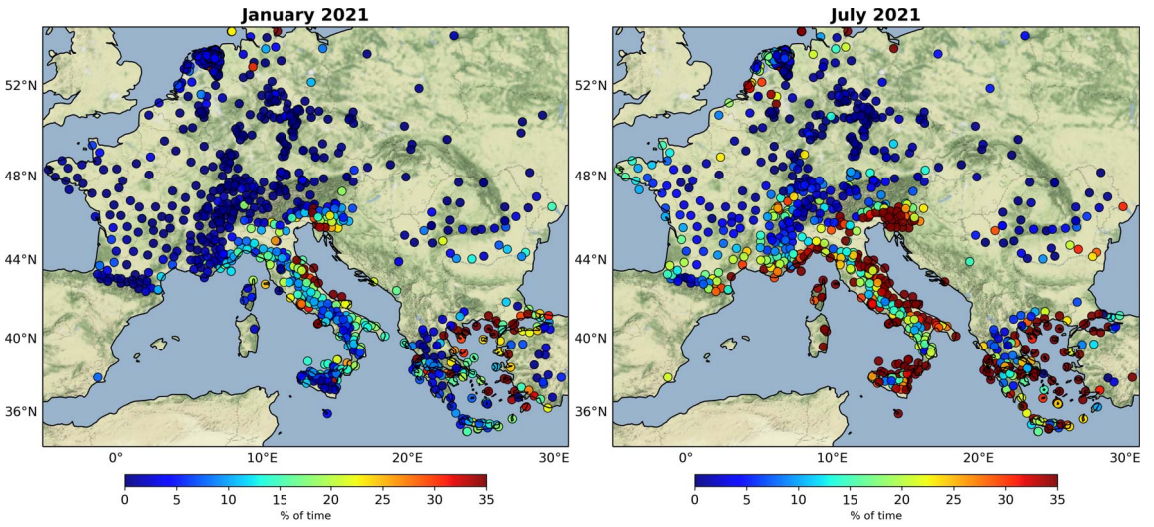

Figure 7. Percentage of time where the stationarity coefficient is less than 0.98 in January 2021 (left) and August 2021 (right) in the 0.5–0.7 Hz frequency band.

4. Dynamic of seismic noise and convergence of auto-correlations coda waves

Central Italy and Greece are amongst the most seismically active areas in Europe so that there is a particular interest to follow the spatial-temporal evolution of the mechanical properties of the earth's crust related to the seismic cycle in these regions. Seismic noise (auto)-correlations coda waves offers a unique opportunity to measure the evolution of seismic wave velocity ($\delta v/v$) over time [Brenguier et al., 2008]. Measuring the $\delta v/v$ on several frequency bands allows in theory to measure the changes at different crustal depths. However, in southern Europe, above 4 s of period, seasonal variations in the distribution of noise sources create apparent velocity variations that are strong enough to mask the dynamics of the crust. Thus several studies such as Poli et al. [2020], Barajas et al. [2021] focus specifically on the 1–2 s period band. Measuring the $\delta v/v$ at different lapse-time makes it then possible to assess at least qualitatively the depth of the detected changes in the crust [Obermann et al., 2013, 2014, Poli et al., 2020].

To monitor the temporal evolution of the medium using seismic noise correlation coda waves, ideally we would like the noise sources to be stable over time so that changes in the coda would reflect only changes in the medium and would not be biased by changes in the distribution of the noise sources. However, we have seen that between 1–3 s the seismic noise field exhibits seasonal variations and that moreover microseismic events lasting several hours up to a few days are regularly detected around the Adriatic and the Aegean Sea. They can represent up to 30% of the records around the Adriatic coast.

We now quantify the impact of these microseismic events on the convergence speed of noise correlations coda waves. In other words, we investigate whether the dynamics of the noise affect the temporal resolution at which changes can be detected in the crust. To monitor the temporal evolution of the crust, the most common approach is to evaluate the relative change in velocity over time by comparing coda waves of a reference correlation with a set of correlations computed with a sliding window of N-days.

Noise correlations coda waves emerge from a constructive averaging process, so that the signal-to-noise ratio of the coda waves depends on the amount of data used to compute the correlations [Sabra et al., 2005, Weaver and Lobkis, 2005]. Weaver et al. [2011], have shown that when the stretching method is used to infer velocity changes, the root mean square of the errors of the estimate of the relative velocity change between a reference correlation and an

N-days (auto)correlations is given by:

$$\mathrm{rms}(\delta v/v) = \frac{\sqrt{1-C^2}}{2C}\sqrt{\frac{6\sqrt{\frac{\pi}{2}}T}{\omega_c^2(t_2^3-t_1^3)}}, \qquad (1)$$

where C is the correlation coefficient between the reference and the N-days correlation, T is the inverse of the frequency bandwidth, ω_c the central pulsation, t_1 and t_2 are begin and end time of the coda window analysed. Hence, the accuracy of the $\delta v/v$ measurements increases with the correlation coefficient between the reference and the N-days correlations. This correlation coefficient C depends on several factors, amongst which the amount of data used to compute the correlations, the dynamic of the seismic noise wavefield, the attenuation and scattering properties of the medium.

To quantify the precision of the $\delta v/v$ measurements, we study how C varies spatially when considering 1-day, 3-days and 20-days auto-correlations. We study specifically the 2–3 s period band which is particularly interesting for monitoring studies of southern Europe, longer periods measurements being contaminated by seasonal changes of the source. We consider specifically auto-correlations to avoid any influence of varying inter-station distance. We study separately the convergence of autocorrelations computed at each European station in summer (July–August) and winter (January–February), and we consider two different time windows in the coda: 5–25 s which correspond to the beginning of the coda and to a single scattering regime and 20–40 s where coda waves are closer to a multiple scattering regime.

Specifically, for each station, we compute daily auto-correlations in summer and winter. We did not apply any temporal or spectral normalization to the noise records as our aim is not to discuss the effect of processing on the convergence of the auto-correlations. The daily auto-correlations are normalized to one and then stacked to obtain N-day correlations. This normalization reduces the contribution of the most energetic days. For each season, we define a reference auto-correlation that is the correlations averaged over the considered season (2 months). To evaluate the average correlation coefficient between N-days auto-correlations and the reference, we select randomly N daily auto-correlations that are then normalized to one and stacked to obtain an N-days auto-correlation. We then compute the correlation coefficient between this N-days auto-correlation and the reference auto-correlation for two different time windows: 5–25 s and 20–40 s that may typically be used for monitoring studies. This procedure is repeated 10 times and we average the result to obtain the average correlation coefficient between N-days auto-correlations and the reference. Here we show the result obtained for daily auto-correlations ($N = 1$), 3-days ($N = 3$) and 20-days auto-correlations ($N = 20$).

4.1. *Results for the 5–25 s time window*

We present the results obtained for the 5–25 s (beginning of the coda) and the 20–40 s time windows in Figures 8 and 9, respectively. The bottom panel of Figure 8 shows an example of auto-correlation computed at station IV.NRCA and filtered between 2 s and 3 s period, with the 2–25 s coda window shaded in yellow. We note immediately a strong correlation between the results presented in Figures 7 and 8a,b: the average correlation coefficients calculated between daily auto-correlations and the reference are strongly correlated to the percentage of time where the stationarity coefficient is less than 0.98 (Figure 7). This is true for the winter (Figure 8a) and in summer (Figure 8b). In winter, the average correlation coefficient is close to 1 in France, Germany, the Netherlands and Romania, where the stationarity coefficient is greater than 0.98 more than 95% of the time. Conversely, around the Adriatic Sea, the coda of daily auto-correlations differs from the reference and the correlation coefficients are around 0.7 in Italy and 0.5 in Slovenia.

In summer, we observe a contrast between the Mediterranean coast and the rest of Europe: the average correlation coefficients are close to 1 everywhere in Europe except along the Mediterranean and Adriatic coast where we observe correlation coefficients between 0.2 and 0.7. This result is directly correlated with the stationarity coefficient analyses presented in Figure 7: the areas where high frequency microseismic events are detected are those where the daily auto-correlations coda waves differ the most from the reference.

Considering 3-day autocorrelations, the correlation coefficient becomes more spatially homogeneous in winter and summer (Figure 8c,d). However, we still observe the imprint of the dynamics of

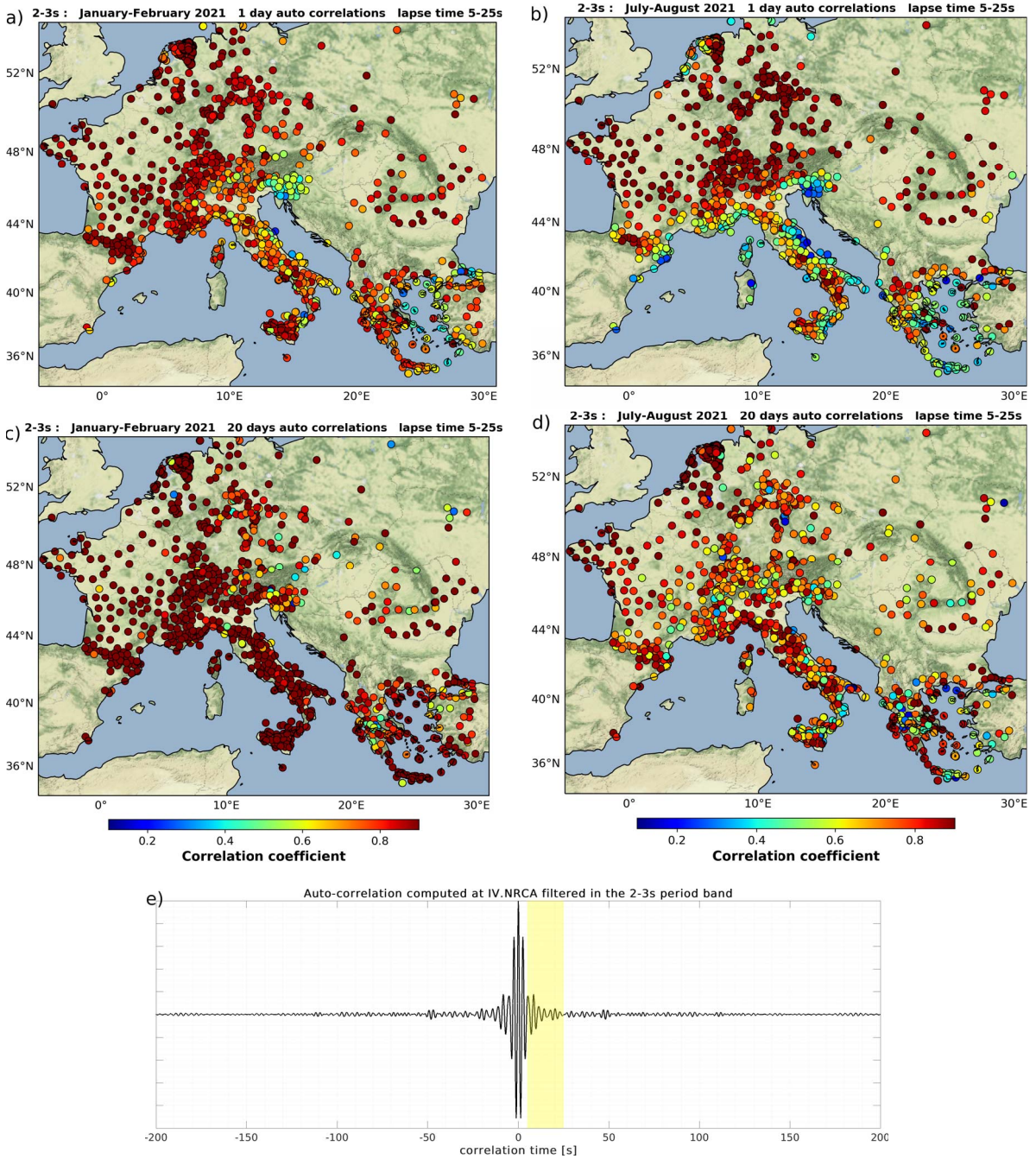

Figure 8. Average correlation coefficient between one day auto-correlations and a reference averaged over two months obtained in the 2–3 s period band and for the time window 5–25 s (a) in January–February and (b) in July–August. (c), (d), (e), (f) are similar to (a) and (b) but for 3 and 20-days auto-correlations. (g) Example of an auto-correlation at the Italian station NRCA filtered in the 2–3 s period band and averaged over one year (2021). The 5–25 s time window that is studied here is shaded in yellow.

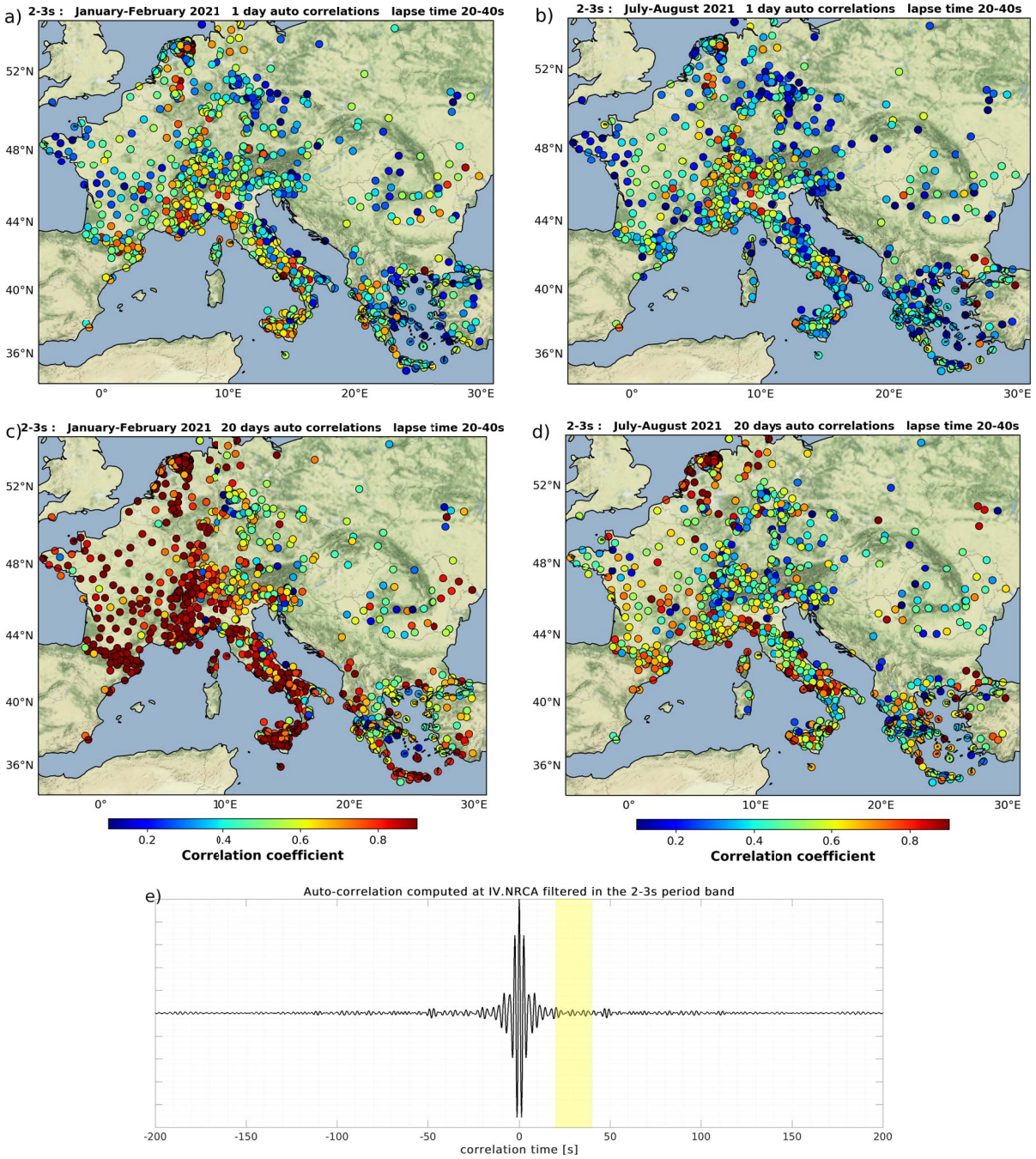

Figure 9. Average correlation coefficient between one day auto-correlations and a reference averaged over two months obtained in the 2–3 s period band and for the time window 20–40 s (a) in January–February and (b) in July–August. (c), (d), (e), (f) are similar to (a) and (b) but for 3 and 20-days auto-correlations. (g) Example of an auto-correlation at the Italian station NRCA filtered in the 2–3 s period band and averaged over one year (2021). The 20–40 s time window that is studied here is shaded in yellow.

noise sources on the convergence speed of the auto-correlations coda waves: the mean correlation coefficient between the 3-days correlations and the reference are close to 0.8 in Italy and around the Aegean Sea and greater than 0.9 further north. In summer correlation coefficients are lower, especially near the Mediterranean and Adriatic coasts. In other words, the noise wavefield is less stationary during the summer than the winter (Figure 7) which slows down the convergence of the auto-correlations coda waves. On the other hand with 20-days autocorrelations, the correlation coefficient are close to one everywhere in Europe whatever the season (Figure 8e,f).

4.2. *Results for the 20–40 s time window*

As we go into larger lapse-time, coda waves are more scattered by the medium heterogeneities, so that we expect to lose gradually the imprint of the source. This could reveal the influence of the later variations of the crust on the convergence speed of the coda waves. Lu et al. [2020] have shown that the wavefield is more random in the Alps which constitute a highly heterogeneous medium. However, as shown in Figure 9, we do not observe a clear correlation between the convergence of the coda waves and the geology: despite the Earth's crust in the Alps and the Apennines is thought to be highly heterogeneous, it does not improve significantly the convergence of the coda waves at least in the 20–40 s lapse time window.

On the other hand, the influence of the dynamic of the seismic noise wavefield is still clearly visible and is two-fold. Firstly, the convergence of the auto-correlation coda waves depends strongly on the season. Considering 3 days or 20-days auto-correlations (Figure 9c–f), the correlation coefficients are larger during winter when the frequency content of the noise is more stable than in summer. This is especially true in the westernmost part of Europe. Secondly, during winter and summer we observe lateral variations. With 3-days auto-correlation (Figure 9c,d) there is a clear contrast between Western and Eastern Europe. In winter the average correlations coefficient with the reference is greater than 0.7 in France and Switzerland, and less than 0.5 in Romania, Greece, Slovenia and Italy along the Adriatic coastline. This lateral variation remains clearly visible in winter and summer when considering 20-days auto-correlation (Figure 9e,f).

4.3. *Temporal resolution for monitoring studies in the 2–3 s period band*

We now look at the extent to which the dynamics of the seismic noise, and in particular the microseismic activity around the Adriatic and Aegean seas limits the temporal resolution with which it is possible to measure velocity changes between 2 and 3 s. To that end, we map the spatial variation of the smallest number of days N for which the average correlation coefficient C between an N-day auto-correlation and a 2-month reference auto-correlation is greater than or equal to a given threshold (Figure 10). The reference auto-correlation being averaged over 60 days, we explore a numbers of days N ranging from 1 to 59.

In Figure 10a,b we represent the number of days N required to get a correlation coefficient C of 0.95 considering the coda time window 5–25 s. According to Equation (1), when measuring relative velocity changes $\delta v/v$ with the stretching method, a correlation coefficient of 0.95 over the time window 5–25 s between 2 and 3 s of period implies that the errors on the estimate of the relative velocity changes have a root mean square of 0.07% [Weaver et al., 2011]. This may seem large, as the velocity changes associated with large magnitude earthquakes and the hydrological cycle are of the order of 0.1% [Sens-Schönfelder and Wegler, 2006, Brenguier et al., 2008, Chen et al., 2010, Zaccarelli et al., 2011, Barajas et al., 2021, Mao et al., 2022]. This is due to the fact that we consider measurements made at a single station over a relatively small time window (5–25 s). In winter, the convergence speed of the auto-correlation in the 5–25 s time window is faster in France ($N < 10$ days) than further east in Germany, Switzerland, and Italy ($N > 15$ days). In summer the speed of convergence decreases as the noise field is less stationary. More than 20 days are required to get a correlation coefficient greater than 0.95 along the Mediterranean Adriatic coast and around the Aegean sea.

Figure 10c,d represent the number of days N needed to obtain on the 5–25 s time window a correlation coefficient C of 0.8. This corresponds to an RMS of the $\delta v/v$ measurement errors of 1.6%. We see a sharp contrast between two regions: in winter it takes less than 3 days in the northwest (France, Germany, Switzerland) to obtain a correlation coefficient of 0.8. On the contrary, it takes more than 3 days in Italy, Austria and Slovenia. In summer, the

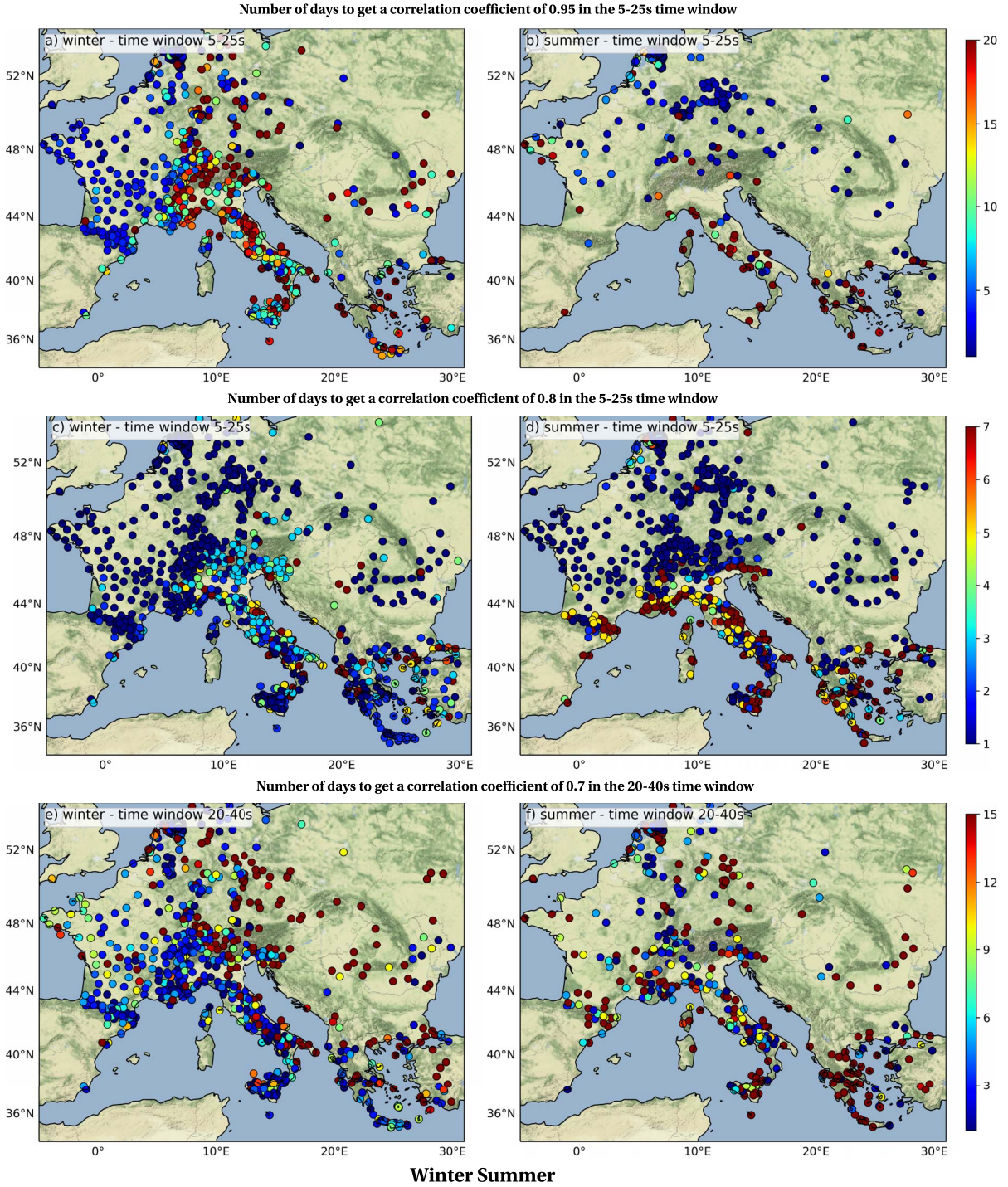

Figure 10. Number of days required to get a correlation coefficient greater than 0.95 between a reference auto-correlation averaged over the season (2 months) and a N-day auto-correlation, in the time window 5–25 s corresponding to the beginning of the coda, in (a) winter (January–February) and (b) summer (July–August). (c) and (d) are similar to (a) and (b) but for a correlation coefficient of 0.8. (e) and (f) are similar to (a) and (b) but for the 20–40 s time window and a correlation coefficient of 0.7.

spatial variation of N relates directly to the percentage of time for which the stationarity coefficient is lower than 0.98 (Figure 7): the coda of correlation converges more slowly in Greece, Italy, on the south coast of France ($N > 10$ days) where short period microseismic events are detected, and the convergence is faster on the rest of the continent ($N < 3$ days) where the noise is more stationnary.

Figure 10e,f presents the speed of convergence of the auto-correlations coda waves over the 20–40 s time window for $C = 0.7$. This corresponds to a RMS of the $\delta v/v$ measurement errors of 1.1%. For this time window the results are different: the effect of the dynamic of the noise sources is less visible. In particular in summer, the number of days required to achieve $C = 0.7$ varies randomly from site to site with no clear regional variations.

These results indicate that the evolution of noise sources over time, the interaction between the north Atlantic and the southeastern Mediterranean source region and its seasonal variations, the dynamics of sources on smaller time scales in the Adriatic and Aegean Seas, limits the convergence speed of the noise auto-correlations coda waves and thus the temporal resolution of monitoring studies. The impact of local noise sources along the coast limits the temporal resolution particularly on the 5–25 s coda window. Seasonal variations in seismic noise affect the two time windows 5–25 s and 20–40 s, the convergence being slower in summer than in winter. Thus, even when going further into the coda, the imprint of the source dynamics is still visible. In winter as in summer, there is a clear difference between Western and Eastern Europe, the temporal resolution of the $\delta v/v$ measurements decreasing towards the East.

5. Conclusion

The aim of this work was to study the relationship between the dynamics of the noise field across Europe and the convergence speed of noise auto-correlation coda waves. It shows that the accuracy and temporal resolution with which it is possible to detect changes in the medium at 2 s period presents strong seasonal and lateral variations that depends on the time window which is analysed.

The noise level maps computed using all available broadband seismic stations in Europe in 2021, complemented by temporary stations from the Pyrope and IberArray networks, show strong seasonal variations at 2 s periods and a clear increase in noise level near the Atlantic and Mediterranean coast. This suggests that the seismic noise originates simultaneously from the Mediterranean Sea and the Atlantic Ocean and attenuates as it propagates across the continent (Figure 2).

To study the dynamics of the noise field, we introduce a proxy that quantifies the non-stationarity of the frequency content of the noise independently of its amplitude. It shows that in the regions mainly influenced by the north Atlantic ocean, the frequency content is stable over time which is favourable for monitoring the Earth's crust (Figure 7). Conversely, this proxy allows us to detect short periods microseismic events originating from the southeast of the Mediteranean sea. This highlights that unlike the north Atlantic ocean, the Mediterranean sources are intermittent and generate an unstable wavefield over time (Figures 5, 6).

Noise level maps and noise stationarity maps (Figures 2, 7) show that the dynamics of the seismic noise operates on two distinct time scales that modulate the speed of convergence of correlations coda waves. First, the noise field evolves seasonally: this results in seasonal changes in the noise level, but also in the relative influence zones of the Atlantic Ocean and the Mediterranean Sea. In addition, there are dynamics on a smaller time scale of the order of hours to days related to the intermittent generation of short period noise by the Adriatic and Aegean Seas, which are closed areas.

The contribution of these two main areas and the existence of these two time scales imply that the convergence speed of the correlation coda waves varies spatially, and that this spatial variation itself depends on the season and the lag-time considered. The beginning of the coda is the most sensitive to the dynamics of the noise sources over short times, and its convergence speed directly reflects the lateral variations of the noise non-stationarity (Figures 7, 8). At longer times, over the 20–40 s coda window, convergence is slower, the influence of Mediterranean dynamics is weaker, but there remains a strong contrast between Western Europe where convergence is faster while as one moves away from the Atlantic Ocean, convergence of correlations slows down (Figure 9).

To summarise, this study shows that the spatial and temporal variability of the noise sources

determines to first order the accuracy and temporal resolution with which it is possible to detect changes in the crust at 2 s of period, while lateral variations of scattering properties have less influence. In particular, the influence of strong heterogeneities of the alpine crust on the convergence speed of the coda is not clearly seen.

6. Origin of data

Waveform data used in this paper belong to the networks with codes:

CL [Corinth Rift Laboratory Team And RESIF Datacenter, 2013], CQ [Geological Survey Department Cyprus, 2013], CR [University of Zagreb, 2001], CZ [Charles University in Prague (Czech) et al., 1973], EI [Dublin Institute for Advanced Studies, 1993], ES [Instituto Geografico Nacional, Spain, 1999], FR [RESIF, 1995], GE [GEOFON Data Centre, 1993], GR [Federal Institute for Geosciences and Natural Resources (BGR), 1976], GU [University of Genoa, 1967], HA [University of Athens, 2008], HC [Technological Educational Institute of Crete, 2006], HL [National Observatory of Athens, Institute of Geodynamics, Athens, 1975], HP [University of Patras, 2000], HS [Hessian Agency for Nature Conservation, Environment and Geology, 2012], HT [Aristotle University of Thessaloniki, 1981], HU [Kövesligethy Radó Seismological Observatory, 1992], IV [Istituto Nazionale di Geofisica e Vulcanologia (INGV), 2005], KO [Kandilli Observatory And Earthquake Research Institute, Boğaziçi University, 1971], LX [Instituto Dom Luiz (IDL) - Faculdade de Ciências da Universidade de Lisboa, 2003], MD [Geological and Seismological Institute of Moldova, 2007], MN [MedNet Project Partner Institutions, 1990], NI [OGS (Istituto Nazionale di Oceanografia e di Geofisica Sperimentale) and University of Trieste, 2002], NL [KNMI, 1993], NS [University of Bergen, 1982], OE [ZAMG - Zentralanstalt für Meterologie und Geodynamik, 1987], OT [University of Bari "Aldo Moro", 2013], OX [Istituto Nazionale di Oceanografia e di Geofisica Sperimentale - OGS, 2016], PM [Instituto Português do Mar e da Atmosfera, I.P., 2006], RD [RESIF, 2018], RO [National Institute for Earth Physics (NIEP Romania), 1994], SJ [Seismological Survey of Serbia, 1906], SK [ESI SAS (Earth Science Institute Of The Slovak Academy Of Sciences), 2004], SL [Slovenian Environment Agency, 1990], SX [University of Leipzig, 2001], UD [Main Center of Special Monitoring, 2010], UP [SNSN, 1904].

We also used data of temporary experiments, PYROPE (network code X7 (2010–2014), Chevrot et al. [2017] and IberArray [Institute Earth Sciences "Jaume Almera" CSIC (ICTJA Spain), 2007].

Declaration of interests

The authors do not work for, advise, own shares in, or receive funds from any organization that could benefit from this article, and have declared no affiliations other than their research organizations.

Dedication

The manuscript was written through the contributions of all authors. All authors have given approval to the final version of the manuscript.

Funding

Real-time Earthquake Risk Reduction for a Resilient Europe (RISE) project Grant agreement number 821115 (LS, ED, PR).

References

Ardhuin, F. (2018). Large-scale forces under surface gravity waves at a wavy bottom: a mechanism for the generation of primary microseisms. *Geophys. Res. Lett.*, 45(16), 8173–8181.

Ardhuin, F. and Herbers, T. H. C. (2013). Noise generation in the solid earth, oceans and atmosphere, from nonlinear interacting surface gravity waves in finite depth. *J. Fluid Mech.*, 716(10), 316–348.

Aristotle University of Thessaloniki (1981). Aristotle university of thessaloniki seismological network. https://www.fdsn.org/networks/detail/HT/.

Barajas, A., Poli, P., D'Agostino, N., Margerin, L., and Campillo, M. (2021). Separation of poroelastic and elastic processes of an aquifer from tectonic phenomena using geodetic, seismic, and meteorological data in the Pollino region, Italy. *Geochem. Geophys. Geosystems*, 22(11), article no. e2021GC009742.

Berbellini, A., Zaccarelli, L., Faenza, L., Garcia, A., Improta, L., Gori, P. D., and Morelli, A. (2021). Effect of groundwater on noise-based monitoring of crustal velocity changes near a produced water injection well in val d'agri (Italy). *Front. Earth Sci.*, 9, article no. 626720.

Beucler, E., Mocquet, A., Schimmel, M., Chevrot, S., Quillard, O., Vergne, J., and Sylvander, M. (2015). Observation of deep water microseisms in the North Atlantic Ocean using tide modulations. *Geophys. Res. Lett.*, 42(2), 316–322.

Boué, P., Denolle, M., Hirata, N., Nakagawa, S., and Beroza, G. C. (2016). Beyond basin resonance: characterizing wave propagation using a dense array and the ambient seismic field. *Geophys. J. Int.*, 206(2), 1261–1272.

Boué, P., Poli, P., Campillo, M., Pedersen, H., Briand, X., and Roux, P. (2013). Teleseismic correlations of ambient seismic noise for deep global imaging of the Earth. *Geophys. J. Int.*, 194(2), 844–848.

Brenguier, F., Campillo, M., Hadziioannou, C., Shapiro, N. M., Nadeau, R. M., and Larose, E. (2008). Postseismic relaxation along the san andreas fault at parkfield from continuous seismological observations. *Science*, 321(5895), 1478–1481.

Campillo, M. (2006). Phase and correlation in 'random' seismic fields and the reconstruction of the green function. *Pure Appl. Geophys.*, 163(2), 475–502.

Charles University in Prague (Czech), Institute of Geonics, Institute of Geophysics, Academy of Sciences of the Czech Republic, Institute of Physics of the Earth Masaryk University (Czech), and Institute of Rock Structure and Mechanics (1973). Czech regional seismic network. https://www.fdsn.org/networks/detail/CZ/.

Chen, J. H., Froment, B., Liu, Q. Y., and Campillo, M. (2010). Distribution of seismic wave speed changes associated with the 12 may 2008 mw 7.9 wenchuan earthquake. *Geophys. Res. Lett.*, 37(18), article no. L18302.

Chevrot, S., Sylvander, M., Benahmed, S., Ponsolles, C., Lefèvre, J. M., and Paradis, D. (2007). Source locations of secondary microseisms in western Europe: Evidence for both coastal and pelagic sources. *J. Geophys. Res.*, 112(B11), article no. B11301.

Chevrot, S., Sylvander, M., and RESIF (2017). Seismic network x7:pyrope pyrenean observational portable experiment (resif-sismob). https://seismology.resif.fr/networks/#/X7__2010.

Chevrot, S., Villaseñor, A., Sylvander, M., Benahmed, S., Beucler, E., Cougoulat, G., Delmas, P., Blanquat, M., Diaz, J., Gallart, J., Grimaud, F., Lagabrielle, Y., Manatschal, G., Mocquet, A., Pauchet, H., Paul, A., Péquegnat, C., Quillard, O., Roussel, S., Ruiz, M., and Wolyniec, D. (2014). High-resolution imaging of the pyrenees and massif central from the data of the PYROPE and IBERARRAY portable array deployments. *J. Geophys. Res.: Solid Earth*, 119(8), 6399–6420.

Clements, T. and Denolle, M. (2018). Tracking groundwater levels using the ambient seismic field. *Geophys. Res. Lett.*, 45(13), 6459–6465.

Colin de Verdière, Y. (2006a). Mathematical models for passive imaging I: general background. Arxiv.

Colin de Verdière, Y. (2006b). Mathematical models for passive imaging II: effective hamiltonians associated to surface waves. Arxiv.

Corinth Rift Laboratory Team And RESIF Datacenter (2013). CL - Corinth Rift Laboratory Seismological Network (CRLNET). RESIF - Réseau Sismologique et géodésique Français.

Craig, D., Bean, C. J., Lokmer, I., and Möllhoff, M. (2016). Correlation of wavefield-separated ocean-generated microseisms with north atlantic source regions. *Bull. Seism. Soc. Am.*, 106(3), 1002–1010.

Díaz, J., Villaseñor, A., Morales, J., Pazos, A., Córdoba, D., Pulgar, J., García-Lobón, J. L., Harnafi, M., Carbonell, R., Gallart, J., and TopoIberia Seismic Working Group (2010). Background noise characteristics at the IberArray broadband seismic network. *Bull. Seismol. Soc. Am.*, 100(2), 618–628.

Dublin Institute for Advanced Studies (1993). Irish national seismic network. https://www.fdsn.org/networks/detail/EI/.

Ekström, G. (2001). Time domain analysis of Earth's long-period background seismic radiation. *J. Geophys. Res.: Solid Earth*, 106(B11), 26483–26493.

ESI SAS (Earth Science Institute Of The Slovak Academy Of Sciences) (2004). National Network of Seismic Stations of Slovakia. Deutsches Geo Forschungs Zentrum GFZ.

Essen, H., Krüger, F., Dahm, T., and Grevemeyer, I. (2003). On the generation of secondary microseisms observed in northern and central Europe. *J. Geophys. Res.*, 108, article no. 2506.

Evangelidis, C. P. and Melis, N. S. (2012). Ambient

noise levels in greece as recorded at the hellenic unified seismic network. *Bull. Seism. Soc. Am.*, 102(6), 2507–2517.

Federal Institute for Geosciences and Natural Resources (BGR) (1976). German regional seismic-network (grsn). federal institute forgeosciencesand natural resources (bgr).

Friedrich, A., Kruger, F., and Klinge, K. (1998). Ocean-generated microseismic noise located with the grafenberg array. *J. Seismol.*, 2, 47–64.

Froment, B., Campillo, M., Chen, J., and Liu, Q. (2013). Deformation at depth associated with the 12 may 2008 MW 7.9 wenchuan earthquake from seismic ambient noise monitoring. *Geophys. Res. Lett.*, 40(1), 78–82.

Gal, M., Reading, A. M., Ellingsen, S. P., Gualtieri, L., Koper, K. D., Burlacu, R., Tkalčić, H., and Hemer, M. A. (2015). The frequency dependence and locations of short-period microseisms generated in the Southern Ocean and West Pacific. *J. Geophys. Res.: Solid Earth*, 120(8), 5764–5781.

Gal, M., Reading, A. M., Ellingsen, S. P., Koper, K. D., and Burlacu, R. (2017). Full wavefield decomposition of high-frequency secondary microseisms reveals distinct arrival azimuths for Rayleigh and Love waves. *J. Geophys. Res.: Solid Earth*, 122(6), 4660–4675.

GEOFON Data Centre (1993). GEOFON Seismic Network. Deutsches GeoForschungsZentrum GFZ.

Geological and Seismological Institute of Moldova (2007). Moldova digital seismic network. https://www.fdsn.org/networks/detail/MD/.

Geological Survey Department Cyprus (2013). Cyprus broadband seismological network. https://www.fdsn.org/networks/detail/CQ/.

Gimbert, F. and Tsai, V. (2015). Predicting short-period, wind-wave-generated seismic noise in coastal regions. *Earth Plan. Sci. Lett.*, 426(15), 280–292.

Gisselbrecht, L., Froment, B., Boué, P., and Gélis, C. (2023). Insights into the conditions of application of noise-based spectral ratios in a highly industrialized area: a case study in the French Rhone Valley. *Geophys. J. Int.*, 234(2), 985–997.

Gualtieri, L., Stutzmann, E., Farra, V., Capdeville, Y., Schimmel, M., Ardhuin, F., and Morelli, A. (2014). Modelling the ocean site effect on seismic noise body waves. *Geophys. J. Int.*, 197(2), 1096–1106.

Guerin, G., Rivet, D., van den Ende, M., Stutzmann, E., Sladen, A., and Ampuero, J. (2022). Quantifying microseismic noise generation from coastal reflection of gravity waves recorded by seafloor das. *Geophys. J. Int.*, 231(1), 397–407.

Hasselmann, K. (1963). A statistical analysis of the generation of microseisms. *Rev. Geophys.*, 1(2), 177–210.

Hessian Agency for Nature Conservation, Environment and Geology (2012). Hessischer erdbebendienst. https://www.fdsn.org/networks/detail/HS/.

Hetényi, G., Molinari, I., Clinton, J., Bokelmann, G., Bondár, I., Crawford, W. C., Dessa, J.-X., Doubre, C., Friederich, W., Fuchs, F., Giardini, D., Gráczer, Z., Handy, M. R., Herak, M., Jia, Y., Kissling, E., Kopp, H., Korn, M., Margheriti, L., Meier, T., Mucciarelli, M., Paul, A., Pesaresi, D., Piromallo, C., Plenefisch, T., Plomerová, J., Ritter, J., Rümpker, G., Šipka, V., Spallarossa, D., Thomas, C., Tilmann, F., Wassermann, J., Weber, M., Wéber, Z., Wesztergom, V., Živčić, M., Abreu, R., Allegretti, I., Apoloner, M.-T., Aubert, C., Besançon, S., Bès de Berc, M., Brunel, D., Capello, M., Čarman, M., Cavaliere, A., Chèze, J., Chiarabba, C., Cougoulat, G., Cristiano, L., Czifra, T., D'Alema, E., Danesi, S., Daniel, R., Dannowski, A., Dasović, I., Deschamps, A., Egdorf, S., Fiket, T., Fischer, K., Funke, S., Govoni, A., Gröschl, G., Heimers, S., Heit, B., Herak, D., Huber, J., Jarić, D., Jedlička, P., Jund, H., Klingen, S., Klotz, B., Kolínský, P., Kotek, J., Kühne, L., Kuk, K., Lange, D., Loos, J., Lovati, S., Malengros, D., Maron, C., Martin, X., Massa, M., Mazzarini, F., Métral, L., Moretti, M., Munzarová, H., Nardi, A., Pahor, J., Péquegnat, C., Petersen, F., Piccinini, D., Pondrelli, S., Prevolnik, S., Racine, R., Régnier, M., Reiss, M., Salimbeni, S., Santulin, M., Scherer, W., Schippkus, S., Schulte-Kortnack, D., Solarino, S., Spieker, K., Stipčević, J., Strollo, A., Süle, B., Szanyi, G., Szücs, E., Thorwart, M., Ueding, S., Vallocchia, M., Vecsey, L., Voigt, R., Weidle, C., Weyland, G., Wiemer, S., Wolf, F., Wolyniec, D., Zieke, T., AlpArray Seismic Network Team, ETHZ-SED Electronics Lab, AlpArray OBS Cruise Crew, and AlpArray Working Group (2018). The AlpArray seismic network: a large-scale European experiment to image the Alpine orogen. *Surv. Geophys.*, 39(5), 1009–1033.

Hillers, G., Ben-Zion, Y., Campillo, M., and Zigone, D. (2015). Seasonal variations of seismic velocities in the San Jacinto fault area observed with ambient seismic noise. *Geophys. J. Int.*, 202(2), 920–932.

Institute Earth Sciences "Jaume Almera" CSIC (ICTJA Spain) (2007). Iberarray. https://www.fdsn.org/networks/detail/IB/.

Instituto Dom Luiz (IDL) - Faculdade de Ciências da Universidade de Lisboa (2003). Instituto dom luiz (idl) - faculdade de ciencias universidade de lisboa. https://www.fdsn.org/networks/detail/LX/.

Instituto Geografico Nacional, Spain (1999). Spanish digital seismic network. https://www.fdsn.org/networks/detail/ES/.

Instituto Português do Mar e da Atmosfera, I.P. (2006). Portuguese national seismic network. https://www.fdsn.org/networks/detail/PM/.

Istituto Nazionale di Geofisica e Vulcanologia (INGV) (2005). Rete Sismica Nazionale (RSN). Istituto Nazionale di Geofisica e Vulcanologia (INGV).

Istituto Nazionale di Oceanografia e di Geofisica Sperimentale - OGS (2016). North-east italy seismic network. https://www.fdsn.org/networks/detail/OX/.

Juretzek, C. and Hadziioannou, C. (2016). Where do ocean microseisms come from? a study of love-to-rayleigh wave ratios. *J. Geophys. Res.*, 121(9), 6741–6756.

Kandilli Observatory And Earthquake Research Institute, Boğaziçi University (1971). Kandilli observatory and earthquake research institute (koeri). https://www.fdsn.org/networks/detail/KO/.

Kedar, S., Longuet-Higgings, M., Webb, F., Graham, N., Clayton, R., and Jones, C. (2008). The origin of deep ocean microseisms in the North Atlantic Ocean. *Proc. R. Soc. A*, 464, 777–793.

KNMI (1993). Netherlands Seismic and Acoustic Network. Royal Netherlands Meteorological Institute (KNMI), Other/Seismic Network.

Kövesligethy Radó Seismological Observatory (1992). Hungarian national seismological network. (Geodetic And Geophysical Research Institute, Research Centre For Astronomy And Earth Sciences, Hungarian Academy Of Sciences (MTA CSFKGGIKRSZO)).

Landès, M., Hubans, F., Shapiro, N. M., Paul, A., and Campillo, M. (2010). Origin of deep ocean microseisms by using teleseismic body waves. *J. Geophys. Res.*, 115(B5), article no. B05302.

Lecocq, T., Longuevergne, L., Pedersen, H. A., Brenguier, F., and Stammler, K. (2017). Monitoring ground water storage at mesoscale using seismic noise: 30 years of continuous observation and thermo-elastic and hydrological modeling. *Sci. Rep.*, 7(1), article no. 14241.

Lepore, S. and Grad, M. (2020). Relation between ocean wave activity and wavefield of the ambient noise recorded in northern Poland. *J. Seismol.*, 24, 1075–1094.

Levander, A. R. (1990). Seismic scattering near the earth's surface. *Pure Appl. Geophys.*, 132(1), 21–47.

Longuet-Higgins, M. S. and Jeffreys, H. (1950). A theory of the origin of microseisms. *Philos. Trans. R. Soc. Lond., A*, 243(857), 1–35.

Lu, Y., Pedersen, H., Stehly, L., and AlpArray Working Group (2022). Mapping the seismic noise field in Europe: spatio-temporal variations in wavefield composition and noise source contributions. *Geophys. J. Int.*, 228, 171–192.

Lu, Y., Stehly, L., Brossier, R., and Paul, A. (2020). Imaging alpine crust using ambient noise wave-equation tomography. *Geophys. J. Int.*, 222, 69–85.

Maeda, T., Obara, K., and Yukutake, Y. (2010). Seismic velocity decrease and recovery related to earthquake swarms in a geothermal area. *Earth Planets Space*, 62(9), 685–691.

Main Center of Special Monitoring (2010). Seismic network main center of special monitoring. https://www.fdsn.org/networks/detail/UD/.

Mao, S., Lecointre, A., van der Hilst, R. D., and Campillo, M. (2022). Space-time monitoring of groundwater fluctuations with passive seismic interferometry. *Nat. Commun.*, 13(1), article no. 4643.

Margerin, L. and Sato, H. (2011). Generalized optical theorems for the reconstruction of Green's function of an inhomogeneous elastic medium. *J. Acoust. Soc. Am.*, 130(6), 3674–3690.

McNamara, D. E. and Buland, R. (2004). Ambient noise levels in the continental united states. *Bull. Seismol. Soc. Am.*, 94(4), 1517–1527.

MedNet Project Partner Institutions (1990). Mediterranean Very Broadband Seismographic Network (MedNet). Istituto Nazionaledi Geofiscae Vulcanologia (INGV).

Meier, U., Shapiro, N. M., and Brenguier, F. (2010). Detecting seasonal variations in seismic velocities within Los Angeles basin from correlations of ambient seismic noise. *Geophys. J. Int.*, 181(2), 985–996.

National Institute for Earth Physics (NIEP Romania) (1994). Romanian seismic network. https://www.

fdsn.org/networks/detail/RO/.

National Observatory of Athens, Institute of Geodynamics, Athens (1975). National observatory of athens seismic network. https://www.fdsn.org/networks/detail/HL/.

Obermann, A., Froment, B., Campillo, M., Larose, E., Planès, T., Valette, B., Chen, J. H., and Liu, Q. Y. (2014). Seismic noise correlations to image structural and mechanical changes associated with the Mw 7.9 2008 wenchuan earthquake. *J. Geophys. Res.: Solid Earth*, 119(4), 3155–3168.

Obermann, A., Planès, T., Larose, E., Sens-Schönfelder, C., and Campillo, M. (2013). Depth sensitivity of seismic coda waves to velocity perturbations in an elastic heterogeneous medium. *Geophys. J. Int.*, 194(1), 372–382.

OGS (Istituto Nazionale di Oceanografia e di Geofisica Sperimentale) and University of Trieste (2002). North-east italy broadband network. https://www.fdsn.org/networks/detail/NI/.

Paul, A., Malusà, M. G., Solarino, S., Salimbeni, S., Eva, E., Nouibat, A., Pondrelli, S., Aubert, C., Dumont, T., Guillot, S., Schwartz, S., and Zhao, L. (2022). Along-strike variations in the fossil subduction zone of the Western Alps revealed by the CIFALPS seismic experiments and their implications for exhumation of (ultra-) high-pressure rocks. *Earth Planet. Sci. Lett.*, 598, article no. 117843.

Pedersen, H. A. and Krüger, F. (2007). Influence of the seismic noise characteristics on noise correlations in the Baltic shield. *Geophys. J. Int.*, 168(1), 197–210.

Poli, P., Marguin, V., Wang, Q., D'Agostino, N., and Johnson, P. (2020). Seasonal and coseismic velocity variation in the region of L'Aquila from single station measurements and implications for crustal rheology. *J. Geophys. Res.: Solid Earth*, 125(7), article no. e2019JB019316.

RESIF (1995). RESIF-RLBP French Broad-band network, RESIF-RAP strong motion network and other seismic stations in metropolitan France. RESIF - Réseau Sismologique et géodésique Français.

RESIF (2018). CEA/DASE broad-band permanent network in metropolitan France. RESIF - Réseau Sismologique et géodésique Français.

Retailleau, L., Boué, P., Stehly, L., and Campillo, M. (2017). Locating microseism sources using spurious arrivals in intercontinental noise correlations. *J. Geophys. Res.: Solid Earth*, 122(10), 8107–8120.

Rivet, D., Campillo, M., Shapiro, N. M., Cruz-Atienza, V., Radiguet, M., Cotte, N., and Kostoglodov, V. (2011). Seismic evidence of nonlinear crustal deformation during a large slow slip event in mexico. *Geophys. Res. Lett.*, 38(8), article no. L08308.

Roux, P., Sabra, K. G., Gerstoft, P., Kuperman, W. A., and Fehler, M. C. (2005). P-waves from cross-correlation of seismic noise. *Geophys. Res. Lett.*, 32(19), 79–84.

Sabra, K. G., Gerstoft, P., Roux, P., Kuperman, W. A., and Fehler, M. C. (2005). Surface wave tomography from microseisms in southern california. *Geophys. Res. Lett.*, 32(14), article no. L14311.

Saito, T. (2010). Love-wave excitation due to the interaction between a propagating ocean wave and the sea-bottom topography. *Geophys. J. Int.*, 182(3), 1515–1523.

Sánchez-Sesma, F., Chávez-Pérez, S., Suárez, M., Bravo, M. A., and Pérez-Rocha, L. E. (1988). The Mexico earthquake of September 19, 1985—on the seismic response of the valley of Mexico. *Earthquake Spectra*, 4(3), 569–589.

Sánchez-Sesma, F. J. and Campillo, M. (2006). Retrieval of the Green's function from cross correlation: the canonical elastic problem. *Bull. Seismol. Soc. Am.*, 96(3), 1182–1191.

Seismological Survey of Serbia (1906). Serbian seismological network. https://www.fdsn.org/networks/detail/SJ/.

Sens-Schönfelder, C. and Wegler, U. (2006). Passive image interferometry and seasonal variations of seismic velocities at Merapi Volcano, Indonesia. *Geophys. Res. Lett.*, 33(21), article no. L21302.

Shapiro, N. M. and Campillo, M. (2004). Emergence of broadband rayleigh waves from correlations of the ambient seismic noise. *Geophys. Res. Lett.*, 31(7), article no. L07614.

Shapiro, N. M., Campillo, M., Stehly, L., and Ritzwoller, M. H. (2005). High-resolution surface-wave tomography from ambient seismic noise. *Science*, 307(5715), 1615–1618.

Slovenian Environment Agency (1990). Seismic network of the republic of slovenia. https://www.fdsn.org/networks/detail/SL/.

Snieder, R. (1986). The influence of topography on the propagation and scattering of surface waves. *Phys. Earth Planet. Inter.*, 44(3), 226–241.

SNSN (1904). *Swedish National Seismic Network*.

Uppsala University, Uppsala.

Soldati, G., Zaccarelli, L., Faenza, L., and Michelini, A. (2015). Monitoring of crustal seismic velocity variations in the l aquila fault zone inferred from noise cross-correlation. *Geophys. J. Int.*, 202(1), 604–611.

Stehly, L., Campillo, M., and Shapiro, N. M. (2006). A study of the seismic noise from its long-range correlation properties. *J. Geophys. Res.*, 111(B10), article no. B10306.

Taira, T., Nayak, A., Brenguier, F., and Manga, M. (2018). Monitoring reservoir response to earthquakes and fluid extraction, Salton Sea geothermal field, California. *Sci. Adv.*, 4(1), article no. e1701536.

Tanimoto, T., Hadziioannou, C., Igel, H., Wasserman, J., Schreiber, U., and Gebauer, A. (2015). Estimate of rayleigh-to-love wave ratio in the secondary microseism by colocated ring laser and seismograph. *Geophys. Res. Lett.*, 42(8), 2650–2655.

Technological Educational Institute of Crete (2006). Seismological network of crete. https://www.fdsn.org/networks/detail/HC/.

Toksoz, M. and Lacoss, R. (1968). Microseisms: Mode structure and sources. *Science*, 159, 872–873.

University of Athens (2008). Hellenic seismological network, university of athens, seismological laboratory. https://www.fdsn.org/networks/detail/HA/.

University of Bari "Aldo Moro" (2013). Otrions. https://www.fdsn.org/networks/detail/OT/.

University of Bergen (1982). University of bergen seismic network. https://www.fdsn.org/networks/detail/NS/.

University of Genoa (1967). Regional seismic network of north western italy. https://www.fdsn.org/networks/detail/GU/.

University of Leipzig (2001). Sxnet saxon seismic network. https://www.fdsn.org/networks/detail/SX/.

University of Patras (2000). University of patras, seismological laboratory. https://www.fdsn.org/networks/detail/HP/.

University of Zagreb (2001). Croatian seismograph network. https://www.fdsn.org/networks/detail/CR/.

Vidal, C. A., Zaccarelli, L., Pintori, F., Bragato, P. L., and Serpelloni, E. (2021). Hydrological effects on seismic-noise monitoring in karstic media. *Geophys. Res. Lett.*, 48, article no. e2021GL09319.

Wang, Q.-Y., Brenguier, F., Campillo, M., Lecointre, A., Takeda, T., and Aoki, Y. (2017). Seasonal crustal seismic velocity changes throughout Japan. *J. Geophys. Res.: Solid Earth*, 122(10), 7987–8002.

Wang, Q.-Y., Campillo, M., Brenguier, F., Lecointre, A., Takeda, T., and Hashima, A. (2019). Evidence of changes of seismic properties in the entire crust beneath Japan after the Mw 9.0, 2011 Tohoku-oki earthquake. *J. Geophys. Res. (Solid Earth)*, 124, 8924–8941. ADS Bibcode: 2019JGRB..124.8924W.

Wapenaar, K. (2004). Retrieving the elastodynamic green's function of an arbitrary inhomogeneous medium by cross correlation. *Phys. Rev. Lett.*, 93(25), article no. 254301.

Weaver, R. L., Hadziioannou, C., Larose, E., and Campillo, M. (2011). On the precision of noise correlation interferometry. *Geophys. J. Int.*, 185(3), 1384–1392.

Weaver, R. L. and Lobkis, O. I. (2001). Ultrasonics without a source: thermal fluctuation correlations at MHz frequencies. *Phys. Rev. Lett.*, 87(13), article no. 134301.

Weaver, R. L. and Lobkis, O. I. (2005). Fluctuations in diffuse field–field correlations and the emergence of the green's function in open systems. *J. Acoust. Soc. Am.*, 117(6), 3432–3439.

Wu, R.-S. and Aki, K. (1985). The fractal nature of the inhomogeneities in the lithosphere evidenced from seismic wave scattering. *Pure Appl. Geophys.*, 123(6), 805–818.

Zaccarelli, L., Shapiro, N. M., Faenza, L., Soldati, G., and Michelini, A. (2011). Variations of crustal elastic properties during the 2009 L'Aquila earthquake inferred from cross-correlations of ambient seismic noise. *Geophys. Res. Lett.*, 38(24), article no. L24304.

ZAMG - Zentralanstalt für Meterologie und Geodynamik (1987). Austrian seismic network. https://www.fdsn.org/networks/detail/OE/.

Zhao, L., Paul, A., Guillot, S., Solarino, S., Malusà, M. G., Zheng, T., Aubert, C., Salimbeni, S., Dumont, T., Schwartz, S., Zhu, R., and Wang, Q. (2015). First seismic evidence for continental subduction beneath the Western Alps. *Geology*, 43(9), 815–818.

ACADÉMIE DES SCIENCES
INSTITUT DE FRANCE

Comptes Rendus. Géoscience — Sciences de la Planète
2024, Vol. 356, Special issue S4, p. 125-145
https://doi.org/10.5802/crgeos.203

Research article

New Developments in Passive Seismic Imaging and Monitoring

Damage in cohesive granular materials: simulations and geophysical implications

Vincent Canel [a,*,a,b], **Michel Campillo** [a,a], **Xiaoping Jia** [b] **and Ioan R. Ionescu** [c]

[a] ISTerre, CNRS, Grenoble Alpes University, 38000 Grenoble, France

[b] Institut Langevin, CNRS, ESPCI Paris, PSL University, 75005 Paris, France

[c] LSPM, CNRS, Sorbonne Paris Nord University, 93430 Villetaneuse France and IMAR, Romanian Academy, Bucharest, Romania

E-mails: canelvince@gmail.com (V. Canel), michel.campillo@univ-grenoble-alpes.fr (M. Campillo), xiaoping.jia@espci.fr (X. Jia), ioan.r.ionescu@gmail.com (I. R. Ionescu)

Abstract. The aim of this paper is to test a simple damage model of a cohesive granular medium to study the relationship between the damage and velocity of elastic waves. Our numerical experiments of edometric compression show that the microscopic deformation quickly becomes very heterogeneous, while our simulations of elastic waves propagation show that a small amount of damage induces a dramatic decrease in the elastic velocity. This shows that cohesive discrete media are very sensitive to strain field heterogeneity, and that the wave velocities in these media can measure subtle transient deformation processes, such as earthquake initiation phases.

Keywords. Granular medium, Damage, Elastic wave, Simulation, Earthquake.

Manuscript received 12 September 2022, revised 18 January 2023 and 22 February 2023, accepted 20 February 2023.

1. Introduction

The damage state of rocks in a fault core is a controlling element of seismic rupture and of the characteristics of fault evolution [Lyakhovsky et al., 1997, Cappa et al., 2014]. The interaction between slip and damage processes is poorly understood, especially as the nature and actual level of rock damage at depth are also poorly known despite some recent studies [Delorey et al., 2021]. On a geological time scale (i.e., over several seismic cycles), fault zones evolve, with the development of damage structures in their vicinity, partly due to dynamic stresses during rupture [Chester, 1993]. The existence of this damaged zone is traditionally shown at depth by seismic tomography, which indicates a lower velocity zone that extends several kilometers in depth [Zigone et al., 2015, Roux et al., 2016, Allam et al., 2014]. More recently, it has been shown that the existence of a several kilometers thick zone of strong scattering around the North Anatolian Fault is required to explain the regional distribution of multiply scattered coda wave energies [van Dinther et al., 2021]. Passive scatterer imaging was made possible by a novel aberration correction method [Touma et al., 2022] that confirmed the presence of intense fracturing at depth around the San Jacinto fault in California.

Indeed, measurements of the temporal evolution of seismic wave velocities give information on the mechanical state of the medium [Poupinet et al., 1984, Schaff and Beroza, 2004, Langlois and Jia, 2014]. Noise-based passive monitoring allows to envision long-term continuous monitoring of the seismic velocity [Brenguier et al., 2008, 2014, Sens-Schönfelder

*Corresponding author

and Wegler, 2006, Rivet et al., 2014]. Examples of these changes are now well documented, and it is possible to detect them continuously with unprecedented precision that can reach a few 10^{-5} for relative velocity changes [Wang et al., 2017] and very short time resolution [Mao et al., 2019b, Sens-Schönfelder and Eulenfeld, 2019].

One difficulty with these measurements is to distinguish between changes related to internally induced deformations and changes related to external forcing, such as precipitation [Sens-Schönfelder and Wegler, 2006, Barajas et al., 2021], temperature [Meier et al., 2010], or tides [Sens-Schönfelder and Eulenfeld, 2019]. As the causes of external forcing are fairly well known, correction strategies have been proposed [Wang et al., 2017]. Assessing these changes in the vicinity of rupture zones will improve through the development of sensitivity kernels for spatial inversion methods [Margerin et al., 2016, Obermann et al., 2016, van Dinther et al., 2021, Barajas et al., 2021, Zhang et al., 2021].

With the striking increase achieved in quantity and quality of seismic observations and the novel methods now possible, a way is opening to revisit the vision of earthquake processes. At the same time, geodetic measures reach impressive precision. At time scales from days to years, evidence for changes in elastic moduli in response to earthquakes [Brenguier et al., 2008] and transient tectonic deformations [Rivet et al., 2014] has been shown in the form of a velocity drop followed by a slow recovery similar to laboratory observations [TenCate et al., 2000]. These changes are also observed at the time scale of days in a mining environment [Olivier et al., 2015] and in laboratory experiments of stick-slip and slow slip [Scuderi et al., 2016], where a drop in the elastic moduli starts even before the slip is observed.

Such effects have been largely studied in rocks with laboratory experiments. They have revealed that the application of a uniaxial stress involves elastic wave velocity anisotropy [Nur and Simmons, 1969] that could be linked to the elastic nonlinear behavior of rocks [Johnson et al., 1996, Johnson and Rasolofosaon, 1996, Pasqualini et al., 2007]. Direct comparisons between rock degradation (linked to a damage quantified by the distribution of microcracks) and wave velocity measurements could be highlighted experimentally [Hamiel et al., 2009]. Furthermore, theoretical considerations based on the inversion of the measured wave velocities and resulting microcrack density tensors allowed to describe the microcracks evolution and anisotropy [Sayers and Kachanov, 1991, 1995, Schubnel and Guéguen, 2003, Stanchits et al., 2006, Hall et al., 2008]. For the following numerical simulations, we consider granular materials rather than real rocks as they have been studied as synthetic rocks in previous experiments [Langlois and Jia, 2014, Canel et al., 2020].

An important issue is to explain how the very small macro-scale deformation that is associated with tectonic deformation can induce an *observable velocity drop*. In this study, we focus on the drop effect without consideration of the slow logarithmic type relaxation effect [TenCate et al., 2000] observed in the earth after a strong drop [Brenguier et al., 2008].

Here we use a simple cemented granular media model [Dvorkin et al., 1994, Langlois and Jia, 2014, Hemmerle et al., 2016] to represent the behavior of rocks around faults that are intensely fractured and cemented by precipitation due to fluid transfer. Our interest in this simulation is to link it to the observed temporal variations of seismic wave propagation velocities. More precisely, in the following, we use numerical simulation models to analyze the relation between the wave velocity drop and the damage evolution. We focus on numerical simulations in an edometric experimental setup, such that some comparisons with real experiments can be done. The edometric experiment is a typical experiment in soils and granular materials [Evesque, 2000, Sawicki and Swidzinski, 1995, Langlois and Jia, 2014], which involve macroscopic deformation of up to 15%. In the first stage, the goal is to deform and damage a medium in which we will later study wave propagation [Langlois and Jia, 2014]. Only small overall deformation (up to 1.5%) will be considered here. However, as even for small macroscopic strain the microscopic bond deformation is large and very heterogeneous, large deformation modeling will be considered at the microscopic scale.

The numerical granular material considered in this paper is made from a dense elastic bead packing that includes some cement. The numerical simulations can highlight the microscopic heterogeneities. For this we used the finite element method, instead of the discrete element method [Radjai and Dubois, 2011], and we meshed both the beads and the bonds. As far as we know, this approach has not

been used in granular modeling. In contrast with the discrete element method approach, which is widely used in granular physics, the finite element method approach provides a fine description of the damage mechanism at bonded contacts and of the elastic wave propagation through the bonds and the particles (beads).

To limit the computational load, we consider only two-dimensional (2D) numerical simulations. The mechanical modeling of the bonds relies on a simple elasto-plastic model with damage, while the beads are assumed to be elastic and isotropic. Following the edometric experimental setup, we first detail the adopted geometry for the cemented granular material, and then we distinguish two processes in the following sections. The first process is quasi-static loading of the heterogeneous macroscopic sample that involves damage to the bonds. This first modeling aims at creation of a realistic state of deformation at the microscopic scale. The second modeling is the dynamic propagation of a small perturbation in a linear elastic regime for a given state of damage of the material. This second process can be considered as the dynamic version of the "tangent problem" associated to the quasi-static evolution. It represents the actual situation encountered in geophysical monitoring of active faults: an elastic, weak amplitude wave propagates in a medium where damage results from a slow internal deformation. Note that the macroscopic damage of the sample, which is defined from the variation of the macroscopic elastic coefficients, cannot be found from the strain–stress curve obtained from quasistatic unidirectional loading. For this, we would need several unloading/reloading experiments. The macroscopic damage is therefore probed by the wave propagation, as in the seismological measurements of the wave speed.

2. Quasistatic loading

2.1. *Macroscopic setting*

Let us first describe the numerical edometric experiment. The "sample" (or cell) of the cemented granular material initially occupies the 2D domain $\mathscr{D}_0^{\text{macro}} = (0, L) \times (0, l_0)$ (with L the constant length and l_0 the initial width of the sample, see Figure 1) in the plane strain configuration. On its boundary, the sample is in contact without friction with four rigid walls. Three of them are at rest while the upper one moves slowly in the vertical direction. The process is strain driven: the sample width l and then the macroscopic displacement $\Delta l = |l - l_0|$ evolve linearly with time. The microscopic deformation process is heterogeneously activated by the macroscopic deformation $\varepsilon_{\text{macro}} = \Delta l / l_0$, which increases slowly from 0 to the final strain $\varepsilon_{\text{macro}}^{\text{f}} = 1.58\%$. During the loading process, to find the macroscopic stress $\sigma_{\text{macro}} = F_{\text{macro}} / L$, we compute the resultant force F_{macro} that acts on the upper plate. In this configuration, the macroscopic Hooke's law at the macroscopic level is written as $\sigma_{\text{macro}} = M_{\text{macro}} \varepsilon_{\text{macro}}$, where M_{macro} is the macroscopic uniaxial strain modulus or P-wave modulus ($M = \lambda + 2\mu = E(1-\nu)/((1+\nu)(1-2\nu))$ with λ and μ the macroscopic first and second Lamé coefficients and E and ν the macroscopic Young and Poisson moduli respectively).

2.2. *Microscopic setting*

The cemented granular material, which occupies at the moment $t \in [0, T^{\text{quasi-static}}]$ the domain $\mathscr{D}_t \subset \mathscr{D}_t^{\text{macro}}$ is composed of grains, denoted by $\mathscr{G}_t$, and bonds, denoted by $\mathscr{B}_t$, i.e. $\bar{\mathscr{D}}_t = \bar{\mathscr{G}}_t \cup \bar{\mathscr{B}}_t$ and $\mathscr{G}_t \cap \mathscr{B}_t = \emptyset$. For the initial geometric settings of grains $\mathscr{G}_0$ we used 382 disks (to model glass beads) of radii 300 μm to 600 μm. The beads are connected by the cement $\mathscr{B}_0$ composed of 956 bonds and gathered in a cell $\mathscr{D}_0^{\text{macro}}$ of size 3 cm × 1 cm. The word "bond" stands for the deformable region which links two beads. The packing fraction (i.e., the ratio between the beads area and the total area of the sample) is initially 77.2% and increases slowly during the compression, to reach 78.4% at the final strain $\varepsilon_{\text{macro}}^{\text{f}}$. The ratio between the bonds area and the beads area is 6.32%, while the ratio between the bond area and the total initial area of the sample is 4.88%. Even if the bonds area is small compared to the beads area, the bonds are modeled as a set of continuum 2D bodies.

After creation of the packing, we checked that the bonds are isotropically generated, so as not to induce any geometric anisotropy from the fabric that might hide or perturb possible anisotropic effects due to the future quasi-static loading. Figure 2b shows the polar probability distribution of the orientation angles of the bonds (i.e., angle between the (Ox) axis and the axis that connects the center of the beads, as schematized in Figure 2d). Half the polar diagram is shown,

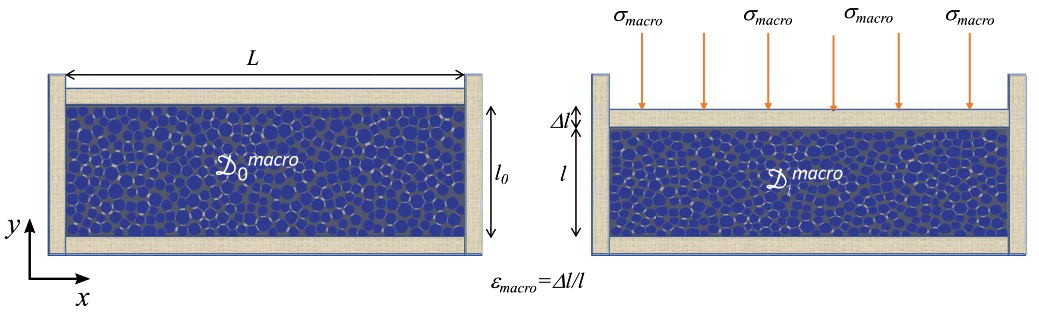

Figure 1. Representation of the quasi-static edometric numerical experiment.

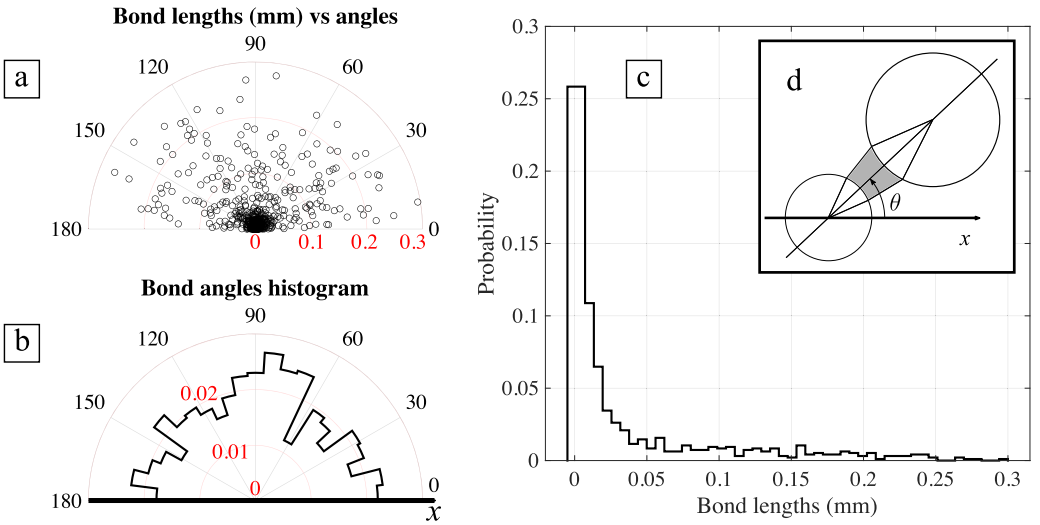

Figure 2. Geometric statistics of the initial isotropic packing. (a) Bond length as a function of the orientation angle of the corresponding bond. (b) Polar probability distribution of the orientation angles of the bonds. (c) Probability distribution of the lengths of the bonds. (d) Definition of the orientation angle θ of a bond.

as it is π-periodic: each bond is indeed indexed on the basis of both its associated bead, with an angle θ, and the other associated bead, with an angle $\theta + \pi$. The distribution is globally isotropic (a sample with more bonds would exhibit a smoother distribution).

Figure 2c shows the distribution of the length of the bonds, defined as the distance between the centers of the beads concerned and the sum of their radii; this then represents a length along the bond symetrical axis. The minimal values correspond to the closest beads and tend towards zero, as there is no minimal limit for the generation of bonds in the sample considered. The majority of the bonds have a length less than 0.05 mm.

Further geometric anisotropy can come from correlations between the lengths and the orientations of the bonds. Indeed, as we expect that short bonds are more affected by the macroscopic deformation, we verified that there is no privileged direction for them. Figure 2a shows the lengths of the bonds as functions of the orientation angles of the corresponding bonds in a polar plot. The isotropic distribution shows that there is no correlation between length and orientation angle.

Table 1. Parameters for simulations

	ρ (kg/m^3)	E_0 (GPa)	ν_0 (GPa)	M_0 (GPa)	c_{p0} (m/s)	c_{s0} (m/s)
Beads	2600	60	0.24	70.72	5200	3100
Bonds	1200	3.5	0.33	5.18	2100	1000

The index 0 refers to the state without damage.

2.3. *Mechanical modeling*

For the mechanical modeling of the bond material, which is detailed in Appendix, we chose the model of Lemaitre and Chaboche [Lemaitre and Chaboche, 1994] coupling isotropic ductile plastic damage and with an elasto-plastic law in the framework of an Eulerian (large deformations) description [see for instance Belytschko et al., 2000].

For this, we considered the additive decomposition of the rate deformation tensor in the elastic and plastic rates of deformation. For the elastic range, we considered an isotropic hypo-elastic law (i.e., the large strain generalization of Hooke's law with the Lamé coefficients λ and μ written in terms of the Jaumann rate of the Cauchy stress tensor and the elastic rates of deformation). The plastic rate of deformation is related to the Cauchy stress tensor through the flow rule associated to the classical Von-Mises yield criterion (without hardening). The weakening effect is characterized by a damage (phenomenological) parameter $d \in [0,1]$ and its evolution law is related to the cumulated plastic strain ϵ_p.

The model parameters used here have not been characterized or calibrated experimentally. This important task is beyond the scope of present numerical study. However, the mechanical parameters have been chosen to correspond to a very ductile cement, as tetradecane or eicosane, that has been used in laboratory experiments showing seismic velocity reduction during compression [Langlois and Jia, 2014, Canel et al., 2020]. The elastic coefficients of the undamaged material are given in Table 1 and the yield limit is $\kappa_0 = 135$ MPa. For simplicity, the dependence of damage rate on the cumulated plastic strain is given through a piecewise linear function. When the cumulated plastic strain reaches an activation level $\epsilon_{p,\text{activation}} = 2\%$, we consider the beginning of damage process, while the maximal level of damage is $d_{\max} = 0.8$ corresponding to $\epsilon_{p,\max} = 20\%$.

The beads material was supposed to be purely elastic (see Table 1 for the Lamé coefficients corresponding to glass), with no damage effects or plastic strains. This choice could appear too simple but corresponds to a granular material made from glass beads used in laboratory experiments for which no bead crushing has been observed [see for instance Langlois and Jia, 2014, Canel et al., 2020]. Moreover, this choice allows us to focus on the bond material, and to analyze the crucial role played by the bonds damage in the wave velocity drop. This is due to damage localization in the bonds, which are pointed out in the next numerical results obtained with the choice of damage parameters presented above. The presence of a maximal level of damage in the model prevents total bonds failure (that would be very difficult to handle in an elasto-plastic FE computation of a large number of bonds) but is not expected to affect the overall results at the low levels of macroscopic deformation at which we limit our simulations.

2.4. *Numerical modeling*

As the bonds are submitted to large deformation (even for small macroscopic deformation), we used an arbitrary Lagrangian Eulerian (ALE) description [Huerta and Casadei, 1994, Wang and Gadala, 1997, Ghosh and Raju, 1996, Rodríguez-Ferran et al., 2002]. This description incorporates the advantages of the Lagrangian and Eulerian descriptions, and can avoid some of their drawbacks. Usually in solid mechanics, where we do not deal with large mass fluxes among different parts of the sample and the strains are not too large, the Lagrangian kinematics formulations are intensively used. However, because of severe distortion of elements in some practical problems, the determinant of the Jacobian matrix can become negative, which results in numerical errors. Eulerian methods coupled with an ALE description (which either uses a fixed mesh or adapts the mesh at each time step) can eliminate the problems associated with distorted meshes. With the ALE

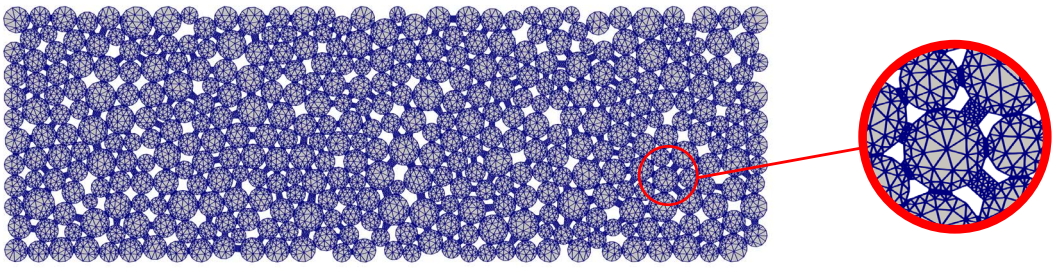

Figure 3. The initial mesh used for the quasi-static computations.

method adopted here, the computational grid can be moved arbitrarily, to optimize element shapes independently of material deformation.

For the numerical integration of the equilibrium of the hypo-elastic-plastic model described above, to find the Eulerian unknowns acting on the domain $\mathscr{D}_{t+\Delta t}$, we used a classical implicite backward radial return mapping scheme [e.g., see Belytschko et al., 2000] with explicit treatment of the damage field on the finite element discretization of domain $\mathscr{D}_t$. The discretization was done with [P2-continuous] finite elements for the velocity fields and [P1-discontinous] for the other unknowns (e.g., stress, damage, plastic deformation).

Since the investigated processes are very different, the quasi-static and dynamic problems require two distinct meshes (one can see the difference by comparing Figures 3 and 8). For the quasi-static problem, as the beads are almost not deformed outside of their peripheral zone, it is not necessary to mesh them finely at the core, but only close to the bonds that need a fine mesh to correctly describe their large deformation. The initial mesh is then finer in the bonds and the periphery of the beads, with a given ratio between the size of the edges (see Figure 3). Moreover, to capture the shear bands, we used an adaptive mesh technique with respect to the plastic strain rate norm $|\boldsymbol{D}^p|$. This means that regions where the plastic strain rate is larger will have a fine mesh, while elsewhere the mesh is coarse. The ratio between the sizes of the fine and coarse meshes was 1/4.

2.5. *Results*

2.5.1. *Macroscopic level*

Figure 4 shows the macroscopic normal load σ_{macro} versus the imposed strain on the sample $\varepsilon_{\text{macro}}$. The macroscopic load initially increases linearly with the displacement, which highlights an elastic behavior. The linear fit close to the origin (see Figure 4) gives an estimation of the initial (undamaged) macroscopic uniaxial strain modulus (P-wave modulus) $M^0_{\text{macro}} \approx 12.6$ GPa, which is larger than the modulus of the bonds but much less than the bead modulus. After some point, the macroscopic strain–stress curve deviates from this linear trend and then reaches a plateau, which is a typical strain–stress curve for an elasto-plastic material without hardening.

However, the macroscopic damage d_{macro} of the sample, defined as

$$d_{\text{macro}} = 1 - \frac{M_{\text{macro}}}{M^0_{\text{macro}}},$$

cannot be found from the strain–stress curve only. Indeed, to get the macroscopic uniaxial stress modulus we cannot use the secant strain–stress modulus and several unloading and reloading experiments during the main loading process are needed.

This kind of quasi-static unloading/reloading experiments with fluid pressure are possible at the laboratory scale or at a small geophysical scale corresponding to reservoirs for example (in the framework of the oil and gas industry). However, as far as we know these techniques have never been applied in Nature to a fault zone at the scale relevant to earth-

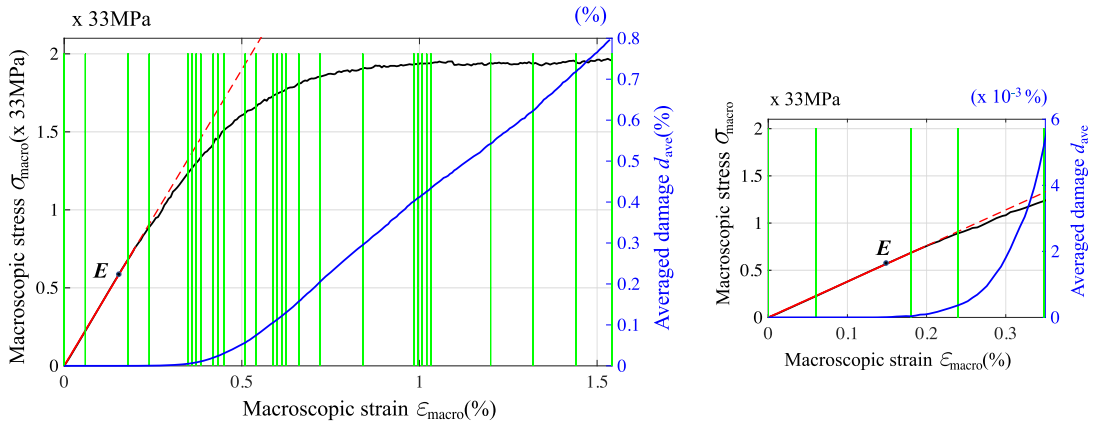

Figure 4. (a) Macroscopic stress σ_{macro} (black; in × 33 MPa) and the averaged damage d_{ave} (blue; in %) as functions of the strain $\varepsilon_{\text{macro}}$ (in %). A linear fit of the load (red) highlights its first elastic trend. The chosen states for the dynamic computations are indicated with vertical green lines. (b) Zoom in around the low strains.

quake studies. One can think about the tides effect but our study does not target it. Indeed, different techniques have been used to study the tide effect and actually highlighted the velocity dependence on tide deformation independently from the presence of a fault system [Sens-Schönfelder and Eulenfeld, 2019, Mao et al., 2019a, Reasenberg and Aki, 1974, Takano et al., 2014, Delorey et al., 2021]. Nevertheless, the continuous nature of tides implies that they are not a source of evolution damage, or over time scales and amplitudes that are incompatible with their measurements. In our perspective, nonlinearity and damage evolution are quite different. This is why we did not use the quasi-static unloading/reloading technique to measure the macroscopic damage but the wave speed probing (see next section), which is much more adapted to the targeted geophysical measurements.

We computed and plotted the microscopic averaged damage $d_{\text{ave}}(t)$, defined as the ratio between the integral of the damage, that vanishes outside the bonds, and the area of the sample $|\mathscr{D}_t|$ which is the area of the set of grains and bonds. Since plastic deformations preserve the area (volume in 3D) the only variation of the area $|\mathscr{D}_t|$ is due to elastic deformations. The deviation of the macroscopic load from a linear trend is clearly correlated to the accumulation of damage. Even when the load reaches a stationary value, $d_{\text{ave}}(t)$ keeps increasing (which can be associated to anisotropic effects of the compression; see Section 4 for more details).

2.5.2. *Microscopic level*

Even for small macroscopic deformation, local plastic irreversible deformation occurs in the bonds. The first microscopic plastic and damage effects occur at $\varepsilon_{\text{macro}} = 0.096\%$ and $\varepsilon_{\text{macro}} = 0.132\%$, respectively (see Figure 4 for the damage). This is consistent with the chosen microscopic laws with successive plastic and damage thresholds (see Section 2.3 and the Appendix for more details). The damage process is very heterogeneous as it occurs along the force chains. Some of the bonds are not damaged, and some of them are completely damaged, although there are a lot of bonds in an intermediary state where the damage is localized in microscopic shear bands. We note that there is no macroscopic localization of the damage (i.e., no noticeable development of a macroscopic shear band).

Figure 5 shows the deformed configuration at the end of the edometric numerical experiment ($\varepsilon^{\text{f}}_{\text{macro}} = 1.58\%$), with a map of the deviatoric stress (top) that shows mainly vertical heterogeneous force chains, and a map of the mean stress (bottom). The damage distribution is plotted in Figure 6. Several examples of deformed and damaged bonds are shown in the enlarged boxes, and illustrate the heterogeneity of the local deformation. Even if at the macroscopic

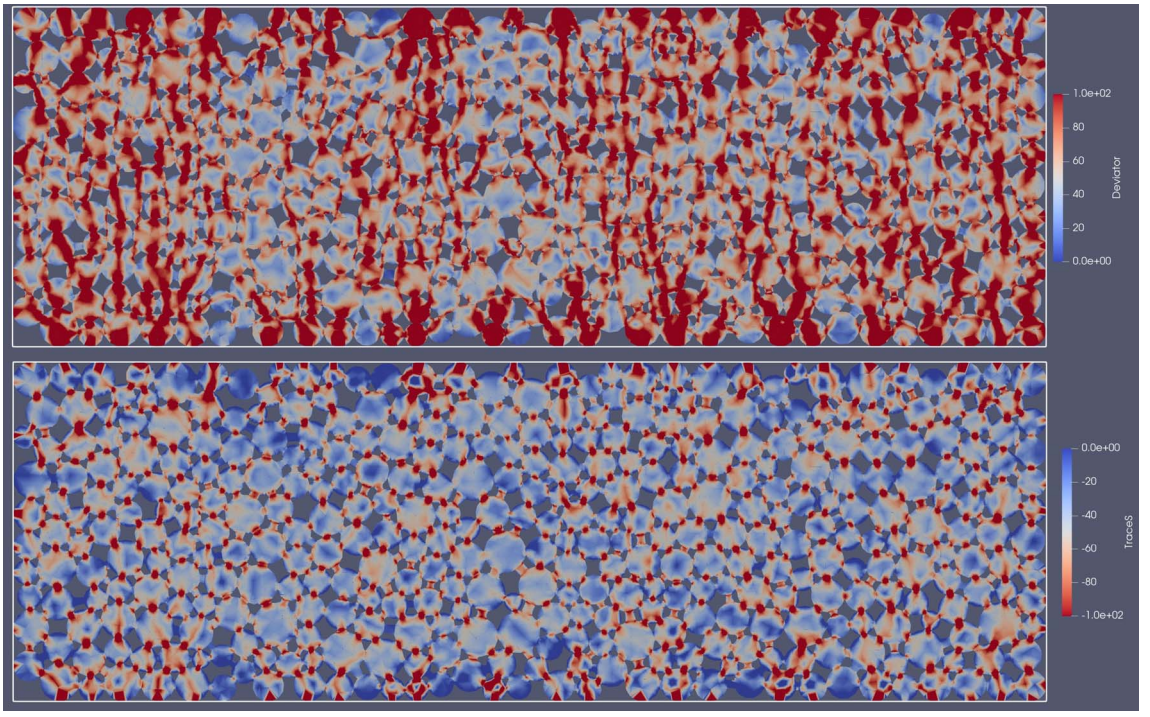

Figure 5. Top: Map of the (Von-Mises) equivalent stress (in MPa) that describes force chains in the cemented packing at the final stage of compression. Bottom: Map of the mean stress (in MPa).

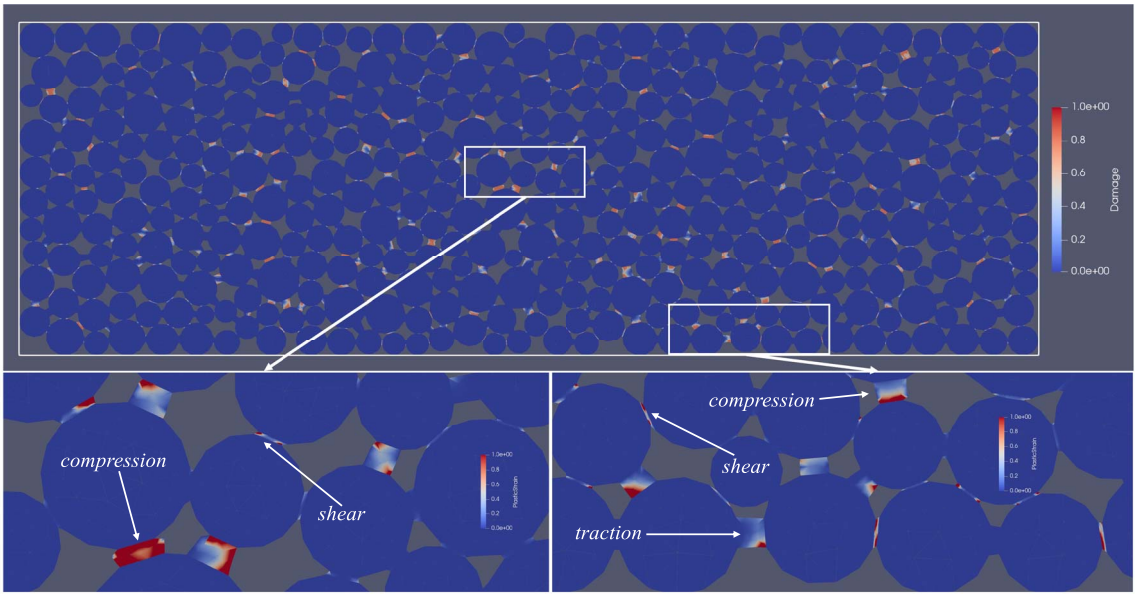

Figure 6. Top: Map of the damage distribution at the final stage of compression. Bottom: Zoom in boxes with the cumulated plastic strain on a color scale.

scale we deal with small strain-driven compression of the sample, at the microscopic scale the bonds are submitted to combinations of different large deformations: compression, traction, rotation, and shear. This is due to the geometrical complexity of the cemented granular material. In almost all cases the bond deformation is localized in a shear band that acts in each damaged bond. The orientation of these shear bands is also very heterogenous.

Even at this low level of compaction we found that new contacts between the grains and the walls are established, but no new contact between the grains appear during the loading. That means that the P-wave propagation is not facilitated by these new intergrains contacts as discussed in the context of "nonclassical nonlinearity" or "clapping interface model" [Chaboche, 1992, Lemaitre and Desmorat, 2005, Pecorari and Solodov, 2006, Lyakhovsky et al., 2009].

3. Elastic wave probing

In this section, we present the simulations of the wave propagation, to highlight the wave speed sensitivity to the damage state of the sample. We want to show that it is possible to monitor the macroscopic damage through the wave speed record. For this, we model the propagation of small amplitude, purely reversible, non-destructive waves in the damaged material at different stages of the quasi-static loading. These stages are chosen to better understand the impact of large and small increments of damage and different regimes of the loading process (i.e., elastic at the beginning, then inelastic with increased damage).

3.1. *Problem setting*

3.1.1. *Macroscopic level*

At different stages $\varepsilon^*_{\text{macro}}$, which correspond to the time $t^* \in [0, T^{\text{quasi-static}}]$ of the quasi-static loading process described in the previous section (indicated by green vertical lines in Figure 4), we analyze the wave propagation in the sample $\mathscr{D}^*_{\text{macro}} = \mathscr{D}^{\text{macro}}_{t^*}$. At the zero acoustic time (here t represents the acoustic time, while the real time is $t^* + t$), a single sinusoidal longitudinal overstress pulse $\sigma^*_{\text{macro}}(t)$ (the total stress is $\sigma^{\text{macro}}(t^*) + \sigma^*_{\text{macro}}(t)$) is emitted at the top of the sample ($y = l$) in the y-direction and propagates along the y-axis (see Figure 7). The transmitted P-wave is recorded on the bottom of the sample ($y = 0$). On the lateral walls, we impose frictionless contact boundary conditions. Two series of simulations are made for two frequencies of the pulse. The first one for 150 kHz, which is a low frequency for this sample as the corresponding wavelength is 20 mm in the glass, almost 50 times the mean radius of the beads. The second simulation is for 1.50 MHz, which we designate as a "medium" frequency as it corresponds to a wavelength of 2 mm in the glass, which is close to five times the mean radius of the beads. As expected, high-frequency simulations (at 7.50 MHz, corresponding to a wavelength of 0.4 mm, as the mean radius of the beads) show that the pulse does not (or hardly) propagate any more due to intense scattering, and these are not investigated here.

Note that in the seismological context, and for fault monitoring, the seismic velocity monitoring relies on relatively low frequency waves (less than a few Hz) due to the rapid attenuation of the waves in the complex, highly fractured rocks of the fault core. This mean that the probe has a wavelength much larger than the typical grain size.

The macroscopic computations of the P-wave speed V^*_P can be used to compute the macroscopic damage $d^*_{\text{macro}} = 1 - M^*_{\text{macro}}/M^0_{\text{macro}}$ (here M_{macro} is the macroscopic uniaxial strain modulus). We know that $V^*_P = \sqrt{M^*_{\text{macro}}/\rho^*_{\text{macro}}}$ and by mass conservation, that $\rho^0_{\text{macro}} = (1-\varepsilon^*_{\text{macro}})\rho^*_{\text{macro}}$; then, we get the formula

$$d^*_{\text{macro}} = 1 - \left(\frac{V^*_P}{V^0_P}\right)^2 \frac{1}{1-\varepsilon^*_{\text{macro}}}. \tag{1}$$

3.1.2. *Microscopic level*

At different stages of the quasi-static loading process described in the previous section, and as indicated by green vertical lines in Figure 4, we stored the deformed meshes and the damage distributions. Let us denote the domain occupied by the cemented granular material by $\mathscr{D}^* = \mathscr{D}_{t^*}$ (with the partition into the phase grains $\mathscr{G}^* = \mathscr{G}_{t^*}$ and the phase bonds $\mathscr{B}^* = \mathscr{B}_{t^*}$), and the damage distribution computed in the quasi-static finite element simulations by $d^* = d_{t^*} : \mathscr{B}^* \to [0,1]$.

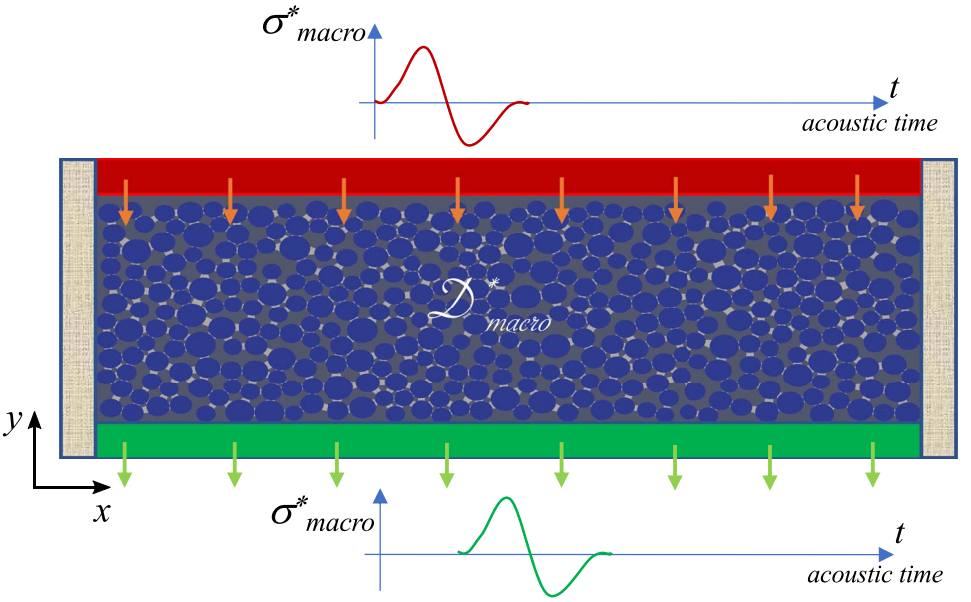

Figure 7. Representation of the ultrasound probing numerical experiment.

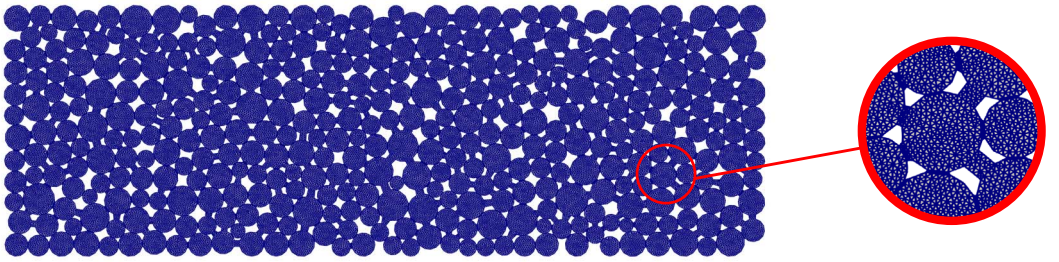

Figure 8. The initial mesh used for the dynamic computations.

3.2. *Mechanical and numerical modeling*

As the waves have a small amplitude, there is no evolution of the damage and plastic strain during the dynamic process, which is said to be nonperturbative or nondestructive. This is why the small perturbation assumption can be considered to be valid and the material can be supposed to be linear elastic, with the mass density ρ^* and the elastic coefficients λ^*, μ^*, given by

$$\rho^* = \begin{cases} \rho_g, & \text{in } \mathscr{G}^*, \\ \rho_b, & \text{in } \mathscr{B}^*, \end{cases} \quad \lambda^* = \begin{cases} \lambda_g, & \text{in } \mathscr{G}^*, \\ (1-d^*)\lambda_b, & \text{in } \mathscr{B}^*, \end{cases}$$

$$\mu^* = \begin{cases} \mu_g, & \text{in } \mathscr{G}^*, \\ (1-d^*)\mu_b, & \text{in } \mathscr{B}^*. \end{cases}$$

The dynamic problem is discretized in time by the classical implicit Newmark method, with $\beta = 1/4$ and $\gamma = 1/2$ [e.g., see Fung, 1997], which is unconditionally stable and thus allows much larger values of the time step than the critical Courant–Friedrichs–Lewy time step. For the space discretization, we used [P2-continuous] finite element discretization for the displacement field and [P1-discontinous] for the stress field.

The quasi-static mesh used previously is not appropriate for wave propagation. For the dynamic wave propagation simulation, the domain $\mathscr{D}^*$ was re-meshed to obtain a uniformly fine mesh (see Figure 8). Indeed, as the waves propagate everywhere in the sample, for the dynamic problem we need a

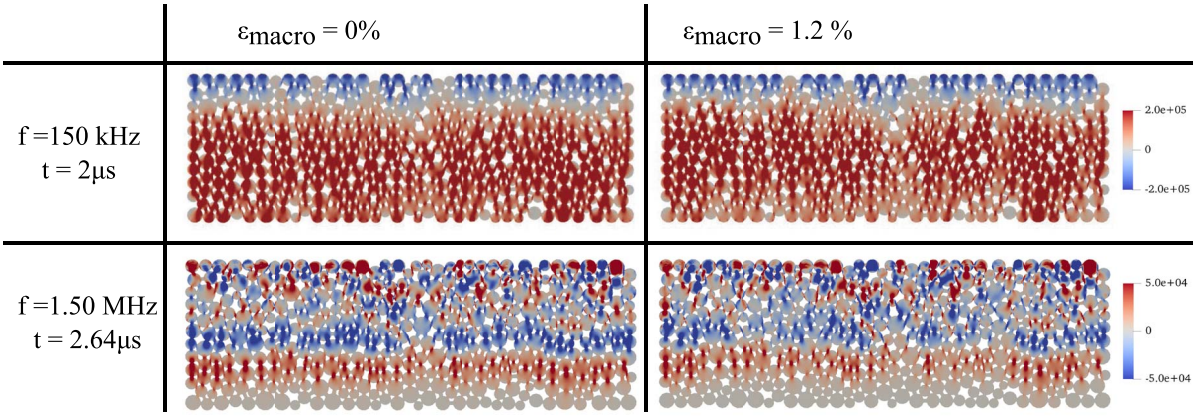

Figure 9. Snapshots of the longitudinal stress σ_{yy} field (as a color scale) at $t = 2$ μs after the low-frequency excitation (top) and at $t = 2.64$ μs after the medium-frequency excitation (top), in the undamaged sample (left) and after compression (right) corresponding to $\varepsilon^*_{\text{macro}} = 1.2\%$ and $d_{\text{ave}}(t^*) = 0.54\%$.

regular mesh without any size contrast between the peripheral and the core edges of the beads. Since the open space results in a free boundary condition for the propagating waves, the beads size and the open spaces sizes are important in choosing the wavelength to probe the average material properties (see the discussion in the next section about the wave behavior for different frequencies).

3.3. *Results*

The low-frequency pulse (for which the wavelength in the glass is almost 50 times the mean radius of the beads) generates a well-established coherent wave, without remarkable multiply scattered waves. It is visible at $t = 2$ μs after the excitation in the first line of Figure 9, which shows several snapshots of the longitudinal stress σ_{yy} field in all of the sample. The left row shows the undamaged sample ($\varepsilon^*_{\text{macro}} = 0\%$ and $d_{\text{ave}}(t^*) = 0\%$), in which the coherent front has not yet reached the reception wall. The right row shows the same snapshot, but computed with a damaged sample ($\varepsilon^*_{\text{macro}} = 1.2\%$ and $d_{\text{ave}}(t^*) = 0.54\%$). This highlights a short delay of the coherent wave, which is especially visible in the beads close to the lower wall.

For the 1.50 MHz pulse (for which the wavelength in the glass is almost 5 times the mean radius of the beads), a similar delay can be observed between clear coherent waves computed with the undamaged state and the same damaged state, as seen in the second line of Figure 9. However, in this case, the coherent waves are followed by multiply scattered waves, producing a tail in the signal similar to the seismic coda. Note the complexity of the field distribution at both the macroscopic scale and the bead scale, due to the high heterogeneity of the granular material.

The transmitted σ_{yy}-waves are recorded along the bottom wall (called the "reception wall"), as discretized in 1000 spatial points and shown for the 1.5 MHz pulse in Figure 10. They are gathered when they belong to the same bead of the reception side, making voids appear between the 26 beads of this side. One of these signals is plotted in Figure 11 (in green) for different states of damage of the sample. The sum of all these signals is visible as the blue curve inside the right box of Figure 10, which enhances the coherent arrivals. Indeed, unlike the coherent wave that is almost uniform along the y-axis, the codas depend on the recording position. So their sum, which is physically defined in the experiments by the large transducer in contact with all of the beads of the reception wall, tends to cancel, whereas the summed amplitudes of the coherent wave and its reflections are enhanced.

The signals plotted in Figure 11 are associated with different levels of damage as they correspond to the macroscopic strains $\varepsilon_{\text{macro}} = 0\%$, $\varepsilon_{\text{macro}} = 0.51\%$,

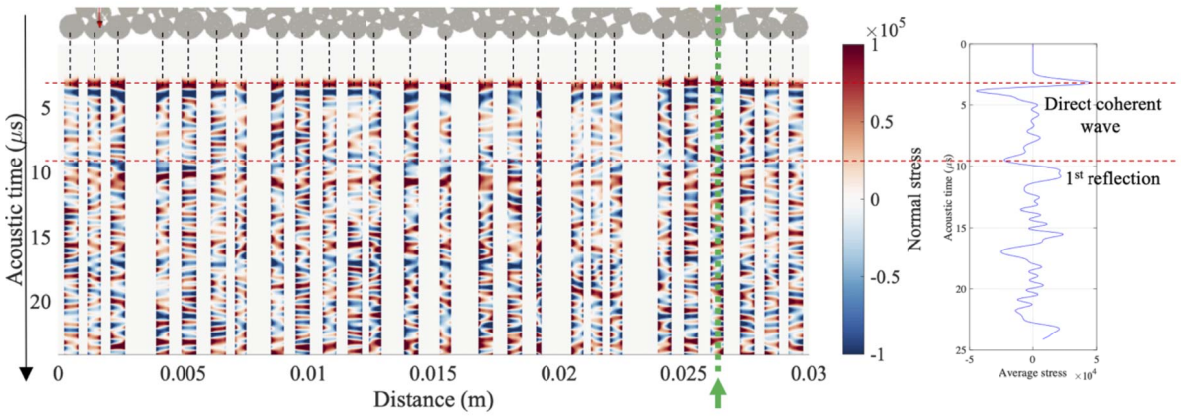

Figure 10. (a) Acoustic signals recorded along the reception wall (represented above) for a 1.5 MHz pulse. The green arrow indicates the position chosen to compare the codas in Figure 11. (b) Summed waves along the reception wall.

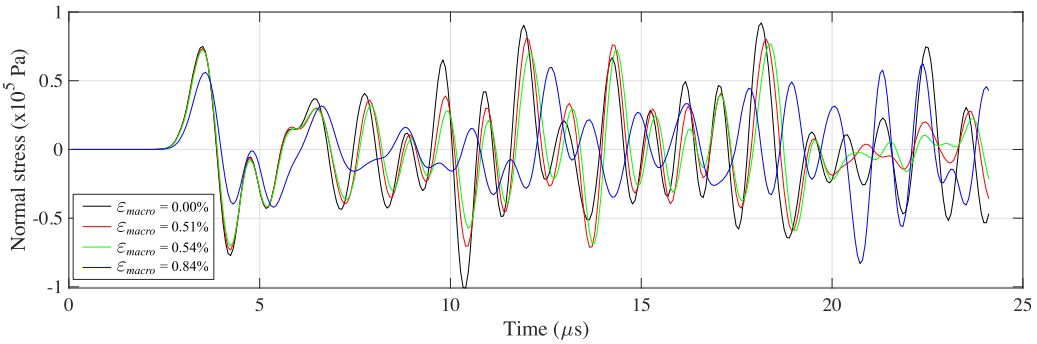

Figure 11. The transmitted acoustic signals recorded for a 1.5 MHz pulse at the same position of the reception wall (indicated in green in Figure 10) for the undamaged sample (black) and after different steps of compression: $\varepsilon_{\text{macro}} = 0.51\%$ (red), $\varepsilon_{\text{macro}} = 0.54\%$ (green), and $\varepsilon_{\text{macro}} = 0.84\%$ (blue).

$\varepsilon_{\text{macro}} = 0.54\%$ and $\varepsilon_{\text{macro}} = 0.84\%$. We observe that the second and third signals in Figure 11 are very similar, which is understandable, with the weak strain and the damage difference between them. The third signal in Figure 11 is slightly delayed compared to the second one, with a small amplitude loss, and this delay increases visibly with the acoustic time t between 7 and 20 μs. After 20 μs, these signals are not coherent anymore. Similar, but more pronounced, observations can be made between these two signals and the first one computed with the undamaged sample. We note that the first coherent peak, which corresponds to the direct transmitted ballistic wave, has almost the same amplitude and time of flight for these three signals. This is not inconsistent, as at the same time the thickness of the sample decreases and the wave velocity decreases. The contrast between the signals is much more obvious with the fourth signal computed, when the quasistatic loading begins to saturate after important damage to the sample. We observe a loss of amplitude of the transmitted ballistic wave and a time of flight increase. At later times, we observe important changes in the coda. These can be explained by the increasing scattering process of the waves due to two changes: the first one is the increasing impedance contrast between the glass and the damaged cement at the interface bead/bond linked to the degradation of the elastic parameters of the cement; the second one is the slight geometric evolution of the sample without true rearrangement,

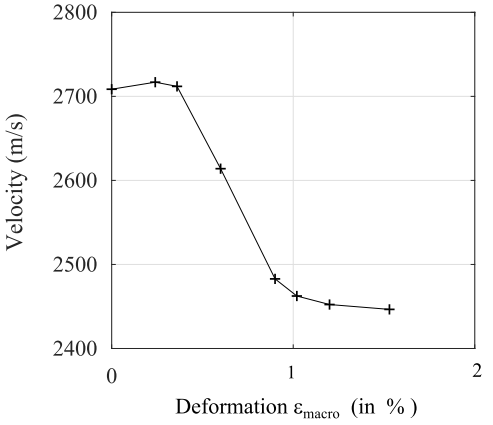

Figure 12. The wave velocity V in the sample during a quasistatic process versus the macroscopic strain $\varepsilon_{\text{macro}}$. The velocity is calculated with the time of flight of the summed signals along the reception wall for a low-frequency pulse (150 kHz).

as the contacts remain the same (i.e., no loss, no creation).

The sum of the signals along the reception wall allows estimation of the time of flight of the transmitted pulse, and therefore of the velocity of the longitudinal coherent wave, as the ratio of the time of flight and the thickness of the numerical sample at the considered state of damage. We choose the time of flight measured from the first peak. The velocities obtained are shown in Figure 12 for the low-frequency pulse, to ensure that the coherent regime is well established, and validate the approximation of the effective medium theory [Digby, 1981]. The velocity can also be calculated from the mean time of flight over the statistics of the signals recorded at 1000 positions along the reception wall, which gives very close results, as can be seen in Figure 14b for a 1.5 MHz pulse.

Figure 12 shows that for a low frequency pulse (150 kHz), the velocity first increases slightly in the elastic part of the deformation, when there is no damage ($\mathrm{d}V/V$ close to +1%); it then decreases dramatically ($\mathrm{d}V/V$ close to −10%). The first phase is associated to a slight increase of the wave velocity and can explained easily on the basis that at the begining some additional disks enter into contact with the rigid piston, which creates new force chains that facilitate the wave propagation. The decrease in wave velocity begins when the bonds are damaged; i.e., when the microscopic damage average d_{ave} starts increasing significantly (see Figure 4). It is remarkable that a very small amount of microscopic damage average can imply such a dramatic loss. Moreover, when the load reaches its stationary value, the velocity keeps decreasing, although by less, despite the almost constant microscopic damage average rate $\dot{d}_{\text{ave}}$ (as also seen in Figure 4). This can be explained on the basis that simulated waves propagate along the deformation axis, which is also the privileged axis of the first bond damaging, while in the last phase, the microscopic damage concerns mainly the bonds orientated mostly in the other directions (see Section 4 for more details). Moreover, it should not be forgotten that in our simple mechanical model there is damage saturation at $d_{\max} = 0.8$, which implies that the velocity drop is also saturated in some sense.

In all of these considerations, it appears clear that the microscopic damage average d_{ave}, defined as the ratio between the integral of the damage and the area of the sample $|\mathscr{D}_t|$ and associated to the quasi-static process, is not adapted to measure the damage of the sample. Figure 13 shows the macroscopic damage d_{macro}, given by (1) and computed with the elastic wave probing method. This overall damage parameter, which can be found without any computation of the quasistatic process, appears to be more adapted to describing the complexity of the problem. Indeed, for $\varepsilon_{\text{macro}} = 1\%$ for instance, we found a value of d_{macro} that was almost 40 times greater than d_{ave}, and in the last phase associated to the load plateau, the damage d_{macro} also has a plateau, as expected.

To check the validity of the velocities calculated with the time of flight in the case of a 1.5 MHz pulse, we use the doublet technique [Poupinet et al., 1984], which is also called the moving-window cross-spectrum technique [Clarke et al., 2011] or coda wave interferometry [Snieder et al., 2002]. We apply this to all the consecutive couples $i-1, i$ corresponding to the consecutive chosen quasistatic steps for the dynamical simulations. This ensures good temporal coherence between the signals $i-1$ and i, as shown in Figure 11, which is necessary to apply this technique. This technique is especially interesting for subtle changes of the material velocity, and it consists of the evaluation of the relative velocity change $\delta v_{ij} = (v_j - v_i)/v_i$ of the medium at a given position between two temporal states i and j. We

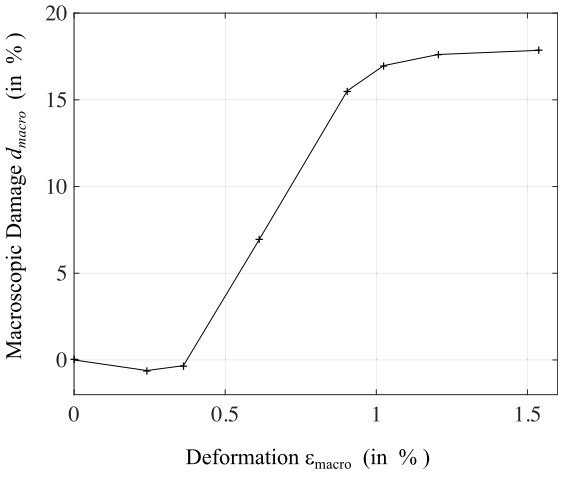

Figure 13. The macroscopic damage d_{macro} computed with elastic wave probing (with a low-frequency pulse of 150 kHz) versus the macroscopic strain $\varepsilon_{\text{macro}}$.

can also write $\delta v_{ij} = \delta l_{ij} - \delta t_{ij}$ with δl_{ij} linked to the strain (calculated from the quasistatic loading), $\delta t_{ij} = \mathrm{d}t_{ij}/t$ as the relative change of the time of flight $\mathrm{d}t_{ij}$ of the wave through the sample, and t as the acoustic time, which is zero at the beginning of the excitation pulse. The procedure to evaluate δt_{ij} has two steps: calculation of $\mathrm{d}t_{ij}(t)$ for different times t in the whole range of the acoustic time (so with the ballistic parts and the codas), as sufficient for the second step, which is linear regression of $\mathrm{d}t_{ij}$ with t. This regression goes through the origin and its slope is directly δt_{ij}. Figure 14a shows the two contributions $\delta l_{ij}(t)$ and $\delta t_{ij}(t)$ as functions of the macroscopic deformation. The two contributions were calculated between consecutive pairs $i-1, i$ and were accumulated, to be compared to the initial step 0. The cumulative error from the last regression of the doublet technique is also plotted in Figure 14a. It increases with the macroscopic deformation, until almost 0.5% at the last step, as the nondeformed configuration is taken as the reference here.

Figure 14b shows the velocity change $\delta v_{ij}(t)$, which is the difference between these two contributions. The same error bars are also plotted. The velocity changes obtained with the times of flight and both of the summed signals and from their statistics (from the same dynamic simulations) are also plotted here. The results are very close.

4. Induced damage anisotropy

In this section, we investigate how the induced damage is related to the loading direction. We also investigate the loss of isotropy of the macroscopic wave propagation. As the effects are similar and more pronounced in the x-axis than in the y-axis direction, we consider the quasistatic edometric compression along the x-axis. For this simulation, the final strain is $\varepsilon_{\text{macro}} = 2.17\%$.

The "norm" of the deviatoric stress tensor is shown in Figure 15a, which corresponds to the last step of the computation. It shows that the force chains tend to be oriented along the axis of the loading. This assumes that the bonds oriented along this same axis are more solicited for the transmission of the stress, and as a consequence they would be more damaged than the others. This can be seen in Figure 15b, which shows the distribution of the damage parameter d in the bonds at the last step. To rigorously demonstrate this observation, Figure 15c shows the value of the damage integrated over each bond independent of the others, as a function of its angle. Clear anisotropy appears and confirms the previous hypothesis: the damage is concentrated in the bonds with angles in $[\pi/6; 5\pi/6]$ modulo π.

Therefore we define the "x-bonds" and "y-bonds" as the two groups of bonds with angles between $[-\pi/6; \pi/6]$ and $[\pi/3; 2\pi/3]$ modulo π, respectively. Figure 15d shows the values of the damage d^x_{ave} and d^y_{ave} of the average damage d_{ave} integrated over these two groups as functions of the macroscopic strain. The x-bonds concentrate always the greatest part of the total damage, and almost three times the damage of the y-bonds at the last step. The average damage initially increases quickly in the x-bonds, then keeps increasing, although more slowly, while it increases later in the y-bonds, with an intermediary and stable slope. First the x-bonds are mainly damaged and then the damage appears in the y-bonds, which are the last bonds possible to damage. This can explain why the normal load in the axis of the loading becomes stationary, whereas the total damage keeps increasing, as can be seen for compression along the y-axis in Figure 4.

These computations on the damage average suggest that the bounds orientated along the propagation axis are mainly implied in the speed wave drop. To confirm this assumption, we can test the

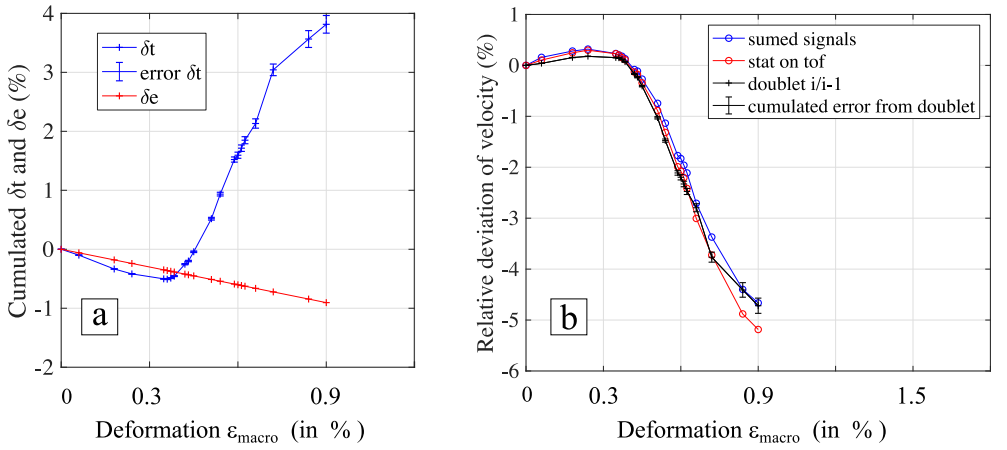

Figure 14. Velocity changes computed with the doublet technique for a 1.5 MHz pulse. (a) Thickness (red) and delay (blue) changes as functions of the quasistatic step. Error bars on the delay come from the last regression of the doublet technique. (b) Velocity changes as a function of the quasistatic step and computed with the doublet technique (black), from the time of flight statistics (red) and the time of flight of the summed signals (blue).

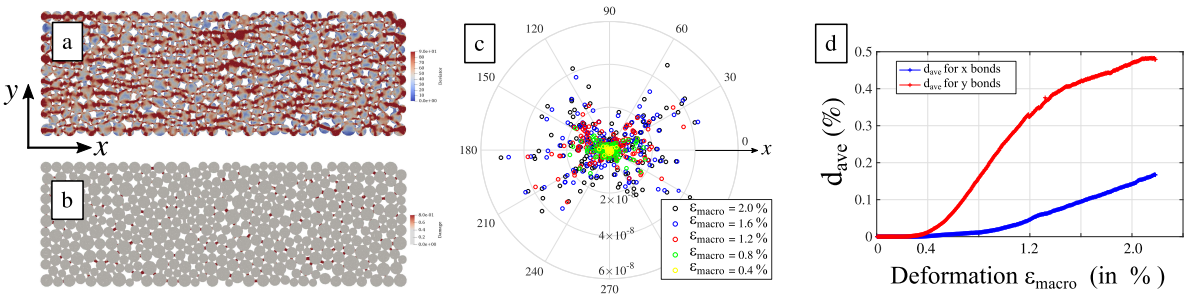

Figure 15. Edometric compression along the x-axis. (a,b) Maps of the deviatoric stress and damage parameter d, respectively, at the last step of the quasi-static computation. (c) Damage integrated over the bonds independently as a function of their angle for different macroscopic strains. (d) Damage integrated over the "x-bonds" and "y-bonds" as a function of the macroscopic strain.

anisotropy of the wave propagation by measuring the wave velocity along the x-axis and y-axis (called V_x and V_y, respectively) in the configuration of this section with compression along the x-axis. We use low frequency pulses (150 kHz), as defined in Section 3, at six different steps of the same quasi-static compression simulation. With the associated wavelength of 20 mm, we consider that no multiple scattering occurs, which would considerably change the comparison between the two axes, as the wall is three times longer than the other one and would accumulate more scattering effects. The velocities are plotted in Figure 16 and are computed with the time of flight of the first peak of the summed signals recorded along the corresponding wall and the thickness (constant for the propagation along the y-axis).

First, we check that V_x and V_y are almost the same at the initial state without compression (step 0), as there should not be any source of anisotropy at this step. We indeed find values that are close, as 2740 and 2690 m/s respectively, with a relative deviation of 1.8%. The small difference might be due to the geometry of the sample and the boundary conditions. Then we observe that both velocities are impacted by the loading and the induced damage, even V_y, and where V_x shows a decrease of 7%, twice the decrease

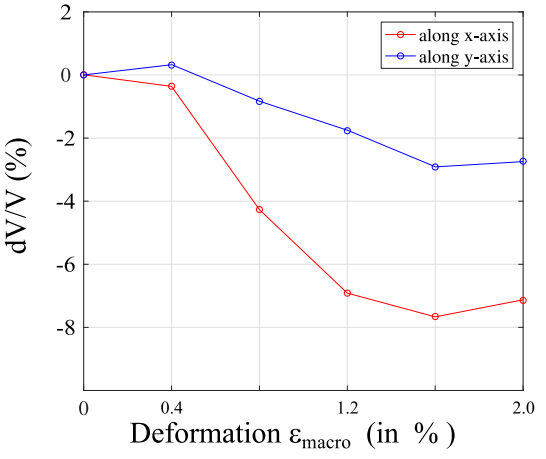

Figure 16. dV_x/V_x and dV_y/V_y divided by their respective initial values as functions of the macroscopic deformation. The velocities are calculated with the time of flight of the summed signals along the reception wall for a low-frequency pulse (150 kHz).

of V_y. This confirms the induced damage anisotropy for the wave propagation.

As they are calculated with the same method, we can also compare V_x and V_y to V, the velocity obtained from the compression and the wave propagation along the same y-axis represented in Figure 12a. V and V_x are very similar, with very close values and the same trend for $\varepsilon_{\text{macro}}$ between 0.3% and 1.5%, with maximal velocity losses dV/V and dV_x/V_x close to 10%. However, unlike V_x, V_y and V show a slight increase for short strains, which is due to the shorter size along the y-axis.

5. Conclusion and discussion

We have presented a series of numerical experiments to discuss the phenomenology responsible for the changes in seismic velocities during deformation of a cohesive granular medium. Our model is simplified to highlight the most important elements, and of course to guarantee the numerical stability of our results. We have considered a 2D model of a cohesive granular medium in an edometer compression test configuration, for which only monotonic loading experiments have been considered. The damage is associated with the nonlinear behavior of the bonds, in the form of a plasticity law. During compression, the deformation quickly becomes very heterogeneous, with a concentration on the force chains where the bonds undergo all of the deformation modes.

In practice, the propagation of waves allows the changes in elastic properties to be highlighted by measuring the propagation speed. Our simulations allow us to observe the velocity drop in the deformation domain where the model is not very sensitive to the maximum damage characteristics that we had to introduce. We can deduce from the propagation velocity an effective macroscopic damage parameter, which turns out to be about 40 times larger than the average damage, which indicates the strong sensitivity of the waves to the deformation and the predominance of the weakening of the force chain elements. We have also shown the anisotropic character of the velocity reduction controlled by the direction of the imposed deformation.

At the microscopic level the damage model used for the bonds is isotropic and involves a Poisson ratio (or equivalently a ratio between P and S-wave velocities) which is not affected by damage. In contrast, at the macroscopic level the model loses the initial isotropy and we have noticed the differences in the P-wave velocities according to the direction of propagation. It will be interesting to see how the S-wave speeds are affected and to analyze how the ratio between P and S-wave speeds depends on the propagation direction. We note that the evolution of the ratio between P and S-wave velocities during the damage evolution is still an observational challenge for seismology. The reason is mainly the difficult localization and spatial extension of the changes that make precise quantitative measurement of the evolution of this ratio very difficult with present-day techniques.

To compare our results with seismic observations, a first order observable is the velocity itself. The earth crust has been subject to damage for a long time and damage has accumulated and persisted in the regions of strongest deformations, as active fault zones. The observed velocity in the shallow crust is diminishing in the vicinity of faults [Zigone et al., 2015], which show the presence of damage. The model qualitatively predicts these observations. Furthermore, measurable temporal changes in velocity can be observed in the Earth in response to various processes, which range from earthquake shaking to rain and Earth tides. These perturbations correspond to very small deformations, typically ranging

from 10^{-6} to 10^{-8}. They would not induce significant global changes, but can affect locally the wave velocity. Our numerical experiments are limited to monotonic compressions and we do not have the precision to analyze the deformation levels encountered in seismology.

We have nevertheless shown high sensitivity of the wave velocity with the deformation during the damaging process for a cohesive granular medium as it has been reported before [Langlois and Jia, 2014]. We can try to put into perspective the simulations for our simplified model and the observations.

We can deduce from the simulations the slope of the velocity-deformation curve (e.g., Figure 12), which measures the sensitivity of the wave velocity. The curve shows an increase in sensitivity with damage. Natural observations do show significant variations in sensitivity as a function of rock conditions. This has been clearly shown on a regional scale in Japan [Brenguier et al., 2014], with active, highly fractured volcanic structures being the regions where the largest velocity drops are observed after large earthquakes.

The model we have studied allows us to highlight the importance of stress heterogeneity and localized nonlinearity at the microscopic scale for macroscopic behavior. Nevertheless, the model is very simple in terms of its geometry, and corresponds to a case where the jumps are few, leaving an important part to the elastic granular behavior. The parameters will have to be adapted so that the simulations correspond quantitatively to seismological observations. The complexity of geophysical environments, with multi-scale heterogeneities and the likely presence of fluids, makes the exercise impossible with the numerical means implemented here.

Based on Figure 12, the sensitivity of the relative velocity to deformation is of the order of 10 for our model in compressional experiments. Natural observations are for much smaller deformations than what is resolved in our simulations. It should be noted, however, that the observed sensitivity is much greater than that calculated in this study. For tectonically driven static expansions of the order of 10^{-6}, a sensitivity of the order of 100 has been reported [Rivet et al., 2014]. This suggests very high spatial concentration of force chains and nonlinearity. In the extreme case of the response to Earth tides, the deformation is of the order of 10^8 and the sensitivity for very shallow materials would reach 10,000 [Mao et al., 2019b, Sens-Schönfelder and Eulenfeld, 2019]. The differences are significant, but the increase in sensitivity for the model can be produced by changing the geometry and the distribution of the elastic elements within the phenomenology described here, although at the cost of heavy computational effort. The most important aspect for comparison is the 2D limitation of the model. We have seen in 2D that the ratio between the macroscopic damage which governs the effective wave velocity and the mean damage is about 40, due to the concentration of the stresses on the force chains. In the transition to the 3D case, this concentration towards linear chains might result in a different (larger or equal) ratio. This leads to sensitivities of the order of some of those observed in Nature. The highest sensitivities to transient or periodic perturbations suggest a model for which the macroscopic response is controlled by very sparse and very localized chains of forces that are extremely sensitive to small macroscopic deformation perturbations. These conditions will be considered in further numerical studies.

Conflicts of interest

Authors have no conflict of interest to declare.

Acknowledgements

The authors acknowledge support from the European Research Council under the European Union Horizon 2020 research and innovation program (grant agreement no. 742335, F-IMAGE).

IRI acknowledges support of the Romanian Ministry of Research (project number PN-III-P4-PCE-2021-0921 within PNCDI III).

Appendix. Mechanical model description

The movement (flow) in the Eulerian description is given by the velocity field, denoted $\boldsymbol{v}(t,\cdot) : \mathscr{D}_t \to \mathbb{R}^d$. The rate of deformation and the spin rate are denoted by $\boldsymbol{D} = \boldsymbol{D}(\boldsymbol{v}) = (\nabla \boldsymbol{v} + \nabla^T \boldsymbol{v})/2$ and by $\boldsymbol{W} = \boldsymbol{W}(\boldsymbol{v}) = (\nabla \boldsymbol{v} - \nabla^T \boldsymbol{v})/2$, respectively. If we denote the Cauchy stress tensor by $\boldsymbol{\sigma}(t,\cdot) : \mathscr{D}_t \to \mathbb{R}^{n\times n}$, then the momentum balance law for the quasi-static loading reads:

$$\operatorname{div} \boldsymbol{\sigma}(t) + \rho \boldsymbol{b}(t) = 0, \quad \text{in } \mathscr{D}_t,$$

where ρ is the mass density and $\boldsymbol{b}$ are the body forces.

For the grains, we consider an isotropic hypo-elastic law [e.g., see Belytschko et al., 2000]

$$\boldsymbol{\sigma}^{\nabla}(t) = \lambda_g \,\mathrm{trace}\,(\boldsymbol{D})\boldsymbol{I} + 2\mu_g \boldsymbol{D}, \quad \text{in } \mathscr{G}_t,$$

where λ_g, μ_g are the elastic coefficients of the grains, $\boldsymbol{\sigma}^{\nabla} = \dot{\boldsymbol{\sigma}} - \boldsymbol{W}\boldsymbol{\sigma} - \boldsymbol{\sigma}\boldsymbol{W}$ is the Jaumman time derivative, and $\dot{\boldsymbol{\sigma}} = \partial_t \boldsymbol{\sigma} + \boldsymbol{v}\cdot\nabla\boldsymbol{\sigma}$ is the material (total) time derivative.

For the mechanical modeling of the bond material, we chose a very simple elasto-plastic model, which couples isotropic ductile damage with Von-Mises plasticity. For this, we considered the additive decomposition of the rate deformation tensor into the elastic $\boldsymbol{D}^e$ and plastic rates $\boldsymbol{D}^p$ of deformation

$$\boldsymbol{D} = \boldsymbol{D}^e + \boldsymbol{D}^p.$$

The weakening effect is characterized by the (phenomenological) damage parameter $d \in (0,1)$. Following the strain equivalence principle proposed by Lemaitre [Lemaitre and Plumtree, 1979], the strain of damaged material ($d > 0$) subjected to the effective stress is the same as that of material without damage ($d = 0$). This means that the Lamé elastic coefficients have to be replaced by $(1-d)\lambda_b$ and $(1-d)\mu_b$, respectively, where λ_b, μ_b are the elastic coefficients of the undamaged bond material (see Table 1). For the elastic range, as for the grains, we considered the generalization of Hooke's law written in terms of the Jaumann rate of the Cauchy stress tensor

$$\boldsymbol{\sigma}^{\nabla}(t) = (1-d)\lambda_b \,\mathrm{trace}\,(\boldsymbol{D}^e)\boldsymbol{I} + 2(1-d)\mu_b \boldsymbol{D}^e, \quad \text{in } \mathscr{B}_t.$$

The plastic rate of deformation is related to the Cauchy stress tensor through the flow rule associated to the classical Von-Mises yield criterion with no hardening. To be more precise, let $\mathscr{F}(\boldsymbol{\sigma}, d) = \sigma_{\mathrm{eq}}/(1-d) - k$ be the yield function, with k the yield limit and $\sigma_{\mathrm{eq}} = \sqrt{2/3}|\boldsymbol{\sigma}^D|$ the Von-Mises stress ($\boldsymbol{\sigma}^D = \boldsymbol{\sigma} - (1/3)\mathrm{trace}(\boldsymbol{\sigma})\boldsymbol{I}$ is the stress deviator). If we denote the accumulated plastic strain by ε^p (given through the differential equation $\dot{\varepsilon^p} = \sqrt{2/3}|\boldsymbol{D}^p|$), then the flow rule reads

$$\boldsymbol{D}^p = \frac{\dot{\varepsilon^p}}{\sigma_{\mathrm{eq}}}\boldsymbol{\sigma}^D,$$

while the loading–unloading conditions read

$$\dot{\varepsilon^p} \geq 0, \quad \mathscr{F}(\boldsymbol{\sigma}, d) \leq 0, \quad \dot{\varepsilon^p}\mathscr{F}(\boldsymbol{\sigma}, d) = 0.$$

We have considered here a very simple basic damage law [following Lemaitre and Chaboche, 1994], where the damage is related only to the (accumulated) plastic strain ε^p.

$$d = d^p(\varepsilon^p).$$

For simplicity the dependence of the damage on the accumulated plastic strain will be a piecewise linear function that involves an activation plastic strain $\varepsilon^p_{\mathrm{activation}}$ (damage threshold) and a maximal level of damage $d_{\max}$, corresponding to the plastic strain $\varepsilon^p_{\max}$ (which might represent the rupture plastic strain), by

$$d^p(\varepsilon^p) = \begin{cases} x\dfrac{d_{\max}}{\varepsilon^p_{\max} - \varepsilon^p_{\mathrm{activation}}}[\varepsilon^p - \varepsilon^p_{\mathrm{activation}}]_+, & \text{if } \varepsilon^p < \varepsilon^p_{\max}, \\ d_{\max}, & \text{if } \varepsilon^p \geq \varepsilon^p_{\max}, \end{cases}$$

where $[x]_+ = (x + |x|)/2$ is the positive part function. Even if the constants $\varepsilon^p_{\mathrm{activation}}, \varepsilon^p_{\max}$ and $d_{\max}$ depend generally on the tri-axiality ratio, in what follows we will assume that they are constants.

References

Allam, A. A. et al. (2014). Seismic velocity structure in the hot springs and trifurcation areas of the San Jacinto fault zone, California, from double-difference tomography. *Geophys. J. Int.*, 198(2), 978–999. ISSN: 1365-246X, 0956-540X.

Barajas, A. et al. (2021). Separation of poroelastic and elastic processes of an aquifer from tectonic phenomena using geodetic, seismic, and meteorological data in the Pollino Region, Italy. *Geochem. Geophys. Geosyst.*, 22(11), article no. e2021GC009742. ISSN: 1525-2027, 1525-2027.

Belytschko, T., Liu, W. K., and Moran, B. (2000). *Nonlinear Finite Elements for Continua and Structures*. John Wiley & Sons, Ltd, Chichester.

Brenguier, F., Campillo, M., Hadziioannou, C., et al. (2008). Postseismic relaxation along the San Andreas fault at Parkfield from continuous seismological observations. *Science*, 321(5895), 1478–1481. ISSN: 0036-8075, 1095-9203.

Brenguier, F., Campillo, M., Takeda, T., et al. (2014). Mapping pressurized volcanic fluids from induced crustal seismic velocity drops. *Science*, 345(6192), 80–82. ISSN: 0036-8075, 1095-9203.

Canel, V. et al. (2020). Monitoring of damage processes in cemented granular materials with acoustic emissions and seismic velocity reduction. Technical Report EGU2020-21891, Copernicus Meetings.

Cappa, F. et al. (2014). Off-fault long-term damage: A condition to account for generic, triangular earthquake slip profiles. *Geochem. Geophys. Geosyst.*, 15(4), 1476–1493. ISSN: 15252027.

Chaboche, J.-L. (1992). Damage induced anisotropy: On the difficulties associated with the active/passive unilateral condition. *Int. J. Damage Mech.*, 1(2), 148–171. ISSN: 1056-7895.

Chester, F. M. (1993). Internal structure and weakening mechanisms of the San Andreas fault. *J. Geophys. Res.*, 98(B1), 771–786.

Clarke, D. et al. (2011). Assessment of resolution and accuracy of the moving window cross spectral technique for monitoring crustal temporal variations using ambient seismic noise. *Geophys. J. Int.*, 186(2), 867–882. ISSN: 0956-540X.

Delorey, A. A. et al. (2021). Probing the damage zone at Parkfield. *Geophys. Res. Lett.*, 48(13), article no. e2021GL093518. ISSN: 1944-8007.

Digby, P. J. (1981). The effective elastic moduli of porous granular rocks. *J. Appl. Mech.*, 48(4), 803–808. ISSN: 00218936.

Dvorkin, J., Nur, A., and Yin, H. (1994). Effective properties of cemented granular materials. *Mech. Mater.*, 18(4), 351–366. ISSN: 0167-6636.

Evesque, P. (2000). Eléments de mécanique quasi-statique des milieux granulaires mouillés ou secs. *Poudres et grains*, NS(1), 1–155.

Fung, T. C. (1997). Unconditionally stable higher-order Newmark methods by sub-stepping procedure. *Comput. Methods Appl. Mech. Eng.*, 147(1), 61–84. ISSN: 0045-7825.

Ghosh, S. and Raju, S. (1996). R–S adapted arbitrary Lagrangian–Eulerian finite element method for metal-forming problems with strain localization. *Int. J. Numer. Methods Eng.*, 39(19), 3247–3272. ISSN: 1097-0207.

Hall, S. A. et al. (2008). Crack density tensor inversion for analysis of changes in rock frame architecture. *Geophys. J. Int.*, 173(2), 577–592. ISSN: 0956-540X.

Hamiel, Y. et al. (2009). Brittle deformation and damage-induced seismic wave anisotropy in rocks. *Geophys. J. Int.*, 178(2), 901–909. ISSN: 1365-246X.

Hemmerle, A., Schröter, M., and Goehring, L. (2016). A cohesive granular material with tunable elasticity. *Sci. Rep.*, 6(1), 1–11. ISSN: 2045-2322.

Huerta, A. and Casadei, F. (1994). New ALE applications in non-linear fast-transient solid dynamics. *Eng. Comput.*, 11(4), 317–345. ISSN: 0264-4401.

Johnson, P. A. and Rasolofosaon, P. N. J. (1996). Nonlinear elasticity and stress-induced anisotropy in rock. *J. Geophys. Res. Solid Earth*, 101(B2), 3113–3124. ISSN: 2156-2202.

Johnson, P. A., Zinszner, B., and Rasolofosaon, P. N. J. (1996). Resonance and elastic nonlinear phenomena in rock. *J. Geophys. Res. Solid Earth*, 101(B5), 11553–11564. ISSN: 2156-2202.

Langlois, V. and Jia, X. (2014). Acoustic probing of elastic behavior and damage in weakly cemented granular media. *Phys. Rev. E*, 89(2), article no. 023206.

Lemaitre, J. and Chaboche, J.-L. (1994). *Mechanics of Solid Materials*. Cambridge University Press, Cambridge. ISBN: 978-0-521-47758-1.

Lemaitre, J. and Desmorat, R. (2005). *Engineering Damage Mechanics. Ductile, Creep, Fatigue and Brittle Failure*. Springer, Berlin, Heidelberg.

Lemaitre, J. and Plumtree, A. (1979). Application of damage concepts to predict creep-fatigue failures. *J. Eng. Mater. Technol.*, 101(3), 284–292. ISSN: 0094-4289.

Lyakhovsky, V., Ben-Zion, Y., and Agnon, A. (1997). Distributed damage, faulting, and friction. *J. Geophys. Res. Solid Earth*, 102(B12), 27635–27649. ISSN: 01480227.

Lyakhovsky, V. et al. (2009). Non-linear damage rheology and wave resonance in rocks. *Geophys. J. Int.*, 178(2), 910–920. ISSN: 0956540X, 1365246X.

Mao, S., Campillo, M., et al. (2019a). High temporal resolution monitoring of small variations in crustal strain by dense seismic arrays. *Geophys. Res. Lett.*, 46(1), 128–137. ISSN: 1944-8007.

Mao, S., Mordret, A., et al. (2019b). On the measurement of seismic travel-time changes in the time-frequency domain with wavelet cross-spectrum analysis. *Geophys. J. Int.*, 221(1), article no. ggz495. ISSN: 0956-540X, 1365-246X.

Margerin, L. et al. (2016). Sensitivity kernels for coda-wave interferometry and scattering tomography: Theory and numerical evaluation in two-dimensional anisotropically scattering media. *Geophys. J. Int.*, 204(1), 650–666. ISSN: 0956-540X, 1365-246X.

Meier, U., Shapiro, N. M., and Brenguier, F. (2010). Detecting seasonal variations in seismic velocities within Los Angeles basin from correlations of ambient seismic noise. *Geophys. J. Int.*, 181(2), 985–996. ISSN: 0956540X, 1365246X.

Nur, A. and Simmons, G. (1969). Stress-induced velocity anisotropy in rock: An experimental study. *J. Geophys. Res. (1896–1977)*, 74(27), 6667–6674. ISSN: 2156-2202.

Obermann, A. et al. (2016). Lapse-time-dependent coda-wave depth sensitivity to local velocity perturbations in 3-D heterogeneous elastic media. *Geophys. J. Int.*, 207(1), 59–66. ISSN: 0956-540X, 1365-246X.

Olivier, G. et al. (2015). Investigation of coseismic and postseismic processes using in situ measurements of seismic velocity variations in an underground mine. *Geophys. Res. Lett.*, 42(21), 9261–9269. ISSN: 1944-8007.

Pasqualini, D. et al. (2007). Nonequilibrium and nonlinear dynamics in berea and fontainebleau sandstones: Low-strain regime. *J. Geophys. Res. Solid Earth*, 112(B1), article no. B01204. ISSN: 2156-2202.

Pecorari, C. and Solodov, I. (2006). Nonclassical nonlinear dynamics of solid surfaces in partial contact for NDE applications. In Delsanto, P. P., editor, *Universality of Nonclassical Nonlinearity: Applications to Non-Destructive Evaluations and Ultrasonic*, pages 309–326. Springer, New York, NY. ISBN: 978-0-387-35851-2.

Poupinet, G., Ellsworth, W. L., and Frechet, J. (1984). Monitoring velocity variations in the crust using earthquake doublets: An application to the Calaveras Fault, California. *J. Geophys. Res. Solid Earth*, 89(B7), 5719–5731. ISSN: 2156-2202.

Radjai, F. and Dubois, F. (2011). *Discrete-Element Modeling of Granular Materials*. Wiley-Iste, London.

Reasenberg, P. and Aki, K. (1974). A precise, continuous measurement of seismic velocity for monitoring *in situ* stress. *J. Geophys. Res. (1896–1977)*, 79(2), 399–406. ISSN: 2156-2202.

Rivet, D. et al. (2014). Seismic velocity changes, strain rate and non-volcanic tremors during the 2009–2010 slow slip event in Guerrero, Mexico. *Geophys. J. Int.*, 196(1), 447–460. ISSN: 0956-540X.

Rodríguez-Ferran, A., Pérez-Foguet, A., and Huerta, A. (2002). Arbitrary Lagrangian–Eulerian (ALE) formulation for hyperelastoplasticity. *Int. J. Numer. Methods Eng.*, 53(8), 1831–1851. ISSN: 1097-0207.

Roux, P. et al. (2016). A methodological approach towards high-resolution surface wave imaging of the San Jacinto fault zone using ambient-noise recordings at a spatially dense array. *Geophys. J. Int.*, 206(2), 980–992. ISSN: 0956-540X, 1365-246X.

Sawicki, A. and Swidzinski, W. (1995). Cyclic compaction of soils, grains and powders. *Powder Technol.*, 85(2), 97–104. ISSN: 0032-5910.

Sayers, C. M. and Kachanov, M. (1991). A simple technique for finding effective elastic constants of cracked solids for arbitrary crack orientation statistics. *Intl J. Solids Struct.*, 27(6), 671–680. ISSN: 0020-7683.

Sayers, C. M. and Kachanov, M. (1995). Microcrack-induced elastic wave anisotropy of brittle rocks. *J. Geophys. Res. Solid Earth*, 100(B3), 4149–4156. ISSN: 2156-2202.

Schaff, D. P. and Beroza, G. C. (2004). Coseismic and postseismic velocity changes measured by repeating earthquakes: Coseismic and postseismic velocity changes. *J. Geophys. Res. Solid Earth*, 109(B10), article no. B10302. ISSN: 01480227.

Schubnel, A. and Guéguen, Y. (2003). Dispersion and anisotropy of elastic waves in cracked rocks. *J. Geophys. Res. Solid Earth*, 108(B2), article no. 2101. ISSN: 2156-2202.

Scuderi, M. M. et al. (2016). Precursory changes in seismic velocity for the spectrum of earthquake failure modes. *Nat. Geosci.*, 9(9), 695–700. ISSN: 1752-0908.

Sens-Schönfelder, C. and Eulenfeld, T. (2019). Probing the *in situ* elastic nonlinearity of rocks with earth tides and seismic noise. *Phys. Rev. Lett.*, 122(13), article no. 138501. ISSN: 0031-9007, 1079-7114.

Sens-Schönfelder, C. and Wegler, U. (2006). Passive image interferometry and seasonal variations of seismic velocities at Merapi Volcano, Indonesia. *Geophys. Res. Lett.*, 33(21), article no. L21302. ISSN: 1944-8007.

Snieder, R. et al. (2002). Coda wave interferometry for estimating nonlinear behavior in seismic velocity. *Science*, 295(5563), 2253–2255. ISSN: 0036-8075, 1095-9203.

Stanchits, S., Vinciguerra, S., and Dresen, G. (2006). Ultrasonic velocities, acoustic emission characteristics and crack damage of basalt and granite. *Pure Appl. Geophys.*, 163(5), 975–994. ISSN: 1420-9136.

Takano, T. et al. (2014). Seismic velocity changes caused by the earth tide: Ambient noise correlation

analyses of small-array data. *Geophys. Res. Lett.*, 41(17), 6131–6136. ISSN: 1944-8007.

TenCate, J. A., Smith, E., and Guyer, R. A. (2000). Universal slow dynamics in granular solids. *Phys. Rev. Lett.*, 85(5), 1020–1023. ISSN: 0031-9007, 1079-7114.

Touma, R. et al. (2022). Distribution of seismic scatterers in the San Jacinto fault zone, southeast of Anza, California, based on passive matrix imaging. *Earth Planet. Sci. Lett.*, 578, article no. 117304. ISSN: 0012-821X.

van Dinther, C., Margerin, L., and Campillo, M. (2021). Laterally varying scattering properties in the North Anatolian fault zone from ambient noise cross-correlations. *Geophys. J. Int.*, 225(1), 589–607. ISSN: 0956-540X.

Wang, J. and Gadala, M. S. (1997). Formulation and survey of ALE method in nonlinear solid mechanics. *Finite Elem. Anal. Des.*, 24(4), 253–269. ISSN: 0168-874X.

Wang, Q.-Y. et al. (2017). Seasonal crustal seismic velocity changes throughout Japan. *J. Geophys. Res. Solid Earth*, 122(10), 7987–8002. ISSN: 2169-9356.

Zhang, T., Sens-Schönfelder, C., and Margerin, L. (2021). Sensitivity kernels for static and dynamic tomography of scattering and absorbing media with elastic waves: A probabilistic approach. *Geophys. J. Int.*, 225(3), 1824–1853. ISSN: 0956-540X, 1365-246X.

Zigone, D. et al. (2015). Seismic tomography of the Southern California plate boundary region from noise-based Rayleigh and love waves. *Pure Appl. Geophys.*, 172(5), 1007–1032. ISSN: 0033-4553, 1420-9136.

Comptes Rendus

Géoscience

Objectif de la revue

Les *Comptes Rendus Géoscience — Sciences de la Planète* sont une revue électronique évaluée par les pairs de niveau international, qui couvre l'ensemble des domaines des sciences de la Terre et du développement durable.

Ils publient des articles originaux de recherche, des articles de synthèse, des mises en perspective historiques, des textes à visée pédagogique, ou encore des actes de colloque, en anglais ou en français, sans limite de longueur et dans un format aussi souple que possible (figures, données associées, etc.).

Depuis 2020, les *Comptes Rendus Géoscience — Sciences de la Planète* sont publiés avec le centre Mersenne pour l'édition scientifique ouverte, selon une politique vertueuse de libre accès diamant, gratuit pour les auteurs (pas de frais de publication) comme pour les lecteurs (accès libre, immédiat et pérenne).

À propos de la revue

Les *Comptes Rendus Géoscience — Sciences de la Planète* sont exclusivement publiés au format électronique.

Toutes les informations sur la revue, ainsi que le texte intégral de l'ensemble des articles, sont disponibles sur son site internet, à l'adresse https://comptes-rendus.academie-sciences.fr/geoscience/.

Informations pour les auteurs

Pour toute question relative à la soumission d'un manuscrit, merci de consulter le site internet de la revue : https://comptes-rendus.academie-sciences.fr/geoscience/.

Contact

Académie des sciences
23 quai de Conti
75006 Paris (France)
cr-geoscience@academie-sciences.fr

Comptes Rendus
de l'Académie des sciences

Géoscience
Sciences de la Planète

Volume 356, nº S4, 2024

Special issue / *Numéro spécial*

New Developments in Passive Seismic Imaging and Monitoring / *Nouveaux développements dans le domaine de l'imagerie et de la surveillance sismique passive*

Guest editors / *Rédacteurs en chef invités*

Michel Campillo (University Grenoble-Alpes, Institut des Sciences de la Terre, Grenoble, France), Andrew Curtis (School of GeoSciences, University of Edinburgh, Scotland), Anne Obermann (Swiss Seismological Service, ETH, Zurich, Switzerland) and Nikolai Shapiro (CNRS, Institut des Sciences de la Terre, Grenoble, France)

Cover illustration / *Illustration de couverture*

Pierre Boué and Lisa Tomasetto, Figure 5 from the article "Opportune detections of global P-wave propagation from microseisms interferometry", this issue, p. 85–100

Contents / *Sommaire*

1778-7025 (electronic)

Académie des sciences — Paris

Comptes Rendus
de l'Académie des sciences

Géoscience

Volume 356, nº S4, 2024